SCUOLA DI DOTTORATO

UNIVERSITÀ DEGLI STUDI DI MILANO-BICOCCA

Source-to-Sink Sediment Dynamics in Humid and Arid Environments from the Modern Minjiang River, South China and Thar Desert, Pakistan

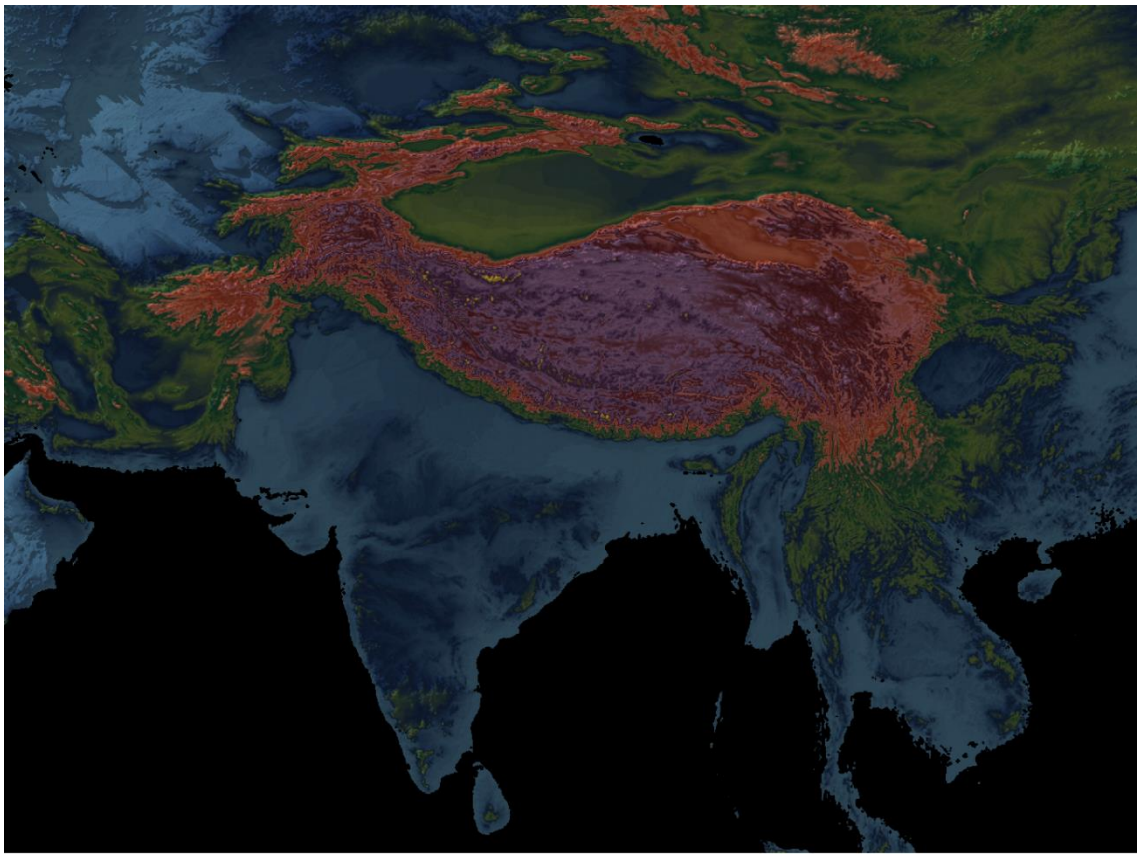

MUHAMMAD USMAN

SCUOLA DI DOTTORATO

UNIVERSITÀ DEGLI STUDI DI MILANO-BICOCCA

Department of Earth and Environmental Sciences

PhD in Chemical, Geological and Environmental Sciences

Cycle XXXVI

Curriculum: Geological Sciences

Source-to-Sink Sediment Dynamics in Humid and Arid Environments from the Modern Minjiang River, South China and Thar Desert, Pakistan

Muhammad Usman

Registration number: 869000

Tutor: Prof. Eduardo Garzanti

Supervisor: Prof. Giovanni Vezzoli

Co-Supervisor: Prof. Peter D. Clift

Coordinator: Prof. Marco Giovanni Malusà

ACADEMIC YEAR 2023

From the earth We created you, and into it We will return you, and from it We will bring you back again. ***(Quran, Ayah Ta Ha (Ta Ha) 20:55)***

Be humble and never think you are better than anyone else. Remember for dust you are and ought dust you shall return.

(Bible, Genesis 3:19)

Abstract

In this comprehensive study, we have delved into the intricate dynamics of source-to-sink systems and provenance studies, shedding light on the processes that govern sediment generation, transportation, and deposition. The term "source-to-sink" encapsulates the excursion of sediments from their ultimate upstream source to the decisive sink area, encompassing erosion, transportation, and deposition with various controlling factors. Provenance studies, rooted in the Latin word "provenire", meaning to originate, have been instrumental in unraveling the lithospheric history of Earth. Over time, advancements in analytical techniques have enabled the determination of sediment sources through compositional frameworks and textural characteristics. The transportation of sediments within drainage systems, governed by sediment-routing systems, preserves a geological record that, as William Blake poetically expressed, allows us to "see a world in a grain of sand". Our exploration extended to understanding the controlling factors for sediment generation, emphasizing the interplay between physical erosion, chemical weathering, tectonics, and climate change. Landscape evolution emerges as a dynamic process shaped by these factors, influencing sediment compositions conserved in the final depocenter. Major siliciclastic transport systems, particularly those draining mountain belts, face complexities due to buffering processes in fluvial-eolian sand seas, where large volumes of sediment are stored and recycled. This PhD thesis presents a comprehensive investigation into sediment dynamics in the Segmented Minjiang River and the western Thar Desert, utilizing an integrated provenance approach.

The Minjiang River (first project), bounded by the tectonically active Songpan Ganzi and the central to southern Longmenshan fault system, offers a unique laboratory for studying geological and geomorphological factors influencing erosion and sediment generation. A detailed provenance budget analysis, incorporating geological domains

and distinct petrographic and heavy-mineral fingerprints, reveals the intricate contributions of various rock units to sediment supply. In the Minjiang River, the results identify quartzo-feldspathic sands within Triassic granites, featuring subequal K-feldspar and plagioclase content. These sands contain granitoid and very-high-rank metamorphic rock fragments, predominantly gneiss and amphibolite. The Triassic strata exhibit varied quartzo-lithic sand compositions, with increasing metamorphic ranks towards Paleozoic units. The study reveals a rich suite of minerals in recycled sands, including tourmaline, apatite, amphibole, and zircon. Silurian units display polymodal zircon distributions. Neoproterozoic granitoid basement showcases a distinct composition dominated by amphibole, epidote, and minor clinopyroxene. Zircon age spectra suggest Tonian source terranes, emphasizing the importance of the Neoproterozoic basement in sediment dynamics. Provenance budget analysis elucidates the complex contributions of various rock units to sediment supply, employing unique petrographic and heavy-mineral fingerprints.

The focus on the Dixie to Yinxiu section demonstrates the crucial role of basement rocks, constituting only 10% of the area but providing 65% of the sediment supply. Sediment generation indices (SGI) based on a commotional framework shed light on the complexities within Songpan Ganzi and the Southern Longmenshan region, including Pengguan massif and Baoxing massif. Comparative analyses with adjacent areas underscore the significance of Precambrian, Paleozoic, and Triassic rock units at the confluence point of the Minjiang River. Extending the study to the Shaotanghe, Heishuihe and Zagunaohe rivers, the research unveils the distinct influence of Triassic, Paleozoic, and basement rock units. The SGI variations within these units suggest relationships with lithological characteristics, altitude, and potential soft rock attributes. The examination of the entire Minjiang catchment further emphasizes the equal contributions of Triassic and basement rock units, elucidating the nuanced interplay of contributing area, rock resistance, and altitude with earthquakes.

The Thar Desert (second project) is a major sediment depocenter in southwestern Asia and borders the Indus drainage system to its east. It is unclear where the sediment that built the desert is coming from, and when the desert experienced phases of construction. Major deserts must be supplied with sediment in order to accrete and the Thar Desert that lies east of the Indus River in SW Asia is expected to be largely derived by supply from that major drainage. In particular, we seek to establish the role of the South Asian monsoon in the initial formation and subsequent expansion of the desert.

Abstract

Here we integrate bulk-petrography and heavy-mineral data with U-Pb ages of detrital-zircon, to understand how the desert relates to the major potential sediment sources in the Himalayan orogen and to the major rivers that surround it. Bulk petrography and heavy mineral data from eolian sand in Cholistan (NE Pakistan) show close similarity with that of Himalayan tributaries, whereas eolian sand in Sindh (S Pakistan) contains heavy-mineral suites close to those of Indus sand largely supplied by erosion of the Karakorum and Kohistan. Kohistan is a particularly rich source of heavy minerals and is thus over-represented in sediment budgets based on that proxy alone. U-Pb ages of detrital-zircon fail to show a sharp difference between dune sands in Sindh and Cholistan, except for revealing somewhat greater supply from the Himalaya in Cholistan and from the Karakorum, Kohistan and Nanga Parbat in Sindh. Zircon ages are similar in Sindh Desert sand and in the Indus Delta and are most similar in deltaic sand dated as 7 ka or older. In parallel, the age signature of Cholistan sands resembles more that of older river channels found along the northwestern edge of the desert (e.g., paleo-Ghaggar-Hakra) than that of modern Himalayan tributaries (e.g., Sutlej). Both Cholistan and Sindh sands suggest that sediment supply to the desert was greater in the early Holocene when the monsoon was stronger. The southwesterly summer monsoon turned out to be the most effective agent of eolian transport and recycling of Indus delta sediments entrained towards the central and northern parts of the desert.

In this study, we use a combination of major and trace element bulk sediment geochemistry, combined with Sr and Nd isotopes, together with trace elements in detrital single rutile grains in order to constrain where the sediment in the desert is coming from. We find that the major and even trace element characteristics are largely controlled by grain size rather than provenance. Bulk sediment isotope data is the best provenance proxy, although trace elements that are sensitive to the influence of mafic igneous rocks can also be useful. This data indicates a stronger influence from mafic source rocks in the southern part of the desert, in Sindh, compared to in the north (Cholistan). The Indus delta and lower reaches appear to be the greatest supplier, but with significant influence from Himalaya-derived tributaries in Cholistan but less influence from that source in Sindh. This implies that NE-directed monsoon winds are controlling the supply of sediment to the desert. Detrital rutile data indicate that most of the sources are from pelitic metamorphic rocks exposed in the Greater Himalaya and Karakorum. The Thar Desert sediments are slightly less weathered than the sediments in the modern river, with the Sindh Desert more weathered than Cholistan. Both deserts

and the modern river are relatively fresh when compared with ancient foreland sedimentary rocks, such as those in the Siwalik Group. Recycling of sediment from temporary storage in the floodplains may be important in explaining the alteration difference between the desert and the river, although long-term recycling via the Siwaliks does not seem to be important. It is difficult to resolve the competing influence of fresh sediment supply in the mainstream of the river compared to recycling from the desert when trying to account for the net supply sediment from the Indus to the Arabian Sea.

In conclusion, our research contributes valuable insights to the broader understanding of source-to-sink systems, provenance studies, and sedimentary processes. The integration of advanced analytical techniques and quantitative approaches enhances our ability to interpret Earth's geological history, providing a foundation for future studies in sedimentary geology, paleoclimatology, and landscape evolution.

Contents

Chapter 1
Introduction

1.1. Source-to-Sink and Provenance Studies

Source-to-sink system is a unique and complete suite of methods that is used to forensic the sediments within the sedimentary system from headwater of source in the continental realm to the sink. The system involves the contribution of sediments to the decisive sink area by erosion, transportation, and deposition with various controlling factors from the ultimate upstream source (Fig. 1.1). The Source-to-sink term was first reported by Meade (1972, 1982), after that their integrating studies were conducted by Dickson (1997) and Hovius and Leeder (1998) to link various sediment sources and basin datasets in sedimentary geology. The advancement of these studies is useful to analysis the complete sedimentary system including paleoclimatic conditions, continental and geomorphological studies, with classic sedimentary analysis and tectonic effects on the sediment generation and provenance.

The term “provenance” is reflected from a Latin word “provenire” that is *to come forth* or *to originate* (Weltje and von Eyantten, 2004), its studies are used to get all the answers related to the lithospheric history of Earth (Basu, 2003). Sediment or sand provenance (sensu lato, used for sand fraction) studies lead to research for temporal and spatial distribution of sand seas and reconstructions of tectonics, volcanism and paleoclimate in different sedimentary systems (Bagnold, 1946; Werner, 1995; Telfer and Hesse, 2013; Liang et al., 2020). Provenance studies, particularly focusing on the sand fraction, play a decisive part in advancing our understanding of Earth's geological history. These deductive investigations offer valued insights into the temporal and spatial distribution of sand seas, aiding in the reconstruction of different geological events in various sedimentary systems, notably in rivers and deserts (Caracciolo, 2020; Weltjie & Von Heynatten, 2004). The clarity of the concept of sand provenance studies is needed to build a conceptual model for the history of sediments, how and from where sediments have been eroded and deposited with which controlling factors. This will be helpful to interpret and to unravel the ambiguities related to sediments history from parent rocks to the depositional basin (Weltje and von Eyantten, 2004). For these targets, analytical studies of sand and sediments provenance play a vital role for the determination of transport paths of sediments to get involvement at basinal scale (Zhang and Wang, 2019). The final products of provenance studies are used to determine the

source areas from the different kinds of analytical analysis which started from the nineteenth (19^{th}) century. These measurements of provenance studies depict the different analogues for compositional framework to the textural characteristics of the sediments (Pettijohn et al., 1987; Weltje and von Eyantten, 2004; Garzanti et al., 2014, 2020; Caracciolo, 2020). First time in the history of the provenance studies, the ancient sediments were studied by the Thürach (1884) through the accessory minerals. The researchers Ludwig (1874), Meunier (1877) and Michel Lévy (1878), first reported the provenance history from the accessory minerals for the beach and river recent sand seas. In 1895, researchers used mineral characterization for the demonstration of paleogeographic topography with ancient drainage directions of rivers and sediments containing igneous and metamorphic accessory minerals from source to sink (Retgers, 1895).

The transportation of the sediments in the drainage system is mainly controlled by the sediment-routing system which preserves the long history of the geological record (Fig. 1.1). That is why a famous poet William Blake said, “see a world in a grain of sand”. Sediment flux and their transportation are controlled by the capacity of fluvial as well as alluvial sand systems that is useful to understand the capacity conditions of the potential source (Pease and Tchakerian, 2002; Field et al., 2009; Belnap et al., 2011; Garzanti et al., 2012; Rittner et al., 2016). These sand systems of fluvial and alluvial (when begin their operation together) are most important agents for the accumulation space of sediments for arid environments (Bullard and Livingstone, 2002; Hollands et al., 2006; Field et al., 2009; Belnap et al., 2011) such as buffering system and desert. The term “desert” frequently having various meanings in scientific fields as verb, adjective, and noun that refers to abandon, uninhabited region, and a bare or water less land (Verstraete, 1986). Deserts are major part of earth curst at the subtropical sides of middle latitudinal zones that contains sand seas of terrestrial landscapes (Pye and Tsoar, 2009; Livingstone and Warren, 2019; Liang et al., 2020). Sand seas of deserts are widely used to unravel the provenance studies that are mainly controlled by topography, climate, and transport conditions of wind energy (Pye and Tsoar, 2009; Warren, 2013; Garzanti et al., 2013; Rittner et al., 2016). The development of deserts for the deposition of sand seas is dependent upon the flux of the sediment supply and availability (Kocurek and Lancaster, 1999; Lancaster, 2013).

1.2. Controlling Factors for Sediment Generation

Landscape evolution is linked to the competing effects of physical erosion and chemical weathering that in turn are controlled by tectonics and climate change (Burbank et al., 2003; Reiners et al., 2003; Riebe et al., 2004; Clift et al., 2020). Changing intensities of physical erosion and chemical weathering result in changing sediment compositions that may be conserved in the final depocenter, albeit modulated by buffering between source and sink (Allen, 2008). Changing climate influences the environment and controls the intensity of chemical weathering by controlling the rate of alteration, as well as the speed and duration of sediment transport between the source and the sink (Herman and Champagnac, 2016; Huntington et al., 2006; Neubeck et al., 2023). Changing climate can influence patterns of erosion and in turn the origin of the sediment, which is eventually found in the lower reaches of any given catchment. Depending on the rate of sediment transport, significant amounts of chemical weathering may occur in floodplains on the way between mountain sources and the river mouth and lower reaches. Patterns and rates of erosion are also influenced by tectonic processes, rejuvenating, or diminishing source terrains, as well as by climate-modulated surface processes that vary over orbital and shorter timescales ($<10^5$ y) (Colin et al., 2010; Fildani et al., 2016; Mason et al., 2019).

Source-to-sink studies in major siliciclastic transport systems, especially those draining major mountain belts are complicated by the buffering processes involved with fluvial-eolian sand seas (Fig. 1.1). Large volumes of sediment may be stored and then recycled as a river system passes through a sandy desert area on its way to the final depocenter. Changing paleoenvironmental conditions may exercise an important control on how sediment is transported through or recycled within desert areas. In particular, changing precipitation amounts and seasonality may have an important impact on the growth or reduction of desert sand areas and their impact on the associated river. The fraction of sandy sediments first stored in a desert system after removal from the river is referred to as the net loss of the sediments from the source system (Trimble, 1983; Petter et al., 2013). These stored sediments may subsequently be eroded and mixed with more fluvial sediment within the drainage basin. Buffering and recycling of sediment in this way may disrupt the propagation of erosional signals related to climatic change or tectonic events (Whipple, 2001; Alizai et al., 2011; East et al., 2015).

1.3. Quantitative Provenance Analysis

Quantitative provenance analysis (QPA) is employed in our studies which is integrating graphical and statistical tools to systematically characterize the quantitative attributes of sediments. The fundamental premise of QPA involves the application of linear mixing forward and inverse modeling techniques to assess the contributions of individual or distinct source rocks to sedimentary sinks or buffering systems (Weltjie and Eynatten, 2004; Caracciolo et al., 2020). This analytical approach, as articulated by Vezzoli et al. (2013), Garzanti et al. (2018a, 2018b), and Fielding et al. (2018), is instrumental in unveiling the controlling factors governing the textural composition and alterations observed in sedimentary deposits. QPA provides a comprehensive suite of analyses, encompassing assessments ranging from sediment generation rates to erosion rates, sediment budgets, and facilitating source-to-sink interpretations (details in Chapters 3 and 4).

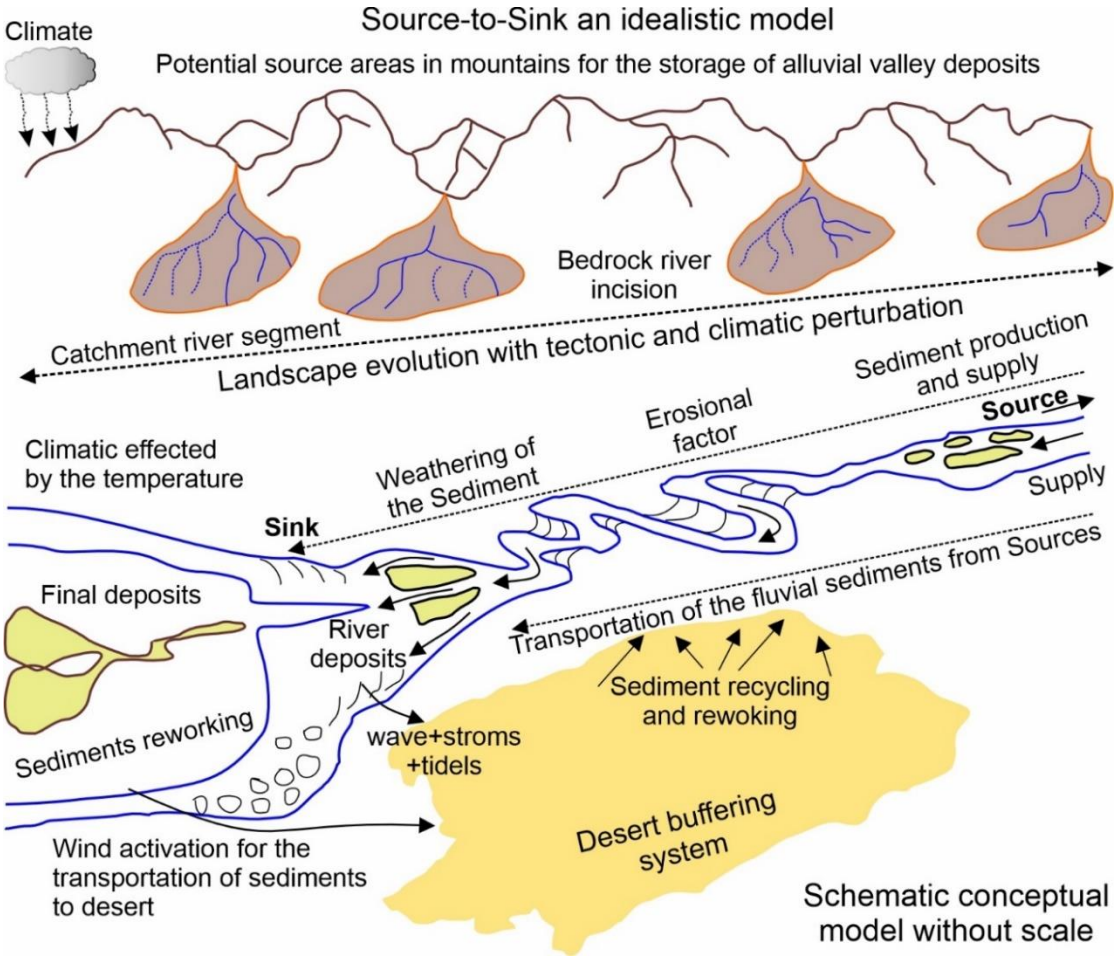

Figure 1.1. Schematic conceptual model for source-to-sink studies including the potential sources from the storage areas of alluvial deposits in mountainous areas with the detailed illustration of the transporting agents to store the sediments into the alluvial buffering system

by the strong wind activation and their further reworking and recycling towards the fluvial environment.

The synthesis of graphical and statistical tools within the framework of QPA serves as a robust methodology for gaining insights into the intricate dynamics of sedimentary systems and their evolution over time (details in Chapters 5 and 6).

1.4. Thesis Projects

The scope of this study encompasses a comprehensive investigation into sediment dynamics within contrasting environmental settings, specifically focusing on two distinct projects (Fig. 1.2). The first project centers on the Minjiang Basin, involving an analysis of sediment generation and budgeting. Concurrently, the second project explores sediments supplying and reworking processes contributing to the buffering depocenter adjacent to the Indus River within the Thar Desert region. Despite the apparent disconnection in both geographical and geological aspects of these projects, their selection was deliberate and strategic. The decision to undertake investigations in these divergent geological settings was primarily predicated on the availability of pertinent samples. Furthermore, the deliberate choice of two dissimilar environments serves the overarching goal of advancing our understanding of sediment dynamics under disparate conditions.

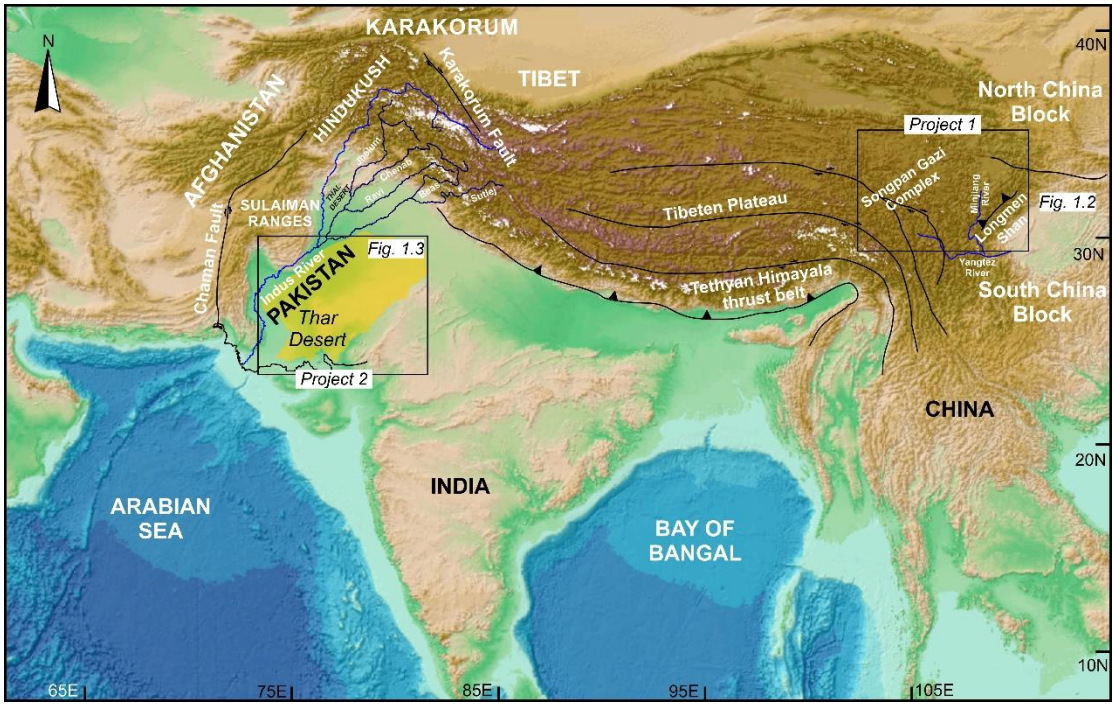

Figure 1.2. Geographical locations of both projects for this study. Project 1 (fig. 1.2): Minjiang River is mainly bounded by the Songpan Gazi complex and Longmenshan Mountains in the

north to South China blocks. Project 2 (fig. 1.3): Thar Desert and it is bounded between the India and Pakistan; Indus River is mainly drained from the NW Himalaya.

This approach allows for a nuanced examination of the diverse factors influencing sediment transportation processes and contributes to a more holistic comprehension of sedimentary systems.

1.4.1. Minjiang Basin, Longmenshan Mountain Belt, SW China

Sediment generation and provenance analysis of the fluvial sediments in the Longmenshan and the segmented Minjiang sediment routing system based on sand petrography, heavy minerals, and detrital U-Pb zircon geochronology analysis (details in Chapters 3 and 4). Provenance budget and sediment yield analysis was also modulated based on the statistical dataset to quantify the erosion rate of the sediments for the Songpan Ganzi and Longmenshan Mountain Belt.

1.4.2. Sediment Routing System in the Minjiang Basin, SW China

Our understanding is to quantify the sediment generation in the Minjiang catchment which is build up by a complete set of routing system of Qinling-Dabie Belt, the Songpan Ganzi Triassic sedimentary basin, and the Longmenshan Belt (Deng et al., 1995; Chen and Wilson, 1996; Wallis et al., 2003) (Fig. 1.3; details in chapter 3). The Minjiang River cuts gorges from 1 to 3 km deep across the Longmenshan in its mountain tract and is originating from eastern margin of Tibetan Plateau and flows along Wenchuan-Maoxian fault and ultimately making confluence into the Sichuan Basin at Dujiangyan (Liu and Yang, 2015). This is a laboratory which is very useful for the investigation of the geological and geomorphological factors on the areal distribution of erosion and sediment generation, including rock uplift, topographic relief, climate, and lithology. The annual sediment discharge in the upper reaches of the Minjiang River before the Wenchuan earthquake presented a downward trend overall. It decreased by about $3.2*10^6$t from 1980 to 2007, which represents approximately 4.5% of the annual average sediment discharge. After the Wenchuan earthquake in 2008 sediments increases from 13.8% to 70%, time of the post seismic flash floods and debris flows have centered with consistency rainfall from July to September. The increasing range of the sediments varied yearly due to the triggering of debris flows. That is interlinked with the rainfall intensity which is more integrated with pre-accumulation rainfall and debris flows. Because of tremendous tectonic activity along major strike-

slip faults, catastrophic landslides frequently occur in the mountainous part of the Minjiang catchment (Xu et al., 2020).

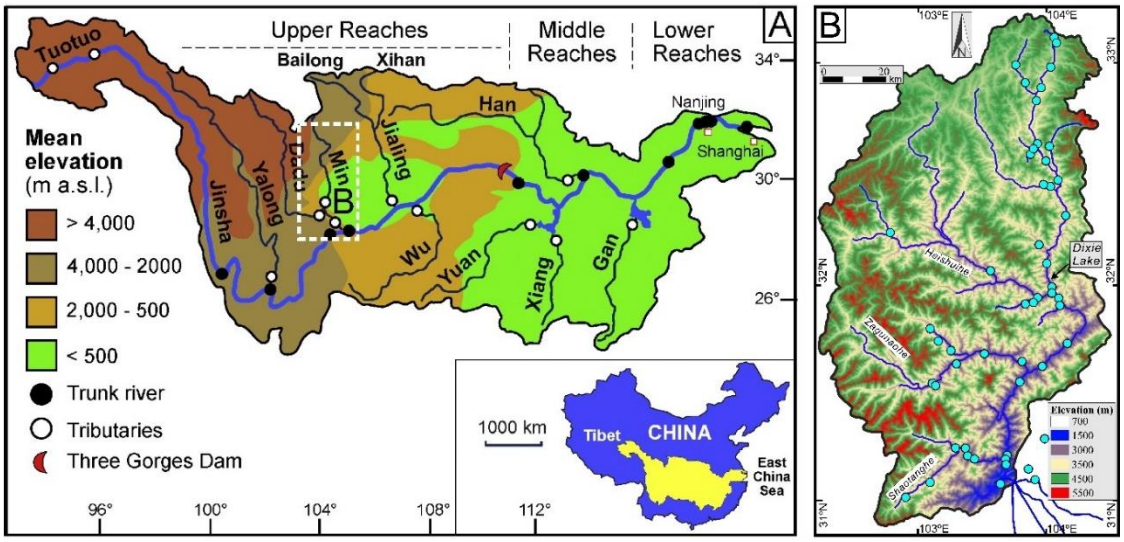

Figure 1.3. A) Location map of the Minjiang River which is a main tributary of the Yangtez River. B) Digital elevation model of the Minjiang River with the location of the collected samples.

1.4.3. Thar (Sindh and Cholistan) Desert, NW Himalaya, Pakistan

First phase of the Thar (Sindh and Cholistan) Desert project (Fig. 1.4; details in Chapters 5 and 6) is to quantify the fluvial and aeolian sediment buffering system for the understanding of the influence that climate change has had on sediment transport through the source to desert using bulk petrography, heavy mineral assemblages and detrital U-Pb zircon age analysis. We demonstrate how sediments are transported to and distributed within the Thar Desert in recent times. The sediments can be used to understand the impact of paleoenvironmental and climatic changes during the Holocene in the Western Himalayas and how these control sediment transport in the modern sand seas of the Thar Desert.

Second phase of the Thar (Sindh and Cholistan) Desert project is to address the origin of sediments in the modern desert through a series of proxies that attempt to quantify the primary sources to different parts of the desert, as well as to understand the impact of chemical weathering on the composition of sediment now preserved in the desert. We use a combination of grain size analysis, bulk sediment geochemistry major and trace element composition to constrain the origin of the desert sands and to better understand the processes that have allowed the desert to form. Sr and Nb radiogenic

isotopes and single grain rutile trace element analyses were used to further constrain the source of Thar dune sediments (Fig. 1.3; details in Chapters 5 and 7).

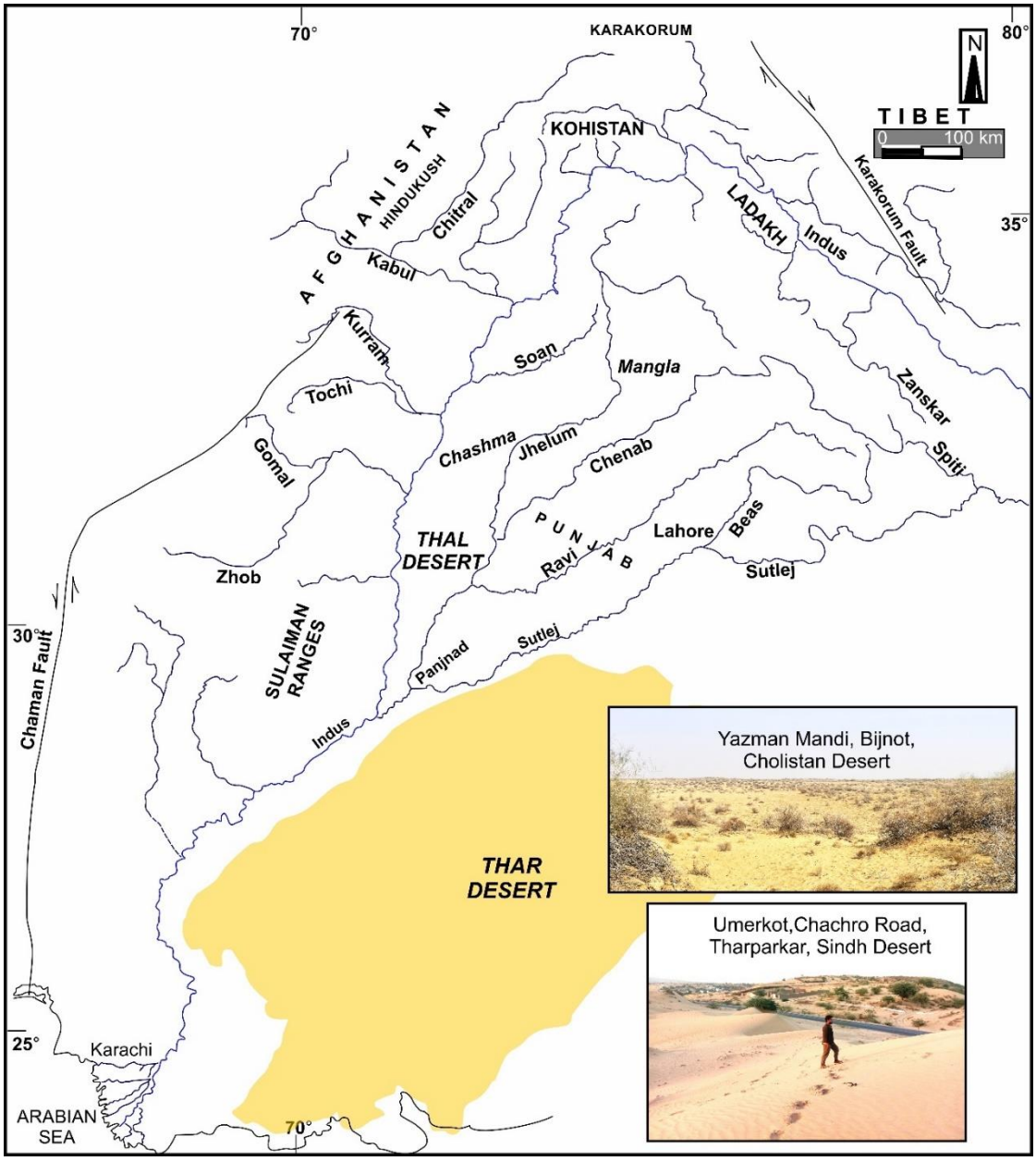

Figure 1.4. Figure shows location of Thar Desert and modern Indus River with tributaries from NW Himalaya. Insert photographs showing the beauty of the Sindh Desert from Umerkot Chachro Road, Tharparkar and Cholistan Desert from Mandi, Bijnot Road.

1.4.4. Quantification of Sediments Transportation for Thar Desert

Our ability to resolve the factors that control the fluvial and aeolian sediment transport is affected by mixing of new and recycled sediment within the basin. we better quantify the processes that control sediment storage and recycling in the Thar Desert in south-west Asia related to the Indus drainage system that dominates the western side of

the Himalayas, Tibetan Plateau, and Karakorum (Fig. 1.4; details in Chapter 5). By understanding how this sediment filtering system works, we enhance our ability to interpret the more continuous marine sedimentary depositional record downstream in the Arabian Sea.

The efficiency of the sediment supply to the Thar Desert is controlled on long timescales (>10^4 y) by the interaction between the monsoon climate and the rock uplift that is occurring in the active mountain belts of the Himalaya and Karakorum. This is a suitable region for studying this type of source-to-sink problem, because of the strong intensity of the Southwest monsoon system, and the large and tectonically active character of the sources, providing strong signals in the sediment that is carried into the lower reaches of the Indus River.

These orogenic belts are the result of the ongoing collision between the Indian and Eurasian continents since 55–60 Ma (Garzanti et al., 1986, 1996; Critelli et al., 1994; Hu et al., 2015; Najman et al., 2003, 2017). These ranges are drained by the Indus River across the western third of the orogeny. Ongoing tectonically driven rock uplift coupled with erosion is responsible for the extreme high relief and rapid exhumation found in the western Himalayan syntaxis (Zeitler et al., 1993; Garzanti et al., 2020a, b). If we are to understand the tectonics and erosion of this mountain belt over million-year timescales, then this can only be achieved using the Indus River and its associated sedimentary system because the record of past exhumation has been removed from the source ranges themselves by erosion. In contrast, the sediment record in the Arabian Sea and Himalayan foreland basin can be used to reconstruct changing patterns and rates of erosion through provenance studies of the detrital sediment flux from the orogenic region (Clift et al., 2001; Clift et al., 2008; Clift and Jonell, 2021). In recent times, all of the sediment flowing from source into the ocean basin has to pass next to or through the Thar Desert, although the processes that operate in this region are not well understood.

1.4.5. Fluvial and Aeolian Interaction for Thar Desert

Studies of sediments in arid and semi-arid regions rarely include consideration of the interactions that occur during fluvial and aeolian transport (Belnap et al., 2011). These are likely to introduce complexities to the original erosional pulse that might be linked to environmental change, and whose composition closely reflects the bedrock.

In the case of the Indus alteration of the sediment may happen in the Thar Desert, which is located in eastern Pakistan and NW India (Fig. 5.1; details in Chapters 6 and 7).

In the Thar Desert the complex nature of sediment transport and recycling in the aeolian system is poorly constrained. However, better understanding is critical if we are to constrain the ongoing interaction of fluvial and eolian processes during source-to-sink transport. The sediments stored in the desert reflect the net effects of sediment transport from hillslope to alluvial channels and finally to the dryland area (Ramsey et al., 1999; Prins et al., 2009; Bracken et al., 2015). This transport may be modulated by changes in the environment, as well as in the development of the drainage system that may also be sensitive to tectonic influences. Because the region of the Thar Desert is arid-semiarid it is sensitive to the influence of fluvial activity and changing climate. The fluvial sourced eolian sands are stored in dunes and transformed through reworking by the wind. Subsequently, the sediments may interact further with the river and continue their journey to the ocean (Bullard and Livingstone, 2002; Bullard and McTainsh, 2003; Alizai et al., 2011). Wind is a strong transforming agent that can move sediments tens to hundreds of kilometers from the original fluvial source (Langford, 1989) where they may be stored in various depositional systems, such as the Thar Desert. In the Thar Desert, studies of fluvial-eolian interactions may be interpreted as a reflection of the climatic changes and evolving tectonics if they occur over $>10^6$ y timescales.

1.4.6. Monsoon System due to Climate Change in the Thar Desert

Over Earth's history, climate-modulated surface processes operating over various timescales have been responsible for changing the position of deserts, although it should be remembered that deserts will also preferentially form in the rain shadow areas of tectonically generated mountain ranges. Deserts may form, significant sediments volumes that may buffer the flux of sediment between mountain sources and their final depocenter. Climate change by the summer monsoon affects the wind across the Thar Desert, which moves sediments from southwest to northeast (Wasson et al., 1984; Singhvi and Kar, 2004; East et al., 2015). This summer interaction, as well as the reverse in the winter, reflect the hot pre-monsoon months in the southwest Indian subcontinent, which include dry, windy conditions and associated dust storms in the late summer rain (Singhvi et al., 2010).

In this study, we attempt to understand the origin of sediment supply to the Thar desert of Southwest Asia, and to understand its links with the drainage of the Indus River, and its tributaries that lie immediately to the west (Figs. 6.1 and 7.1; details in Chapters 6 and 7). The semi-arid Thar Desert in the north-western Indian sub-continent is significantly influenced by the southwest Monsoon system. The sediments of the Thar Desert are largely derived from the western Himalaya with supply from tributaries flowing from the east, as well as from the Indus mainstream that brings material from the Karakorum and associated ranges such as Kohistan and Nanga Parbat. This zone of sediment dunes is affected by monsoon winds over a variety of timescales. These same winds bring rain especially focused on the southern flank of the western Himalaya (Bookhagen and Burbank, 2006) from where much of the sediment is supplied. In general, warmer conditions with higher humidity play a significance role in enhancing chemical weathering and the production of clay minerals, due to the strong linkage between climate and rates of chemical weathering (Kump et al., 2000; West et al., 2005). Weathering results in a relative loss of water-mobile elements (i.e., Na, K, Sr) from the original bulk composition, allowing weathering intensity to be quantified (Nesbitt et al., 1980).

Chapter 2
Sampling Strategy and Methodology

2.1. Sampling Strategy

The best modern sand sample in everywhere is simultaneously consists of approximates “neutral” composition, that would have no effects of local hydraulic sorting. Sand is in the drainage and buffering systems, however, is a crucial factor to collect the representative samples. The main factors are the grain sizes and the local enrichment or depletion in heavy minerals, which may change from place to place. To avoid the main crucial problem for representative samples, Garzanti and Andò (2019) reported a detailed method for different environments as concerning for the grain size, representative samples from all sites within the area should be possible similar to the dominant grain size and for practical reasons it also should be in consideration to have the lower-fine to lower-medium sand range. Sample volume does not need to exceed 50–100 g and, provided the collected grain-size window is appropriate and separation procedures designed to maximise recovery, which is more than enough for the geochemical or geochronological study of any accessory mineral. Besides representativeness, the sampling plan must follow criteria that maximise consistency and comparability among samples. The criterion we currently use in dune fields is to collect sand systematically from the crest at the top of the largest dune in the area (Fig. 2.2a-i). River sand samples were collected from the main point bar sections of the main and tributaries of the complete drainage (Fig. 2.1a-i).

2.1.1. Minjiang Drainage or River System Site

For this study, we have collected 58 sand samples from active fluvial bars across the Minjiang catchment, from the Tibetan headwaters to the Sichuan Basin (Fig. 3.1). Full information on sampling sites is given in the Appendix. Significant detrital components are listed in order of abundance (high to low) throughout the text. Key compositional parameters are summarized in Table 4.1. The complete petrographic, heavy-mineral, and geochronological datasets are provided in the Appendix.

2.1.2. Thar Desert Site

For this study, we collected 50 sand samples from the Sindh province in the southern Thar Desert and 40 sand samples from the Cholistan province in the northern Thar Desert (Fig. 5.1). Complete information on sampling sites is given in the Appendix. The

complete petrographic, heavy-mineral, and geochronological datasets are provided in the Appendix.

2.2. Methodology

Representative sand samples were selected from both the Minjiang River and the Thar Desert and were used in different methodologies (Table 2.1).

2.2.1. Grain Size Analysis

Sand samples of Minjiang River and Thar Desert were used to measure the sediment grain size by the set of mechanical sieves according to the Folk and Ward, (1957) classification in the Laboratory for the provenance analysis at University of Milano-Bicocca, Italy. Assemble the sieve stack in downward descending order in terms of mesh diameter from 2 millimeter (mm) to 63 micrometer (μm) and a pan on the bottom. The known weight of sample (almost 100g) was taken, which is the initial weight (M2). Then pour the sample on the topmost sieve and vibrate the sieve stack by the mechanical vibrator for 5 minutes and note the retained fraction of the sample in each pan as weight after sieve (MI). For the weight of retained fractions (MD), following formula was used in each sieve equation,

Figure 2.1. Different sand sampling sites of the Minjiang River, South China.

"MD (Difference) = M2 (Initial Weight) – M1 (Weight after sieve)"

Then converted the net sample weight into percentage. The same procedure of the sieve analysis was done with all sand samples. Conversion of this percentage fraction data into cumulative weight percentage was used for calculating the other statistical parameters i.e., sorting, mean, median, standard deviation and skewness.

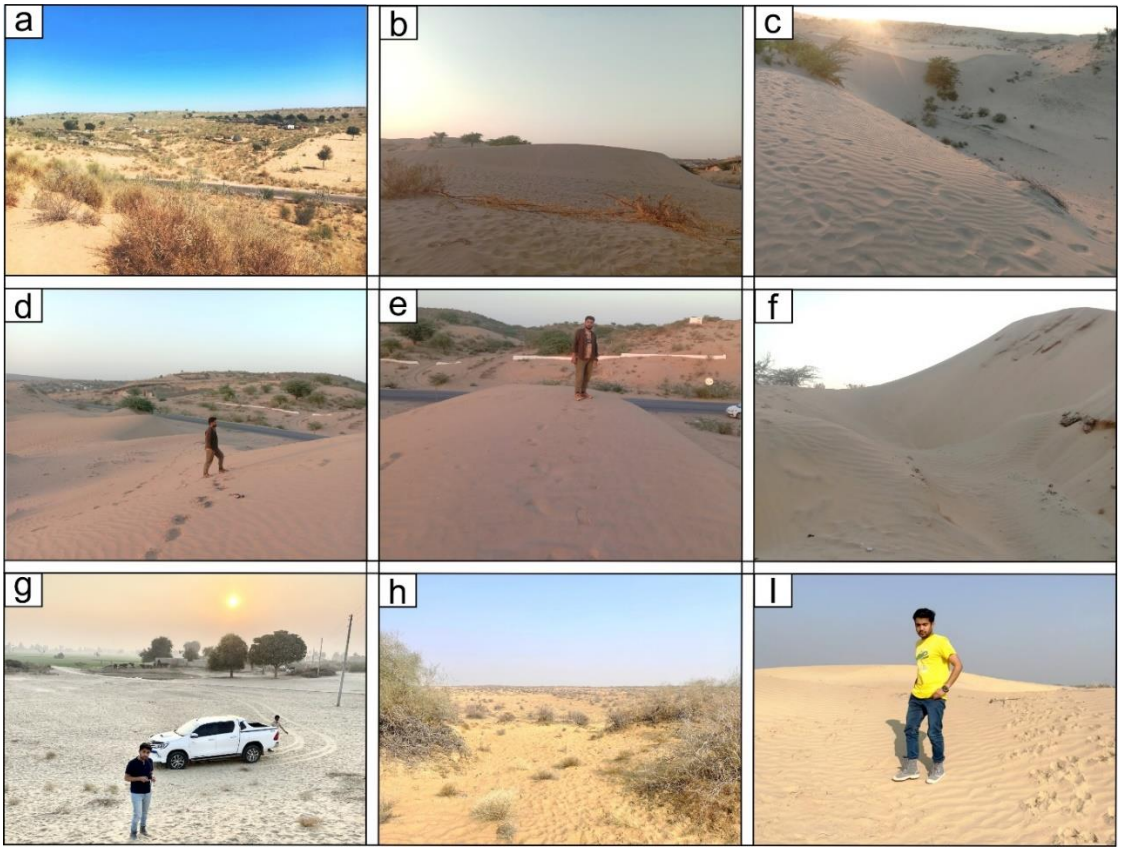

Figure 2.2. Different sand sampling sites of the Thar Desert, NW Himalaya, Pakistan.

Table 2.1. Representative sand samples were used in different methodologies.

Projects	GSZ	PT	HM	DZ	XRF	Rutile	Sr/Nd
Minjiang	58	58	58	18	-	-	-
Thar	27	27	27	5	27	5	16

2.2.2. Sand Petrography

A quartered fraction of each sand sample from Minjiang River and Thar Desert was impregnated with araldite epoxy and cut into a standard thin section stained with alizarine red to distinguish dolomite and calcite. Petrographic analysis was carried out by counting ~450 points under the microscope according to the Gazzi-Dickinson method (Ingersoll et al., 1984). Sand classification was based on the relative abundance of the three main framework components quartz (Q), feldspars (F) and lithic fragments

(L), considered if exceeding 10%QFL. According to standard use, the less abundant component come first in the naming and the most abundant last (e.g., a sand is named feldspatho-litho-quartzose if Q > L > F > 10%QFL or quartzo-lithic if L > Q > 10%QFL > F; classification scheme after Garzanti, 2019). Metamorphic grains were classified according to their protolith and metamorphic rank, expressed by the metamorphic indices MI and MI* (Garzanti and Vezzoli, 2003). MI varies from 0 (detritus shed by sedimentary and volcanic cover rocks exclusively) to 500 (very-high-rank detritus exclusively shed by high-grade basement rocks). MI* considers only metamorphic rock fragments and thus varies from 100 (very-low-rank detritus shed by very low-grade metamorphic rocks) to 500. Petrographic parameters used in this article include the plagioclase/total feldspar (P/F) ratio; feldspar identified by crosshatch twinning is referred to as microcline. Median grain size was determined in thin section by ranking and visual comparison with in-house standards composed of mounts of sieved Φ/4 classes. Significant detrital components are listed in order of abundance (high to low) throughout the text. Key compositional parameters are summarized in Tables 4.1 and 6.1. The complete petrographic, heavy-mineral, and geochronological datasets are provided in the Appendix.

2.2.3. Heavy Minerals

From a split aliquot of the 15–500 μm size window obtained by wet sieving, heavy minerals were separated by centrifuging in Na-polytungstate (2.90 g/cm^3) and recovered by partial freezing with liquid nitrogen. For each sample, ~250 transparent heavy minerals (or all of those present in the grain mount) were point-counted at appropriate regular spacing to minimize overestimation of smaller grains. Transparent heavy-mineral assemblages, called for brevity “tHM suites” throughout the text, do not include alterites, phyllosilicates and carbonates (Garzanti and Andò, 2019). According to the transparent-heavy-mineral concentration in the sample (tHMC), tHM suites are defined as extremely poor (tHMC < 0.1), very poor (0.1 ≤ tHMC < 0.5), poor (0.5 ≤ tHMC <1), moderately poor (1 ≤ tHMC <2), moderately rich (2 ≤ tHMC <5), rich (5 ≤ tHMC < 10), or very rich (tHMC > 10). The sum of zircon, tourmaline, and rutile over total transparent heavy minerals (ZTR index of Hubert, 1962) measures the relative proportion of durable minerals in the tHM suite and can thus be considered as an index of recycling (Garzanti, 2017). Key heavy mineral parameters are provided in Tables 4.1 and 6.1 and the complete dataset in Appendix.

2.2.4. Detrital Zircon Geochronology

Detrital zircons were identified by automated phase mapping (Vermeesch et al., 2017) with a Renishaw inVia^{TM} Raman microscope on the heavy-mineral separates of eighteen samples from Minjiang River and five samples from Thar (two from the Cholistan and three from the Sindh Desert). These grains were concentrated with standard magnetic techniques and directly mounted in epoxy resin without any operator selection by hand picking. U-Pb zircon ages were determined at the London Geochronology Centre using an Agilent 7900 LA-ICP-MS system, employing a NewWave NWR193 Excimer Laser operated at 10 Hz with a 25-lm spot size and ~ 2.5 J/cm^2 fluence. No cathodo-luminescence imaging was done, and the laser spot was always placed blindly in the middle of zircon grains to treat all samples equally and avoid bias in inter sample comparison ('blind-dating strategy' as discussed in Garzanti et al., 2018b). The mass spectrometer data were converted to isotopic ratios using GLITTER 4.4.2 software (Griffin, 2008), employing Plešovice zircon (Sláma et al., 2008) as a primary age standard and GJ-1 (Jackson et al., 2004) and 91500 (Wiedenbeck et al., 1995) as a secondary age standard (Appendix). A NIST SRM612 glass was used as a compositional standard for U and Th concentrations. GLITTER files were post-processed using IsoplotR (Vermeesch, 2018). Concordia ages were calculated as the maximum likelihood intersection between the concordia line and the error ellipse of $^{207}Pb/^{235}U$ and $^{206}Pb/^{238}U$ (Ludwig, 1998). The discordance cutoff was set at –5/+15 of the concordia distance (Vermeesch, 2021). Concordant Ages are provided in the Appendix.

2.2.5. Geochemical Analysis (XRF)

Bulk powder of twenty-seven samples for major and trace element geochemistry were processed and analyzed in the Chevron Geomaterials Characterization Laboratory at Louisiana State University (LSU), USA. The samples were ground in a mortar and pestle and then transferred into a hardened steel vial to be milled to a grain size of <30 μm using a SPEX Sample Prep 8000M Mixer/Mill. Approximately 2.00 ± 0.02g of powder from each sample were weighed and placed in a furnace at 900°C for two hours. Upon removal from the furnace, the sample powders were re-weighed and their loss on ignition (LOI) was calculated.

Analysis was carried out using the Bruker S2-PUMA energy-dispersive X-ray fluorescence (XRF) instrument. The analyses were calibrated using nineteen international standards, including AGV-2, BIR-1a, G-2, GSP-2, RGM-1, SDC-1, and W-2 from the United States Geological Survey (USGS), JA-3, JB-2, JB-3, JG-2, JG-3, JR-1, and JP-1 from the Geophysical Survey of Japan (GSJ), and BCS-309, BCS-313-2, BCS-375, BCS-376/1, and BCS-388 from British Chemical Standard (BCS). Replicate analysis (N=5) of the USGS AGV-2, BIR-1a, and SDC-1 standards was performed to check for drift and assess the quality of the calibration prior to analysis. Secondary standards were analyzed during every analytical run-in order to monitor for instrumental drift and assess the continued quality of the calibration. These secondary standards were chosen according to their homogeneity and similarity to the estimated compositional range of the unknown samples. Results are presented in Tables 7.1 and 7.2.

2.2.6. Sr and Nd Isotope studies

Sr and Nd isotopes of eleven samples were measured from powdered whole sediment samples. After decarbonation with 10% acetic acid and dissolution, Sr and Nd were concentrated using standard column extraction techniques, and isotopic compositions were determined by Thermo "Neptune" multi-collector inductively coupled plasma mass spectrometer (MC-ICP-MS) at Woods Hole Oceanographic Institution. Sr results were corrected against NBS 987 standard $^{87}Sr/^{86}Sr=0.710240$ and Nd data were corrected against JNdi-1 standard $^{143}Nd/^{144}Nd = 0.512104$. We calculate the parameter ε_{Nd} (DePaolo and Wasserburg, 1976) using a depleted-mantle model age and a $^{143}Nd/^{144}Nd$ value of 0.512630 for the Chondritic Uniform Reservoir (CHUR (Bouvier et al., 2008)). Results are presented in Table 7.3.

2.2.7. Rutile Geochemistry

Starting from the heavy-mineral separates of five samples (two from the Cholistan Desert and three from the Sindh Desert), From the heavy-mineral separate of 5 dune sands samples, detrital rutiles were concentrated with standard magnetic techniques, directly mounted in epoxy resin, exposed, polished, and identified by automated phase mapping (Vermeesch et al., 2017) with a Renishaw QONTOR™ Raman microscope (laser 532 nm; 15 cycles of 0.5 s each; 50× magnification; laser power 10 mW on samples). The collected spectra were classified, after baseline

correction, based on a reference database, selecting the higher-matching reference mineral phase. Raman automatic mapping for provenance studies is proven to be beneficial for many mineral phases (e.g., zircon, Resentini et al., 2020; Pastore et al., 2023; garnet, Mark et al., 2023; epidote, Limonta et al., 2022; pyroxenes, Borromeo et al., 2022). This study reveals that Raman automatic approach is not appropriate for the identification of rutile phases. Rutile matching spectra proven (by optical observation and geochemical composition) to contain also grains of authigenic rutile and pseudo rutile possibly derived from ilmenite alteration (Grey and Reid 1975, Mücke and Chaudhuri, 1991). Threshold for discarding spurious mineral phases were thus placed at 10 ppm of thorium (Th) as in primary rutile usually display low concentration of Th (Zack et al., 2011). Rutile geochemical data were determined at the London Geochronology Centre using an Agilent 7900 laser-ablation inductively-coupled-plasma mass-spectrometry system, employing a NewWave NWR193 Excimer Laser operated at 10 Hz with a 40 μm spot size and ~2.2 J/cm^2 fluence. The mass spectrometer data were converted to element concentrations using *GLITTER 4.4.2* software (Griffin, 2008), employing a NIST SRM612 glass as a compositional standard. Rutile standards R632 (Axelsson et al., 2018) and RMJG (Zhang et al., 2020) were added to the analysed grains and treated as unknown (Appendix). Masses monitored were ^{25}Mg, ^{27}Al, ^{49}Ti, ^{52}Cr, ^{55}Mn, ^{91}Zr, ^{93}Nb, ^{121}Sb, ^{177}Hf, ^{204,206,207,208}Pb, ^{232}Th, and ^{238}U. The complete rutile geochemical dataset is provided in Appendix.

2.2.8. Graphical/Statistical Tools

To visualize heavy-mineral data we use the compositional biplot (Gabriel, 1971), a statistical/graphical display that allows discrimination among multivariate observations (points) while shedding light on the mutual relationships among multiple variables (rays). The biplot, drawn using CoDaPack software (Comas-Cufí and Thió-Henestrosa, 2011), allows discrimination between multivariate observations (points) while shedding light on the mutual relationships among variables (rays). The length of each ray is proportional to the variance of the corresponding variable in the dataset. If the angle between two rays is close to 0°, 90° or 180°, then the corresponding variables are correlated, uncorrelated, or inversely correlated, respectively.

The statistical tools applied to the zircon U-Pb grain age populations include Multidimensional Scaling (MDS; Kruskal and Wish, 1978; Vermeesch, 2013). This multivariate ordination technique takes a dissimilarity matrix as input and produces a

map of samples as output, in which similar samples plot close together and dissimilar samples plot far apart. For detrital zircon U-Pb age spectra, a dissimilarity matrix can be constructed using the Kolmogorov-Smirnov statistic (i.e., the maximum vertical difference between two cumulative distribution functions; Feller, 1948). MDS produces a map of points in which the distance among samples is approximately proportional to the Kolmogorov-Smirnov dissimilarity of their compositional or chronological signatures. Closest and second closest neighbors are linked by solid and dashed lines, respectively, and the goodness of fit is evaluated using the "stress" value of the configuration (0.2 = poor; 0.1 = fair; 0.05 = good; Kruskal, 1964; Vermeesch, 2013, 2018).

2.2.9. Forward Mixing Model

Modern (fluvial and aeolian) sediments are very heterogeneous due to the amalgamated mixture of the detrital minerals and lithic fragments. This heterogeneous mixture is eroded from different tectonic rock units that are contributing and supplying in various proportions into the trunk rivers through the numerous segmented river tributaries (Vezzoli et al., 2013). With the help of forward mixing model (details in Appendix), the relative supply from each source into the total sediment load is determined through the known compositional signatures of detritus of end members (Draper and Smith, 1981; Weltje, 1997; Garzanti et al., 2012; Vezzoli et al., 2004, 2013, 2020). Forward mixing model is a linear relationship of dependent variable with the set of explanatory and independent variables. This is a stochastics model which is not exactly correct but has random variation as a disturbance term. Let y be the row vector of compositional data with D columns representing variables, X a matrix of end-member compositions with n rows representing observations and D columns representing variables, and β a row vector of coefficients with $q = n$ columns representing the proportional contribution of the end members to the observation. In matrix notation, a forward mixing model can be expressed as,

$$y=\beta X + e \quad (1)$$

The row vector y consists of non-negative linear combination β of q end-member compositions, and e is a row vector of errors with D columns representing variables. In order to solve the linear regression problem, we must determine an estimation of the row vector β describing a functional linear relation b between a matrix of end-member

compositions *X* and an output row vector *y*. The solution of Equation (1) consists in the calculation of the row vector of coefficients *b* such that,

$$\hat{y} = bX$$

where ŷ is a row vector of calculated compositional data with D columns representing variables. This equation represents a forward mixing model (or "perfect mixing").

Goodness of fit of the forward mixing model can be assessed by the coefficient of multiple correlation (R), obtained by Vezzoli and Garzanti (2009).

$$R = \sqrt{1 - (RSS/TSS)}$$

where RSS is the residual sum of squares,

$$RSS = \sum i(yi - \hat{y}i)2$$

and TSS is the total sum of squares,

$$TSS = \sum i(yi - \hat{y}i)2$$

The R value is a measure of how much of this decomposition is due to the model and takes on a value between zero and one. High R values suggest that the model explains the variation in the dependent variable well. Hence, R quantifies the similarity between detrital modes from each main tributary or any of their mixtures and the detrital modes of the trunk river. Comparison with main tributaries is considered satisfactory for R values 0.9.

Chapter 3
Geological and Geomorphological Features of Minjiang River, South China

3.1. Geology of the Minjiang Catchment

Three geological domains can be identified in the Minjiang catchment: the Qinling-Dabie Belt, the Songpan Ganzi Triassic sedimentary basin, and the Longmenshan Belt (Deng et al., 1995; Chen and Wilson, 1996; Wallis et al., 2003) (Fig. 3.1a). Qinling-Dabie Belt is a part of Central China Orogenic Belt that is associated across Central China towards east west. There are traverse portions from the greatest mountain ranges of Shaanxi, Henan, and Gansu provinces along the Qinling Belts. Songpan Ganzi is the western part of Sichuan Basin and Eastern part of the Tibetan Plateau that is bounded by the South China, North China, Kunlun–Qaidam and Qiangtang (North Tibet) continental blocks. Longmenshan Belt is a thrust-nappe belt that is responsible for the separation of Songpan Ganzi from the Sichuan basin (Roger et al., 2010).

3.1.1. Qinling-Dabie Belt

Qinling-Dabie Belt is mostly exposed in the northeastern part of the basin where it is represented by basement rocks with alkaline dyke intrusion, metasedimentary rocks, shallow marine clastic and terrestrial sedimentary rock and carbonate, and meta-basaltic rock. It has experienced very complex tectonic activities. Based on these tectonic activities, it has been divided into 9 main groups: South-North China Block, Kuanping Group, Erlangping Group, North Qingling Block, Shangdan suture zone, North-South Qinling Block, South-South Qinling Block, Mianlue Suture zone and Dabie terrane. Qinling-Dabie Belt was developed by the collision of Sino-Korean (North China) Craton and Qinling microcontinent during early Paleozoic era, followed by the Middle/Late Triassic collision between the South China Block and North China Block (Zhao et al., 2021). There is subduction polyhistory evolution recorded by the high to ultra-high pressure Precambrian, Paleozoic, and Triassic rocks consisting of magmatic arcs ophiolites of lower to upper Paleozoic with wide separation of syn to post 225 and 200 Ma kinematic granitoids (Dong et al., 2011). Qinling-Dabie Belt orogenic collapse is also associated with the subduction and retreat of the ancient Pacific oceanic slab and extensive magmatism in the Jurassic to the Cretaceous (Hacker et al., 1998). The southern part of Qingling belt is composed of Mesoproterozoic

metavolcanic rocks including greenschist to lower amphibolite-facies that was deformed during early Neoproterozoic orogenic event. There are also sedimentary strata that begin Neoproterozoic tillites and overlying dolostones, followed by lower Paleozoic shelfal carbonates and siliciclastic rocks. Shallow marine carbonate and siliciclastic rocks are Devonian to Permian in age, with minor sequences deposited between the Upper Triassic to the Jurassic. The Cretaceous and Cenozoic red-beds were deposited in fault-bounded basins (Meng and Zhang, 2000), which have been deformed with the numerous tectonic activities in different eras from Archean (3.8–2.5 by ago) to Cretaceous (142–65.5 my ago) including medium to high grade greenschist, amphibolite, mica schist, ophiolite, volcanic, gneiss, and marble.

3.1.2. Songpan Ganzi

Songpan Ganzi is exposed at the high altitude of the western part of the Tibetan Basin. It includes large flysch turbidite sequence, thicker >10,000 m and consists of demarcation of eastern paleo-Tethys that is surrounded by continental pre-Sinian basement. This basin includes Triassic turbidites and was closed due to the regional scale compressional zone in the Triassic to early Jurassic age. There are many northwest-southeast folds and thrust faults due to the shortening of the flysch rocks. This tectonic activity is responsible for the thickness of Triassic flysch but there is no true thickness due to its strong internal interfering deformation. These turbiditic sequences are genetically related to the diachronous orogenic uplift and erosion of the Qinling Dabie Mountains (He et al, 2014). The continental-continental exhumation during Triassic time of the Dabire-Sulu Mountains were acting like Himalayan collision that favoured the transportation of huge amounts of remanent detritus for Qinling Belt (Chang, 2000) towards the Songpan Ganzi area. Songpan Ganzi is now a fold belt which is also the western end of Qinling Dabie-Sulu fold belt as consequence of the collision of the North China and South China cratons (Ingersoll et al., 1995; He et al, 2014). The northern side of the Songpan Ganzi comprises of calciturbidites and complete sequence was deposited during Triassic and overtops the Paleozoic platform sequence. It consists mainly of detrital sediments of flysch facies as described above. The series is intensely folded and underwent moderate metamorphism, whose grade increases westward (Wallis et al., 2003). Those sediments are intruded by several granitic plutons, contemporary with the main Indosinian (late Triassic) deformation stage (Harrowfield and Wilson, 2005; Godard et al., 2010).

3.1.3. The Longmenshan

Longmenshan Mountains (long = dragon; men = gate; shan = mountains). The Minjiang River cuts gorges from 1 to 3 km deep across the Longmenshan in its mountain tract, originating from eastern margin of Tibetan Plateau and flowing along Wenchuan-Maoxian fault and ultimately making confluence into the Sichuan Basin at Dujiangyan (Liu et al., 2015). The Longmenshan Belt is the most significant topographic barrier which is in the eastern margin of Tibet with a lot of structural features that consists of high topographic gradient. This is almost 60 km horizontally passing through with mean elevation of ~4000 m on the plateau to ~500 m in the Sichuan Basin (Fig. 3.1a, b). This is an extremely high-relief and tectonically active narrow range reaching almost 5,000 a.s.l. in elevation and representing the eastern border of the Tibetan Plateau (Zhang et al., 2002) with an NE trend of Qinghai-Tibetan Plateau. That is a reactivated suture zone for Yangtze and the Songpan Ganzi block by the far-field compression of the India-Asia collision (Wu et al., 2021). The Longmenshan formed during the late Triassic age is transpressional fold-thrust belt separating the Songpan Ganzi terrane from the Sichuan foreland. The exhumation and formation of the Longmenshan has controlled by both south Qinling orogenic event and the Mesozoic-Cenozoic India-Tibet collision. In the Longmenshan Belt, the latter consists of are two important orogenic events: the thrusting and folding were developed by the compressional late Triassic zone which were later on transformed into the large fold system by the late Cenozoic deformation. By these activities, there are series of nappes and klippen in both directions as northwest to southeast respectively that have double-vergent chain along the Longmenshan Belt (Lining et al, 2014). It consists of Proterozoic schists, granitoids as basement rocks dated from 1043–1017 to 776–647 Ma with felsic/ intermediate volcanic rocks. These rocks are overlain by Neoproterozoic to Permian rocks that are marine carbonates and clastic rocks of passive-margin. There are also Triassic turbidites with recent continental clastic rocks that are intercalated with deposited volcanic rocks and evaporites until the Neogene (Chen and Wilson, 1996).

The Longmenshan range marks the geological transition between the low elevated Sichuan Basin and the Tibetan Plateau. It has a complex structure resulting from a polyphase tectonic event. The easternmost frontal units of the range are made of Mesozoic detrital sediments, which mainly consist of sandstone and siltstone of Triassic to Jurassic age characterized by thin-skinned fold and thrust deformation (Chen and

Wilson, 1996). Those sediments belong to the thick Meso-Cenozoic continental detrital series of the Sichuan Basin (Burchfiel et al., 1995), constituting the foreland of the Longmenshan. The limited Late Cenozoic sedimentation in this basin suggests an absence of significant flexural loading associated with recent thrusting activity along the Longmenshan by the easternmost faults such as the Beichuan Fault (Royden et al., 1997).

The basement core of the Proterozoic granitoids and metamorphic (metavolcanics and metasediments) rocks of the Yangtze craton, such as the Pengguan Massif, constitutes the highest part of the range (Burchfiel et al., 1995; Chen and Wilson, 1996). These are the oldest formations encountered in this part of Eastern Tibet and have an important role in shaping the morphology of the abrupt topographic front. The main structural features of the Central Longmenshan are the Wenchuan and Beichuan faults that bound the Pengguan Massif on its western and eastern flank, respectively. During most of the Paleozoic times the western part of the Yangtze craton was a passive margin, on which an important sedimentary platform sequence accumulated. This series is mainly constituted of shallow water detrital deposits (sandstone and shales) and limestone. From a structural point of view those units are directly deposited on the Proterozoic basement blocks and mark the transition between the Longmenshan and the Songpan Ganzi fold belt. As a whole, the series underwent low grade (green schist) metamorphism. Those sediments are also present in the frontal part of the range as klippes overlying the Mesozoic formations of the Sichuan Basin (Godard et al., 2010).

3.2. Geomorphology of the Minjiang Basin

The Minjiang (jiang = river in Chinese) was named as “Blue River” (Qing Shui in local Chinese dialect: qīng = blue; shui = water) by western authors in the 19th century. The originating point (appendix) of Minjinag is southern foot of Minshan Mountain that is a junctional point for Sichuan and Gansu. The source of eastern side of Minjiang is starting from Lungangling where Zhangjin River flows through Zhangla. The western side source begins from Langjialing where Yangdong River flows through Huangshengguan. These rivers congregate at Hongqiao Pass of Songpan Yuanba Township and flow together southward along the Minshan Mountains. The mainstream is draining from north to south from Songpan and confluence at Chengdu Plain through Maoxian county,where Wenchaun and Dujiangyan demonstrate a typical example of an

asymmetric dendry-shaped system. Here at the exit point of the confluence the average estimated annual flow is 452 m^3/s which usually drops by 8.2%.

The first level tributaries (appendix) of Minjiang are Lianghekou, xiaoerbian, Puxi, Lixian, Putouzhen, Sima, Shangmeng, Laoyazhai, Yingou, Sanshenggou, Laofangzi, and Longtangou which flows along these rivers Songpinggou, tributary of Heishuihe, Zagunaohe, and Shaotanghe river. These sites are considered as end members of the Minjiang River for first level tributaries. Same as for second level which has been consider as major tributaries, the sites are Chuanzhusi, Xiaobaosi, Minjiangxiang, Zhenjiangguan, Zhubie, Huilongxiang, Songxibao, Xiaokeku, Lixian, Leshan, Gengda, Yingxiu, Xihe, Ziping and Xiangzhangping which are flowing along many rivers as Mounigou, Shaotanghe, Xihe, Baishahe, and Zagunaohe. For the third level tributaries of Minjiang which are trunk, and the sites are Gonggaling, Gamisi, Chuanzhusi, Yuanbazicun, Xintangguan, Yuntunbao, Beidingguan, Dapingba, Xiaozhai, Musubao, Wowodian, Shigu, Wenchuan, Modaoxi, Baihuatan, Leshan, Yingxiu, and Dujiangyan. These third level tributers all flow mostly along the main Minjiang River.

Heishui River also known as Tibetan cuoqu which is a first level tributary which originates from Xiniang Mountain, crosses Heishui county, passes the Lianghekou of Maoxian County, and enters the Minjiang River (appendix). The rivers belonging to this tributary are Maergai River, XiaoHeishui River and Chiwusu River. The other tributary of the first grade is The Zegatuo River (Tuo River in history), which originates from the side of Partridge Mountain and flows into the Minjiang River in Weizhou Town through Miyara, Zegatuo, Xuecheng, Longxi and other places. The river of this tributary is the Mendong River. Another tributary is Yuzixi (also known as Erhe), which originates from the eastern slope of Balang Mountain in the southwest of Wolong, Wenchuan, and falls into the Minjiang River at Yingxiu Zhongtanpu (Liu, 2020). At Dujiangyan the river enters the Sichuan Basin where it receives the Dadu He (He means river in Chinese) and the Qingyi Jiang at Leshan before joining with the Changjiang at Yibin (Xu et al., 2020). The Dadu He runs from north to south, separated from the Minjiang mainstem by the Qionglai Mountains, reaching an elevation of 6250 m a.s.l. in Mount Siguniang (si = four; guniang = girl).

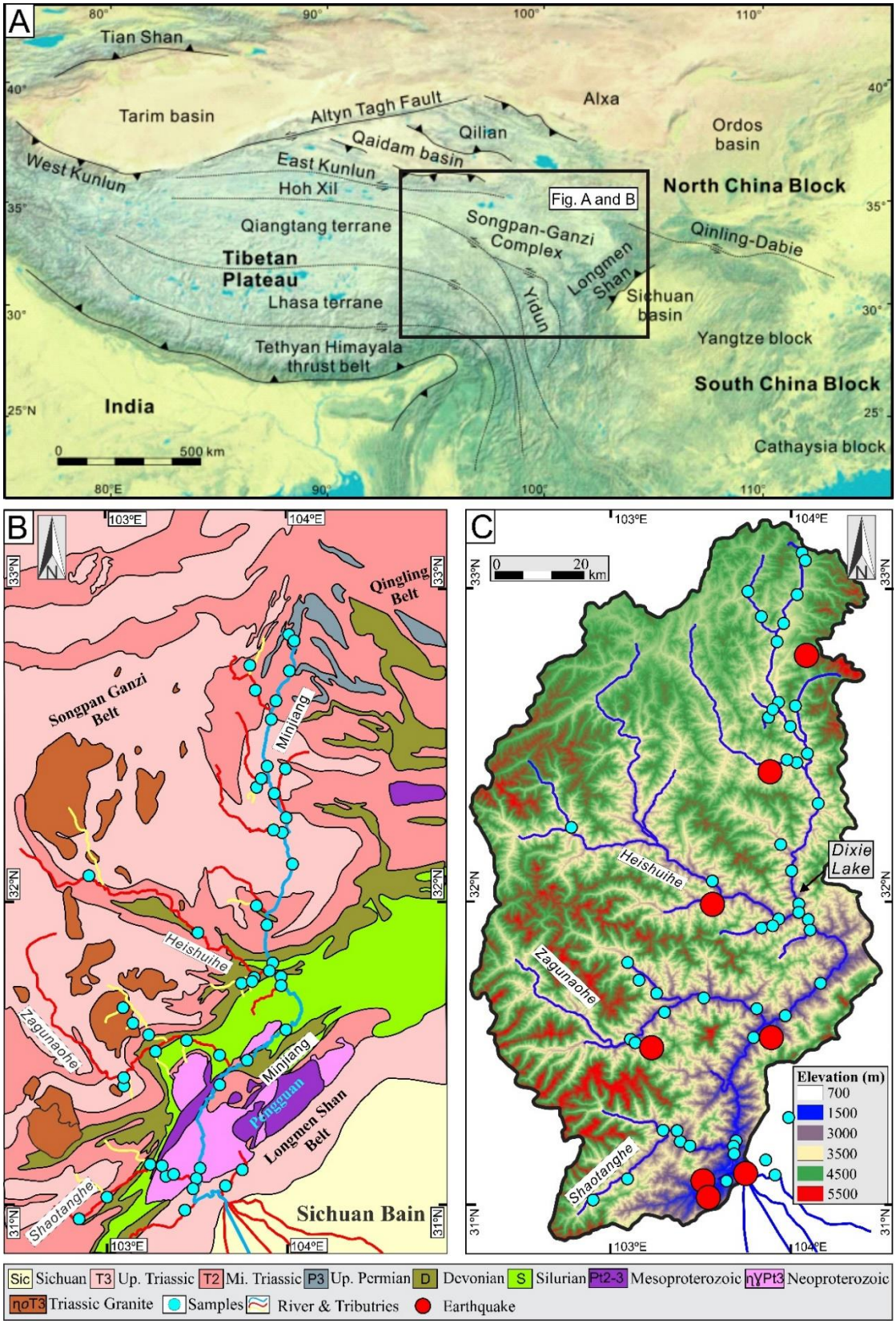

Figure 3.1. (A) Regional geological map of the Qingling, Songpan Ganzi and Longmenshan Mountain Belt. (B) Geographical and aerial distribution of geological units that are Qingling, Songpan Ganzi and Longmenshan Mountain Belt. Different colors are showing various outcrops that are exposed in these units along Minjiang River in the study area. Sic = Sichuan

Basin; T3 = Upper Triassic; T2 = Middle Triassic; P3 = Upper Permian; D = Devonian; S = Silurian; Pt2-3 = Mesoproterozoic; ηγPt3 = Neoproterozoic; ηοT3 = Triassic Granite; Blue color small circles = samples locations; blue, red and yellow curves = Minjiang River with different tributaries. (B) Elevation map of the Minjiang catchment. Analyzed by *QGIS* on the DEM, according to this elevation varies from 700 to 5500 m in the study area.

Most of the terrain of the upper Minjiang River belongs to the Minjiang Mountain range, and the southeast border belongs to the tail section of Longmen Mountain. It slopes from the northwest to the southeast, with the highest altitude of 6250 m (Sigungshan mountain) and the lowest altitude of 780 m (the Southeastern Xuankou area). According to the unified classification of geomorphic types in Sichuan Province, the upper reaches of Minjiang River can be divided into four basic types: low Zhongshan 1108.6 km^2, high Zhongshan 18,205.6 km^2, high mountain 5415.9 km^2, and high mountain 737.9 km^2. Most of the geology in the area belongs to the Markang and Longmenshan geological zones and belongs to the zonal tectonic system. Metamorphic rocks, such as schist, phyllite, sand slate, marble and so on, are mainly distributed in the area. The terrain of this area is basically presented according to the pattern of plane-inclined valley anticlinal mountain. The terrain slopes towards the southeast Sichuan basin, present typical alpine canyon landform. In terms of the overall landform of the area flowing through the upper reaches of the Minjiang River, the three-level landform has the obvious segmentation structure (Liu, 2020) (Fig. 3.1b).

3.2.1. Climate (Rainfall, and Temperature)

Minjiang River basin mostly belongs to subtropical climate. The upper reaches of Minjiang River are affected by mountain terrain, belonging to mountain plateau climate (Table 3.2). The annual average temperature in the north of Zhenjiangguan is 5°C ~9°C, and the minimum temperature is -14.4 °C ~-21.1°C. The annual average temperature at Dujiangyan is about 15°C, the minimum temperature is -5 °C ~-10°C, and the maximum temperature is 34 °C ~36°C. The diurnal temperature range in the upper reaches of the mountains is large. In the valley, the snow accumulation period is generally from December to March of the next year, and the snow depth is 10~30 cm. In the mountain area, the snow accumulation period can be from October to May of next year, and the snow depth is 150~400 cm. From Dujiangyan city to Yibin, where the Minjiang joins into the Yangtze River, there is no significant difference in

temperature. The annual average temperature is about 17℃, the lowest temperature is about -4℃, and the highest temperature is about 38℃.

Average annual precipitation is 725 mm in the Minjiang basin, ranging from 1190.9 mm in the mountains to 492.7 mm in the plains (Liu, 2020). The precipitation in Minjiang River basin is mainly controlled by the advance and retreat of southeast monsoon, southwest monsoon and Pacific subtropical high. The rainfall season changes obviously, with frequent rainstorms in flood season, especially concentrated in June to September, and the rainfall in summer and autumn can account for more than 80% of the whole year. The annual precipitation varies greatly due to topography. The annual average precipitation of the upper reaches of the mainstream from Songpan County to Wenchuan is 400~700 mm. The rainfall center of the mainstream of the Minjiang River is located from Wenchuan County to Dujiangyan City, which annual average precipitation is 1100~1600 mm. The average annual precipitation in the middle and lower reaches of the Minjiang River ranges from 900 mm to 1300 mm. The maximum annual precipitation measured in the whole Minjiang River Basin was 2434.8 mm (1947) of Zipingpu Station. By Hairong et al., 2014, the altitude of Minjiang above sea level is 700-6253 m. The river basin is located in the transition zone between the humid monsoon region in eastern China and the high, cold area of the Qinghai-Tibet Plateau. Mean annual precipitation in the basin is 500-850 mm. The rainy season is from May to October, during which more than 75% of the annual precipitation occurs. The basin is located mainly in the orographic heavy-rain area along the eastern margin of the Qinghai-Tibet Plateau.

3.2.2. Water Fluxes

In terms of water discharge it is the main tributary of the upper Yangtze/Changjiang (chang = long), and hence originally considered the main headwater branch before discovery of its Tibetan sources. The Minjiang (length 735 km, basin area 140,000 km^2, annual water discharge 861×10^6 km^3/yr (Li et al., 2008), pre dam 90.6 km^3/yr post dam 77.4 km^3/yr (Yang et al., 2018) or $3.2*10^6$ km/s^3, daily water discharge is $26.66*10^6$ km/s^3, average annual runoff 57.34 billion m^3) flows from north to south in the central part of the Sichuan Province, cutting across the Longmenshan. Water discharge is low in the dry season (October to March) and minimum up to 25% in January. The upper reaches of the Dadu He River basin is plateau mountain climate. The annual precipitation is 500-750 mm, and the snowfall period can reach 5 months. The rest of

the region has a monsoon climate, with annual precipitation of 1000 mm, and parts of the downstream can reach 1200-1900 mm. Heavy rain is mainly concentrated in the middle and lower reaches of the region from May to September, especially in July and August.

3.2.3. Sediment Fluxes

The annual sediment flux in the Minjiang is estimated to be 6 million tons. Intense rainfall in the mountain part of the catchment (24,000 km^2) plays a crucial role in the seasonal transportation of sediments (Guo et al., 2016; Jian et al., 2020). Three quarters of the sediment flux occurs during the monsoon season (April to September), when water discharge may reach up to 75% during peak floods triggered by tropical cyclones in June (Yin et al., 2010). Because of high topographic relief, there is a marked temperature gradient, with up to 15°C differences from the edge of the Tibetan Plateau to the Sichuan Basin in both dry and rainy seasons (Liu, 2020). The average annual flow is 1500 m^3/s measured at Fulu hydrographic station. Dadu He suspended load was 31.51 $\times 10^6$t/a, according to the Tongjiezi station in 1956-1986. By Hairong et al., 2014**,** Minjiang River has an average annual $144*10^4$ m^3 runoff (Table 3.1). The runoff in the wet season from May to October accounts for 75% of the annual runoff. The average annual sediment discharge is $7.08*10^6$t (Table 3.1).

3.2.4. Earthquakes and Landslides

This reservoir was affected by the Wenchuan earthquake in 2008 with 7.9 moment magnitude (Mw). The 2008 Wenchuan earthquake and 2013 Lushan earthquake are recognized as the result of the activity of Longmenshan fold-and-thrust belt caused by the ongoing India-Tibet collision (locations of earthquakes in Fig. 3.1c). This earthquake was along with Longmenshan mountain front at the eastern margin of Tibetan Plateau. By this earthquake, 56000 landslides were triggered with 2.8 km^3 area and 7.4Gt mass that is 4 to 7 times of the total annual sediments 1 to 2 Gt export from Himalayas. There was co and post seismic landslides were associated with this earthquake that was subsequently responsible for the changes to the rates of erosion and fluvial sediment transfer.

There is a strong relationship among heavy rainfall, flash flood and sediment transport that are responsible causes to influence the surface erosion and geomorphic growth of mountains. After the Wenchuan earthquake in 2008 sediments increases from 13.8% to 70%, time of the post seismic flash floods and debris flows have centered with

consistency rainfall from July to September (Table 3.2). There are many landslide effects on the upper reaches of Minjiang River and one of the biggest induced effects is by 1933 earthquake that was responsible for Diexi landslide. With this large size landslide, Minjiang river stopped and give a suitable environment for the deposition of 200 m thick lacustrine sediments at the trunk river of Minjiang (Wang et al., 2017). The long river profile shows many knickpoints that are propagating towards the upstream. These knickpoints were not only formed by landslides but also by tectonic activities. Manaoding landslide at the downstream that is consist of marble with two sets of joints that are plunging valley wards and intersect the joints and bedding plains. Due to this destabilized wedge-failure structural defect and the continuous incision of Minjiang River caused the large landslide.

3.2.5. Anthropogenic Modifications

The anthropogenic modification of the Minjiang river fluxes due to the Zipingpu Reservoir that is behind the 156-m-high dam completed in September 2004. This reservoir is fed by the Minjiang River at the downstream of the catchment with 22811 km^2 drainage area. The Zipingpu reservoir is located at the Minjiang River at the Longmenshan mountain front, upstream of the Sichuan Basin. The water depth of 110 m at the highest water level and 57 m at the lowest water level in 2016. The entrance of the reservoir at the highest water level is ~2 km downstream from the epicenter of the 2008 Wenchuan earthquake. According to the records from the Zipingpu Reservoir Company, the Min Jiang River channel was intercepted on 23 November 2002 when dam construction began. The reservoir started to impound water with a maximum water depth of 23 m (an elevation of 775 m) on 30 September 2004, and operations fully began 1 year later, when water level increased abruptly to an elevation of 821 m (a water depth of 69 m near the dam). The daily water level has been monitored by the Zipingpu Reservoir Company since 2004. With a view to dam safety and requirements for irrigation during dry seasons, the water level of the reservoir is regulated artificially. There are two periods with high water level each year. The first is during monsoonal rainy season (June and July), although the reservoir is discharged at this time to release the large volume of water received; and the second is during the dry season, when the highest level (an elevation of ~877 m) is achieved from late September to January to ensure adequate agricultural irrigation and drinking water for the following spring (Zhang et al., 2019) (Table 3.2).

3.2.6. Sediment Discharge in the Upper Reaches of the Minjiang River Before and After the Wenchuan Earthquake

The annual average sediment discharge in the upper reaches of the Min River (the Zipingpu Hydrological Station) was $7.04*10^6$t during 1980-2007 (Table 3.2). The maximum level was $9.00*10^6$t (1992), while the minimum level was $5.62*10^6$t (2002). The coefficient of interannual variation was 0.14. In addition, the annual sediment discharge in the upper reaches of the Min River before the Wenchuan earthquake presented a downward trend overall. It decreased by about $0.0032*10^6$t from 1980 to 2007, which represents approximately 4.5% of the annual average sediment discharge. The average annual precipitation (at the Zipingpu Hydrological Station) was 1201 mm in the upper reaches of the Min River during 1980-2007. The minimum was 763 mm (2007), while the maximum was 1805 mm (1990). Conclusions could be drawn. (1) The annual sediment discharge in the upper reaches of the Min River presented a downward trend overall before the Wenchuan earthquake. (2) There was a strong correlation between precipitation and sediment discharge before the Wenchuan earthquake. The change in annual sediment discharge in the upper reaches of the Min River was controlled mainly by annual precipitation. If precipitation decreased, sediment discharge was reduced correspondingly (Ding et al., 2023).

From the Zipingpu Hydrological Station during 2000-2010 data on sediment discharge, Sediment load and rainfall were collected (Table 3.2). The changes in sediment discharge in the upper reaches of the Min River before and after the Wenchuan earthquake (2008-2009) were compared. The following preliminary conclusions can be drawn. (1) As, the average annual sediment discharge in the basin was $7.04*10^6$t before the Wenchuan earthquake (2000-2007), which was relatively stable. (2) The annual sediment discharge reached $9.05*10^6$ t in 2008 after the Wenchuan earthquake, an increase of 27.56% compared with that before the earthquake. (3) The annual sediment discharge in 2009 was $8.08*10^6$ t, an increase of 11.47% compared with that before the earthquake. (4) There was no heavy rainfall in 2008 and 2009 in the upper reaches of the Min River. However, the sediment discharge increased by approximately 30% compared with that before the earthquake. This observation indicated that the increase in sediment discharge of approximately 30% resulted only from coseismic uplift, landslides, and debris flows after the Wenchuan earthquake, excluding the influence of heavy rainfall (Ding et al., 2023).

Table 3.1. Literature review data for the rainfall, runoff, and annual sediment discharge from different (Minjiang, Zipingpu and Dujiangyan) hydrometric station from Hairong et al, (2014).

				Annual Sediment Discharge (10^6 t)		
Year	**Rainfall (mm)**	**Runoff ($10^8 m^3$)**	**Precipitation (mm)**	**Minjiang Hydrometric**	**Zipingpu Hydrometric station**	**Dujiangyan Hydrometric station**
2000	50	110	627.2	6.32	5.82	6.43
2001	150	115	779.3	6.60	6.18	6.96
2002	47	107	506.1	6.10	5.58	6.10
2003	260	118	869.4	6.80	6.28	7.27
2004	100	113	697.2	6.44	5.95	6.68
2005	425	121	954.1	6.92	6.45	7.57
2006	100	109	584.3	6.07	5.73	6.28
2007	125	119	879.7	6.80	6.30	7.31
2008	500	130	1222.4	9.66	9.05	11.06
2009	125	117	834.8	8.72	8.08	9.21
2010	1000	173	2545.8	12.96	12.39	17.06

Table 3.2. Literature review for the sediment load or suspended load in different time durations from Lin, (1995); Ding et al., (2013); Li et al. (2021) and River sediment bulletin of China, (1955-2020).

Minjiang Catchment	**Data Source**	**Time period**	**Drainage area (km^2)**	**River Length (km)**	**Sediment Load (10^6 t/a)**	**Affecting factors**
Main Catchment						
Zipingpu Station	Lin, 1995	avg. 1955-1982	22811	735	8.45	
Zipingpu Station	Ding et al., 2013	avg. 1980-2007	22811	735	7.04	
Zipingpu Station	Ding et al., 2013	2008	22811	735	9.06	**Earthquake**
Zipingpu Station	Ding et al., 2013	2009	22811	735	8.08	
Zipingpu Station	Ding et al., 2013	2010	22811	735	12.39	**High Precipitation**
Zipingpu Station	Li et al., 2021	avg. 1955-1990	22811	735	7.92 + 0. 7 (bed laod)	
Other Catchments (after Zipingpu)						
Pengshan station (Middle Minjiang)	Lin, 1995	avg. 1955-1982			10.50	
Jiajiang station (Qingyi River)	Lin, 1995	avg. 1963-1985			10.22	
Tongjiezi station (Dadu River)	Lin, 1995	avg. 1956-1986			31.51	
Gaochang station (whole Minjiang)	Lin, 1995	avg. 1953-1985			50.20	
Gaochang station (whole Minjiang)	River sediment bulletin of China	2020			66.30	

Gaochang station (whole Minjiang)	River sediment bulletin of China	2019			34.90	
Gaochang station (whole Minjiang)	River sediment bulletin of China	2018			31.00	
Gaochang station (whole Minjiang)	River sediment bulletin of China	2017			14.00	
Gaochang station (whole Minjiang)	River sediment bulletin of China	2016			10.70	
Gaochang station (whole Minjiang)	River sediment bulletin of China	2015			4.80	
Gaochang station (whole Minjiang)	River sediment bulletin of China	2014			11.90	
Gaochang station (whole Minjiang)	River sediment bulletin of China	2013			21.10	
Gaochang station (whole Minjiang)	River sediment bulletin of China	2012			22.80	
Gaochang station (whole Minjiang)	River sediment bulletin of China	2011			14.30	
Gaochang station (whole Minjiang)	River sediment bulletin of China	2010			31.50	
Gaochang station (whole Minjiang)	River sediment bulletin of China	2009			18.40	
Gaochang station (whole Minjiang)	River sediment bulletin of China	2008			15.30	
Gaochang station (whole Minjiang)	River sediment bulletin of China	2007			30.60	
Gaochang station (whole Minjiang)	River sediment bulletin of China	2006			20.60	
Gaochang station (whole Minjiang)	River sediment bulletin of China	2005			58.50	
Gaochang station (whole Minjiang)	River sediment bulletin of China	2004			33.20	
Gaochang station (whole Minjiang)	River sediment bulletin of China	2003			47.50	
Gaochang station (whole Minjiang)	River sediment bulletin of China	2002				
Gaochang station (whole Minjiang)	River sediment bulletin of China	2001			~41	
Gaochang station (whole Minjiang)	River sediment bulletin of China	2000			~17	
Gaochang station (whole Minjiang)	River sediment bulletin of China	avg. 1956-2010			45.30	
Gaochang station (whole Minjiang)	River sediment bulletin of China	avg. 1956-2020			41.90	
Gaochang station (whole Minjiang)	River sediment bulletin of China	avg. 1956-2000			~50	

Chapter 4

Segmented Minjiang Sediment Routing System and Sediment Generation in the Longmenshan Belt

Muhammad Usman, Eduardo Garzanti, Giovanni Vezzoli, Wendong Liang, Sergio Andò

Keywords: Provenance analysis; Sand petrography; Heavy minerals; Detrital-zircon geochronology; Longmenshan thrust belt; Minjiang River

Note: This work is not published due to the political issue and conflicts with the Chinese collaborators for the U-Pb Zircon Dating, but it is allowed to use in the PhD Dissertation.

4.1. Sediments Framework for Provenance Studies

The multi-technique analysis of sand samples collected throughout the Minjiang drainage basin allow us to monitor the compositional change across the Longmenshan belt and the Sichuan plains. In this section we shall illustrate first the end-member composition of sand derived from single lithologic domains, next the compositional signatures of sand contributed by all major tributaries and finally the evolution of petrographic modes (Fig. 4.1), heavy-mineral suites (Fig. 4.2), and zircon-age spectra (Fig. 4.3) downstream the segmented Minjiang sediment-routing system (petrographic framework details in Table 4.1a, b).

4.2. End-member Compositions

The precise definition of end-member compositions represents an essential step to understand the lithological structure of source-rock domains exposed in each river catchment (first-order sampling scale of Ingersoll, 1990) and thus to calculate provenance budgets used in turn to evaluate sediment yields and erosion rates (Garzanti et al., 2012; Resentini et al., 2017). Four main tectono-stratigraphic source-rock domains are identified in the Minjiang catchment: 1) Triassic granites; 2) Triassic Songpan Ganzi Group; 3) Lower and Upper Paleozoic strata; 4) Neoproterozoic granitoid basement.

4.2.1. Triassic Granites

Sand of small rivers draining dominantly within Triassic granitic intrusions were sampled in the Mengtun Valley (5744, 5745). These quartzo-feldspathic sands with subequal amounts of K-feldspar and plagioclase contain granitoid and a few very-high-rank metamorphic rock fragments (gneiss, amphibolite; MI* = MI = 450-460) (Figs. 4.1a and 4.2a, b). Biotite is common. The poor tHM suite is dominated by mostly blue/green hornblende with common epidote and minor titanite, clinopyroxene, and apatite (ZTR 0) (Figs. 4.2c, d). The feldspatho-litho-quartzose sand of the upper Heishuihe tributary largely draining Triassic granite (5730) yielded zircon grains displaying a distinct Late Triassic peak (32% of ages; mode at 213 Ma) (Figs. 4.3 and 4.4).

4.2.2. Triassic Strata

Sand of small rivers draining dominantly within the Triassic Songpan Ganzi Group were sampled in the northern (5716, 5717, 5720, 5722, 5723), central (5725, 5742), and southern parts (5694, 5695) of the Minjiang mountain catchment. In the north, quartzo-lithic sands recycled from siliciclastic and subordinate carbonate strata contain sporadic plagioclase, rare K-feldspar, and dominant sedimentary to low-rank metasedimentary rock fragments (shale/slate/phyllite, siltstone/sandstone/metasandstone, sparitic to micritic limestone, and dolostone; MI* 100-145, MI 65-100) (Figs. 4.1b, c and 4.2a, b). Mica is minor. In the central part, sands are litho-quartzose with metasedimentary (paragneiss with minor schist and marble), sparitic limestone, and sandstone rock fragments. Mica is abundant (dominantly biotite). Closer to Paleozoic units, MI* increases markedly, from 265 to 390, and MI from 220 to 375. The same trend of increasing metamorphic rank closer to Paleozoic units, although less pronounced (MI* from 220 to 270, MI from 195 to 250) is displayed by quartzo-lithic sands in the south, dominated by metasedimentary (metasandstone/paragneiss, metacarbonate/marble, shale/phyllite/schist) and sedimentary (impure carbonates, minor siltstone, and shale) rock fragments. The extremely poor tHM suite of all these recycled sands includes tourmaline, apatite, amphibole, and zircon (ZTR 27-86) (Figs. 4.2c, d).

4.2.3. Lower Paleozoic Strata

Sand of small rivers draining dominantly within Silurian units were sampled in the Songxibao (5735), Zagunaohe (5740), and Shaotanghe Valleys (5697; 5696). These

litho-quartzose to quartzo-lithic metamorphiclastic sands contain minor plagioclase, rare K-feldspar, abundant metasedimentary rock fragments (mostly schist and metapsammite; MI* ≈ MI ≈ 370), and common micas (more biotite than muscovite) (Figs. 4.1d and 4.2a, b).

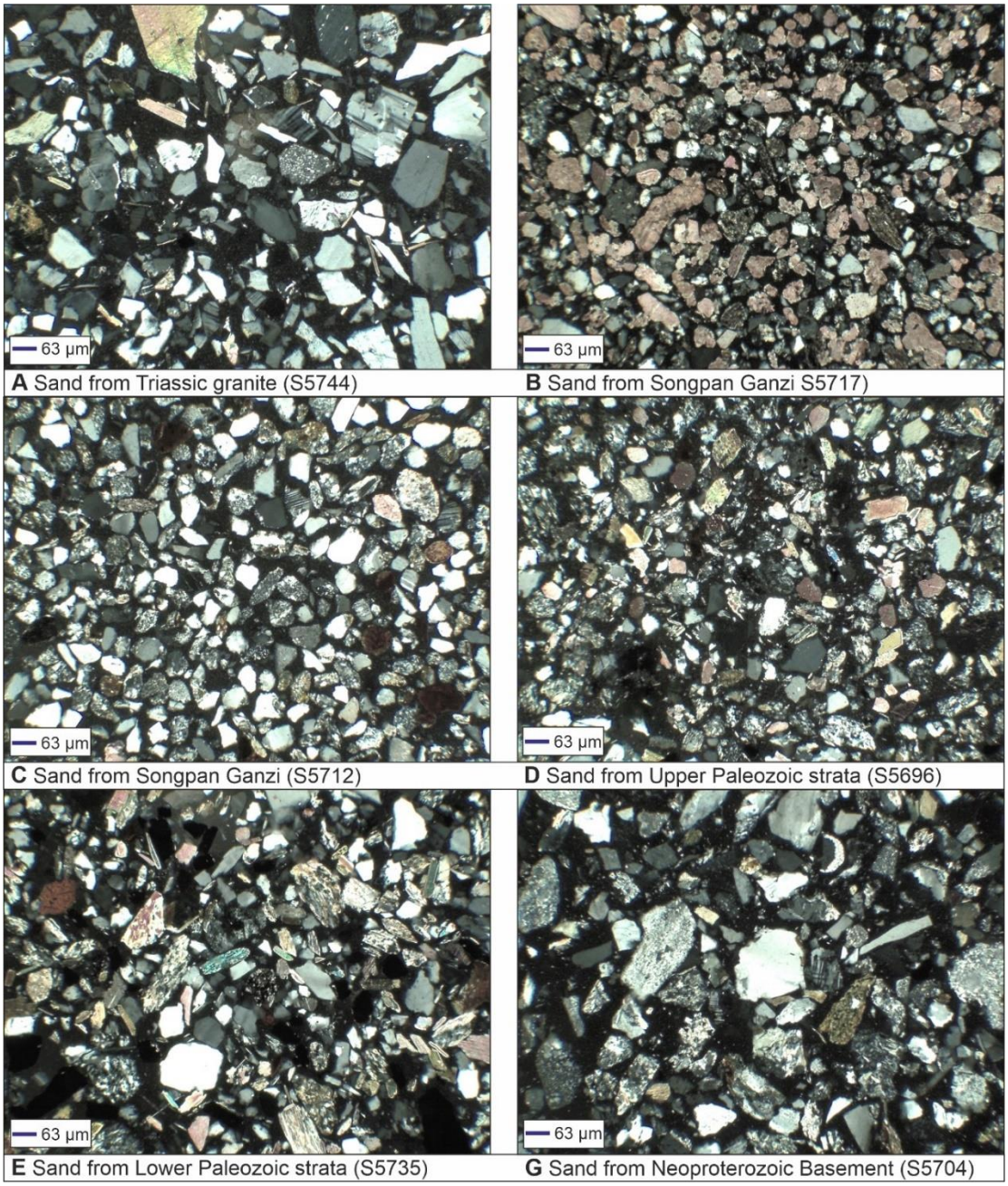

Figure 4.1. Petrography of the Minjiang River sand from the Songpan Ganzi and Longmenshan Mountain. End-member compositions: Triassic granites sand of small rivers draining dominantly within Triassic granitic intrusions were sampled in the Mengtun Valley: A) quartzo-feldspathic sands with subequal amounts of K-feldspar and plagioclase contain granitoid and a few very-high-rank metamorphic rock fragments (S5744); B) quartzo-lithic sands recycled from siliciclastic and subordinate carbonate strata contain sporadic plagioclase, rare K-feldspar

(S5717); C) quartzo-lithic sands sands recycled from siliciclastic contain sporadic plagioclase, rare K-feldspar (S5712); D) litho-quartzose to quartzo-lithic metamorphiclastic sands contain rare feldspar, abundant metasedimentary rock fragments (S5696). Sand of small rivers draining dominantly within Silurian units were sampled in the Songxibao: E) These litho-quartzose to quartzo-lithic metamorphiclastic sands contain minor plagioclase, rare K-feldspar, abundant metasedimentary rock fragments (mostly schist and metapsammite; MI* ≈ MI ≈ 370) (S5735). River sands Neoproterozoic granitoid basement were sampled in the Baisha (5704) Valley: F) quartzo-feldspathic sand with strongly sericitized plagioclase prevailing over K-feldspar, common granitoid and metamorphic (amphibolite, minor gneiss) rock fragments (MI* = MI = 410) (S5704).

The tHM suites are varied, extremely poor and including apatite, amphibole, epidote, and tourmaline (ZTR 17; 5740), moderately poor and dominated by blue/green hornblende (ZTR 4; 5697), or moderately rich and garnet-dominated with amphibole and minor epidote and clinopyroxene (ZTR 3; 5735). Zircon grains in sample 5735 display a polymodal distribution with mainly Tonian (30%) and subordinate Silurian-Triassic (25%), Orosirian (12%), and Siderian-Neoarchean (9%) ages (Figs. 4.3 and 4.4).

4.2.4. Upper Paleozoic Strata

Sand of small rivers draining dominantly within Devonian to Lower Triassic successions were sampled in the Sanlong Valley (5727, 5728, 5732 and 5735) These litho-quartzose to quartzo-lithic metamorphiclastic sands contain rare feldspar, abundant metasedimentary rock fragments (phyllite, schist, metapsammite, and marble; MI* ≈ MI ≈ 350), and common micas (subequal muscovite and biotite) (Figs. 4.1e and 4.2a, b). The extremely poor tHM suite mainly consists of tourmaline and apatite, with amphibole, epidote, and minor rutile, garnet and zircon (ZTR 21-62) (Figs. 4.2c, d).

4.2.5. Neoproterozoic Basement

Sand of small rivers draining entirely within the Neoproterozoic granitoid basement were sampled in the Shaotanghe (5699) and Baisha (5704) Valleys. Sample 5704 is a quartzo-feldspathic sand with strongly sericitized plagioclase prevailing over K-feldspar, common granitoid and metamorphic (amphibolite, minor gneiss) rock fragments (MI* = MI = 410) (Figs. 4.1g and 4.2a, b). The very rich tHM suite is dominated by amphibole (mainly blue/green hornblende with subordinate green/brown hornblende and actinolite) with common epidote and minor clinopyroxene (green to

brown augite and aegirine) (Fig. 4.2c, d). Apatite, titanite, and zircon are rare (ZTR < 1). The unimodal zircon-age spectrum of sample 5704 is dominated by Tonian ages (98%, 88% between 800 and 860 Ma) (Figs. 4.3 and 4.4). Sample 5699 is litho-quartzo-feldspathic with low- to high-rank metabasite (epidosite, amphibolite) and metasedimentary (gneiss, schist, marble) rock fragments (MI* =MI =342). The very rich tHM suite is dominated by epidote (including rare allanite) with subordinate amphibole (mainly blue/green hornblende and anthophyllite). Lower MI*, extensive sericitization of plagioclase, and high epidote/amphibole ratio testify to very intense retrogression of basement rocks in the Shaotanghe Valley (Figs. 4.2c, d).

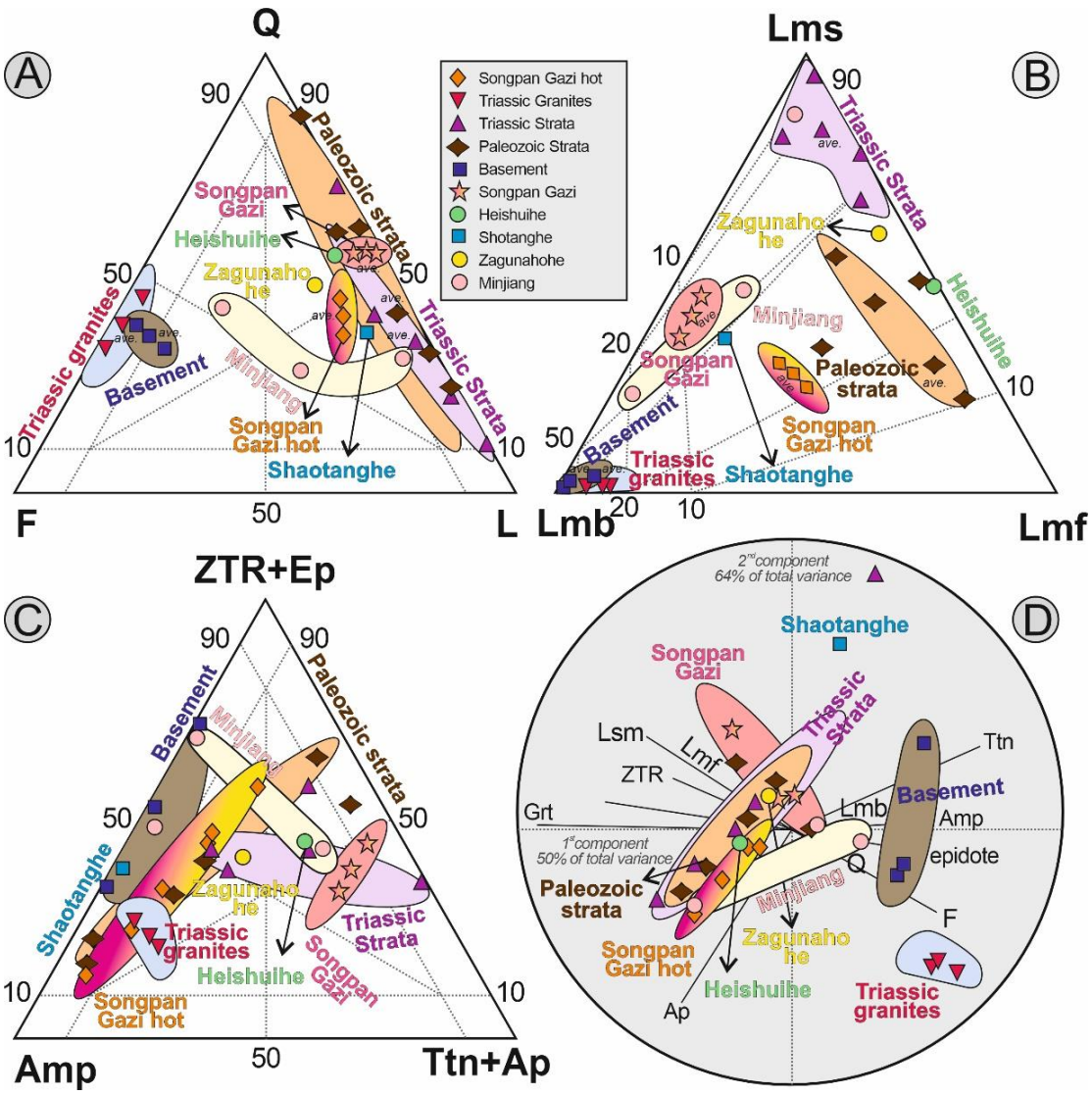

Figure 4.2. Detrital modes of Minjiang River sediments compared with sand carried by the Triassic strata, Triassic granites, Paleozoic strata and basement with its tributaries draining the diverse geological domains of the Songpan Ganzi and Longmenshan mountains (QFL and

LmsLmbLmf diagrams after Ingersoll et al., 1984). Triassic granites and basement sand contains more feldspars, more volcanic, metavolcanic, and metabasite rock fragments, more heavy minerals, and more hypersthene than Paleozoic strata and Triassic strata, indicating greater contribution from the Songpan Ganzi by draining Heishuihe, Zagunaohe and Shaotanghe rivers as main tributaries of Minjiang River. Q = quartz; F = feldspar; L = lithic grains (Lmf = metamorphic; Lmb = volcanic; Lms = sedimentary); other parameters as in Table 4.1a. Data in the LmsLmbLmf and heavy-mineral triangular diagrams are centered to allow better visualization (Von Eynatten et al., 2004).

4.3. Major Tributaries and Minjiang Sand

Major tributaries of the Minjiang are the Heishuihe and Zagunaohe in the mountain catchment, the Shaotanghe, Xihe, and Baishahe in the Dujiangyan area near the mountain front, and the Daduhe and its Qingyijiang tributary in the Sichuan Basin lowlands near Leshan. The Minjiang sediment-routing system has been drastically segmented by both natural (earthquake-induced landslides) and anthropic (large reservoirs) processes into three parts, characterized by distinct compositional signatures of modern sands: 1) the headwaters from Tibet to Diexi Lake; 2) the mountain drainage between the Diexi Lake and the Zipingpu Reservoir.

4.3.1. Mountain Tributaries

The Heishuihe (*hei*, black; *shui*, water; *he*, river) largely drains the Triassic Songpan Ganzi Group in a region where Upper Triassic granite intrusions are widespread, and traverses' Upper Palaeozoic strata in the lower course before joining the Minjiang mainstem. Sand composition changes from feldspatho-litho-quartzose in an upstream branch largely draining Triassic granite (5730), to quartzo-lithic metamorphiclastic in the middle course (5731), and finally to litho-quartzose (5733). Plagioclase predominates over K-feldspar. Metamorphic rank of metapelite and metapsammite rock fragments increases progressively downstream (MI* from 250 to 345, MI from 235 to 340). The very poor tHM suite contains apatite, epidote, amphibole, tourmaline, garnet, zircon, and minor titanite (ZTR 23). Zircon grains in sample 5733 yielded a polymodal distribution with 70% of ages between the Triassic and the Stenian, with minor Statherian-Orosirian (17%) and Siderian-Neoarchean (11%) clusters.

The Zagunaohe flows subparallel to the Heishuihe ~35 to the south. It also largely drains the Triassic Songpan Ganzi Group in a western region where Upper Triassic granite intrusions are widespread, and next skirts around a basement-cored antiform

crossing Upper and Lower Paleozoic strata before joining the Minjiang mainstem. Sand composition changes from litho-quartzose upstream of Paleozoic outcrops (5741) to finally feldspatho-litho-quartzose with plagioclase predominating over K-feldspar and abundant metapsammite rock fragments (5738; MI* 380, MI 375). The tHM suite changes from moderately rich with mostly blue/green hornblende and clinopyroxene upstream to poor and garnet-dominated with epidote, blue/green to green/brown amphibole, and titanite downstream (ZTR 2). Zircon grains in sample 5738 yielded mostly Tonian (66%, peak at 757 Ma) and Cryogenian (11%) ages, with a few earliest Jurassic-Triassic (8%) and Orosirian ages (4%).

4.3.2. Headwaters

In Minjiang headwaters, quartzo-lithic sedimentaclastic sand largely recycled from the Songpan Ganzi domain in Tibet (samples 5709, 5710, 5711, 5714, 5715, 5718, 5719, 5721, and 5724) contains more plagioclase than K-feldspar and is dominated by sedimentary (sparitic and subordinately micritic limestone, dolostone, sandstone, shale) to very-low-rank metasedimentary rock fragments (slate, metasandstone, phyllite, metacarbonate; MI*< 150, MI mostly < 100). Mica is rare. The extremely poor tHM suite includes amphibole, apatite, garnet, zircon, and tourmaline (ZTR 5-40). Zircon grains in sample 5715 yielded mainly Upper Carboniferous to Early Triassic grains (32%, 24% of which Permian), together with Devonian to Cambrian (21%), Tonian (8%), Statherian to Rhyacian (26%, 17% of which Orosirian), and Neoarchean (4%) ages.

4.3.3. Downstream of Diexi Lake

The composition of Minjiang sand changes radically between upstream and downstream of the Diexi Lake, pointing to efficient sequestration of Upper Minjiang sediment in Diexi Lake, Minjiang sand being reconstituted by tributary supply downstream. In the ~25 km separating Diexi Lake and the confluence with the Heishuihe (samples 5726 and 5729), the Minjiang drains narrow antiforms exposing Upper Paleozoic strata at the core and eventually leaves the Songpan Ganzi Group to enter the Paleozoic domain. Sand composition is quartzo-lithic with abundant carbonate (sparite, marble) and subordinate high-rank metapsammite rock fragments (MI* ~410, MI ~350). Mica is abundant (mostly biotite). The very poor tHM suite contains mostly green hornblende, epidote, and garnet (ZTR 3). Detrital-zircon ages in sample 5729 are

mainly Carboniferous-Triassic (21%), Silurian-Ordovician (12%), Tonian (11%), Statherian-Ordovician (30%) and Siderian (7%), with an increase in Neoproterozoic and especially Paleoproterozoic ages and a decrease of Permian ages relatively to the sample upstream of Diexi Lake.

Between the confluences with the Heishuihe and Zagunaohe (samples 5734, 5736, 5737), the Minjiang cuts across the entire Paleozoic succession incising into Neoproterozoic basement as well. Sand composition is quartzo-lithic with minor feldspars (mostly plagioclase) and abundant carbonate (sparite, dolostone, marble) and medium/high-rank metasedimentary rock fragments (paragneiss, schist; MI* surprisingly decreasing from 370 to 320 and MI from 350 to 300). Mica (mostly biotite) is common. The very poor tHM suite mainly consists of amphibole (blue/green and green hornblende) associated with epidote, garnet, and apatite (ZTR ≤ 13). Zircon-age spectra in sample 5737 yielded notably more Tonian (24%) and less Orosirian ages than samples upstream.

Between the Zagunaohe and Shaotanghe confluences, the Minjiang incises for ~60 km into Neoproterozoic granitoid basement (samples 5746 and 5701). Sand composition changes markedly downstream from litho-quartzose to litho-feldspatho-quartzose. Feldspars (plagioclase > K-feldspar), granitoid and metabasite (amphibolite, epidosite) grains markedly increase at the expense of carbonate and metasedimentary rock fragments (MI * ≈ MI ≈ from 370 to 350). Micas (dominantly biotite) also decreases. The tHM suites also change markedly from poor with amphibole, epidote, and garnet to rich and epidote-dominated with subordinate amphibole (blue/green hornblende and minor actinolite) (ZTR 1). The unimodal zircon-age spectrum of sample 5701 is dominated by Tonian ages (92%, 72% between 730 and 790 Ma).

Feldspatho-quartzo-lithic sand (5747) deposited downstream of the Shaotanghe confluence just upstream of the Zipingpu Reservoir contains more plagioclase than K-feldspar and carbonate (sparite, dolostone, marble) and medium/high-rank metamorphic rock fragments (gneiss, schist, minor metabasite; MI* ≈ Mi ≈ 330). Mica (mostly biotite) is common. The moderately rich tHM suite is dominated by amphibole (mainly blue/green hornblende) and epidote in equal proportion (ZTR 2). Sample 5747 yielded less Tonian ages (78%, 41% between 802 and 831 Ma) and a few more Triassic-Carboniferous (11%) and Statherian-Orosirian (4%) ages, revealing additional supply from the Shaotanghe.

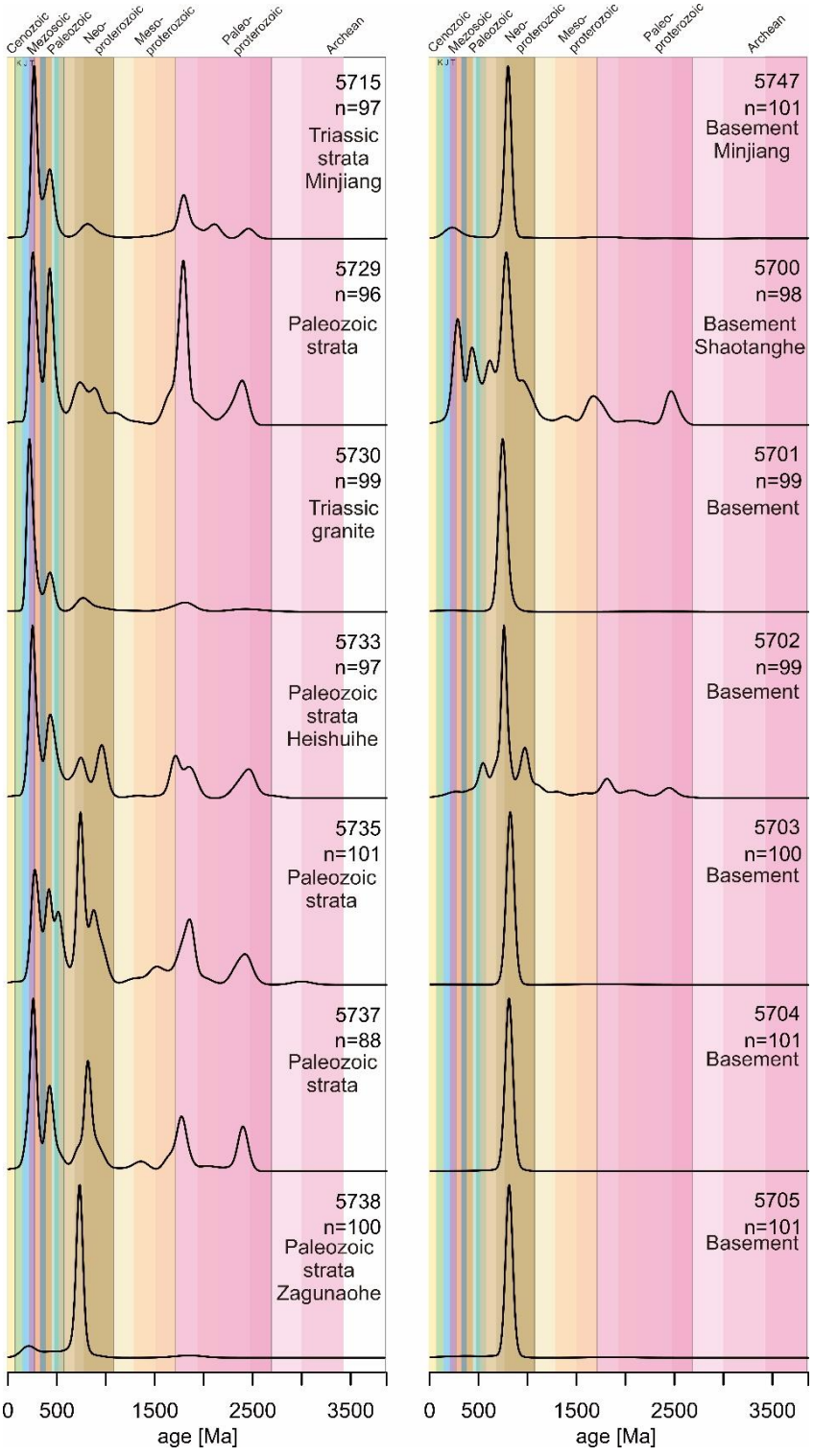

Figure 4.3. U-Pb age spectra of detrital zircons in Minjiang drainge basin and in sands carried by the Minjiang River and its tributaries. Main events of crustal growth in the Longmenshang Mountian by the basement rocks are indicated. The multimodal spectrum of different rock units by sand indicates dominant zircon supply from the different sources, including the Songpan Ganzi (Triassic, Paleozoic stratas with Triassic granites) and basment rocks (ages from 700 to 1000 Ma), together with the Shaotanghe Tributariy. Contribution from the basment and traissic granite is subordinate (mostly Neoproterozoic ages).

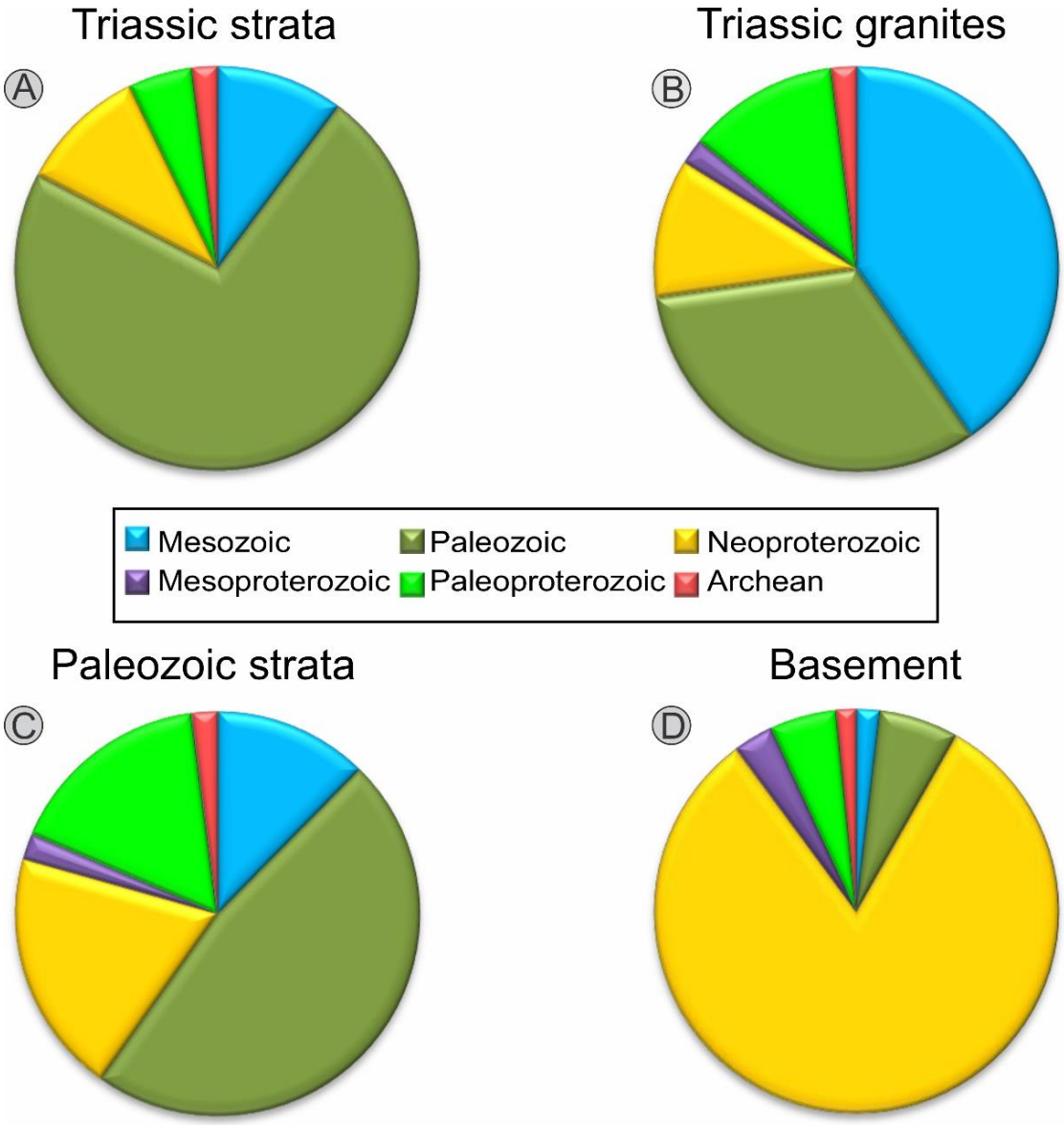

Figure 4.4. Pie charts for the U-Pb age distribution of detrital zircons in Minjiang drainge basin with respect to the for end members. A) Triassic strata is mainly composed by the Mesozoic and Paleozoic with other older ages sediments which is mainly coming from the Songpan Ganzi rock unit. B) Triassic granites is cmposed of precambrain rock units with contribution of other other age group rocks like Mesozoic and Paleozoic. C) Paleozoic strata is mailny consiting of Mesozoic and Paleozoic sediemnts with other older precambrian sediments from the Longmenshang Mountian. D) Basement sediments are eroding from the Neoproterozoic of the Longmenshang Mountian with other older rocks like Mesoproterozoic, Paleopoterozoic and Archean rock units from the Pengguan unit.

Notes: Detrital-Zircon Geochronology

Inspection of the entire dataset highlights two major age concentrations in the Late Triassic-earliest Jurassic (195-215 Ma), corresponding to late Indosinian granite

intrusions, and in the Tonian (two clusters, one between 730 and 780 Ma, mode at ~770 Ma, another between 800 and 850 Ma), corresponding to granitoid intrusions and metamorphism in the Neoproterozoic basement. Other age clusters around 250 Ma, 270 Ma, and 430 Ma need an explanation (Table 4.2).

The petrographic and heavy-mineral signatures of Minjiang and Daduhe sands are similar, and consequently composition does not change much from upstream to downstream of their confluence. Zircon-age spectra, however, are distinct and allow to assess that the Daduhe contributes at least as many zircon grains as the Minjiang upstream to the mainstem downstream.

4.4. Provenance Budgets

Fluvial sediments are very heterogeneous due to the amalgamated mixture of the detrital minerals and lithic fragments. This heterogeneous mixture is eroded from different tectonic rock units that are contributing and supplying in various proportions into the trunk rivers through the numerous segmented river tributaries. If end-member compositional signatures of detritus are known, then relative contributions to total sediment load from each of these sources can be quantified mathematically with forward mixing models (Draper and Smith, 1981; Weltje, 1997; Garzanti et al., 2012).

Forward mixing models based on bulk-petrography data integrated with the complete heavy-mineral dataset were used to assess the relative amount of sand contributed to the Minjiang River by four lithological end-members (Triassic granites, Triassic and Palaeozoic strata and basement) drained by its different tributaries (Shaotanghe, Zagunaohe and Heishuihe rivers with Dixie Lake,) (Figs. 4.5 and 4.6). During rivers transit, sand compositions are believed to be constant (i.e., the effects of both hydraulic sorting and selective mechanical breakdown of sand grains are assumed to be negligible). This hypothesis is supported by the fact that even sand grains that are generally thought to be unstable, such as feldspar and pyroxene, survive ultralong-distance transport in aqueous media (Russell, 1937; Garzanti et al., 2015a, 2015b), and that the tHMC index in the studied sands is invariably ≤ 6.1 and the SRD index varies between 2.65 and 2.77 (Appendix), that are fully harmonious with provenance from the exposed and sedimentary rocks, volcanic, basement, (Garzanti et al., 2009). In the mountainous region for the climate of the Songpan Ganzi and Longmenshan as Minjiang catchment, chemical weathering is likewise not considered as important factor in the present study. Chemical and physical mechanisms that alter the sand

mineralogy, including heavy-mineral enrichment by selective entrainment, can thus be regarded minimal in our samples.

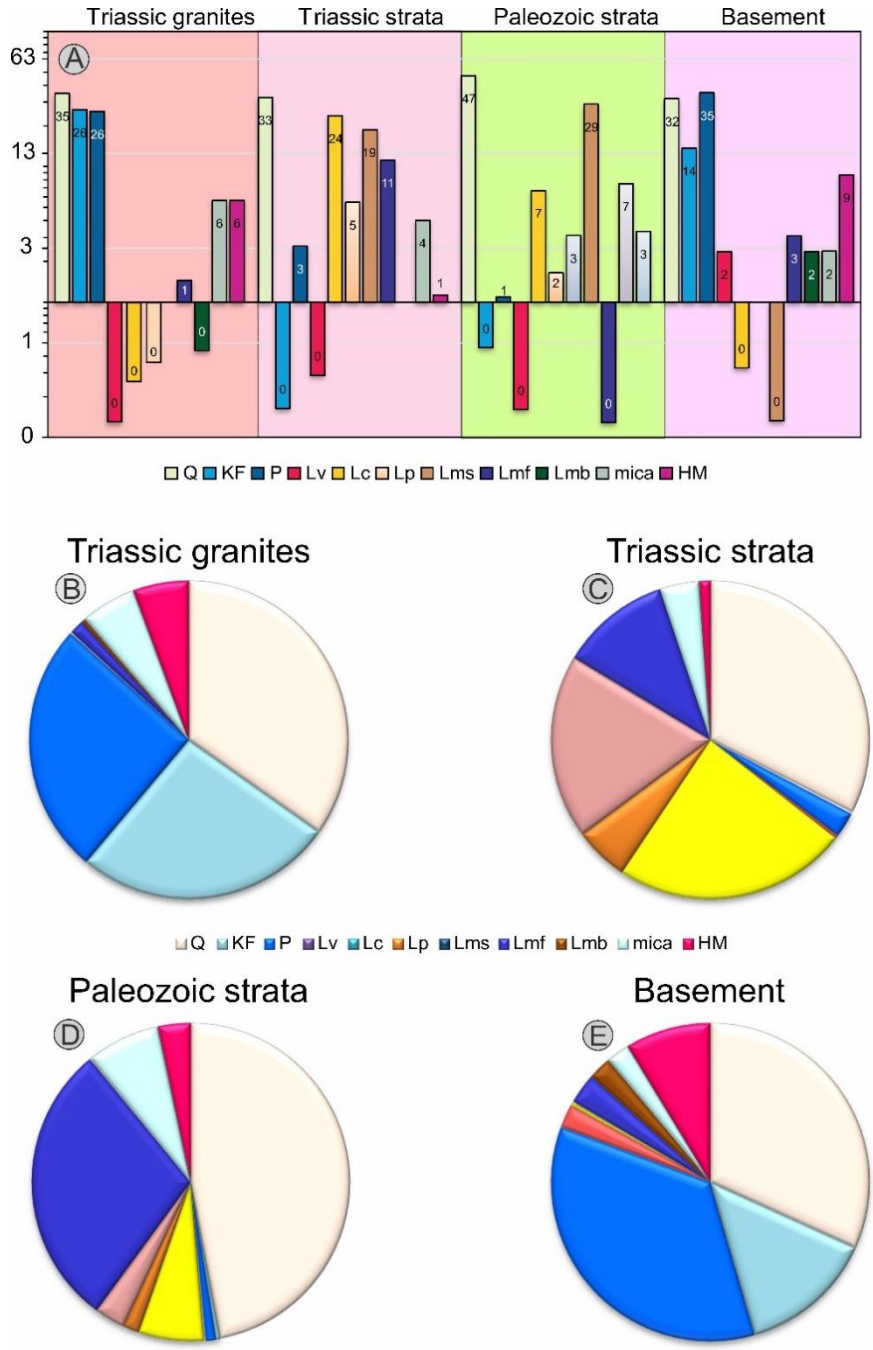

Figure 4.5. Petrographical framework of the complete Minjiang drainage basin. A) Histograms for the distribution of the petrographic framework in the main four end members. Pie charts for petrographic distribution (B-E). B) Triassic granites are rich in quartz and feldspar including plagioclase and k-feldspar with other lithic fragments. C) Triassic strata are rich in quartz with carbonate and metacarbonate grains also includes Lmb and other lithic fragments. D) Paleozoic strata are mainly composed of quartz and Lms with other lithic fragments. E) Basement rocks from the Longmenshan consist of quartz and feldspar including plagioclase and k-feldspar with

other lithic fragments and high content of heavy minerals. Q = quartz; F = feldspars (KF = K-feldspar; P = plagioclase; L = lithic grains (Lvm = volcanic and metavolcanic; Lc = carbonate and metacarbonate; Lh = chert; Lsm = shale, siltstone, slate, and metasiltstone; Lmf = felsic metamorphic; Lmb = metabasite; Lu = ultramafic).

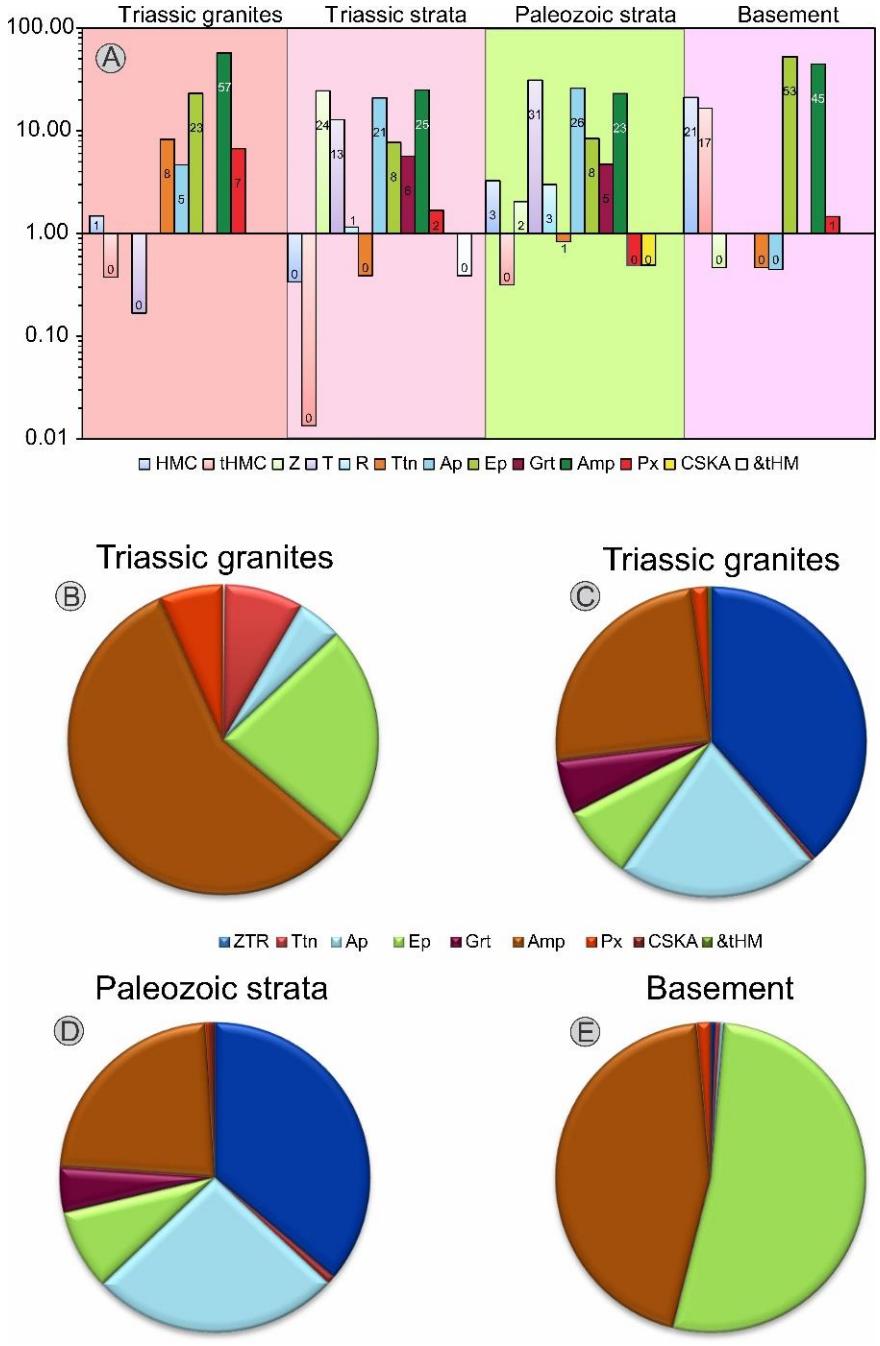

Figure 4.6. Heavy Minerals framework of the complete Minjiang drainage basin. A) Histograms for the distribution of the heavy mineral framework in the main four end members. Pie charts for heavy mineral distribution (B-E). B) Triassic granites are rich in epidote and amphibole including titanite, appetite, and pyroxene with other heavy minerals. C). Triassic strata are rich in ZTR with apatite, epidote, garnet, and amphibole also includes pyroxene with

other heavy minerals. D) Paleozoic strata are mainly composed of ZTR with apatite, epidote, garnet, and amphibole also includes pyroxene with other heavy minerals. E). Basement rocks from the Longmenshan mainly consisting of epidote and amphibole with other heavy minerals. HM = heavy minerals; MI* = Metamorphic Index; tHMC = transparent heavy-mineral concentration. ZTR = zircon + tourmaline + rutile; Ttn = titanite; Ep = epidote-group minerals; Grt = garnet; SKS = staurolite + kyanite + sillimanite; Amp = amphibole; Px = pyroxene (Cpx = clinopyroxene; Opx = orthopyroxene, mostly hypersthene); & tHM = other transparent heavy minerals (apatite, chloritoid, Cr-spinel, olivine, prehnite, pumpellyite, brookite, andalusite, barite).

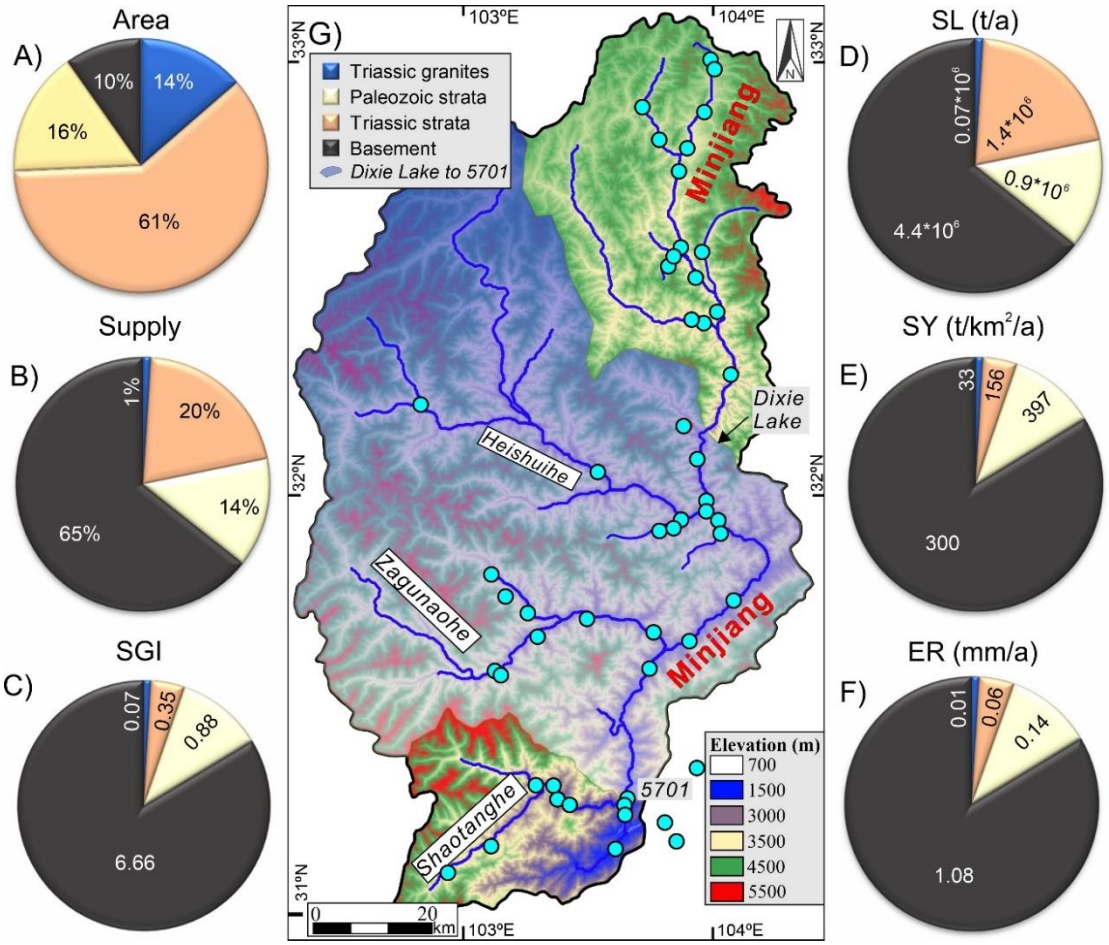

Figure 4.7. Quantitative assessments of the relative contribution (Dixie Lake to 5701Yinxiu sample). A) each end member (Triassic granite, Paleozoic strata, Triassic strata, and Basement) has a different area. B) supply is calculated from the entire petrographic and mineralogical data set, indicating that the main supply of sediments in the catchment is mainly from the Neoproterozoic Basement with Triassic strata to Paleozoic strata. C) for the sediment generation Index (SGI). D) sediment load (t/a) depends on the supply of the sediments to catchment. E) sediment yield (SY) t/km^2 depends on both distributional area of the rocks and sediments load. F) Erosion rate (mm/a) depends on the density of the rocks with calculated

sediment yield. G) blue shaded area on the DEM is showing the catchment area for the sediments from Dixie Lake to 5701 Yinxiu samples which is main Minjiang confluence point at the downstream.

Heavy minerals, being supplied by various source terrains in concentrations that differ by order of magnitude, were treated separately. A distinct, complementary set of provenance estimates was thus calculated, which proved to be essential in testing the overall consistency of the results. Uncertainties in assessing such contributions arise from several factors. It must be remembered that estimates are based on data from sand-sized sediments only, that constitute the bulk of the bed load but represent only an unknown percentage (commonly held as low as 10% but demonstrated to exceed 50% in mountain rivers; Gurnell et al., 1988; Billi et al., 1998) of the total sediment load.

4.4.1. Sand Contribution/Supply of Dixie Lake to Yinxiu

The Quantitative studies through the mixing model according to the linear regression analysis show that four main contributors/supplier for the Dixie to Yinxiu (15217 km^2) are Triassic granites (0±1/2%), Triassic strata (21±1/2%), Palaeozoic strata (14±1/2%), and Basement (65±1/2%) rock units (Fig. 4.7 and Table 4.3).

The main supply rock units for the Dixie to Yinxiu are belong to the basement rocks (1486 km^2) which is 10 percent of the whole catchment but is providing 65% sediment supply to the confluence point to the Minjiang River. The supply from the Triassic granites (2077 km^2) by the linear mixing model is zero which is not reliable therefore it should be more than zero (maybe 1 or 2%). Triassic (9231 km^2) and Palaeozoic (2423 km^2) strata is providing 21% and 14% respectively. This calculation of the supply is showing that the contribution from the basement rock is relatively high (65%). There is an inverse relationship of the area catchment and the sediment supply for the rock units. By comparing to the adjacent area along strike, less crystalline basement in the hinterland but more Mesozoic sedimentary rocks along the Shaotanghe River that is why main contributor at the confluence point of Minjiang River are Precambrian, Palaeozoic and Triassic rock units.

4.4.2. Sand Contribution/Supply of Heishuihe River

In the Heishuihe, there is no influence of the basement rocks that is way there are just three (3) end members for the catchment. Triassic granite (1149 km^2) is 16% of the whole catchment but contribution is just 1±1/2% and the contribution from Triassic

(5325 km^2, 75±1/2% area) and Palaeozoic (1582 km^2, 9% area) strata is 20±1/2% and 79±1/2% (Fig. 4.8 and Table 4.3). This variation is dependent on the altitude of the rock units as Palaeozoic strata is at high altitude as compared to the Triassic strata.

4.4.3. Sand Contribution/Supply of Zagunaohe River

Triassic (2018 km^2) and Palaeozoic (1582 km^2) strata is supplying 37±1/2% and 53±1/2% the sediments to the Zagunaohe catchment that is 4581 km^2. While other two end menders are Triassic granites (935 km^2) which is supplying 9±1/2% and basement is just 1±1/2% to adjust the final model sample (Fig. 4.9 and Table 4.3). Triassic and Palaeozoic strata is supplying more due to the large contributing area in the catchment and less resistant rock units. Triassic granite in the Zagunaohe catchment is relatively less contributing due to the resistance of the hard rocks and also due to the low altitude of the units.

4.4.4. Sand Contribution/Supply of Shaotanghe River

Shaotanghe River (1730 km^2) is getting influence of three (3) end members including Triassic strata (45±1/2%), Palaeozoic strata (25±1/2%), and Basement (30±1/2) rock units (Fig. 4.10 and Table 4.3). Triassic strata (1109 km^2) are occupying the 64% area of the Shaotanghe River with 45% supply of the sediments in the catchment and the final influence point of the Minjiang River. Palaeozoic (306 km^2) and basement (315 km^2) rocks are having same distribution area 18% but with different contribution 25% and 30% respectively. There is direct relation of the area and supply (Fig. 4.8 and Table 4.3). There could be two reasons for the direct relationship, maybe due to soft rocks of the Triassic strata from Songpan Ganzi unit or also with high altitude.

4.4.5. Sand Contribution/Supply of Whole Minjiang Catchment

Whole Minjiang (22811 km^2) from upstream to 5747 having four end members Triassic granites (9%±1/2%), Triassic strata (39±1/2%), Palaeozoic strata (19±1/2%), and Basement (40±1/2%) rock units (Table 4.3). This contribution model is representing that Triassic (15320 km^2) and Basement (1906 km^2) rock units are relatively equal contributor as 39% and 40% respectively for the whole Minjiang catchment. The other end members as Triassic granite (2123 km^2) and Palaeozoic strata (3304 km^2) having 9% and 14% area of the whole Minjiang, and their contribution is also 1% and 19% (cumulatively just 20%) of the whole Minjiang (Fig. 4.11 and Table

4.3). The reason of this different contributions of the end members is that Triassic strata is having large percentage of the whole area and consists of soft rocks while basement rocks having low area but having high altitude and steep slope at the catchment. Triassic granite having low area and supply due to the low altitude and hard lithology. While Palaeozoic end members area of supply is relatively low, but the supply as compared to the Triassic granite is quite high due to soft lithology and high altitude of the mountains.

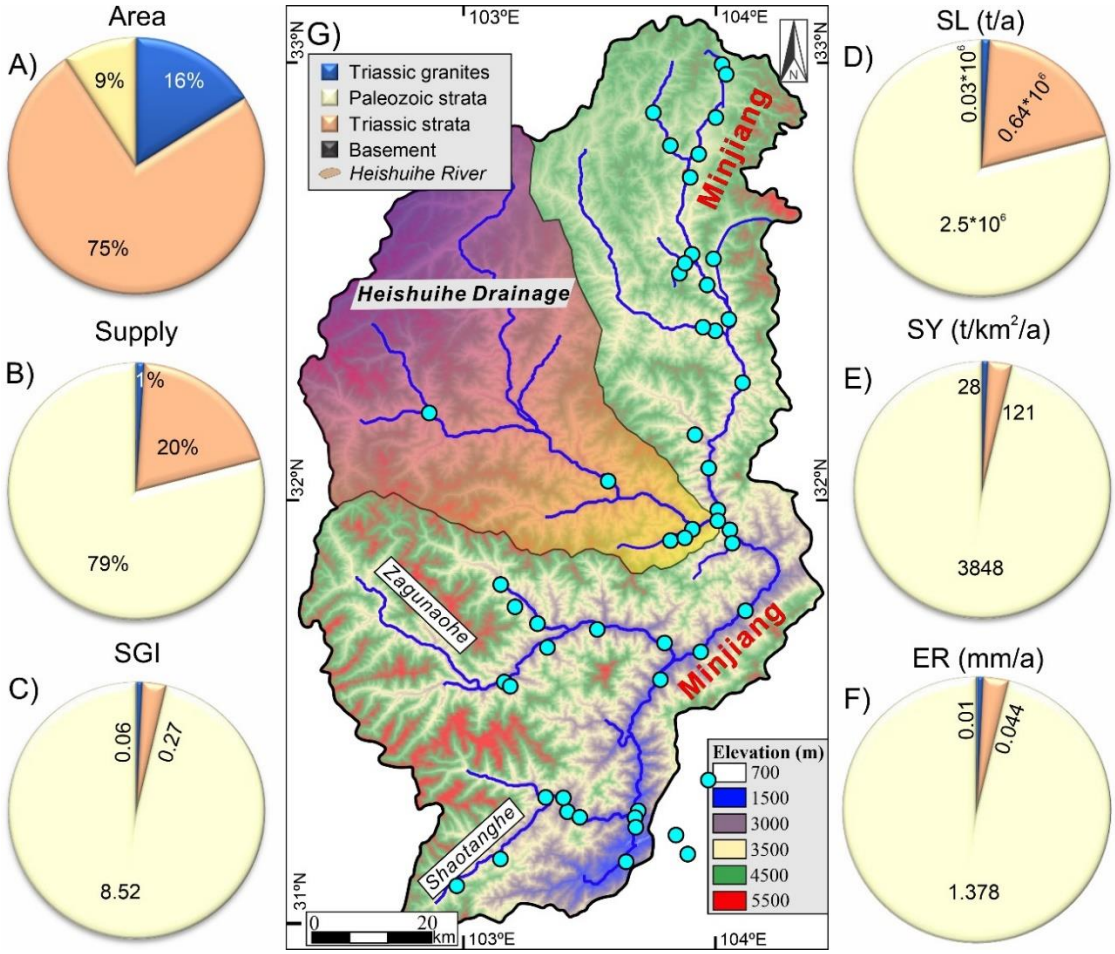

Figure 4.8. Quantitative assessments of the relative contribution (Heishuihe River). A) each end member (Triassic granite, Paleozoic strata, Triassic strata, and Basement) has a different area. B) indicates that the main supply of sediments in the catchment is mainly from the Paleozoic strata and subordinately with Triassic strata. C) for the sediment generation Index (SGI). D) sediment load (t/a) depends on the supply of the sediments to catchment. E) sediment yield (SY) t/km^2 depends on both distributional area of the rocks and sediments load. F) Erosion rate (mm/a) depends on the density of the rocks with calculated sediment yield. G) Dark blue to red shaded area on the DEM is showing the catchment area for the sediments of Heishuihe Drainage.

4.5. Sand Generation Index (SGI) and River Morphometry

The quantitative contribution in terms of provenance with sediment budget of each end member for all major and tributary catchments has calculated from the entire petrographic and mineralogical data set based on the contribution of the representative end members. Quantifying erosion rates in different mountain regions is essential to assess what has been there, which is "sand generation index" (SGI), defined as the capacity of a given rock unit A to generate sand relative to other rock units (Palomares and Arribas, 1993). Under the assumption of uniform erosion rates across the considered source area, the SGI of rock unit A is dependent only on its mineralogical and textural characteristics and can be calculated as the ratio between its proportional sand contribution S_A/S and its proportional outcrop area A/A_A ($SGI = S_A/S*A/A_A$; Vezzoli et al., 2004). The present area of the rock units in the Minjiang catchment with the trunk rivers and tributary catchments was individually calculated through QGIS (Table 4.3). With this area calculation in km^2 and their percentage according to the different catchments is very helpful to determine the erosion rate R with sediment generation index (SGI) of each lithological units and later on for the whole catchment. SGI is commonly based on the lithological properties of the rock units and average erosion rate in the catchment. For the river morphometry in terms of relief and flow pathways the Minjiang River has been quantified through digital elevation models (DEM) in the TopoToolbox, a set of MATLAB functions (Schwanghart and Scherler, 2014; Vezzoli et al, 2020). DEM was downloaded from the Shuttle Radar Topography Mission Global (SRTM GL1; https://opentopography.org) at 30 m resolution (Fig. 6). On the downloaded DEM, longitudinal profile analysis was carried out for the presentation of the abrupt gradient changes in the bedrock channels in order to strength and/or uplift rate. TopoToolbox is used to normalize the channel steepness indices (k_{sn}) which is depended on the power-law relationship $S = k_s A^{-\theta}$ between the local channel slope S and the contributing drainage area A considered as a proxy for discharge (Hack, 1957; Flint, 1974). According to the Snyder et al. (2000), Whipple (2004), Wobus et al. (2006), Norton and Schlunegger (2011), Vezzoli et al. (2020),, a fixed reference concavity (θ ref = 0.45) is used to simplify the comparison of channel slopes with widely varying drainage area and connectivity. Normalized channel steepness indices (k_{sn}) for the Minjiang River are 350 to 570 with average 0.28 connectivity. Due to this lithological variations and abrupt changes in the steepness indices (k_{sn}), sediment generation and erosion cannot be consistent for all rocks in the rugged mountainous

areas as Minjiang catchment which is composed of Songpan Ganzi and central and southern Longmenshan Fault. This section is containing the prediction of the erosional processes and later on investigation of the erosion rates and potential of sediments generations for all rock units with different lithologies which are well exposed in the Minjiang catchment in the form of Songpan Ganzi and central and southern Longmenshan Fault. To follow the methodology of Vezzoli et al. (2020) the estimated and untested calculations by the petrographic and heavy mineral dataset the provenance budget has been extrapolated into for the entire sediment load. This estimated and extrapolated provenance budget is used to validate the average bedload in the term of flux of suspended load with sediment yield for each single stream/tributary and trunk river for the whole Minjiang catchment.

4.5.1. SGI from Dixie Lake to Yinxiu

Sediment provenance belongs to the three main contributors as end members for this Dixie Lake to Yinxiu catchments. These are basements, Triassic with Palaeozoic strata which are producing sediment generation index (SGI) from 0.35-6.66 based on commotional framework belong to Songpan Ganzi and Sothern part of the Longmenshan. Basement is mainly the source of the sand sized bed sediments in the Minjiang River catchment (almost 65% supply, 10% area and SGI is 6.66) from central to southern Longmenshan consists of Pengguan massif (PM) and Baoxing massif (BM). Relatively the second main source of the sediments for this catchment after the basement rocks are Triassic and Paleozoic strata start (61% and 16% area of the catchment with 21% and 14% supply/ contribution with 0.35 and 0.88 SGI respectively). The Triassic granite contribution is 0% with the linear mixing model but in presence there is some 1 to 2% contribution because it is 14% area of the whole catchment which has 0.07 SGI. The Sediment generation index (SGI) shows that metamorphic grains in the confluence point are generated by the granitoid rocks from the basement regimes which is 6.66. This contribution of the different rock units is cumulatively 100% of the entire Minjiang catchment (Fig. 4.7 and Table 4.3).

4.5.5. SGI for Heishuihe River

Heishuihe is mainly getting their sediments supply from the Triassic and Palaeozoic strata 20% and 79% with 0.27 and 8.52 SGI (Fig. 4.8 and Table 4.3). Which is depicting that the main provenance for the Heishuihe river catchment is Songpan Ganzi rock

units. There is Triassic intrusion of granites, but they have no as such dominant influence maybe due to the high compatibility of the rock units and less erosion rate.

4.5.4. SGI for Zagunaohe River

In the Zagunaohe river catchment, Songpan Ganzi rock units Triassic (37%) and Paleozoic (53%) are the main supplier for the provenance budget in the catchment with 0.84 and 1.53 SGI respectively. The other two units from the Triassic granites and basement are 20% and 1% supplier respectively but they have a quite strong SGI index 0.44 and 1.00 (Fig. 4.9 and Table 4.3).

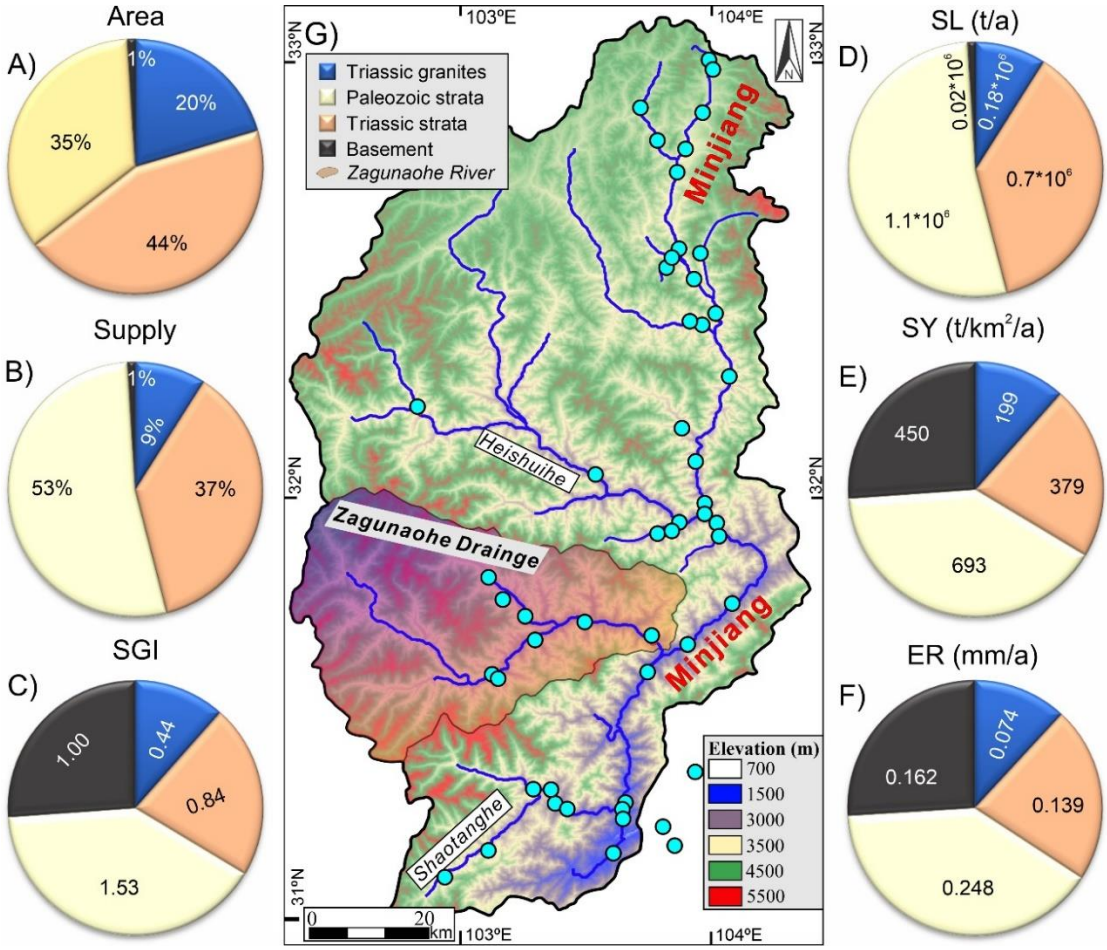

Figure 4.9. Quantitative assessments of the relative contribution (Zagunaohe River). A) each end member (Triassic granite, Paleozoic strata, Triassic strata, and Basement) has a different area. B) supply is calculated from the entire petrographic and mineralogical data set, indicate that the main supply of sediments in the catchment is mainly from the Paleozoic strata and Triassic strata with subordinately Triassic granites to Neoproterozoic Basement. C) for the sediment generation Index (SGI). D) sediment load (t/a) depends on the supply of the sediments to catchment. E) sediment yield (SY) t/km^2 depends on both distributional area of the rocks and sediments load. F) Erosion rate (mm/a) depends on the density of the rocks with calculated

sediment yield. G) Dark red to blue shaded area on the DEM is showing the catchment area for the sediments of Zagunaohe Drainage.

4.5.2. SGI for Shaotanghe River

Triassic and Paleozoic strata provide 45% and 25% sediments from Songpan Ganzi that is rich in flysch sediments and mainly influencing the provenance budget of the Shaotanghe catchment. These flysch sediments belong to the turbiditic turbidities which are more than 10000 m thick. The SGI from these units is 0.70 to 1.42 but the SGI from the basement rocks is relatively high, which is 1.65 due to the 30% supply of the sediments and relatively high altitude (Fig. 4.10 and Table 4.3). Accordingly, to the supply of the sediments the provenance of the catchment belongs to the Songpan Ganzi rock units while the main sediment generator is basement.

4.5.3. SGI for Whole Minjiang River-Upstream to 5747

Triassic strata supply 39% sand sediments with 67% area of the whole catchment and Paleozoic strata is 14% with 19% supplying of the sediments from Songpan Ganzi tectonic units with 0.58 and 1.31 SGI. The SGI is showing that generation of the sediments is quite high in Paleozoic strata as compared to Triassic strata due to the high altitude of the Paleozoic strata. In the catchment, there is also a strong influence of the sediment generation from the basement rocks which is 4.79 index, and it is generating from just 8% area of the catchment. The supply from the basement is 40%, which is relativity high from all end members due to the steepness of the slope at the Longmenshan (Fig. 4.11 and Table 4.3). This shows that the provenance units for the Minjiang river are mainly Triassic strata from Songpan Ganzi and basement rocks from Longmenshan.

4.6. Erosion Rates in the Minjiang catchment

According to Hinderer et al., 2013, sediment volume or mass passing through a certain portion of the river channel per unit of time is referred to as sediment flux or load in large drainage systems. The total sediment load is calculated by the sum up of bedload, suspended load and dissolved load. sediment yield is total sediment load normalized by drainage area. Because information on suspended load is not always available or consistent, and bedload data is also mostly unattainable, these values of sediment yield, bedload, and dissolved load are normally evaluated/consistent erroneously (Vezzoli et al., 2020). Minjiang catchment is relatively attractive due to

the steepest drainage area of the Tibetan Plateau due to which bedload data is not available and hard to measure. and a diverse estimation of suspended load has been summarized of the entire catchment (Table 4.3). Bedload is particularly difficult to measure, and in the absence of particular data, it is commonly believed to be 10% of suspended load or between 5 and 20% of total load (e.g., Lane and Borland, 1951; Hay, 1998).

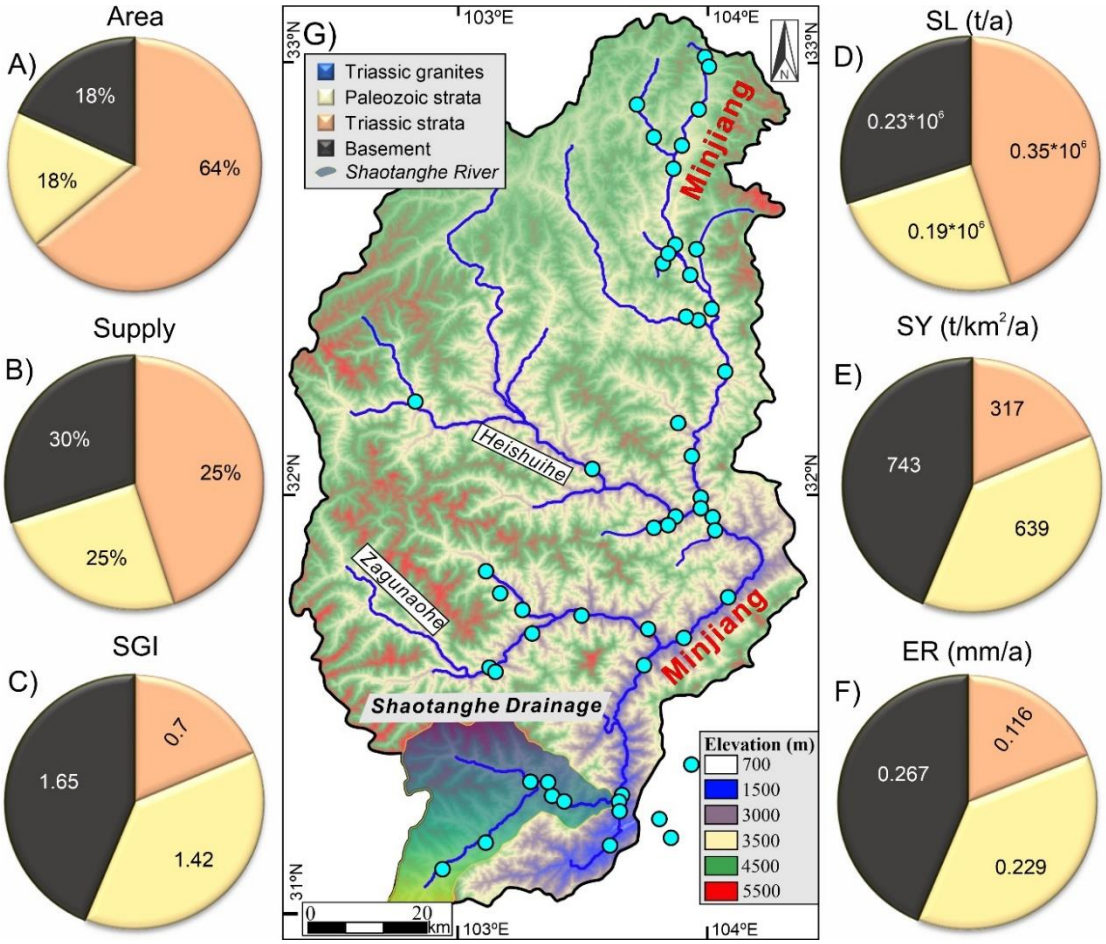

Figure 4.10. Quantitative assessments of the relative contribution (Shaotanghe River). A) each end member (Triassic granite, Paleozoic strata, Triassic strata, and Basement) has a different area. B) indicates that the main supply of sediments in the catchment is mainly from the Triassic strata, Paleozoic strata, and Basement. C) for the sediment generation Index (SGI). D) sediment load (t/a) depends on the supply of the sediments to catchment. E) sediment yield (SY) t/km^2 depends on both distributional area of the rocks and sediments load. F) Erosion rate (mm/a) depends on the density of the rocks with calculated sediment yield. G) Dark blue to green shaded area on the DEM is showing the catchment area for the sediments of Shaotanghe Drainage.

However, in mountain streams, bedload can account for up to half of sediment transport (Turowski et al., 2010), and a suspended/bedload proportion of whole catchment area percent was predicted for the Minjiang River's Mountain basin. In our analysis, we've assumed that bedload accounts for a third of total load in mountain catchments, and that it accounts for just 10% of total load in the alluvial plain. There is a strong relationship between erosion rate E and the annual sediment volume V which is equal to $E = \frac{V\rho s}{\rho r}[\frac{mm}{a}]$ where a is the drainage area, ρs the bulk-sediment density, and ρr the solid-rock density. Moreover, Einsele and Hinderer, (1998) and Hinderer, (2001), have analyzed that erosion rate is usually impacted by the notorious sediments density due to the inaccuracy with uncertainty of estimated density of sediment fluxes.

The range of the densities for mud and poorly sorted gravels is usually noticed between ~1.1 g cm^{-3} and ~1.9 g cm^{-3}. In our calculations, we used the grain density of daughter sand assessed by integrated petrographic and heavy-mineral data as a proxy for the average density of parent rocks ρr. (i.e., SRD index). All computed values in this study assumed ρs = 1.5 g cm^{-3} and ρr = 2.80 g cm^{-3} because SRD values around 2.70 g cm^{-3} (from 2.67 to 2.80 g cm^{-3}) were consistently obtained for all the analyzed catchments.

The annual sediment flux in the Minjiang is estimated to be 6 million tons. Intense rainfall in the mountain part of the catchment (24,000 km^2) plays a crucial role in the seasonal transportation of sediments (Guo et al., 2016; Jian et al., 2020). Three quarters of the sediment flux occurs during the monsoon season (April to September), when water discharge may reach up to 75% during peak floods triggered by tropical cyclones in June (Yin et al., 2010). Because of high topographic relief, there is a marked temperature gradient, with up to 15℃ differences from the edge of the Tibetan Plateau to the Sichuan Basin in both dry and rainy seasons (Liu, 2020). The average annual flow is 1500 m^3/s measured at Fulu hydrographic station. Dadu He suspended load was 31.51 $\times 10^6$t/a, according to the Tongjiezi station in 1956-1986 (Lin Chengkun 1995). By Hairong et al., 2014**,** Minjinag River has an average annual $144*10^4$ m^3 runoff. The runoff in the wet season from May to October accounts for 75% of the annual runoff. The average annual sediment discharge is $70.8*10^6$t.

4.7. Sediment Yield/Flux and Focused Erosion Rate from Suspend Load (SL)

The Erosion rate for the Minjiang Catchment has been calculated from the suspended load dataset that is reported by Hairong et al., 2014 and 2019 (Table 4.3).

From the suspended load of the Zipingpu station that is covering the upper Minjiang River till the Dixie Lake. The catchment area from the Zipingpu to the Dixie Lake is 17715 km^2 that is 78% of the upper Minjiang (23606 km^2). Dixie lake formed by the 1933 earthquake that splinted the Upper Minjiang River into two segments. The upper part of Minjiang from Dixie Lake is not contributing to the suspended load in the Zipingpu hydro station. So that is why the suspended load ($8.0*10^6$ t/a) that is accumulated into the Zipingpu is between the Dixie Lake and Zipingpu hydro station. And the area for the Dixie to Yinxiu is 15217 km^2 (86% of 17715 km^2). For this reason, for this catchment the suspended load is also 86% of the $8.0*10^6$ t/a which is 6871775 t/a. After finding the suspend load for Dixie to Yinxiu, finding out the sediment yield (SY) is also easy which is the ratio between suspend load and catchment area. So, the calculated sediment yield (SY) for the catchment is 452 $tkm^{-2}a^{-1}$. For the Erosion rate (R) into mm/a, sediment yield has been divided to rock density (g/cm^3), by which the calculated erosion rate is 0.166 mm/a (Fig. 4.7 and Table 4.3).

According to this procedure, the sediment yield and erosion rate from the end member Triassic granites is 33 $tkm^{-2}a^{-1}$ and 0.012 mm/a respectively that is 1% contributor of the catchment into the confluence point of the Minjiang river. The sediment yield and erosion rate from the Triassic strata is 156 $tkm^{-2}a^{-1}$ and 0.058 mm/a, 21% contributor. The sediment yield and erosion rate from the Paleozoic end member is 397 $tkm^{-2}a^{-1}$ and 0.142 mm/a, 14% contributor. And from the Precambrian basement is 1486 $tkm^{-2}a^{-1}$ and 1.081 mm/a with 65% contribution into the confluence of Minjiang (Fig. 4.7 and Table 4.3). Precambrian basement rocks in the catchment are mainly high focused erosion rate end member due to the high slope and altitude that is producing main sediment flux in the Minjiang confluence. The second grade in terms of sediment load and erosion rate end member is Paleozoic strata due to the soft lithological variation of the Songpan Ganzi flysch sediments. Triassic granite is negligible due to very minimal contribution and all other factors as sediment load flux and focused erosion rate due to the low altitude and high resistant rocks.

4.7.1. Shaotanghe River

The catchment area of Shaotanghe is 1730 km^2 through which basement rocks (315 km^2, 18% of area with 30% supply) are producing 743 $tkm^{-2}a^{-1}$ sediment yield with 0.267 mm/a erosion rate from the southern Longmenshan. Triassic and Paleozoic strata supply 45% and 25% sand sized sediments with 317 $tkm^{-2}a^{-1}$ and 639 $tkm^{-2}a^{-1}$ sediment

yield with 0.116 mm/a, and 0.229 mm/a respectively (Fig. 4.10 and Table. 4.3). Basement rocks in the Shaotanghe catchment are the main high focused erosion rate end member due to the high slope and altitude. The second-grade end member is Paleozoic strata due to the soft lithological variation of the Songpan Ganzi flysch sediments.

4.7.2. Whole Minjiang (Dixie Lake to 5747)

The catchment area of whole Minjiang is 22811 km^2 through which basement rocks (1906 km^2, 8% of area with 40% supply) are producing 1679 $tkm^{-2}a^{-1}$ sediment yield with 0.604 mm/a erosion rate from the central and southern Longmenshan. Triassic granites, Triassic and Paleozoic strata supply 9%, 67% and 14% sand sized sediments with 38 $tkm^{-2}a^{-1}$, 204 $tkm^{-2}a^{-1}$ and 460 $tkm^{-2}a^{-1}$ sediment yield with 0.014 mm/a, 0.075 mm/a, and 0.165 mm/a respectively (Fig. 4.11 and Table 4.3). Again, basement rocks in the catchment are the main high focused erosion rate end member due to the high slope and altitude although have hard rock means low resistant rocks. The second-grade end members are Triassic and Paleozoic strata due to the soft lithological variation of the Songpan Ganzi flysch sediments. Triassic granite is less important due to the low altitude and high resistant rocks.

One of the important factors that should be considered is the quick mobilization of land sliding and debris flow triggered by the 1993 and 2008 earthquakes events (Dixie Lake and Wenchuan respectively) that effected the sediment discharge directly towards the final Minjiang influence.

4.7.3. Zagunaohe River

The catchment area of Zagunaohe is 4581 km^2 through which Paleozoic strata (1580 km^2, 35% of area with 53% supply) are producing 693 $tkm^{-2}a^{-1}$ sediment yield with 0.248 mm/a erosion rate from the Songpan Ganzi unit. Triassic granites, Triassic strata and basement rocks supply 9%, 37% and 1% sand sized sediments with 199 $tkm^{-2}a^{-1}$, 379 $tkm^{-2}a^{-1}$ and 450 $tkm^{-2}a^{-1}$ sediment yield with 0.074 mm/a, 0.139 mm/a, and 0.162 mm/a respectively (Fig. 4.9 and Table 4.3). In this catchment Paleozoic strata is the main high focused erosion rate end member due to the high slope and altitude moreover having flysch sediments from Songpan Ganzi unit. The second-grade end members are Triassic strata and basement rocks due to the soft lithological variation of the Longmenshan and Songpan Ganzi flysch sediments with different altitudes. Triassic granite is less important due to the low altitude and high resistant rocks.

4.7.4. Heishuihe River

The catchment area of Heishuihe is 7135 km^2 through which Paleozoic strata (661 km^2, 9% of area with 79% supply) are producing 3848 $tkm^{-2}a^{-1}$ sediment yield with 1.378 mm/a erosion rate from the Songpan Ganzi unit. Triassic granites, and Triassic strata are supplying 1%, and 20% sand sized sediments with 28 $tkm^{-2}a^{-1}$, and 121 $tkm^{-2}a^{-1}$ sediment yield with 0.010 mm/a, and 0.044 mm/a, respectively (Fig. 4.8 and Table 4.3). In this catchment Paleozoic strata is the main high focused erosion rate end member due to the high slope and altitude. Again, Triassic granite is less important due to the low altitude and high resistant rocks.

4.8. Relationship of Sediment Contribution with Sediment Yield and Focused Erosion Rate

Similarly, the active tectonism of the area deeply influenced the sediment generation system of the Minjiang River catchment. This complete procedure of the estimated calculation of sediment yield and erosion rate shows that there is an inverse relationship between the sediment supply, catchment area with sediment yield and erosion rate (Fig. 4.12 and Table. 4.3). Area of Triassic granites is 2077 km^2 which is 14% area of the catchment and is supplying 1% of sediments, while its erosion rate is 0.012 mm/a. Area of Triassic strata is 9231 km^2 which is 61% of the catchment and it is supplying almost 21% of sediments, while its erosion rate is 0.058 mm/a. The area of Paleozoic strata is 2423 km^2 and it is the 16% of the catchment which is supplying almost 14% sediments. The sediment yield of Paleozoic is 397 $tkm^{-2}a^{-1}$ while its erosion rate 0.142 mm/a. Area of Precambrian basement is 1486 km^2 and it is the 10% of the catchment which is supplying almost 65% sediments. The sediment yield of basement is 3006 $tkm^{-2}a^{-1}$ while its erosion rate is 1.081 mm/a.

Note: Sediment provenance and budget are commonly based on the lithological properties of the rock units and average erosion rate in the catchment with the altitude level. So, sediment generation and erosion cannot be consistent for all rocks in the rugged mountainous areas as Minjiang catchment which is composed of Songpan Ganzi and central and southern Longmenshan Fault. The other reason in this Minjiang River catchment is the influence of extensive earthquakes to generate the sediments.

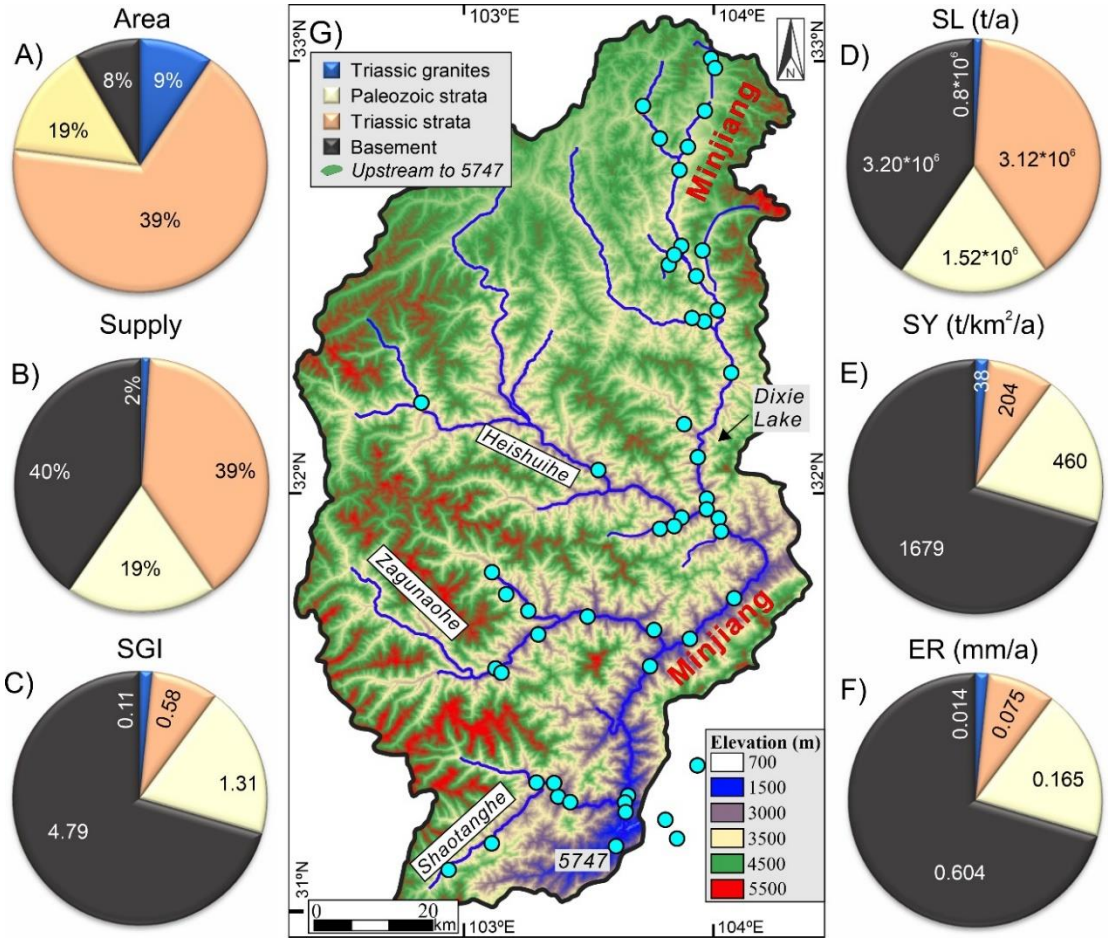

Figure 4.11. Quantitative assessments of the complete relative contribution. A) each end member (Triassic granite, Paleozoic strata, Triassic strata, and Basement) has a different area. B) indicates that the main supply of sediments in the catchment is mainly from the Paleozoic strata and Basement with subordinate Triassic strata. C) for the sediment generation Index (SGI). D) sediment load (t/a) depends on the supply of the sediments to catchment. E) sediment yield (SY) t/km^2 depends on both distributional area of the rocks and sediments load. F) Erosion rate (mm/a) depends on the density of the rocks with calculated sediment yield. G) DEM is showing the complete Drainage of Minjiang catchment area.

4.9. Provenance Studies Based on Zircon Dating

The multidimensional scaling (MDS) (Fig. 4.13) based on the U-Pb zircon age spectra (blue color box defined by six pure basement sand samples downstream of the main Minjiang confluence with one sample is mixed with Minjiang and basement sand dominantly eroded by the Longmenshan Mountain with some Songpan Ganzi rock units). Basement sand is mostly drained by the Shaotanghe Tributary that is eroded from the Longmenshan Mountain Belt. Zagunaohe and Heishuihe tributaries are the

main source for eroding the Triassic strata and Paleozoic Triassic from the Songpan Ganzi rock unit with Triassic granites (intrusion in the Songpan Ganzi).

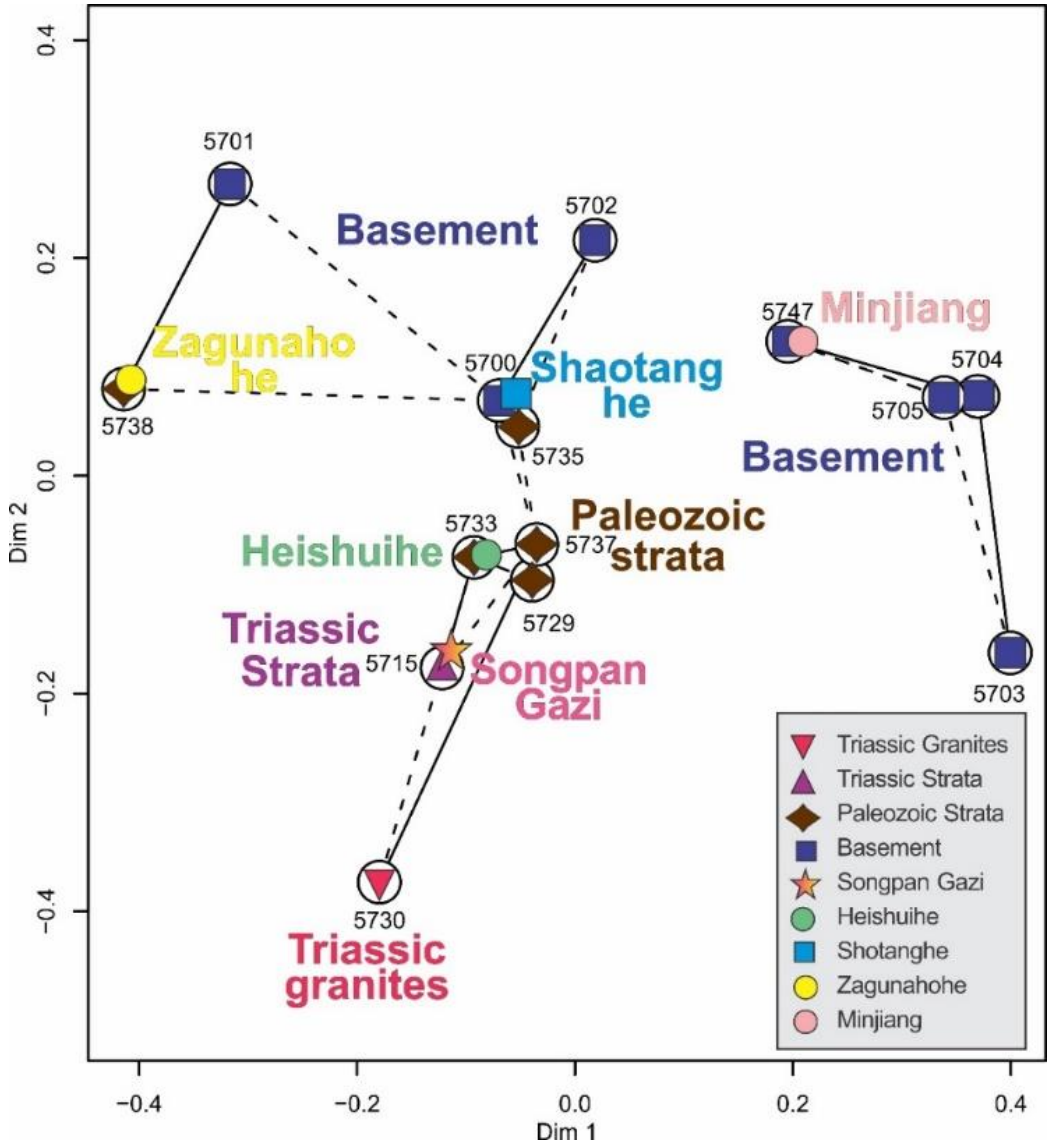

Figure 4.13. Multidimensional scaling (MDS) map based on U-Pb zircon age spectra to show that basement sand is mostly drained by the Shaotanghe Tributary that is eroded from the Longmenshan Mountain Belt. Zagunaohe and Heishuihe tributaries are the main source for eroding the Triassic strata and Paleozoic Triassic from the Songpan Ganzi rock unit with Triassic granites. Closest and second-closest neighbors are linked by solid and dashed lines, respectively.

The KDEs diagrams of the U-Pb zircon age spectra with the map of Minjiang catchment from its different tributaries (Zagunaohe, Heishuihe and Shaotanghe rivers) are representing the more prices studies and analysis about the final contribution and source of the zircon grains into the final confluence of the Minjiang River (Fig. 4.14**)**. It is clearly scene that the upper most part of the Minjiang above the Dixie Lake (formed

by a 1933 earthquake) is not contributing from the Qingling Belt and Songpan Ganzi into the final confluence point due to the complete storage of the sediments from the Qingling Belt and Songpan Ganzi rock units. Detrital-zircon ages in sample 5729 from Paleozoic strata as a Songpan Ganzi rock unit are mainly Carboniferous-Triassic (21%), Silurian-Ordovician (12%), Tonian (11%), Statherian-Ordovician (30%) and Siderian (7%), with an increase in Neoproterozoic and especially Paleoproterozoic ages and a decrease of Permian ages relatively to the sample upstream of Diexi Lake. Sample 5747 from the basement rock units yielded less Tonian ages (78%, 41% between 802 and 831 Ma) and a few more Triassic-Carboniferous (11%) and Statherian-Orosirian (4%) ages, revealing additional supply from the Shaotanghe Tributary. This is the main contributor and supplier as a source of the Minjiang River at the confluence of the drainage system with the lesser contribution of the Paleozoic and Triassic strata with the Triassic granites that are eroded through Zagunaohe and Heishuihe tributaries.

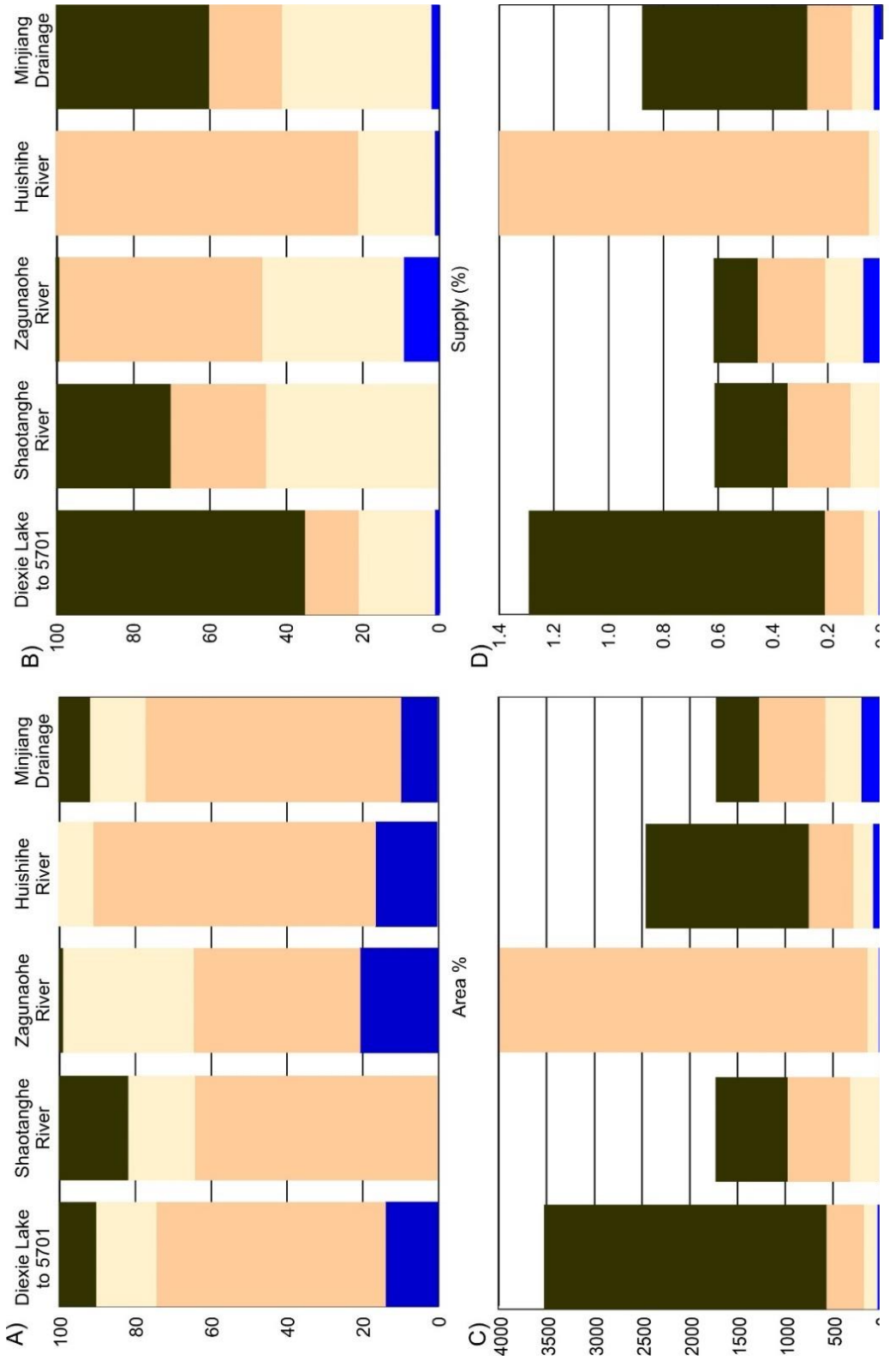

Figure 4.12. Summary of the sediment supply, sediment yield, erosion rate and supplying area in the Minjiang catchment and its tributaries.

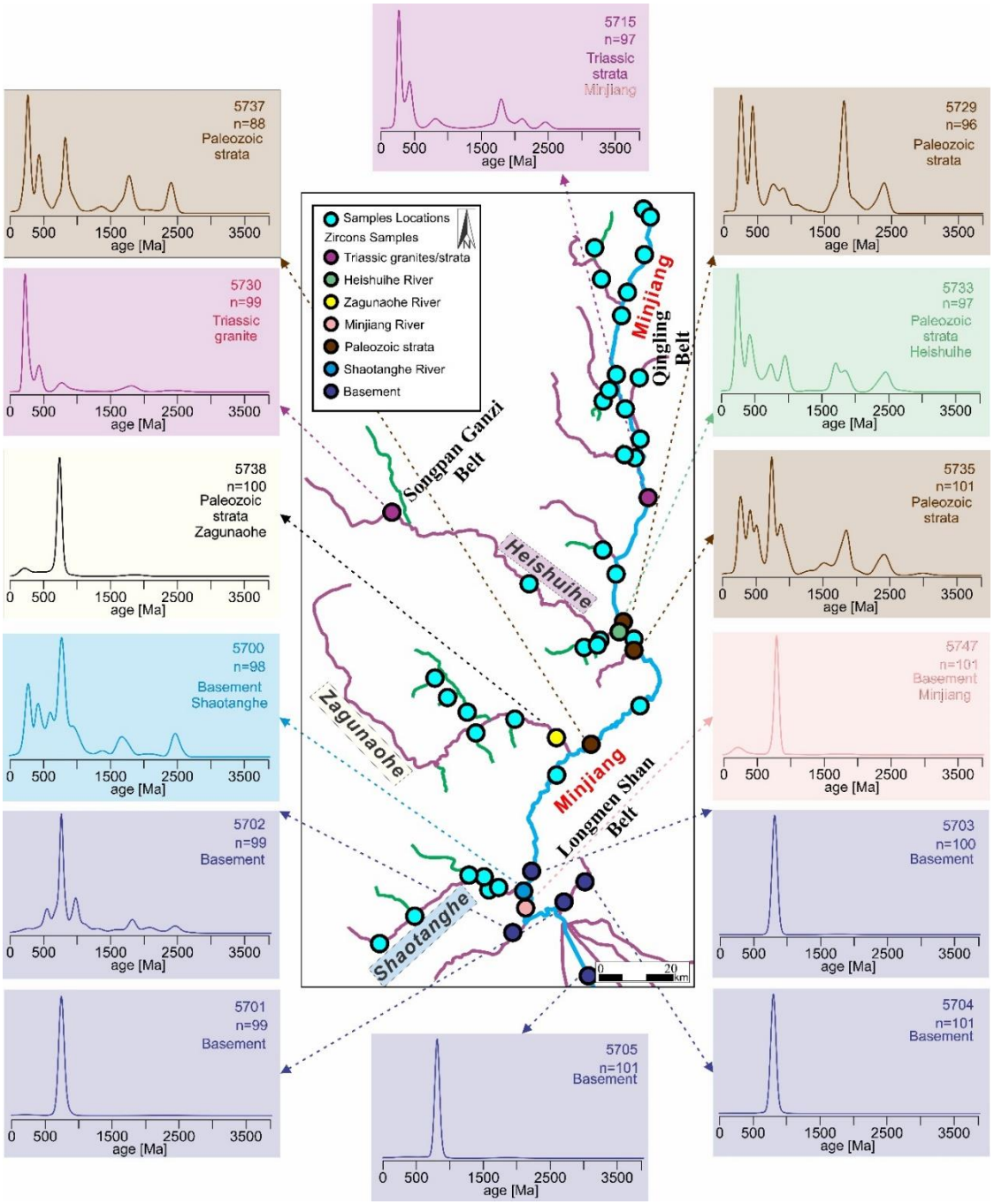

Figure 4.14. U-Pb detrital zircons age spectra. Archean ages are common in Triassic strata, Triassic granites with Paleozoic strata and less common in basement sediments sourced in the Minjiang Drainage Basin. Paleoproterozoic ages are common in Triassic strata and Paleozoic strata sands recycling Songpan Ganzi and in Basement sand largely derived from the Neoproterozoic form Longmenshan Mountain Belt. Paleozoic ages are widespread, overwhelming in Triassic granites with Paleozoic strata and dominant in Triassic strata from Songpan Ganzi sand. Triassic granites are also dominant by the Mesozoic with Cenozoic ages that is draining to the Minjiang by the Heishuihe Tributary.

Conclusions

Segmented Minjiang river is bounded by the tectonically active Songpan Ganzi and central to southern Longmenshan fault system that is one of the steepest regions of the Tibetan plateau. The vigorously important provenance budget of the Minjiang River we have used geological domains and clearly distinct petrographic and heavy-mineral fingerprints. According to the provenance budget, contributors/supplier for the Dixie to Yinxiu (15217 km^2) are Triassic granites (0±1/2%, 33 $tkm^{-2}a^{-1}$ and 0.012 mm/a), Triassic strata (21±1/2%, 156 $tkm^{-2}a^{-1}$ and 0.058 mm/a), Palaeozoic strata (14±1/2%, 397 $tkm^{-2}a^{-1}$ and 0.142 mm/a), and Basement (65±1/2%, 1486 $tkm^{-2}a^{-1}$ and 1.081 mm/a) rock units. The main supply rock units for the Dixie to Yinxiu are belong to the basement rocks (1486 km^2) which is 10 percent of the whole catchment but is providing 65% sediment supply to the confluence point to the Minjiang River with sediment yield 1486 $tkm^{-2}a^{-1}$ and erosion rate 1.081 mm/a. The sediment generation index (SGI) is from 0.35-6.66 based on commotional framework belong to Songpan Ganzi and Sothern part of the Longmenshan consists of Pengguan massif (PM) and Baoxing massif (BM). The main supply rock units for the Dixie to Yinxiu are belong to the basement rocks (1486 km^2) sand sized bed sediments which is 10 percent of the whole catchment but is providing 65% sediment supply to the confluence point to the Minjiang River. By comparing to the adjacent area along strike, less crystalline basement in the hinterland but more Mesozoic sedimentary rocks along the Shaotanghe River that is why main contributor at the confluence point of Minjiang River are Precambrian, Palaeozoic and Triassic rock units. Shaotanghe River (1730 km^2) is getting influence of three (3) end members including Triassic strata (45±1/2%, 317 $tkm^{-2}a^{-1}$ and 0.116 mm/a), Palaeozoic strata (25±1/2%, 639 $tkm^{-2}a^{-1}$ and 0.229 mm/a), and Basement (30±1/2, 743 $tkm^{-2}a^{-1}$ and 0.267 mm/a) rock units. Triassic strata (1109 km^2) are occupying the 64% area of the Shaotanghe River with 45% supply of the sediments in the catchment and the final influence point of the Minjiang River. The SGI from these units is 0.70 to 1.42 but the SGI from the basement rocks is relatively high at 1.65 due to the 30% supply of the sediments with 317 $tkm^{-2}a^{-1}$ sediment yield and 0.116 mm/a erosion rate. There could be two reasons for the direct relationship, maybe due to soft rocks of the Triassic strata from Songpan Ganzi unit or also with high altitude. Whole Minjiang (22811 km^2) from upstream to 5747 having four end members Triassic granites (9%±1/2%, 38 $tkm^{-2}a^{-1}$ and 0.014 mm/a), Triassic strata (39±1/2%204 $tkm^{-2}a^{-1}$

and 0.075 mm/a), Palaeozoic strata (19±1/2% 460 $tkm^{-2}a^{-1}$ and 0.165 mm/a), and Basement (40±1/2%, 1679 $tkm^{-2}a^{-1}$ and 0.165 mm/a) rock units. This contribution model is representing that Triassic (15320 km^2), and Basement (1906 km^2) rock units are relatively equal contributor as 39% and 40% respectively for the whole Minjiang catchment. The reason of this different contributions of the end members is that Triassic strata is having large percentage of the whole area and consists of soft rocks while basement rocks having low area but having high altitude and steep slope at the catchment with 0.58 and 1.31 SGI. The SGI is showing that generation of the sediments is quite high in Paleozoic strata as compared to Triassic strata due to the high altitude of the Paleozoic strata. Triassic (2018 km^2) and Palaeozoic (1582 km^2) strata is supplying 37±1/2% and 53±1/2% the sediments to the Zagunaohe catchment that is 4581 km^2 and are the main supplier for the provenance budget in the catchment with 0.84 and 1.53 SGI with 199 $tkm^{-2}a^{-1}$ and 693 $tkm^{-2}a^{-1}$ sediment yield with 0.074 mm/a and 0.248 mm/a respectively. While other two end menders are Triassic granites (935 km^2) which is supplying 9±1/2% and basement is just 1±1/2% 450 $tkm^{-2}a^{-1}$ sediment yield with 0.162 mm/a. Triassic and Palaeozoic strata is supplying more due to the large contributing area in the catchment and less resistant rock units. In the Heishuihe, Triassic granite (1149 km^2) is 16% of the whole catchment but contribution is just 1±1/2% and the contribution from Triassic (5325 km^2, 75±1/2% area) and Palaeozoic (1582 km^2, 9% area) strata is 20±1/2% and 79±1/2% with 0.27 and 8.52 SGI. In this catchment Paleozoic strata produces 3848 $tkm^{-2}a^{-1}$ sediment yield with 1.378 mm/a erosion rate is the main high focused erosion rate end member due to the high slope and altitude. The annual sediment discharge in the upper reaches of the Minjiang River before the Wenchuan earthquake presented an overall trend represents approximately 4.5% of the annual average sediment discharge. After the Wenchuan earthquake sediments discharge increases upto 70%, due to the post seismic flash floods and debris flows. due to the rainfall intensity. The other reason isa tremendous tectonic activity along major strike-slip faults in the mountainous part of the Minjiang River and catchment.

Table 4.1a. Petrographic and heavy-mineral fingerprints of major Minjiang River branches and their main end-members sources of detritus.

River	Samp	GSZ	Q	F	Lv	Lc	Lp	Lms	Lmf	Lmb	mica	HM	Total	MI*	MI
SONGPAN GANZI		***138***	***40***	***15***	***4***	***3***	***13***	***25***	***0***	***0***	***0***	***0***	***100***	***119***	***73***
Chuanzhusi	5712	110	45	13	4	3	14	21	0	0	0	0	100	113	64
Songpan Ganzi	5713	165	36	16	4	2	13	29	0	0	0	0	100	125	83
SONGPAN GANZI Hot		***124***	***46***	***2***	***1***	***5***	***1***	***3***	***26***	***0***	***15***	***1***	***100***	***384***	***375***
Zagunaohe	5741	122	46	5	1	5	0	4	23	0	15	2	100	380	374
	5742	125	47	0	1	6	1	2	28	0	15	0	100	389	375
Triassic granites		***205***	***35***	52	*0*	*0*	***0***	***0***	***1***	***0***	***6***	***6***	***100***	***453***	***453***
Triassic granite	5744	80	30	59	0	0	0	0	1	0	7	2	100	446	446
Triassic granite	5745	330	39	45	0	0	0	0	2	1	4	9	100	459	459
Triassic strata		***198***	***33***	***3***	***0***	***24***	***5***	***19***	***11***	***0***	***4***	***1***	***100***	***179***	***138***
Songpan Ganzi	5722	135	11	1	0	53	9	26	1	0	1	0	100	144	66
trib. mainly SG	5723	210	41	8	1	12	7	31	0	0	0	0	100	142	100
Songpan Ganzi	5725	125	57	0	0	9	3	5	8	0	15	4	100	119	79
Songpan Ganzi	5694	320	22	2	0	22	3	13	37	0	1	0	100	272	253
Paleozoic strata		***160***	***33***	***3***	***0***	***7***	***0***	***0***	***38***	***0***	***11***	***8***	***100***	***364***	***350***
Devonian	5728	75	78	0	0	1	2	2	7	0	9	1	100	376	324
Devonian	5727	90	31	1	0	6	3	11	43	0	4	0	100	323	306
Devonian	5732	97	60	1	1	13	3	2	19	0	2	1	100	352	313
Songxibao	5735	120	46	5	0	7	0	0	18	0	9	14	100	371	367
Silurian slate	5697	200	20	1	0	6	0	1	58	0	13	2	100	369	369
Basement		***155***	***32***	***49***	***2***	***0***	***0***	***0***	***3***	***2***	***2***	***9***	***100***	***376***	***376***
Basement	5699	170	29	48	4	1	0	0	4	4	2	9	100	342	342
Baisha He	5704	140	34	50	1	0	0	0	3	0	3	9	100	410	410
TRUNK RIVER SAMPLES		***266***	***33***	***22***	***1***	***16***	***3***	***12***	***7***	***1***	***3***	***3***	***100***	***264***	***254***
Minjiang	5724	119	31	7	1	23	8	30	0	0	0	0	100	108	89
Minjiang	5701	450	41	35	1	8	0	2	5	2	3	2	100	350	344
Minjiang	5747	230	25	25	1	17	0	3	17	1	5	6	100	334	329
Major Tributaries															
Heishuihe	5733	220	53	6	0	7	0	3	27	0	3	1	100	339	339

Zagunahohe	5738	205	41	14	0	11	0	1	19	0	12	2	100	381	376
Shaotanghe	5700	107	31	10	0	15	1	4	22	3	7	8	100	343	333

Table 4.1b. Heavy-mineral fingerprints of major Minjiang River branches and their main end-members sources of detritus.

River	Samp	Z	T	R	Ttn	Ap	Ep	Grt	Amp	Px	CSKA	&tHM	Total	ZTR
SONGPAN GANZI		11	10	1	1	33	6	27	10	0	0	1	100	22
Chuanzhusi	5712	10	12	2	1.9	39	6	14	16	0	0	0	100	23
Songpan Ganzi	5713	13	7	1	0	28	5	40	5	0	0	1	100	21
SONGPAN GANZI Hot		3	13	1	3	6	9	4	39	19	2	2	100	16
Zagunaohe	5741	0	1	1	2	2	7	2	47	38	0	0	100	2
	5742	6	24	1	4	10	11	6	32	1	3	3	100	31
Triassic granites		0	0	0	8	5	23	0	57	7	0	0	100	0
Triassic granite	5744	0	0	0	9	7	20	0	57	6	0	0	100	0
Triassic granite	5745	0	0	0	7	2	26	0	58	8	0	0	100	0
Triassic strata		15	17	2	5	27	4	3	18	1	0	8	100	34
Songpan Ganzi	5722	6	21	1	0	17	14	0	38	3	0	0	100	28
trib. mainly SG	5723	43	5	2	1	25	2	11	12	0	0	1	100	49
Songpan Ganzi	5725	12	21	0	0	61	1	3	2	0	0	0	100	33
Songpan Ganzi	5694	8	23	3	23	0	5	0	38	0	0	3	100	33
Paleozoic strata		1	14	2	1	10	8	21	40	2	1	1	100	17
Devonian	5728	1	30	2	2	15	6	2	41	0	1	0	100	33
Devonian	5727	3	32	4	0	37	10	8	5	1	0	0	100	39
Devonian	5732	3	57	3	0	27	2	0	8	0	0	0	100	62
Songxibao	5735	0	1	2	0	2	6	55	27	5	0	2	100	3
Silurian slate	5697	0	3	1	3	3	11	3	74	0	2	0	100	4
Basement		0	0	0	0	0	53	0	45	1	0	0	100	0
Basement	5699	0	0	0	0	1	71	0	27	0	0	0	100	0
Baisha He	5704	0	0	0	0	0	34	0	62	3	0	0	100	0
TRUNK RIVER SAMPLES		4	8	1	0	13	39	3	30	0	0	1	100	13
Minjiang	5724	11	23	1	0	36	5	7	15	1	0	2	100	35
Minjiang	5701	0	0	1	0	1	66	3	28	0	1	0	100	1
Minjiang	5747	1	1	0	0	3	46	0	47	1	0	0	100	2

Major Tributaries														
Heishuihe	5733	10	12	1	3	29	19	7	17	1	1	0	100	23
Zagunahohe	5738	0	2	0	8	2	16	56	14	1	0	0	100	2
Shaotanghe	5700	0	0	1	1	0	37	0	59	0	0	0	100	2

Q = quartz; K (K+P) = K-feldspar; P = plagioclase; L = aphanitic lithic grains (Lv = volcanic; Lcc = limestone; Lcd = dolostone; Ls = other sedimentary and very-low rank metasedimentary; Lm = metamorphic; Lb = metavolcanic, metabasite, and serpentinite); HM = heavy minerals; MI = Metamorphic Index (Garzanti and Vezzoli, 2003); tHMC = transparent heavy mineral concentration; ZTR = zircon + tourmaline + rutile; Ttn = titanite; Ap = apatite; Ep = epidote; Grt = garnet; And = andalusite; Sil = sillimanite; Amp = amphibole; Cpx = clinopyroxene; Hy = hypersthene; & tHM = other transparent heavy minerals (staurolite, kyanite, prehnite, pumpellyite, chloritoid, barite, anatase, brookite, olivine, Cr-spinel). Mean values in **bold**; range of values for end-member compositions in ***italics***.

Table 4.2. An average age structure of the zircon U-Pb ages from the most representative samples of the Minjiang River.

River	Samp	Tr	P	Cf	Dv	Sil	Od	C	Edi	Cri	Ton	Ste	Ect	Cal	Sta	Oro	Rhy	Sid	Archean
		200- 252	252- 299	299- 359	359- 419	419- 444	444- 485	485- 541	541- 635	635- 850	850- 1000	1000- 1200	1200- 1400	1400- 1600	1600- 1800	1800- 2050	2050- 2300	2300- 2500	>2500
Minjiang	5715	5 %	24 %	13 %	9 %	8 %	12 %	5 %	2 %	5 %	3 %	0 %	0 %	0 %	0 %	3 %	1 %	1 %	2 %
Minjiang	5729	9 %	8 %	10 %	9 %	8 %	6 %	5 %	4 %	8 %	7 %	2 %	0 %	0 %	1 %	9 %	3 %	3 %	2 %
trib. Heishuihe	5730	40 %	11 %	5 %	2 %	8 %	5 %	1 %	0 %	8 %	3 %	1 %	1 %	0 %	3 %	7 %	0 %	2 %	2 %
Heishuìhe	5733	11 %	10 %	6 %	4 %	4 %	5 %	3 %	3 %	11 %	9 %	2 %	0 %	1 %	7 %	10 %	0 %	7 %	6 %
Songxibao	5735	2 %	7 %	5 %	3 %	8 %	0 %	6 %	4 %	21 %	11 %	2 %	2 %	2 %	4 %	12 %	2 %	4 %	5 %
Minjiang	5737	8 %	3 %	11 %	6 %	2 %	2 %	3 %	1 %	19 %	5 %	3 %	2 %	1 %	8 %	7 %	1 %	7 %	2 %
Zaguna ohe	5738	5 %	2 %	0 %	2 %	1 %	1 %	3 %	2 %	74 %	3 %	0 %	0 %	0 %	1 %	3 %	0 %	0 %	0 %
Minjiang	5701	2 %	0 %	0 %	0 %	0 %	0 %	1 %	0 %	94 %	2 %	0 %	0 %	0 %	0 %	0 %	0 %	1 %	0 %
Shaotanghe	5700	3 %	7 %	6 %	3 %	4 %	3 %	3 %	7 %	27 %	12 %	4 %	2 %	1 %	7 %	1 %	2 %	1 %	6 %
Minjiang	5747	7 %	2 %	2 %	0 %	0 %	2 %	0 %	0 %	72 %	7 %	1 %	1 %	0 %	2 %	2 %	0 %	0 %	2 %

Xi He	5702	1 %	2 %	0 %	0 %	1 %	2 %	1 %	8 %	41 %	10 %	10 %	1 %	2 %	4 %	7 %	2 %	4 %	3 %
Baisha He	5704	0 %	0 %	0 %	0 %	0 %	0 %	0 %	1 %	85 %	14 %	0 %	0 %	0 %	0 %	0 %	0 %	0 %	0 %
Baisha He	5703	0 %	0 %	0 %	0 %	0 %	0 %	0 %	0 %	67 %	31 %	0 %	0 %	0 %	0 %	2 %	0 %	0 %	0 %
Minjiang	5705	0 %	1 %	2 %	0 %	0 %	0 %	2 %	0 %	79 %	14 %	0 %	0 %	0 %	0 %	1 %	1 %	0 %	0 %

Table 4.3. Provenance budget = sediment provenance budget and erosion model for the Minjiang drainage basin based on the following assumptions: area in km^2 of each catchment and end-members, sediment supply for each end-member proportional to catchment area (i.e., equal average erosion rate in each catchment), SGI is sediment generation index.

Catchments	Area	Area	Supply	SGI	Suspended (SL)	Sediment Yield (SY)	Erosion Rate (ER)	Density
	(km^2)	(%)	(%)		10^6t/a	(t/km^2/a)	mm/a	g/cm^3
Diexi lake to Yinxiu	**15217**	**86**	**100**	**1.16**	**6.87**			
Triassic granites	2077	14	1	0.07	0.07	33	0.012	2.68
Triassic strata	9231	61	20	0.33	1.37	149	0.055	2.70
Paleozoic strata	2423	16	14	0.s88	0.96	397	0.142	2.80
Basement	1486	10	65	6.66	4.47	3006	1.081	2.78
Total	***15217***	***100***	***100***			***452***	***0.166***	***2.72***
Heishuihe River	**7135**	**40**	**0**		**3.22**			
Triassic granites	1149	16	1	0.06	0.03	28	0.010	2.69
Triassic strata	5325	75	20	0.27	0.64	121	0.044	2.73
Paleozoic strata	661	9	79	8.52	2.55	3848	1.378	2.79
Basement	-	-	-	-	-	-	-	-
Total	***7135***	***100***	***100***			***452***	***0.164***	***2.75***
Zagunaohe River	**4581**	**26**	**0**		**2.07**			
Triassic granites	935	20	9	0.44	0.19	199	0.074	2.69
Triassic strata/SG	2018	44	37	0.84	0.77	379	0.139	2.73
Paleozoic strata	1582	35	53	1.53	1.10	693	0.248	2.79
Basement	46	1	1	1.00	0.02	450	0.162	2.78
Total	***4581***	***100***	***100***			***452***	***0.164***	***2.75***
Shaotanghe River	1730	10	100	10.24	0.78			
Triassic granites	-	-	-	-	-	-	-	2.69
Triassic strata	1109	64	45	0.70	0.35	317	0.116	2.73
Paleozoic strata	306	18	25	1.42	0.20	639	0.229	2.79
Basement	315	18	30	1.65	0.23	743	0.267	2.78
Total	***1730***	***100***	***100***			***452***	***0.164***	***2.75***
Upstream to 5747	**22811**	**100**	**100**	**1**	**8.00**			
Triassic granites	2123	9	2	0.21	0.16	75	0.028	2.69
Triassic strata	15320	67	39	0.58	3.12	204	0.075	2.73
Paleozoic strata	3304	14	19	1.31	1.52	460	0.165	2.79
Basement	1906	8	40	4.79	3.20	1679	0.604	2.78
Total	***22652***	***99***	***100***		***8.00***	***353***	***0.129***	***2.74***

Diexi Lake to Zipingpu	**17715**	**100**	**100**	**1**	**8.00**	**452**	**0.165**	
Upstream to 5724	5091	22	0	1.00	1.79			
Sonpang Ganzi	165	3	36	0.00	0.64	3897	1.451	2.69
Triassic strata	4366	86	64	0.75	1.14	262	0.096	2.73
Paleozoic strata	560	11	0	0.00	0.00	0	0.000	2.79
Basement	-	-	-	-	-	-	-	-
Total	***5091***	***100***	***100***			***351***	***0.128***	***2.74***

The sediment generation index SGI = SA/S A/AA (Palomares and Arribas, 1993; Vezzoli et al., 2004) assumes uniform erosion rates across the source area. Sand load = bedload (i.e., gravel in bedload = sand in suspended load (SL) sand. Sediment yield (SY) for the generation of sand detritus material per year. Erosion rate for each lithological domain.

Table 4.4. Summary of the sediment load (10^6 t/a) and the factors affecting for controlling the sediment yield and load from different literature (Lin, 1995; Ding et al., 2013; 2014).

Minjiang Catchment	Data Source	Time period	Drainage area (km2)	River Length (km)	Sediment load (106 t/a)	Affecting factors
Zipingpu Station	Lin, 1995	avg. 1955-1982	22811	735	8.45	
Zipingpu Station	Ding et al., 2013	avg. 1980-2007	22811	735	7.04	
Zipingpu Station	Ding et al., 2013	2008	22811	735	9.06	Earthquake
Zipingpu Station	Ding et al., 2013	2009	22811	735	8.08	
Zipingpu Station	Ding et al., 2013	2010	22811	735	12.39	High Precipitation

Chapter 5

Geological and Geomorphological Features of Thar Desert, Pakistan

5.1. Geographical and Geomorphological Characterization

The term "desert" was derived from the Egyptian hieroglyphics *Tésert* to the Latin word *desertum* (place of abandoned wilderness), as describing arid dune field areas (El-Baz, 1983). El-Baz (1983) argued that a desert is "*a vast area of dune fields and arid land where wind blows dust in the air and moves sand grains across dune profiles*". Dune sediments are easily eroded and transported by wind action from the sand dunes. Sand originally eroded from mountain source areas is also affected within the dunes by frequent reworking and recycling during fluvial-eolian interactions. The Thar Desert is situated in an arid environment of sandy rolling hills in the western Indian subcontinent. The Thar Desert derives its name from the Arabic word "Thul", which means sand, and covers ca. 200,000 km^2 including Punjab and Sindh in Pakistan, and Gujarat and Rajasthan in India (Figs. 5.1 and 5.2). The arid environment is composed of sand dunes that stretch from North to South for ca. 800 km^2. In its western part the desert extends up to the fertile alluvial plains of the Indus River in Pakistan, although it originates in and drains from the western Himalaya and Karakorum ranges. The southern side of the desert is bounded by the foothills of the degraded, NNE to SSW-trending Aravalli ranges (Gujarat) (Kar, 2013). The Thar Desert can be subdivided into two sections. The Cholistan Desert is the northern part of Thar within the Pakistani district of Bahawalpur, Punjab. The Sindh Desert is the southern branch that extends into Sindh Province, Pakistan.

Cholistan covers ca. 26,000 km^2, forming a rough triangle ~480 km in length. The width varies between ~23 km in the south to ~192 km in the north (Akbar et al., 1996) (Figs. 5.1 and 5.2). Differences in topography and geomorphology allow us to divide the Cholistan Desert into two regions, known as Lesser Cholistan (12,370 km^2) and Greater Cholistan (13,960 km^2) (Akhtar and Arshad, 2006; Ahmed, 2011). Lesser Cholistan is the most northerly marginal region dominated by alluvial flats and sparse, very flat sand dunes (Mughal, 1997) and lies around the Ghaggar-Hakra palaeochannel (Srivastava et al., 2020). The abandoned Ghaggar-Hakra River may have formerly joined with the Nara River south of Cholistan (Clift et al., 2012). The Ghaggar-Hakra contains remnants of sandy fluvial terraces (Ahmad, 2008), and Akbar et al. (1996) described this area as being characterized by alluvial flats with alternating sandy ridges.

Greater Cholistan on the southern margin is dominated by wind sorted sediments stored in the modern sand dunes.

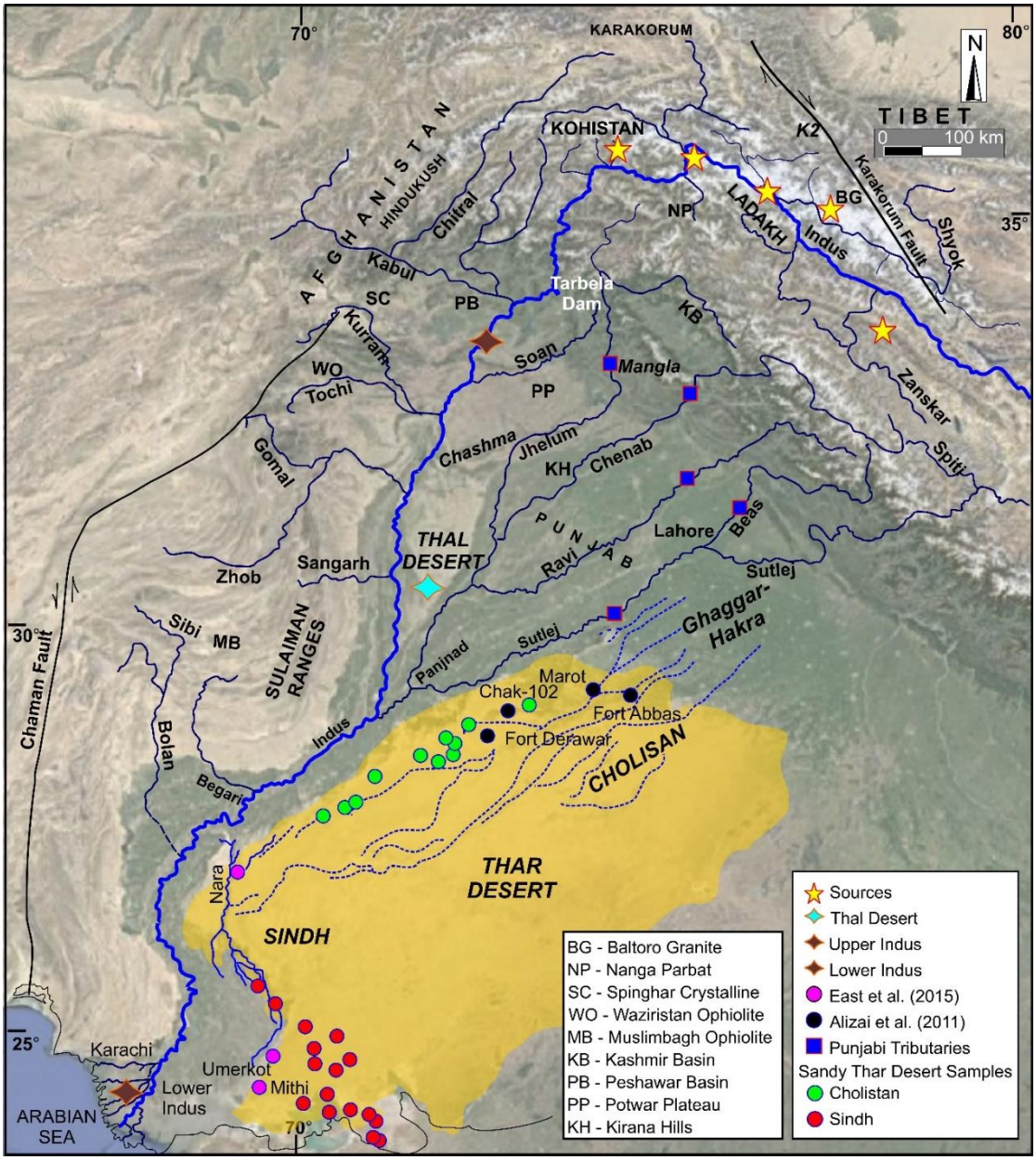

Figure 5.1. Satellite image of Pakistan and adjacent regions (from Google Earth™). Figure shows sampling locations for desert sand and modern rivers. Note the distribution of the sediments collected during this study in Cholistan and further south in eastern Sindh. Original image from Google Earth. Location of modern sand samples from both Thar Desert and Indus drainage system are shown.

The Sindh Desert covers ~45,790 km^2, roughly ~500 km in length and with a width varying between ~38 km in the north to and ~200 km in the south (Figs. 5.1 and 1.2). It is characterized by a series of undulating sand dunes that vary in height across the

desert (Chauhan, 2003). While sand dunes are a common sight in deserts around the world, the Thar Dunes are remarkable for their constant movement (Sam et al., 2015). The movement of the dunes is mainly caused by wind erosion and deposition. The wind erodes the sand particles from one area and deposits them in another, creating new dunes and altering the shape and size of existing ones. The constant movement of the dunes has a prohibitive effect on permanent human settlement, as sand can easily be blown over structures (Nordstrom, 2014).

5.2. Thar Desert Climate and Interaction with the Monsoon

The geographic position of the Thar Desert surrounded by mountain ranges, rivers and alluvial plains contributes significantly to the weather patterns that shape its distinctive, hot and dry environment. The Thar Desert region is characterized by aridity, with very low amounts of precipitation (100–200 mm/y) throughout the year (Akbar et al., 1996). The Himalayan front controls the climate and plays a role in lowering precipitation in the Thar Desert (Rahaman et al., 2009). The Himalaya serves as a barrier to the winds and allows a low-pressure system to develop adjacent to the mountains in the summer by trapping hot air over the plains (Boos and Kuang, 2010). Seasonal winds carry moisture from the Indian Ocean towards the Indian subcontinent. These winds rise and lose moisture as they approach the Himalaya where most of their precipitation is released on the windward side of the mountains. The Thar region has relatively little rainfall because it lies on the western edge of this circulation system and is also affected by dry westerly winds coming from the arid Makran and Afghanistan. These winds are dry and depleted with moisture when they arrive in the desert (Wang et al., 2005). The Thar desert’s location in the Aravalli Range's rain shadow, further reduces the quantity of moisture reaching the area, and is one of the additional causes contributing to its aridity. Moreover, the Thar Desert's high temperatures cause high rates of evaporation, which dry the land and air (Kumari et al., 2023). The environment around the Thar Desert effectively absorbs all the rain that is carried in the monsoon clouds before the clouds can reach the desert. The resulting monsoon winds in the desert are hot and dry, and the desert does not share in the wet season experienced further east. The Asian Monsoon is crucial to the Thar Desert region, delivering 90% of its rainfall (100–500 mm/y average) during the summer months in Cholistan (May to July and September, Bookhagen, 2010). In contrast, the winter monsoon is weaker and typically provides little precipitation, although some rainfall is associated with the winter

Westerlies although mostly affecting regions north of the desert. In Sindh the Thar Desert receives low annual rainfall, ranging from about 100 mm in the west to 500 mm in the east. Fluctuations in precipitation are common from year to year. The hottest months are May and June, with temperatures reaching up to 50°C. In January, the coldest month, the mean minimum temperature ranges from 5°C to 10°C, and frost is frequent. Dust storms and dust-raising winds, blowing at velocities of up to 145 km/hr, are common in May and June.

Studies of the Asian Monsoon system indicate that it is a linear response of orbital forcing with dominance from obliquity (41 ka) and precession (23 ka) cycles (Prell, 1984; Clemens et al., 1996; Clemens and Prell, 2003). The intensity of the monsoon is affected by changes in Arctic and Antarctic ice volumes, and northern and southern hemispheric temperatures due to cross-equatorial exchanges of atmospheric heat and pressure (Blinkhorn, 2014). Maximum monsoonal intensity is observed during glacial minima, while a steep inter-polar temperature gradient often produces a monsoonal minimum about 20 k.y. before the glacial maximum (Zhisheng et al., 2011). Consequently, paleoenvironmental data suggests that the Thar Desert may have experienced reduced monsoonal rainfall between approximately 40 ka and 20 ka.

5.3. Paleochannels and Sediment Flux

The western Himalayan foreland is dominated by the Indus fluvial system. The modern flood plains have been incised in their northern parts since the start of the Holocene following earlier aggradation during deglaciation (Giosan et al., 2012). The geomorphology is mainly governed by the fluvial discharge that is controlled by regional precipitation and the monsoon rainfall, as well as snow and ice melt in the upper drainage (Bookhagen, 2010; Giosan et al., 2012; Durcan et al., 2010). Many tributaries supply sediment from Himalayan sources to the Indus lower reaches including the Shyok, Shigar, Gilgit and Kabul rivers from the north, and the Jhelum, Chenab, Ravi, Beas and Sutlej Rivers from the east (Fig. 5.1).

The Indus River is characterized by the flow from the mainstream Indus, which rises from glaciers north of Mt. Kailas, and the eastern tributaries that originate in the Himalaya and that flow to the SE through Punjab. The mainstream flows for a third of its course along the suture zone in the southern Tibetan Plateau and then cut southwards across the Western Himalayan Syntaxis, where it meets the alluvial plain south of Tarbela Dam (Fig. 5.1). The Punjabi River system originates from the Tethys Himalaya

and then cuts across Greater and Lesser Himalayan domains. The five main Punjabi tributaries are the Jhelum, Chenab, Ravi, Beas and Sutlej rivers with an annual flux that represents 44% of the total discharge (Alizai et al., 2011a). The Indus River has undergone several changes in its drainage pattern.

Many courses of the Indus have been detected in Sindh where migration to the west has occurred since the Last Glacial Maximum (LGM) (Kazmi, 1984). Other major changes include the capture of the Yamuna River between 10 and 50 ka, and the drying up of the Ghaggar-Hakra River tributary (Valdiya, 2002; Saini et al., 2009; Clift et al. 2012; Giosan et al., 2012). Other Punjabi tributaries have also experienced dynamic changes (Amundson et al., 1986; Wright et al., 2005). In the middle Holocene the Ravi drainage path moved northwards, while confluence of the Sutlej River with the Yamuna and Ghaggar-Hakra rivers was abandoned likely before 17 ka (Stein, 1942; Sinha et al., 2013; Sinha et al., 2019). During the Holocene ~11% of the sediment reaching the Arabian Sea was supplied by incision into the northern floodplains, with another ~6.4% supplied by recycling from the Thar Desert, although this latter value is poorly constrained (Clift and Jonell, 2021). Reworking of older sediments in the Thar Desert occurred after 10 ka because of the incision of the Indus with its tributaries since early Holocene at the downwind side of the Punjabi floodplains (Giosan et al., 2012). The Indus and Ganges–Brahmaputra fluvial systems are also supplied by erosion of Himalayan mass wasting deposits, moraines and valley fills that are incised during the Holocene and which date back to 100 ka or more (Blöthe and Korup, 2013; Clift and Jonell, 2021). Sediments deposited in the Thar Desert date from at least mid-Pleistocene time (Glennie et al., 2002; Singhvi et al., 2010). In addition, fluvial channels dating to 173 ka have been identified in the central Thar Desert (Blinkhorn et al., 2020). More recent fluvial channels found around the western edge of the desert were abandoned at approximately 4–5 ka and were eventually buried under the Thar Desert's parabolic dunes around 1.4 ka (Clift et al., 2012). Younger fluvial activities (2.9–0.7 ka) have also been reported from both the upper and lower Ghaggar-Hakra floodplains (Giosan et al., 2012). A meandering river system constantly changes its course and creates numerous abandoned channels so that depositional ages of sand from only a few sections may not reveal the true temporal extent of the river (Valdiya, 2013). Furthermore, Pb isotope studies of K-feldspar grains (Alizai et al., 2011b) and major elements in garnet (Grt) grains (Alizai et al., 2016) in sediments of the Nara Valley

suggest that either the Nara River was a former distributary of the river Indus, or it was an ephemeral stream receiving reworked sediments.

5.4. Climatic Changes

Climatic changes have a strong influence over the sediment source and composition within a fluvial and alluvial drainage system (Haughton, 1991; Gábris, and Nádor, 2007). Fluvial and alluvial reworked sediments can be useful in establishing paleoclimatic influences over sediment provenance (Van de kamp and Leake, 1985; Velbel and Saad, 1991). For example, a first cycle quartz arenite would likely be formed under prolonged chemical weathering in tropical conditions (Russell and Allison, 1985; Johnsson et al., 1988). The composition of detrital sediment can be influential in determining changes from dry to wet climates because of changes in chemical weathering rates (Du et al., 2018). During the Holocene the present arid climate was established around 4 ka and followed dry conditions in the early Holocene but a wetter climate in the middle Holocene (Dhir and Singhvi, 2012). Luminescence ages show that during the LGM aeolian sediment transport was not high (Singhvi and Kar, 2004; Singhvi et al., 2022). In contrast, during the Holocene stronger summer Monsoon winds increased sediment transportation and heavier rains reworked material from the fluvial system into the Thar Desert. Wet conditions and strong summer monsoons favor sediment transport and reworking within the desert. The sedimentary profiles of the Thar Desert and neighboring settings reveal the timing of sediment storage and erosion and show rapid sediment accumulation in the central part of the desert throughout the Holocene (Singhvi et al., 2010; Chatterjee and Ray, 2017). The dunes along the western edge of the desert have advanced over the floodplains more recently, and the connectivity between fluvial and eolian sedimentary systems in the Indus watershed and Thar Desert has been documented by stratigraphic studies (East et al., 2015). Because the Thar Desert is located to the west of the Indus River sedimentation since the mid-Pleistocene, including the Holocene, was influenced by the southwest Asian summer monsoon, with eolian sediment transport mostly from southwest to northeast. This general pattern is supported by sediment composition, mineralogy, and optically stimulated luminescence (OSL) and thermoluminescence (TL) ages (Singhvi et al., 2010). The Thar Desert expanded after the LGM, during phases of strengthened summer monsoon, and continued its advance westward during a weakening of the summer monsoon starting after 8 ka. Pb isotope compositions of detrital K-feldspar

grains, along with U-Pb zircon and Nd isotopic data, demonstrate a similarity between the lower reaches of the Indus River and the northern Cholistan Thar Desert (Alizai et al., 2011a, 2011b).

5.5. Geological Setting of the Thar Desert

Thar Desert is usually described as having three low relief sides to the North, East, and West facing the foothills of the Himalayas, the Iranian Plateau, and the Aravalli range. The southern part of the desert is bounded by the coastline of the Arabian Sea. Quaternary sediments are common throughout the desert, together with partially exposed rocks Tertiary hills. The sand of the Thar Desert overlies Archean gneiss, formed at 4.0-2.5 Ga, Proterozoic sedimentary rocks (~2.5 Ga to 541 Ma), and more-recent alluvium (Roy and Smykatz-Kloss, 2007; Jain and Banerjee, 2020). The desert has accumulated on the Indo-Gangetic Plain, a flexural trough, which lies between the foothills of the Himalaya and Indian Shield. The foreland basin in filled with >5 km of alluvium mostly derived from the Himalaya and deposited by the Indo-Gangetic fluvial system (Burbank et al., 1996). In the desert there is a complex amalgamation of fluvially and aeolian deposited reworked sediments. These sediments are reworked by different processes. After initial deposition from different sources the sediment may be reworked by wind into sand ridges. Sediment in spill channels and clay-rich material in flat dunes can be further reworked into the present-day dunes. Modern sediments of the northern Cholistan Desert comprise material from different igneous and metamorphic sources derived from the Lesser Himalayas and supplied from the Sutlej or reworked from the abandoned Ghaggar-Hakra Rivers (Ahmed, 2008; Clift er al., 2012). The southern Sindh Desert sediments are mainly sourced by the Indus River which is mainly supplied from the western Himalaya and Karakorum ranges (Henderson et al., 2010). The Indus has a long evolutionary history which includes the abandonment of tributaries including the Yamuna River that formed the headwater of the northeastern Punjabi flood plain prior to 10 ka, likely pre-17 ka, as well as the Ghaggar-Hakra before 4 ka (Saini et al., 2009, Giosan et al., 2012; East et al., 2015). The Indus River is the primary source for sediments in the Arabian Sea (Clift et al., 2002; Garzanti et al., 2005) and forms the second biggest submarine fan on the modern Earth. The main sources for the Indus River and Thar Desert are the Western Himalayan Syntaxis (WHS, i.e., Nanga Parbat Massif), as well as the Karakorum and Hindukush, Transhimalayan arcs and sutures, the NW Lesser and Greater Himalaya, and the ranges bounding Pakistan to the west,

i.e., Kirthar and Sulaiman ranges (Guillot et al., 2003; Garzanti et al., 2005, 2020b; Liang et al., 2019). The Kohistan and Ladakh arcs are bound by the Shyok and Indus Sutures to their north and south (Treloar et al., 1996; Rolland et al., 2000). The Nanga Parbat Massif is cut by the Indus River but supplies a modest amount of sediment compared to the eastern syntaxis despite rapid exhumation (Clift et al., 2022). In addition, erosion supplies sediment from the Karakorum Askole-Dassu-Mangol Bluk tectonic domes that are cut by the Braldu and Basha rivers (Lemennicier et al., 1996; Searle et al., 1999; Rolland et al., 2001; Searle et al., 2010).

5.6. Thar Sand Dune Accretion

The hot and dry environment of the Thar Desert reflects its geographical isolation between the Himalayan Mountain ranges and the adjacent floodplains. Furthermore, the desert is located on the edge of the influence of monsoon rains (Fig. 5.2). Previous studies of the eastern Thar Desert showed that sand dunes experienced multiple phases of accretion through the last 200 ka (Singhvi et al., 2010). The growth of the desert is a reflection both of the sediment supply and the strength of the winds that transport material into that region. It might be expected that periods of weak monsoon rains, such as during the Last Glacial Maximum (LGM, ~20 ka) would be a time when the desert would expand (Garzanti et al., 2020). However, limited provenance analysis suggests that much of the sediment supply occurred when the summer monsoon was strong, after the end of the LGM and when the climate became wetter (East et al., 2015). A recent re-examination of detrital zircon single grain U-Pb dates now suggests that much of the sediment was supplied from the lower reaches to the desert after the LGM, during the Latest Pleistocene, and particularly during the early to mid-Holocene.

Thermoluminescence dating of eolian sediments in the Thar Desert has revealed multiple phases of dune accretion spanning the last 200 ka, alternating with precession-driven interludes of weak or low sediment supply (Singhvi et al., 2010). The last major phase of dune growth in the eastern Thar Desert took place under a transitional climate, when SW monsoon winds were strengthening following a peak in aridity during the LGM, which was a time characterized by a very weak SW monsoon. Sand aggradation in the eastern desert took place between 17 ka and 14 ka and lasted until 9 ka, at the onset of the early Holocene wet stage (Dhir et al., 2010; Singhvi et al., 2010).

As well as using the different chemical compositions of the source bedrocks to resolve between the different sediment sources. We also consider the role played by

chemical weathering because this has a large impact on the major element composition of sediments which are found in the river, as well as in the desert.

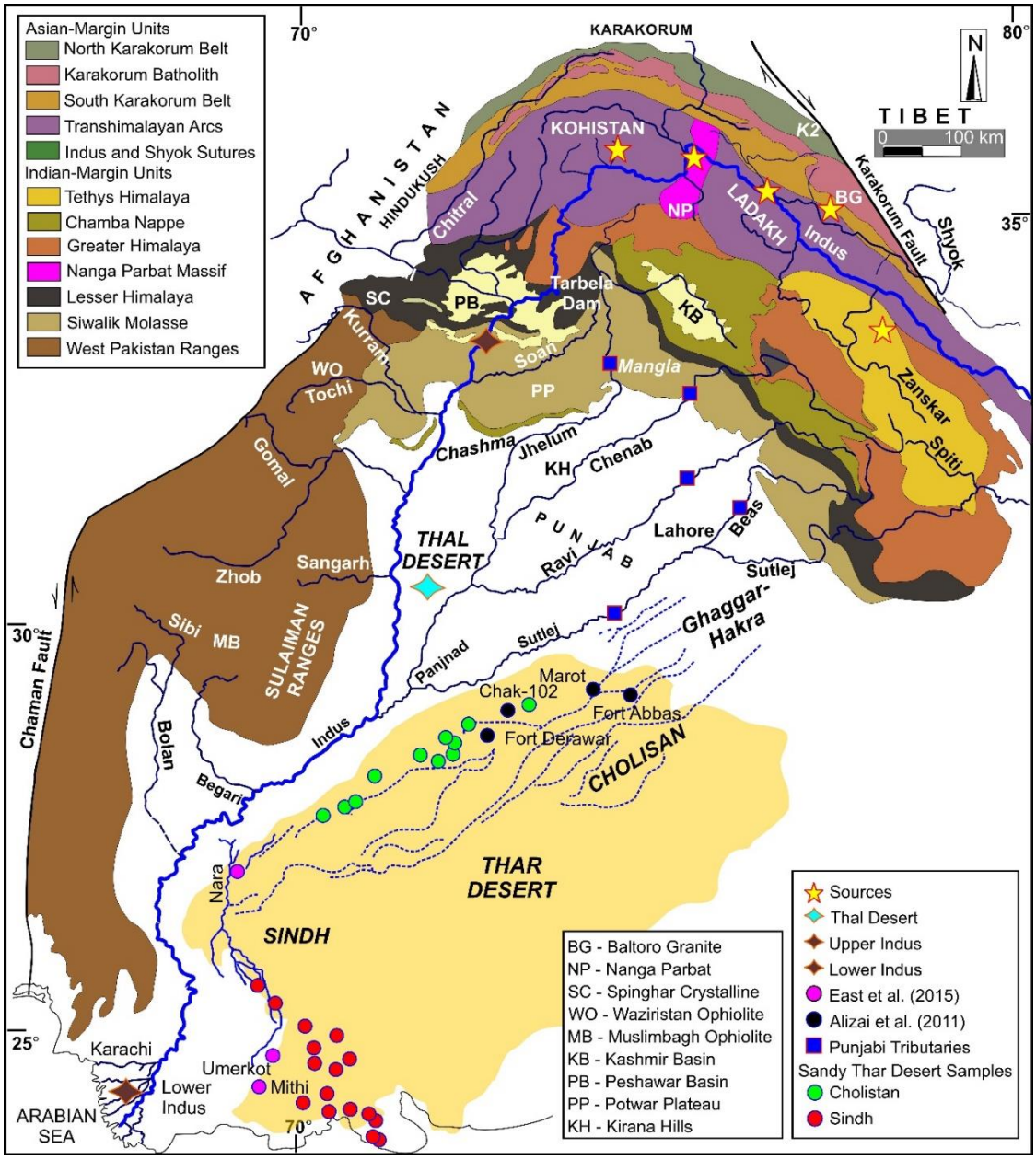

Figure 5.2. Geological map of the western Himalaya syntaxis and other ranges drained by the Indus River system, showing the major tectonic blocks of these regions which form the primary sources of sediment to the Indus River modified after Garzanti et al. (2020). Location of modern sand samples from both Thar Desert and Indus drainage system are shown.

Contrasting degrees of chemical weathering can help constrain where the sediment is being supplied from, although it should be remembered that this will change with time as the monsoon strengthened and weakened. In general, warmer conditions with higher humidity play a significant role in enhancing chemical weathering and the

production of clay minerals, due to the strong linkage between climate and rates of chemical weathering (Kump et al., 2000; West et al., 2005). Weathering results in a relative loss of water-mobile elements (i.e., Na, K, Sr) compared to immobile elements (e.g., Si, Al, Ti) from the original bulk composition, thus allowing weathering intensity to be quantified (Nesbitt et al., 1980). Changing climate also influences the speed and duration of sediment transport between the source and the sink (West et al., 2005; Herman and Champagnac, 2016; Huntington et al., 2006; Neubeck et al., 2023), which also impacts the degree of alteration experienced by the sediment grains.

5.7. Fingerprinting Sand Sources

Sand in the Thar and Thal deserts is supplied from the Upper Indus, as well as the Punjabi tributaries (Sutlej, Beas, Ravi, Jhelum and Chenab). In turn these rivers receive sediment from the Ladakh and Kohistan arcs, the Karakorum and Hindukush, the Himalaya, and the Nanga Parbat Massif. The compositional framework used to resolve these different sources by petrography and mineralogy is from Garzanti et al. (2005), Liang et al. (2019) and Garzanti et al. (2020b) (Table 5.1). The Ladakh Arc supplies quartzo-feldspathic to feldspar-rich feldspatho-quartzose, plutoniclastic sand with a rich to very rich transparent heavy mineral (tHM) suite dominated by amphibole (Amp; mostly hornblende), and with minor epidote (Ep), titanite, apatite, and clinopyroxene (mainly diopside). Hypersthene or allanite are found locally. The Kohistan Arc is drained by local rivers and resulting sand is composed of feldspatho-quartzo-lithic to litho-quartzo-feldspathic metamorphiclastic sand with common prasinite and epidote-amphibolite grains. The sediment is a very rich to extremely rich tHM suite dominated by amphibole (mainly hornblende or pargasite associated with actinolite or hastingsite and rare tschermakite). Epidote-group minerals (mostly clinozoisite) and pyroxene (diopside, pigeonite, augite, and hypersthene) are common, whereas Ca-rich or Mg-rich garnet is mostly rare. The Karakorum Belt supplies quartzo-feldspatho-lithic sand (North Karakorum) to quartzo-feldspathic plutoniclastic sand (Central Karakorum), and litho-feldspatho-quartzose metamorphiclastic sand with marble grains (South Karakorum). Mainly moderately rich tHM suites include common amphibole (mainly hornblende with pargasite, hastingstite, or actinolite), epidote-group minerals (epidote, clinozoisite, and allanite), mostly Bi-type garnet, titanite, common diopsidic clinopyroxene, and minor kyanite (Ky), staurolite (St) and sillimanite (Sil). The Zanskar River draining the Greater Himalaya to the north contributes sand that is litho-

feldspatho-quartzose metamorphiclastic, with a moderately rich tHM suite including amphibole (pargasite and hornblende with minor hastingsite), mostly Bi-type garnet, fibrolitic sillimanite, kyanite, epidote-group minerals (epidote, clinozoisite, minor allanite), and pyroxene (diopside, augite, and locally hypersthene). The contribution of the sand from Nanga Parbat Massif tributaries is mainly in the form of feldspar-rich feldspatho-quartzose sand with a very rich tHM suite dominated by amphibole (mainly hornblende with common tschermakite and minor pargasite). Garnet (mainly Ci and minor Bii types), pyroxene (diopside with rare augite), epidote, clinozoisite, and sillimanite are identified. Cenozoic foreland basin sedimentary strata are eroded by the Soan River, which supplies feldspatho-litho-quartzose sand with a moderately rich, epidote-dominated tHM suite with garnet, hornblende, and tourmaline. Of the rare earth element (REE)-rich minerals, allanite is habitually common (2–3 tHM%) in sand supplied by the Hushe, Braldu, Hispar, and Hunza rivers draining the Karakorum. The sand from the Karakorum contains two to five times more allanite than sand shed from the Greater Himalaya and Nanga Parbat, and one order of magnitude more allanite than sand shed by the Ladakh and Kohistan arcs. Monazite is rarer and was detected in sand derived from the Karakorum and in the Zanskar River.

Table 5.1. Summary of the sand sources from different potential sources.

Sources	Mechanism	Lithology	Petrography	Ages
North Karakorum	Ordovician to Cretaceous affected with multi tertiary phase tectonic deformation and low-grade metamorphism, mid-Cretaceous (95–110 Ma).	Black slates are backbone of Karakorum intruded by calc-alkaline gabbro- quartz diorite, granodiorite, granite, and tonalite, andalusite, chloritoid, and epidote.	quartzo-feldspatho-lithic sediment mostly amphibole, epidote-group minerals, diopsidic clinopyroxene, and minor kyanite, staurolite and sillimanite	Zircon ages (16-26, 35-43, 57-66)
Southern Karakorum	Migmatitic domes which is undergoing while rapid exhumation and representing the increment of metamorphism	structurally lower phyllites to staurolite-, kyanite-, and eventually at the top metasediments of sillimanite-bearing rocks.	quartzo-feldspathic plutoni clastic (Central Karakorum)	sealed by ~37 Ma granites.
Central Karakorum batholith	granitoids intruded before the India-Asia collision	amphibole with residual clinopyroxene and accessory titanite, epidote, allanite, apatite, zircon	litho-feldspatho-quartzose metamorphi clastic with marble grains (South Karakorum)	mid-Cretaceous
Mantle to upper crustal igneous rocks is exposed at the Trans-Himalayan arc zone in the Cretaceous to Paleogene times (143-23 my).				
Ladakh Batholith	Ladakh batholith is non-conformably overlain by Upper Cretaceous to Paleogene strata of the	includes olivine-norite to granitic intrusions and yielding hornblende, augite,	quartzo-feldspathic to feldspar-rich feldspatho-quartzose, plutoniclastic sand, dominated by	Zircon ages (49-65, 78-87)

	Indus Group, Cretaceous to Paleogene mafic to felsic.	titanite, apatite, epidote, and zircon	amphibole (mostly hornblende), with minor epidote, titanite, apatite, and clinopyroxene.	
Southern Kohistan		peridotites and granulite facies metagabbros		(73-95)
Kamila Amphibolite-facies are metaigneous rocks and Gilgit Complex is greenschist-facies metasediments, these were intruded under the layered gabbronorites at the Chilas Complex and it was developed in the sub-arc magma chamber.				
Northern Kohistan	Chilas ultramafic-mafic complex, containing ortho-clinopyroxene with minor olivine, magnetite,	mainly volcanic, volcaniclastic, and carbonate rocks	Feldspatho-quartzo-lithic to litho-quartzo-feldspathic metamorphiclastic with common prasinite and epidote-amphibolite grain. dominated by amphibole	
Kohistan batholith is mainly yielding hornblende and locally clinopyroxene.				
Northeast Himalayas	Zanskar Synclinorium has entire evolution from Neoproterozoic to Eocene Tethys Himalayas, late Paleogene around 24-18my.	intrusion of slate and Ordovician granitoids with sillimanite-bearing metasedimentary at the top part of GH with inverted metamorphic sequence	litho-feldspatho-quartzose metamorphiclastic with a moderately rich tHM suite including amphibole, fibrolitic sillimanite, kyanite, epidote-group minerals	Zircon ages (751-856, 337-476, 1040-3117)
Naga Parbat Massif	Western Himalayan Syntaxis including the crustal scale Nanga Parbat antiform is crosscut by the Indus	Precambrian Indian gneissic basement rocks are exposed at Nanga Parbat antiform by the overprinting of HM	feldspar-rich feldspatho-quartzose, dominated by amphibole, garnet, pyroxene, epidote, clinozoisite, and sillimanite.	Zircon ages (1787-1941, 1850)

Chapter 6

Climatic Influence on Sediment Distribution and Transport in the Thar Desert of Sindh and Cholistan, Pakistan

Muhammad Usman, Peter D. Clift, Guido Pastore, Giovanni Vezzoli, Sergio Andò, Marta Barbarano, Pieter Vermeesch, Eduardo Garzanti

Publication: Earth Sciences Review https://doi.org/10.1016/j.earscirev.2024.104674

Key words: Thar Desert, Provenance studies, Sand Petrography, Heavy Minerals, Detrital-Zircon geochronology, Climatic changes

6.1. Introduction

Source-to-sink studies in major siliciclastic transport systems, especially those draining major mountain belts are complicated by the buffering processes involved with fluvial-eolian sand seas. Large volumes of sediment may be stored and then recycled as a river system passes through a sandy desert area on its way to the final depocenter. Changing paleoenvironmental conditions may exercise an important control on how sediment is transported through or recycled within desert areas. In particular, changing precipitation amounts and seasonality may have an important impact on the growth or reduction of desert sand areas and their impact on the associated river. The fraction of sandy sediments first stored in a desert system after removal from the river is referred to as the net loss of the sediments from the source system (Trimble, 1983; Petter et al., 2013). These stored sediments may subsequently be eroded and mixed with more fluvial sediment within the drainage basin. Buffering and recycling of sediment in this way may disrupt the propagation of erosional signals related to climatic change or tectonic events (Whipple, 2001; Alizai et al., 2011a; East et al., 2015). Our ability to resolve the factors that control the fluvial and aeolian sediment transport is affected by mixing of new and recycled sediment within the basin. In this study, we better quantify the processes that control sediment storage and recycling in the Thar Desert in south-west Asia related to the Indus drainage system that dominates the western side of the Himalayas, Tibetan Plateau, and Karakorum. By understanding how this sediment filtering system works, we enhance our ability to interpret the more continuous marine sedimentary depositional record downstream in the Arabian Sea.

The efficiency of the sediment supply to the Thar Desert is controlled on long timescales (>10^4 y) by the interaction between the monsoon climate and the rock uplift that is occurring in the active mountain belts of the Himalaya and Karakorum. This is a suitable region for studying this type of source-to-sink problem, because of the strong intensity of the Southwest monsoon system, and the large and tectonically active character of the sources, providing strong signals in the sediment that is carried into the lower reaches of the Indus River. These orogenic belts are the result of the ongoing collision between the Indian and Eurasian continents since 55–60 Ma (Garzanti et al., 1986, 1996; Critelli et al., 1994; Hu et al., 2015; Najman et al., 2003, 2017). These ranges are drained by the Indus River across the western side of the orogeny. Ongoing tectonically driven rock uplift coupled with erosion is responsible for the extreme high relief and rapid exhumation found in the western Himalayan syntaxis (Garzanti et al., 2020a, b; Zeitler et al., 1993). If we are to understand the tectonics and erosion of this mountain belt over million-year timescales, then this can only be achieved using the Indus River and its associated sedimentary system because the record of past exhumation has been removed from the source ranges themselves by erosion. In contrast, the sediment record in the Arabian Sea and Himalayan foreland basin can be used to reconstruct changing patterns and rates of erosion through provenance studies of the detrital sediment flux from the orogenic region (Clift et al., 2001; Clift et al., 2008; Clift and Jonell, 2021). In recent times, all of the sediment flowing from source into the ocean basin has to pass next to or through the Thar Desert, although the processes that operate in this region are not well understood.

Studies of sediments in arid and semi-arid regions rarely include consideration of the interactions that occur during fluvial and aeolian transport (Thomas and Wiggs, 2008; Belnap et al., 2011). These are likely to introduce complexities to the original erosional pulse that might be linked to environmental change, and whose composition closely reflects the bedrock. In the case of the Indus alteration of the sediment may happen in the Thar Desert, which is located in eastern Pakistan and NW India (Figs. 5.1 and 5.2). In the Thar Desert the complex nature of sediment transport and recycling in the aeolian system is poorly constrained. However, better understanding is critical if we are to constrain the ongoing interaction of fluvial and eolian processes during source-to-sink transport. The sediments stored in the desert reflect the net effects of sediment transport from hillslope to alluvial channels and finally to the dryland area (Ramsey et al., 1999; Prins et al., 2009; Bracken et al., 2015). This transport may be modulated by

changes in the environment, as well as in the development of the drainage system that may also be sensitive to tectonic influences. Because the region of the Thar Desert is arid-semiarid it is sensitive to the influence of fluvial activity and changing climate. The fluvial sourced eolian sands are stored in dunes and transformed through reworking by the wind. Subsequently, the sediments may interact further with the river and continue their journey to the ocean (Bullard and Livingstone, 2002; Bullard and McTainsh, 2003; Alizai et al., 2011b). Wind is a strong transforming agent that can move sediments tens to hundreds of kilometers from the original fluvial source (Langford, 1989) where they may be stored in various depositional systems, such as the Thar Desert. In the Thar Desert, studies of fluvial-eolian interactions may be interpreted as a reflection of the climatic changes and evolving tectonics if they occur over $>10^6$ y timescales.

Climate change by the summer monsoon affects the wind across the Thar Desert, which moves sediments from southwest to northeast (Wasson et al., 1983; Singhvi and Kar, 2004; East et al., 2015). This summer interaction, as well as the reverse in the winter, reflect the hot pre-monsoon months in the southwest Indian subcontinent, which include dry, windy conditions and associated dust storms in the late summer rain (Singhvi et al., 2010). We attempt to understand the influence that climate change has had on sediment transport through the source to desert using bulk petrography, heavy mineral assemblages and detrital U-Pb detrital zircon age analysis. We demonstrate how sediments are transported to and distributed within the Thar Desert in recent times. The sediments can be used to understand the impact of paleoenvironmental and climatic changes during the Holocene in the Western Himalayas and how these control sediment transport in the modern sand seas of the Thar Desert.

6.2. Compositional Fingerprints of Thar Sand Dunes

6.2.1. Petrography and Heavy Minerals Framework of Sand Dunes

Sediments from the Cholistan Desert are mainly litho-feldspatho-quartzose sand, including variable amounts of sedimentary and metamorphic rock fragments. Monocrystalline quartz is dominant with the association of subequal amounts of K-feldspar and plagioclase (Figs. 6.1 and 6.2). Quartz content decreases from north to south (from 70% to 57%). Samples S6117 and S6124 have sedimentaclastic to lithic carbonaticlastic framework compositions (Table 6.1a, b). The rock-fragment distribution consists of metasedimentary (paragneiss, schist, slate, calcschist, phyllite,

metasandstone), metabasite (prasinite, chloritoschist, amphibolite), carbonate (limestone, dolostone), other sedimentary (shale, siltstone, minor chert), granitoid, felsic to mafic volcanic and metavolcanic, and minor ultramafic (serpentine schist, cellular serpentinite) grains (MI 256–326, MI* 239–314) (Figs. 6.1 and 6.2).

Minor flakes of muscovite and biotite are present. The rich suite of transparent heavy minerals (tHM) dominantly comprises hornblende with epidote, garnet, and minor clinopyroxene, hypersthene, staurolite, titanite, kyanite, and fibrolithic sillimanite. ZTR values are minor (≤ 4). In the Cholistan samples metamorphic and sedimentary lithics decrease from NW to SE, similarly to the MI (327-288). The modern sand dunes of the Cholistan Desert are most similar to sediment from the eastern Greater Himalaya, Tethyan Himalaya (Zanskar and Punjabi tributaries) or Transhimalayan arcs.

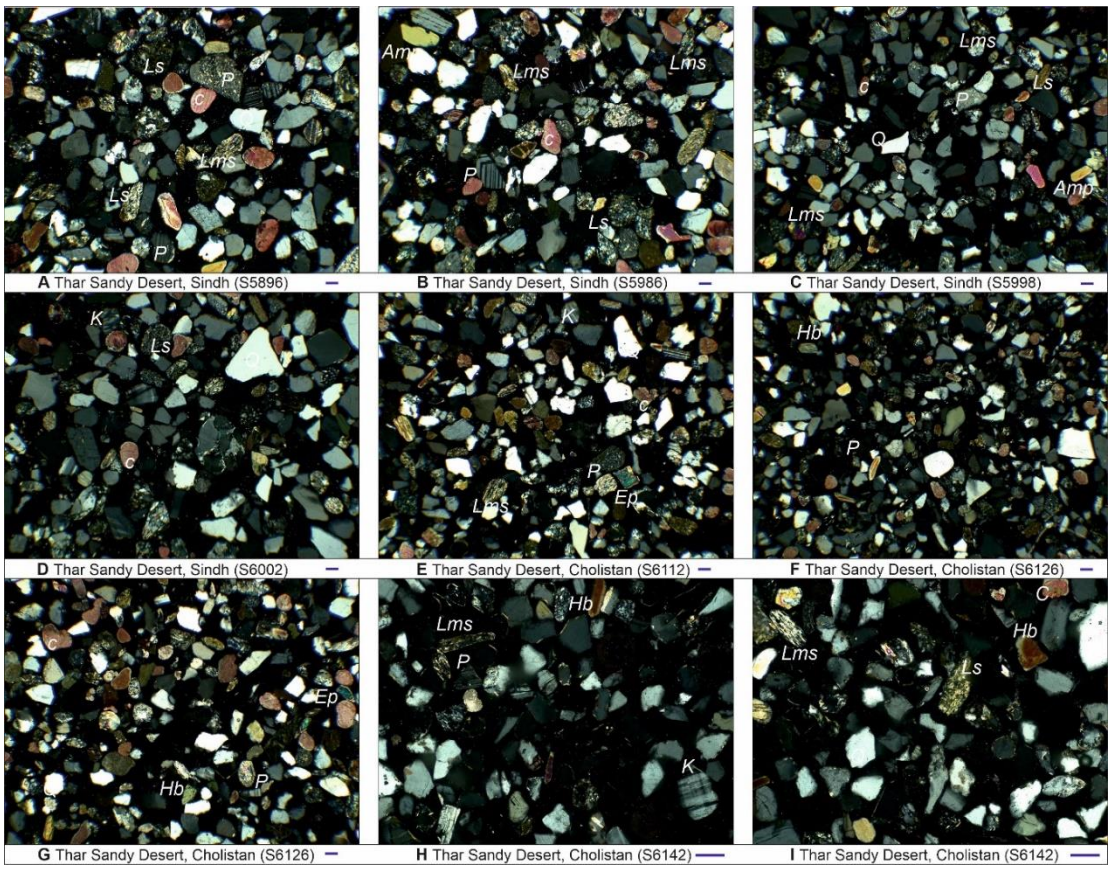

Figure 6.1. Photomicrographs of representative sediment samples from both Sindh and Cholistan deserts showing the overall petrography and similarity between these different areas. Note that sediments are slightly more angular from Sindh. Quartz and feldspars dominate but with significant influence from rock fragments and mafic heavy minerals. P = Plagioclase, c = carbonate, Ls = Sedimentary lithic, Lms = Metamorphic lithic, Amp = Amphibole, Hb = Hornblende, Ep = Epidote, K = K-feldspar, Q = Quartz

Sindh Desert sediments have a litho-felshpatho-quartzose composition, with equal proportions of plagioclase and K-feldspar (P/F 49-60) (Figs. 6.1 and 6.2).

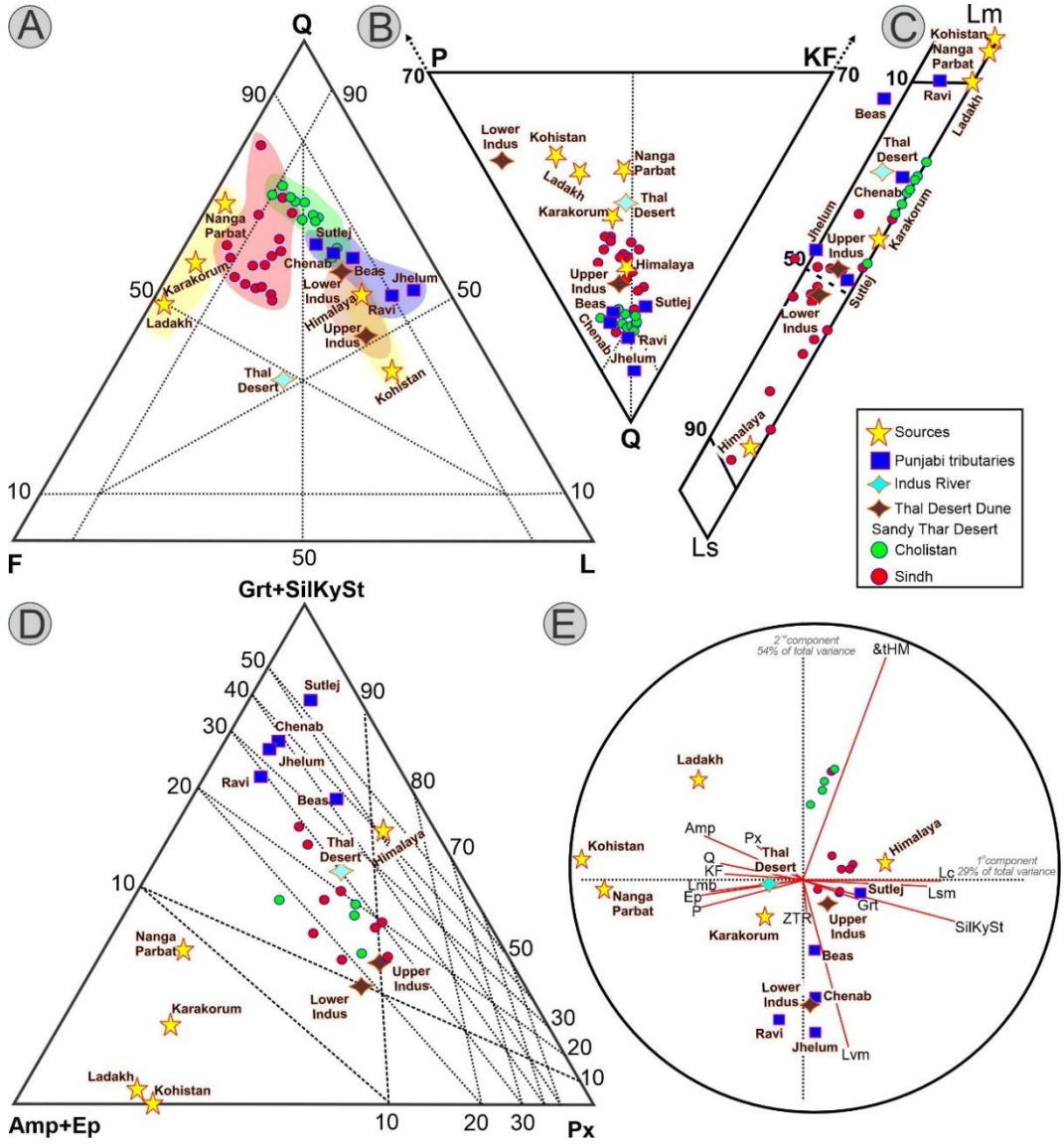

Figure 6.2. Diagrams comparing the overall petrography of the samples studied from the Thar Desert and comparing them with potential source regions in the upstream Indus, the lower reaches, as well as with the Punjabi tributaries that supply the Indus River from the east. A) QFL diagram, B) QFP diagram and C) Ls-Lm-Lv diagram from Ingersoll et al. (1984). Note that in general, the desert sediments from Thar are closer in composition to those from the suture zone, whereas sediment from Cholistan shows more similarity with the eastern tributaries and Himalaya. D) Heavy mineral discrimination diagram Triangular Garnet+(Silliminite+Kynaite+Staurolite) – (Amphibole+Epidote) – Pyroxene from Morton et al. (1999), E) principal component analytical plot from Vermeesch et al. (2016). Source region and tributary data are from the synthesis Garzanti et al. (2020).

Among the lithics, sedimentary clasts dominate, followed by metapelitics, metapsammites and metavolcanics. The Metamorphic Index is lower compared to the Cholistan samples (MI 263–220). The rich suite of HM (tHMC 8-10) is composed of green-blue to brown hornblende, together with garnet and epidote, minor clinopyroxene and hypersthene, sillimanite, kyanite apatite, titanite and ultrastable minerals. Cholistan sediments differ from those from Sindh in the high abundance of quartz (60±2 vs 53±2) and the dominance of metamorphic lithics over sedimentary clasts (Lm 62±2 Ls 37±2 vs. Lm 39±6 Ls 58±5). Heavy mineral concentrations increase in the Sindh Desert as well as a negligible increase of hornblende and garnet fraction (Fig. 6.2). Thal Desert sediment has similar compositions to that in the Upper to Lower Indus River which is mainly carrying feldspatho-litho-quartzose sand to the Indus Delta. These include numerous sedimentary and metamorphic lithic fragments, and a rich hornblende-dominated tHM suite with epidote, garnet, and minor clinopyroxene, hypersthene, staurolite, titanite, kyanite, and sillimanite (Garzanti et al., 2020). There is strong influence from the Indus River on the southern Sindh side of the desert compared to the northern Cholistan desert. The main compositional fingerprints of the Thar Desert, based on petrography and heavy minerals, are most similar to the Indus River. These sediments are feldspatho-litho-quartzose sand with a rich hornblende-dominated tHM suite with epidote, garnet, and some clinopyroxene with minor hypersthene, staurolite, titanite, kyanite, and sillimanite (MI 196–316, MI* 137–206).

6.2.2. Geochronology from Detrital Zircons

Five representative samples were selected for detrital zircon geochronology, two from the Cholistan Desert which yielded 191 concordant ages and three from Sindh Desert which yielded 330 concordant ages. We further integrated these with two samples from Sindh and one from Cholistan previously published by East et al. (2015) in order to increase total grain age numbers and improve the statistics. Now, there are a total of 841 concordant ages overall from the desert (Table 6.2).

Detrital zircons from Cholistan Desert sand dunes yielded primarily with Paleoproterozoic (1600–2500 Ma) which accounts for ~26% of the total. The second dominant age population is ~25% Neoproterozoic ages (540–1000 Ma; Fig. 6.3) of total zircon populations, followed by Paleozoic ages (~8%) and Miocene (~1.5%), Oligocene-Eocene (~9%), Paleocene (~5%), Late Cretaceous (~5%), Early Cretaceous

(~10%), Triassic (~1%), with an association of Mesoproterozoic (~5%) and Archean including Neoarchean (~2%) (Appendix).

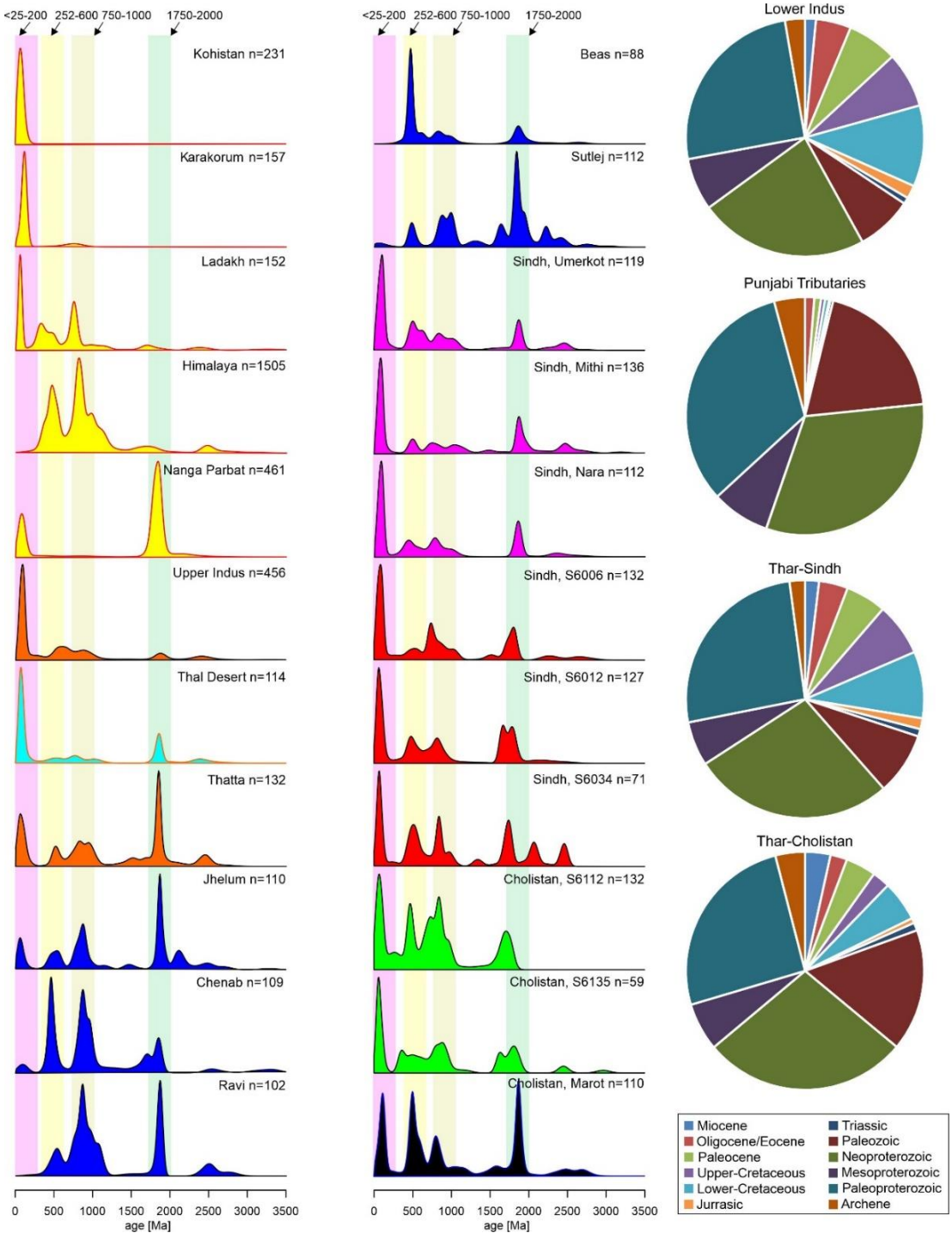

Figure 6.3. Left and center panels: KDE diagrams for U-Pb ages from detrital zircon grains in river and desert sands along the modern Indus, showing the overall pattern of the age spectra and the location from where the samples were taken. We also show KDE diagrams for modern river sediments in the Indus Suture Zone. See text for original source of potential sediment supplies. Right panel: Pie diagrams showing the average age structure of the zircon U-Pb ages

from Sindh and Cholistan, together with the lower Indus and an average of all the Punjabi tributaries. Detrital zircons from the Sindh Desert yielded primarily Neoproterozoic ages (540–1000 Ma) accounting for ~28% of the total zircon population. The second most important age population is Paleoproterozoic (1600–2500 Ma) having ~24% of the total. The third dominant age population is Paleozoic, including Carboniferous (315–342 Ma), Silurian (359–434 Ma), Ordovician (454–483 Ma), totally ~14% of the total grains. Younger age populations are Miocene (~3%), Oligocene-Eocene (~4%), Paleocene (~6%), Late Cretaceous (~3%), Early Cretaceous (~9%), Jurassic (~1%), Triassic (~1%), with an association of Mesoproterozoic (~7%) and Archean including Neoarchean (~1%) (Appendix).

6.3. Provenance of Thar Desert Dune Sands

6.3.1. Petrography and Heavy Minerals

The compositional petrographic framework indicates that the desert sediments are litho-felspatho-quartzose sands similarly to those found in the Thal Desert. Lithics are mainly sedimentary and high to medium metamorphic grade. Heavy mineral concentrations are poor to moderately rich and these assemblages are dominated by an orogenic suite of heavy minerals (Amp, Grt, and Ep).

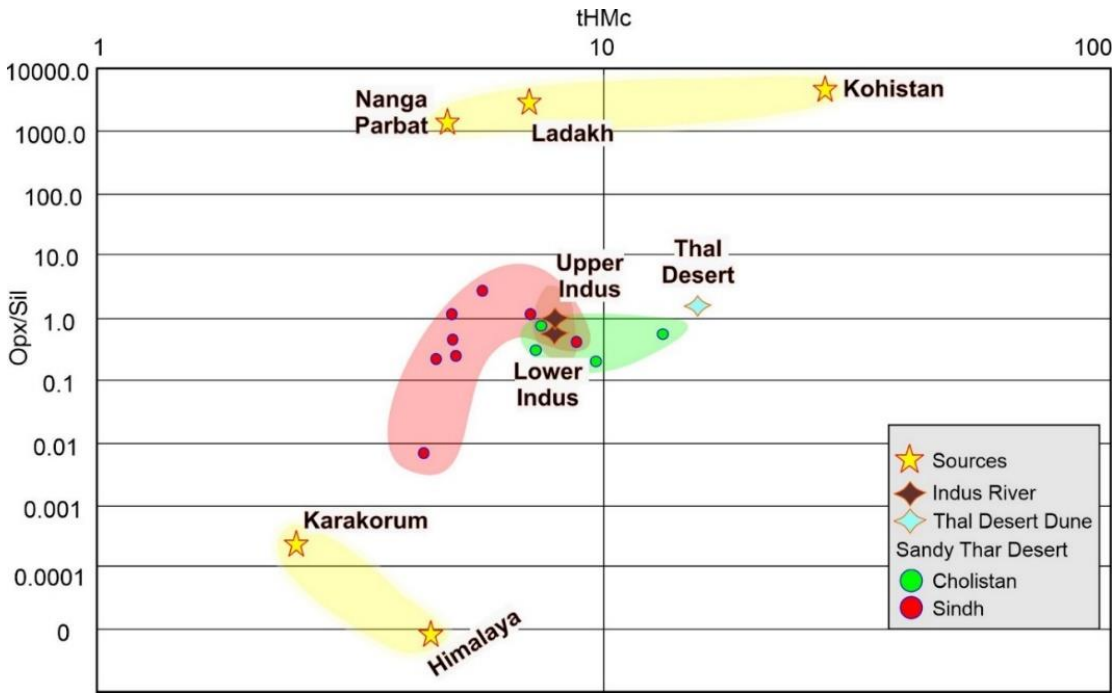

Figure 6.4. Diagram plotting orthopyroxene/sillimanite (Opx/Sil) values against total heavy mineral concentrations (tHMc). The samples from the desert sands lie between the end members of the Karakorum and Himalaya, as well as those from Ladakh, Kohistan and Nanga

Parbat. Note that the samples from Sindh plot are closer to the Karakorum and Himalaya, while those from Cholistan are closer to Kohistan.

Desert sediments are dominated by the orogenic signal. Compared to the Sindh Desert Cholistan sediments are richer in metamorphic lithics while the Sindh sediments are richer in orthopyroxene (Opx), but only slightly. The biggest difference is in the Opx/(Sil) and tHMC, which are a good way to estimate the sources of desert sediments (Fig. 6.4). The Cholistan sands are most similar to a Punjabi tributary source according to HM and petrography. In contrast, Sindh sediments are more similar to the Thal Desert and Upper Indus.

6.3.2. Zircon Age Populations

In the Thar Desert (Table 6.2), Miocene grains (~2% Cholistan and 1.5% Sindh) were found and are only known in sand from the Hushe Rivers draining the Baltoro Granite. The youngest age population found in Cholistan (13–21 Ma; ~2% of total zircons) and Sindh sand (17–25 Ma; ~1.5% of total zircons) are thus most likely derived from the Karakorum (MDS, Fig. 6.5).

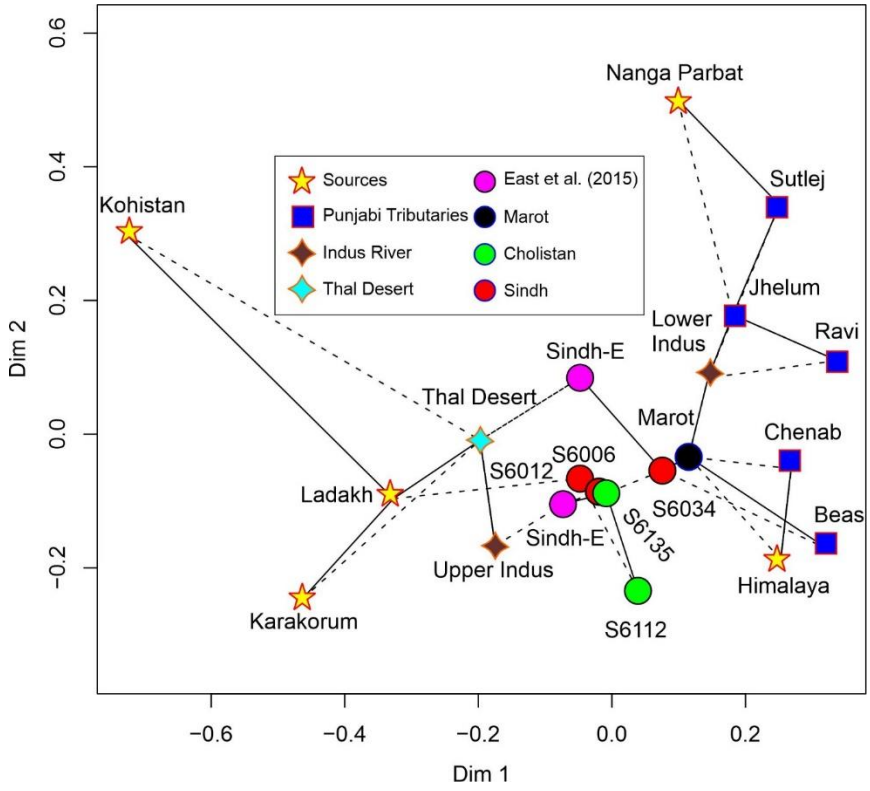

Figure 6.5. MDS diagram comparing the U-Pb age spectra of the desert sediment detrital zircon ages from both Cholistan and Sindh, in comparison with potential bedrock sources in the upper reaches, as well as with the major Punjabi tributaries draining the Himalaya on the eastern side

of the Indus basin. We further show modern sediments from the Indus lower reaches at the delta. The data was compiled from existing sources, as described in the main text.

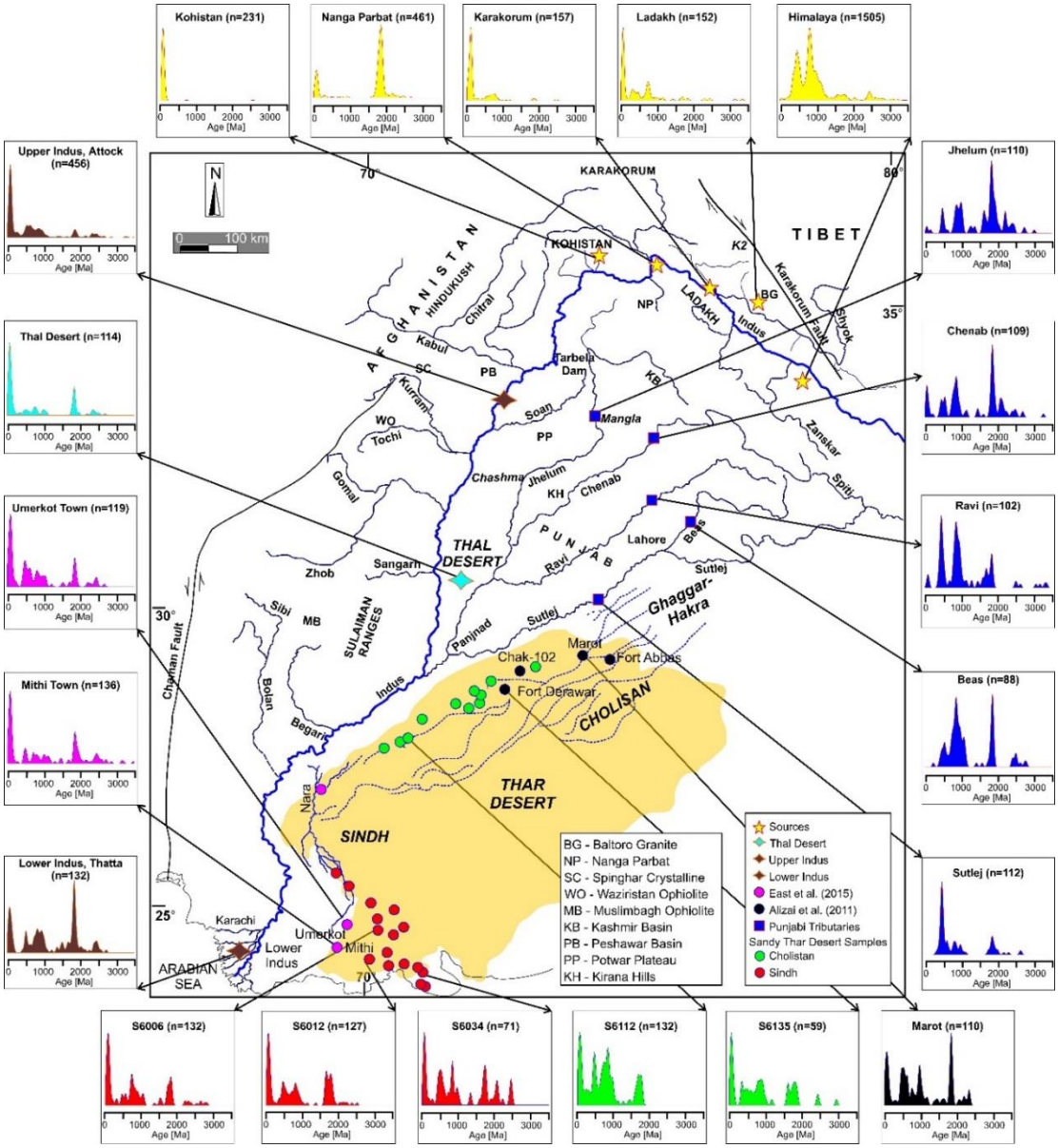

Figure 6.6. KDE diagrams showing U-Pb ages from detrital zircon grains for the major source terrains within the Indus Suture Zone, as well as modern river sediment samples from the eastern Punjabi tributaries, and from the upper and lower modern Indus, compared with sediments from the Thar desert, both in Cholistan and Sindh. We plot desert data from this study as well as from East et al. (2015). Note how the desert sands all have the <200 Ma peak that mirrors data from the Karakorum, but also show major populations correlating with the Himalaya as measured in Zanskar, as well as in the eastern tributaries. See text for origin of the source and tributary data.

6.4. Sedimentary Budget

The relative contributions from each geological domain to the aeolian sand of the Thar Desert is estimated by forward mixing models using the method proposed by Garzanti et al. (2012) and Resentini et al. (2017), based on the detailed compositional information from end-member sources. The analysis involves calculations that are nonunique and inherently uncertain, impacted by various source errors and dependent on unverified assumptions. To ensure accurate results, independent tests must be conducted using different criteria for each dataset, including petrography, heavy minerals, and zircon age population (Garzanti et al., 2020). It is important to note that each estimate obtained from these tests applies only to the specific components and grain size range under investigation, such as sand, transparent heavy minerals, and zircon. Achieving this requires careful consideration of mineral fertilities within each source-rock domain (Malusà et al., 2016; Garzanti et al., 2020). Nonetheless, it is a necessary step to calculate sediment yields and erosion rates in different parts of the catchment.

6.4.1. Petrography and Heavy Minerals

The major compositional character of dune sediment from the desert is strongly influenced by the fluvial and aeolian processes that have transported this material from source to sink. Heavy mineral and petrographic studies from different sources allow their relative contributions to be constrained (Garzanti et al., 2005; 2020). Petrographic results analyzed by the linear mixing model for the Upper Indus River show that the supply of detrital material is ~32% from Ladakh-Kohistan Arcs combined, compared to sediment eroded from the Karakorum–Hindukush (~2%), Nanga Parbat (~9%), and Himalayan units (~57%). In contrast, the detrital material in the Lower Indus River is derived from Ladakh-Kohistan Arcs (~14%), the Karakorum–Hindukush (~1%), Nanga Parbat (~30%), and Himalayan units (~55%). However, these percentages need to be treated with caution as the abundance of particular minerals is strongly affected by hydraulic sorting, as well as source fertility, and may not be the best provenance indicator.

Heavy minerals in the Upper Indus River are derived from the Ladakh-Kohistan Arcs (~33%), as well as from the Karakorum-Hindukush (~17%), Nanga Parbat (~13%), and Himalayan units (~37%) (Fig. 6.7a). Heavy minerals for the Lower Indus River come from the same sources but in different proportions, i.e., Ladakh-Kohistan

Arcs (~36%), the Karakorum-Hindukush (~36%), Nanga Parbat (~9%), and Himalayan units (~19%) (Fig. 6.7b). Differences are noted between the estimated sources in the deserts and the Indus River. Desert dune sediments in Sindh and Cholistan are predicted to come from Ladakh-Kohistan Arcs (~34% and ~30% respectively), Karakorum–Hindukush (~31% and ~5%), Nanga Parbat (~16% and ~17%), and Himalayan units (~31% and ~48%) (Figs. 6.7c and 6.7d).

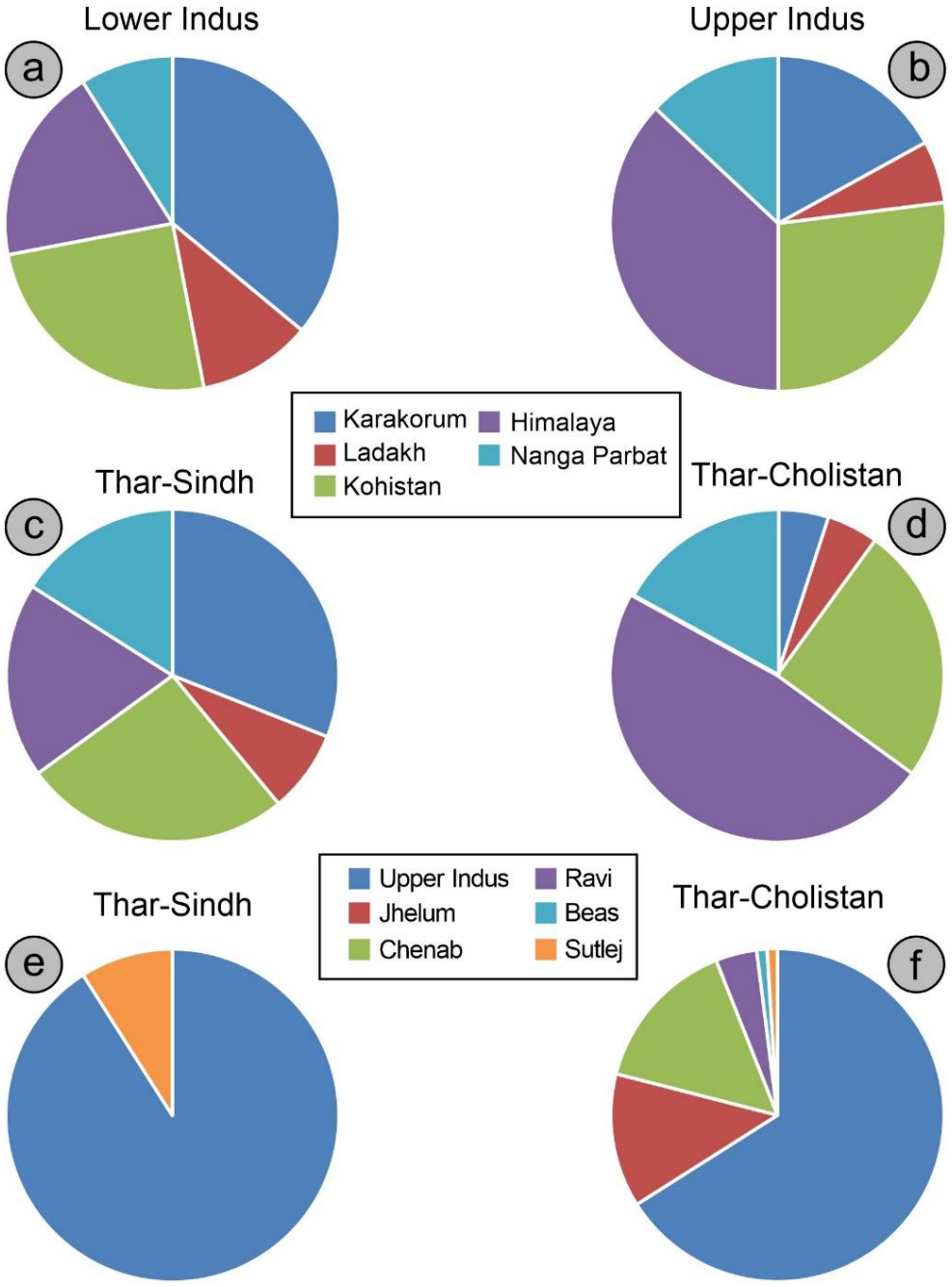

Figure 6.7. Pie diagrams based on the heavy mineral assemblages used to estimate the percentage contribution from various bedrock sources to the sediments from the a) upper and b) lower Indus, as well as c) the Sindh and d) Cholistan areas within the Thar Desert. Estimates

of the contribution of sediments from the modern tributaries to e) Sindh and f) Cholistan based on heavy mineral suites. This dataset includes new data integrated with existing heavy mineral data from Garzanti et al. (2005, 2020).

The concentration of heavy minerals in the sediment varies depending on the supply from contrasting source units, and thus varies between different tributaries with unique bedrock exposures in their headwaters. There are examples where sediments appear to have been partially eroded from source areas that are not present upstream of the sampling location in the adjacent river system. For example, in northern Cholistan it might not be expected to see sediment eroded from Nanga Parbat, Ladakh-Kohistan or the Karakorum. Although the percentage of heavy minerals from those areas is less than other parts of the desert the values are not zero and require recycling via aeolian transport from the south. It should also be remembered that different source areas may have contrasting degrees of fertility in the different heavy minerals, so that the proportion of sediment derived from each source and calculated from heavy mineral percentages may not be representative of the total mass flux. Hydraulic sorting is a crucial factor for the concentration and variety of heavy minerals from which we derive provenance information. Compared to the modern Upper Indus and Thal Desert sands, Cholistan Desert sand is notably poorer in quartz and sedimentary to low-rank metasedimentary rock fragments. Cholistan sediments are however richer in feldspars, volcanic, metavolcanic and metabasic rock fragments, heavy minerals and especially hypersthene, documenting a significantly greater relative contribution from the Kohistan arc (Fig. 6.4).

According to the petrographic results, Cholistan sand dunes are mostly derived from the Sutlej River (89±2%) which is the nearest large Punjabi tributary draining the Himalaya in the eastern part of the Indus catchment. The main compositional sediment type found eroded from the Greater Himalaya is litho-feldspatho-quartzose metamorphiclastic sands (Garzanti et al., 2020). However, Cholistan Desert sand dunes also have similar petrographic compositions as sand from the other contributing tributaries (in total 11%), i.e., Beas (contributing 9±2%), Chenab (1±1/2%), and Ravi (1±2%). It is questionable whether the different Punjabi tributaries are really distinguishable in terms of their bulk petrography. In contrast, when considering the heavy mineral assemblage, the Cholistan Desert sediment appears to be dominantly from the Upper Indus River (66±3%). Further supply is inferred from the Punjabi

tributaries (34±2%), including the Sutlej River (1±2%), Jhelum (13±2%), Chenab (15±2%), and Ravi (1±2%) with 3.81±2% error from the estimated linear mixing model (Fig. 6.7e).

Based on their petrography Sindh sand dunes can be explained by a dominant supply from the Sutlej River (90±2%) with minimal contributions from the Lower Indus River, but with 10±1% contribution from the Upper Indus River. Alternatively, the Sindh petrography could be formed by a mixture of 90% Sutlej sediment and lesser amounts from the Punjabi tributaries (in total 10%), i.e., the Jhelum (3±2%), Chenab (5±1/2%), Beas (1±2%) and Ravi (1±2%), with 8.79±2% error from the estimated linear mixing model.

Modelling does not give a unique provenance based on petrography alone. Some of the Sindh sediment may previously been supplied by the Ghaggar-Hakra River before it was abandoned**.** If that channel formerly connected with the Nara River in Sindh, then this stream could also partly have supplied the Sindh Desert. According to the heavy mineral assemblages, the Sutlej River is the second largest contributor to the Sindh Desert, accounting for 9±2% of the total, while the main contributor is the Lower Indus River that accounts for 91±2% for the Sindh Desert (Fig. 6.7d). It is clear that the mixing calculations for the petrography and the heavy minerals result in substantially different conclusions about the source of the sand in the desert. The bulk petrography is likely less unique in sediment from different sources and so heavy minerals are the preferred provenance tool.

Thal sand dunes were derived from erosion of the Transhimalayan arcs (40–45%, predominantly from the Kohistan arc; Garzanti et al. (2020be)), the Karakorum-Hindukush Ranges (40–50%, at least a third of which is carried via the Kabul River, according to suspended-load data of Rehman et al. (1997), the Nanga Parbat Massif (<10%; Clift et al., 2022), and the Himalayan belt (<10%, including detritus recycled by the Soan River). Further clues are obtained from electron-microprobe geochemical data (Liang et al., 2019), which showed that the Kohistan arc played the role as the principal source of the most common groups of transparent heavy minerals, especially pyroxene and epidote. The South Karakorum gneiss domes are undergoing fast exhumation (Shroder et al., 2011), and represent important additional sources of amphibole, garnet and zircon. The Nanga Parbat Massif is a lesser contributor of these minerals. The contribution from other Himalayan domains is significant only for Lower

Indus sand downstream of the Thal and Thar Deserts (Lee et al., 2003; Alizai et al., 2016).

6.4.2. Detrital Zircon

A set of forward mixing calculations were performed using the *DZMix* software of Sundell and Saylor (2017). This approach is based on the age populations discussed above in each detrital sample. In this approach the potential sources are mixed in order to replicate the sediments from the Thar Desert and constrain where the sediment is derived from. In each case 10,000 attempts are made to replicate each detrital age spectrum and match the observed zircon age spectrum, with the best 1% selected. The fit is assessed using a statistical analysis with three methods applied in the *DZMix* software (i.e., cross correlation, Kuiper test and K-S test). In order to derive the best statistical result, we group together all the sediments analyzed from desert dunes in Sindh and Cholistan into two large sample groups, which we analyzed to understand how they differ from one another, and how they compare with the nearby rivers. Of course, this type of mixing can only be as good as the definition of the source areas.

In this study, we did not use zircon data from the bedrock sources, but instead use modern river sediments to characterize potential source regions because these provide a better regional average of source composition because erosion tends to sample the source areas more evenly than geologists. Karakorum and Hindukush sources were derived from the work for Zhuang et al. (2018) and Clift et al. (2022). Nanga Parbat ages are from Garzanti et al. (2020b) and Clift et al. (2022). Kohistan data are from Zhuang et al. (2018) and Garzanti et al. (2020b). Ladakh data are from Garzanti et al. (2020b) and Clift et al. (2022). Zanskar data are from Jonell et al. (2017) and Garzanti et al. (2020). Sutlej, Beas and other Punjabi tributaries are from Alizai et al. (2011b). We opted to examine the Sutlej and Beas samples separately from the other Punjabi tributaries because these rivers lie adjacent to the Cholistan part of the Thar Desert and are most likely to supply sediment to the desert. As well as looking at modern Thar desert dunes, we also applied the same mixing calculations to the Upper Indus at Attock bridge (Alizai et al., 2011b; Garzanti et al., 2020b; Clift et al., 2022), and the modern Indus River mouth at Thatta (Clift et al., 2004). We also examined older Holocene and post-LGM sediments from the delta (Clift et al., 2012), and sediments from older rivers in Cholistan, drawing on data from the Marot borehole from Clift et al. (2012).

The results of the mixing analysis are provided in Appendix and shown graphically in Figure 6.8a-h, with the latter showing the preferred contributions based on the V factor of the Kuiper test. The Sindh and Cholistan sand averages are quite different, with much more sediment from the Punjabi tributaries in Cholistan. We note that in the Cholistan sands around ~69% of the total population is linked to supply from Punjabi tributaries, including the Sutlej and Beas, with the remaining ~31% coming from further north, largely from along the Upper Indus, despite the lack of a direct transport connection. In contrast, the Sindh dunes are richer in supply from the Karakorum, Nanga Parbat, Ladakh and Kohistan (Fig. 6.8a). The Punjabi contribution is ~46% of the total here and with much higher contributions from Kohistan (~10% compared to ~2% in Cholistan) and Nanga Parbat (~8% compared to ~3% in Cholistan) (Table 6.3).

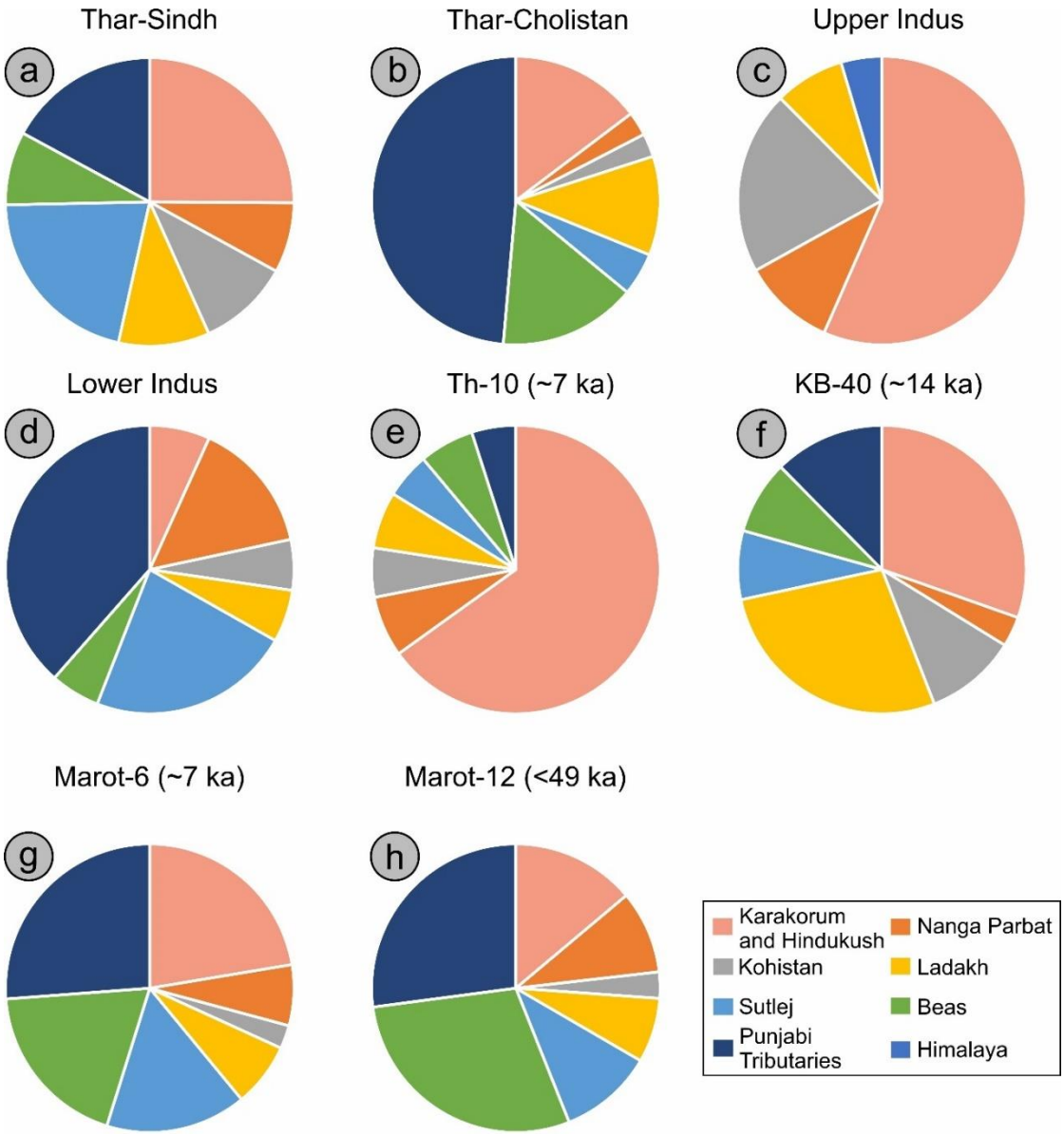

Figure 6.8. Pie diagrams showing the relative contributions from the major bedrock source terrains and based on detrital zircon U-Pb spectra, as estimated using the DZMix program from Sundell and Saylor (2017). a) Sindh and b) Cholistan areas of the Thar Desert. C) the upper Indus at Attock Bridge from Alizai et al. (2011) and Clift et al. (2022), d) the lower Indus at Thatta from Clift et al. (2004), e) the Indus delta at 7 ka and f) at 14 ka from Clift et al. (2008), the paleo-Ghaggar-Hakra channel at g) 7 ka and h) <49 ka at Marot from Clift et al. (2012). The desert populations include new data provided in this study integrated with existing ages from East et al. (2015). The *DZMix* analysis results are provided in the Appendix. The plots shown here are based on the V factor of the Kuiper test. The Sindh and Cholistan sand averages are quite different from one another, with much more sediment from the Punjabi tributaries present in Cholistan.

East et al. (2015) argued that at least the southern Thar Desert was largely derived from the Indus Delta. We compare our Sindh dunes to the modern river at Thatta (Fig. 6.8c). The modern river is much richer in supply from the western Punjabi tributaries (~38% vs ~17%) but similar in supply from the Sutlej (~23% vs ~21%) compared to the desert and much lower in supply from the Karakorum and Kohistan. Neither desert area appears to be like the Upper Indus at Attock which is heavily dominated by the Karakoram (~57%), Nanga Parbat (~10%) and Kohistan (~21%). We further compare the Sindh desert with older Indus delta sand compositions. Sample TH-10, dated ~7 ka (Clift et al., 2008), has most similarity with the Upper Indus sample, being dominated by Karakoram zircons (~65%), and showing a rapid change in provenance at the river mouth since 7 ka. This sample appears to be unlike the Sindh or Cholistan sands, whereas Sample KB-40, dated ~14 ka, has a closer match to the Sindh, but not the Cholistan dunes, albeit with more predicted erosion from Ladakh (~27% in KB-40 vs ~10% in Sindh dunes). We note that this TH-10 sample comprises ~16% of zircons from all Punjabi tributaries compared to ~46% in Sindh. If we compare the Cholistan average with Thatta (modern river mouth) we note that the total Punjabi contribution is similar to that in Cholistan, although the Sutlej is more important to the delta than to Cholistan dunes. The Cholistan average dunes do however closely resemble the Marot channel samples (6 and 12), although the Sutlej is more important at Marot, especially to Marot-6 (dated ~7 ka; Clift et al., 2012), while Marot-12 (>49 ka) is very rich in Beas-derived zircons (Table 6.3).

6.5. Influence of Climatic Changes with Asian Monsoon System

6.5.1. Summary of Provenance Results

Provenance studies utilize various methods to investigate the origin of sedimentary deposits based on their composition. Each method provides complementary information, but frequently no one method offers a definitive interpretation on its own. Petrographic analysis, for example, is best applied to bedload sand, while major element geochemistry is affected by grain size and has limited discrimination power, with the exception of resolving flux from mafic source rocks (Garzanti et al., 2020b). Heavy-mineral suites are strongly affected by hydraulic sorting and selective chemical dissolution, while detrital zircon age spectra can be distorted by fertility effects and biased towards felsic igneous and metaigneous sources (Gehrels, 2014). Additionally, recycled zircon grains cannot be distinguished from first-cycle grains.

Despite these limitations, the combination of different methods provides robust evidence regarding the provenance of sand dunes in the Thar Desert. We argue that the sand dunes in the north-eastern Cholistan area were largely fed by erosion from the Himalaya, and supplied by the paleo-Ghaggar-Hakra, Sutlej River and other Punjabi tributaries. The southern Sindh dunes were supplied by the Lower Indus River at a time when erosion was focused north of the Himalaya, especially in the Karakorum-Hindukush, with lesser erosion from Nanga Parbat and Kohistan.

Provenance budgets based on integrated petrographic-mineralogical data indicate that the Cholistan heavy minerals were originally derived mostly from erosion of the Himalaya (~48%), with lesser input from the Karakorum (~5%), Nanga Parbat (~17%) and Ladakh-Kohistan (~30%). The high proportion of heavy minerals from Ladakh-Kohistan reflects the high fertility of these sources for heavy minerals. The Sindh dunes are less Himalayan (~19%) but more strongly enhanced by erosion of heavy minerals from the Karakorum (~31%), Ladakh-Kohistan (~34%) and Nanga Parbat (~16%). In contrast, petrography indicates that ~60% of the modern Indus sand upstream of Tarbela Dam is derived from the Karakorum (Garzanti et al., 2020b), similar to the ~70% estimated from zircon U-Pb ages at Attock Bridge (Clift et al., 2022). The remainder of that sediment was supplied in subequal amounts by the Ladakh-Kohistan arcs and the Himalaya. Zircon mixing calculations indicate ~25% and ~15% respectively in Sindh and Cholistan dunes from the Karakorum. Likewise, contributions to Sindh and Cholistan from Nanga Parbat are ~8% and ~3%, from Kohistan-Ladakh are ~20% and ~14%, and ~46% and ~69% from the Punjabi tributaries (Himalaya).

We can explore the provenance of the desert dunes further using the *DZStats* program from Saylor and Sundell (2016) (Appendix). In this approach, a series of samples are directly compared using a statistical test, in this case the Kuiper Test to quantify their similarity. We compare the Sindh and Cholistan dune averages with potential sources, i.e., the Upper Indus at Attock, the modern delta at Thatta, two post-LGM delta samples (TH-10 at ~7 ka and KB-40 at ~14 ka), together with the modern Sutlej and two older fluvial channel sands from Marot (Marot-6 at ~7 ka and Marot-12 >49 ka). These sands are from the Ghaggar-Hakra which is a now abandoned Himalayan-sourced Punjabi tributary flowing closest to the desert. There is no direct measurement of what the Sutlej or other Punjabi tributaries looked like during the Mid Holocene or older times. The results are shown in Figure 6.9 and Table 6.4.

It is clear that neither dune field is very similar to the Upper Indus or to the modern Sutlej. Sindh dunes are more like delta sediments than the dunes in Cholistan. Sindh dunes are most like the delta sediments from ~7 and 14 ka. The Cholistan dunes are most like the Marot-6 and -12 samples. We do not think that this is because of large-scale erosion of the desert sands because these channels significantly pre-date the demise of flow in the Ghaggar-Hakra. The Cholistan dunes do share moderate similarity to the Indus delta, which is presumably the source of the younger zircons that originally were eroded from the Karakorum, and Ladakh-Kohistan. This statistical test implies that the Cholistan dunes represent a mixture of sediment transported by wind from the delta together with locally derived sediment from the Ghaggar-Hakra, presumably before 7 ka. The Thar Desert surface sediments therefore were largely supplied to the dunes before or at ~7 ka, potentially during the early Holocene when SW to NE directed summer monsoon winds were at a maximum.

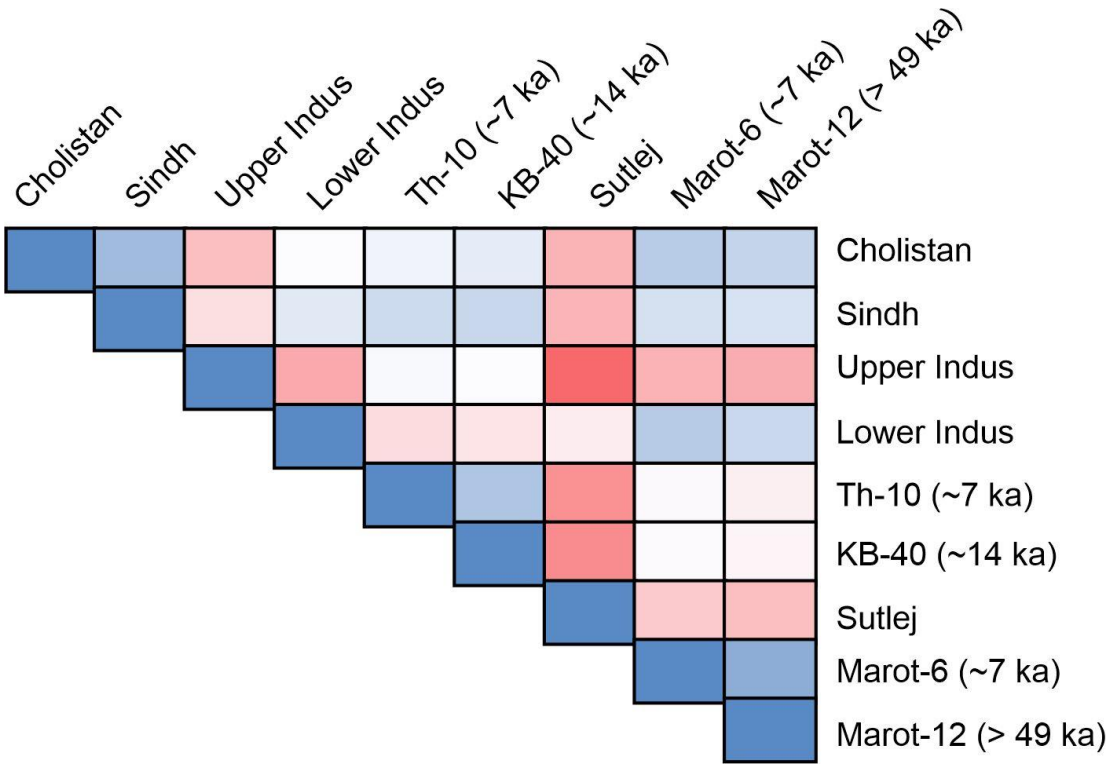

Figure 6.9. Heat map showing the similarity of desert dune sands and select stream sediment as determined from K-S testing using the *DZStats* program of Saylor and Sundell (2016), with details provided in Appendix. Note the similarity of the modern Cholistan sands with the Marot channel sands predating 7 ka, and the match between Sindh sediments and those from the delta, especially prior to 7 ka. Both desert sands are similar to one another and likely share some common sources.

6.5.2. Aeolian Sedimentation since the LGM

An initial chronology of the evolution of the Thar Desert has been established through thermoluminescence dating of aeolian sediments (Singhvi et al., 2010). The dating revealed that the desert has experienced multiple phases of dune accretion since 200 ka, which were interspersed with hiatuses linked to precession-driven climate. The last major phase of dune growth in the eastern Thar Desert started between 17 ka and 14 ka and lasted until 9 ka, at the onset of the early Holocene wet stage (Dhir et al., 2010, 2012; Singhvi et al., 2010; Garzanti et al., 2020b). During this time, the region experienced a transitional climate, with Southwest monsoon winds strengthened following a period of weak summer monsoon during the LGM. In contrast, the western Thar Desert, the subject of this study, has been supplied with sediment since the beginning of the wetter Holocene and expanded further west as the climate dried after the mid-Holocene (East et al., 2015). Mesolithic artifacts dated to the first millennium of the Holocene have been found on top of sand dunes in both Thar and Thal Deserts,

indicating that an accretion history similar to the eastern Thar Desert may be extrapolated to the Thal Desert (Biagi et al., 2019), but contrasting with later growth in the western Thar Desert.

The compositional framework of the Thar sand dunes indicates that detrital material is eroded from the Himalaya, Nanga Parbat, Karakorum and Ladakh-Kohistan. The incision of moraines and fluvial terraces in the mountains led to increased sediment fluxes during the deglaciation period that followed the Last Glacial Maximum (LGM). (Blöthe et al., 2014; Garzanti et al., 2020b; Clift and Jonell, 2021). During the LGM and early deglacial period, the summer monsoon rains were weak, but meltwater fluxes from shrinking mountain glaciers were high and carried sediment to the lower reaches and delta, as well as accumulating on the northern flood plains (Saini et al., 2009; Giosan et al., 2012). As monsoon rains strengthened in the Early Holocene the river sediment load increased but sedimentation became focused in the lower reaches, as the northern flood plains incised. Fluvial sediments were deposited through the Holocene in the lower reaches and delta, and before 10 ka in the northern flood plains (Giosan et al., 2012). Sediments on the flood plains and delta were reworked by wind into the eastern Thar dunes from 17 to 9 ka and through the Holocene in the western Thar Desert (East et al., 2015; Singhvi et al., 2010). This implies that the Thar Desert migrated to the west as the monsoon weakened, starting in the Mid Holocene.

6.5.3. Paleo-Climatic Effects and the Asian Monsoon

The intensity of the Asian Monsoon varies not only over tectonic timescales (>10^6 years) but also over millennial and shorter timescales (Clemens and Prell, 2003; Jonell et al., 2018). The Quaternary period experienced significant variations in monsoon intensity, which were influenced by insolation maxima and the export of latent heat from the ocean system (Clemens et al., 1991; Clemens and Prell, 2003; Clark et al., 2006; Caley et al., 2011). The relationship between monsoon intensity and orbital forcing is clear, although with a delayed response. The climate of the Thar Desert in the Holocene was highly sensitive to changes in Asian Monsoon strength, as evidenced by the discovery of a "lost river" in the Cholistan Desert and related fluvial deposition upstream in the Ghaggar-Hakra River system (Oldham, 1886; Durcan, 2012; Alok et al., 2023). The weakening of fluvial activity in the Ghaggar-Hakra occurred around 4.5 ka, consistent with a weakening of the Monsoon rains (Durcan et al., 2019), which occurred along a west to east gradient. Local reactivation of fluvial systems, in the form

of floods at around 600–800 years ago was observed in the Ghaggar-Hakra, in the Luni River within the central Thar Desert, as well as further south in the Penner River basin, in response to a period of enhanced precipitation regionally (Thomas et al., 2007; Singhvi et al., 2022). The climate during the LGM was enhanced aridity at ~23–20 ka and with an increase in monsoon intensity from 20 ka onwards, and especially in the Holocene (Durcan, 2012). The period of regional precipitation that led to the incision of the Sutlej River into the Ghaggar-Hakra interfluve at the top of the anabranch transect is driven fluvial activity after 10 ka, during an intensification of the Asian Monsoon system. Wet conditions, accompanied by strong winds, are preferred for sediment movement and reworking within the Thar Desert, with sediment accumulation occurring rapidly in the central part of the desert throughout the Holocene (Singhvi et al., 2010; Chatterjee and Ray, 2017). The dunes in the western edge of the desert have advanced over the floodplains after 4–5 ka. Stratigraphic studies have documented the connectivity between fluvial and eolian sedimentary systems between the Indus River and Thar Desert, with the dunes in the western edge of the desert advancing over the floodplains after 4–5 ka (East et al., 2015; Durcan et al., 2019).

Conclusions

This study employs an integrated provenance approach, combining bulk petrography, heavy minerals and detrital zircon dating to constrain the origin of sediments in the western Thar Desert. Both sediments from Sindh and Cholistan have similar bulk petrographic characteristics, and are litho-feldspatho-quartoze sands, similar to those found in the Thal Desert. The heavy minerals in the dunes sand are largely reflective of erosion from the Himalayan orogeny, including the Karakorum. In Cholistan, there is a preference towards metamorphic lithic fragments, and these are generally similar to the heavy minerals found in the Punjabi tributaries that drain the Himalaya to the east of the mainstream. In contrast, heavy minerals in Sindh dune sands have greatest similarity with the upper Indus River. When we consider detrital zircon grain ages, we see that both Sindh and Cholistan have zircon grains derived dominantly from erosion of the Karakorum, the Himalaya and Nanga Parbat. Because there is no way to directly supply material from the Karakorum and Nanga Parbat to Cholistan this implies aeolian reworking, probably from the south.

We note that the different provenance methods result in quite different conclusions about the origin of the sediment and although some of this can be explained by

hydraulic sorting it appears that the bulk petrography is in general a poor indicator of sediment source. Heavy minerals indicate that desert sand in Sindh is preferentially derived from Karakorum sources and supplied from the lower Indus River, accounting for around 91% of the total heavy mineral assemblage. In contrast, Cholistan sand is more Himalayan in character but also includes significant heavy mineral supply from Kohistan. It is noteworthy that Kohistan is a major supplier of heavy minerals because its bedrocks are fertile sources of these phases. In order to transport these heavy minerals to Cholistan we require transport by aeolian processes since there is no direct river channel between Kohistan and Cholistan.

Although detrital zircons also have fertility issues in terms of showing preferential erosion, we use this data set to demonstrate that the sand dunes in Sindh and Cholistan are statistically different from one another. In general, there is more sediment delivery from Punjabi tributaries to the Cholistan Desert, material originally eroded from Himalayan bedrocks. Concerning the original source of the sediment, there is a bias towards the Karakorum in Sindh, as well as sediment from Kohistan and Nanga Parbat. If we compare the desert sediments with the adjacent rivers, we see that the Sindh sands show most similarity with the modern delta but especially with older delta sediments dating from 7 and 14 ka. Likewise, the Cholistan sands do not show much similarity to the modern tributaries that lie next to the NW edge of the desert (e.g., the Sutlej River) but have more similarity to old river sediments presumably linked to the now ephemeral Ghaggar-Hakra and deposited before 7 ka. Both these datasets imply that the desert was largely supplied by sediment before 7 ka. If this construction happened in the early Holocene or latter parts of the pre-Holocene deglaciation, then this would have been a time of strong summer monsoon. Transport by aeolian processes, when the summer monsoon was strong, seems most likely. The desert has migrated more recently but may not have received large amounts of additional sediment since 7 ka.

Table 6.1a. Petrography composition of Thar (Cholistan and Sindh) Desert sand carried by the Indus River and Punjabi tributaries from the different NW Himalayan sources.

River/Desert	Sample	Q	F	Lv	Lc	Lh	Lp	Lm	Lu	total	Qp/Q	P/F	MI*
Thar Sindh West	**Average**	50	30	1	10	0	1	7	0	100	14	48	190
	Stand Devi	*0*	*0*	*1*	*1*	*0*	*0*	*1*	*0*		*7*	*2*	*22*
Thar Sindh Center	**Average**	58	27	1	6	0	2	6	0	100	10	58	161
	Stand Devi	*5*	*5*	*1*	*1*	*0*	*1*	*1*	*0*		*4*	*7*	*20*
Thar Sindh South	**Average**	58	28	0	7	0	2	5	0	100	8	54	167

	Stand Devi	*5*	*5*	*0*	*3*	*0*	*0*	*2*	*0*		*2*	*9*	*17*
Thar Cholistan NE	**Average**	62	17	0	7	0	1	13	0	100	5	50	268
	Stand Devi	*3*	*1*	*0*	*2*	*0*	*1*	*2*	*0*		*2*	*4*	*20*
Thar Cholistan C	**Average**	67	19	0	5	0	0	9	0	100	8	58	319
	Stand Devi	*1*	*2*	*0*	*1*	*0*	*1*	*1*	*0*		*3*	*5*	*13*
Thar Cholistan SW	**Average**	67	18	0	6	0	0	9	0	100	8	51	309
	Stand Devi	*4*	*1*	*0*	*4*	*0*	*0*	*2*	*0*		*1*	*4*	*12*
Thal	**S1462**	37	34	1	7	0	3	18	0	100	9	51	292
Karakorum	S1749	55	41	0	2	0	0	3	0	100	6	59	405
Ladakh	S4430	47	50	0	0	0	1	2	0	100	18	68	403
Kohistan	S1439	32	18	0	2	0	0	48	0	100	17	88	320
Swat-Kohistan	S1440	26	47	2	0	0	0	21	3	100	14	82	339
Himalaya	S4419	49	15	0	29	0	1	6	0	100	3	60	356
Nanga Parbat	S1432	67	30	0	0	0	0	3	0	100	18	50	390
Upper Indus	S1447/1455/1461	43	21	1	12	2	7	14	1	100	12	54	281
Lower Indus	S1489	53	17	1	12	1	5	11	0	100	5	54	364
Jhelum	S1449	50	6	3	12	3	10	16	0	100	17	39	216
Chenab	S1450	58	16	0	5	0	8	13	0	100	8	42	261
Ravi	S1451	49	10	1	1	1	17	20	0	100	18	50	198
Sutlej	S1467	59	17	0	8	0	6	9	0	100	7	38	266
Beas	S2284	55	15	4	3	1	3	20	0	100	21	47	164

Table 6.1b. Heavy minerals composition of Thar (Cholistan and Sindh) Desert sand carried by the Indus River and Punjabi tributaries from the different NW Himalayan sources.

River/Desert	Sample	tHMC	ZTR	Ttn	Ep	Grt	SKS	Amp	Cpx	opx	&tHM	total
Thar Sindh West	**Average**	6	1	1	16	16	6	54	3	2	1	100
	Stand Devi	*1*	*1*	*1*	*3*	*0*	*3*	*5*	*2*	*0*	*0*	
Thar Sindh Center	**Average**	5	2	0	15	13	2	59	6	2	1	100
	Stand Devi	*1*	*0*	*1*	*3*	*4*	*2*	*5*	*1*	*1*	*1*	
Thar Sindh South	**Average**	6	3	2	11	13	4	61	4	1	2	100
	Stand Devi	*3*	*3*	*2*	*1*	*4*	*1*	*3*	*1*	*1*	*1*	
Thar Cholistan NE	**Average**	15	3	2	26	9	6	44	4	4	2	100
	Stand Devi	*2*	*1*	*1*	*5*	*4*	*0*	*4*	*1*	*1*	*0*	
Thar Cholistan C	**Average**	10	4	4	29	10	2	46	3	0	1	100
	Stand Devi											
Thar Cholistan SW	**Average**	11	2	2	19	10	6	50	5	2	3	100
	Stand Devi											
Thal	**S1462**	15	2	1	17	12	2	56	5	4	0	100
Karakorum	S1749	2	7	10	11	2	1	67	1	0	0	100
Ladakh	S4430	8	2	2	7	0	0	86	0	1	0	100
Kohistan	S1439	33	0	0	38	0	0	60	1	0	0	100

Swat-Kohistan	S1440	28	1	0	8	0	0	67	8	15	0	100
Himalaya	S4419	5	6	1	12	14	23	31	10	0	4	100
Nanga Parbat	S1432	17	1	0	19	7	0	71	1	0	0	100
Upper Indus	S1447/1455/1461	10	1	2	22	11	3	52	5	3	1	100
Lower Indus	S1489	9	2	1	17	6	3	61	6	2	0	100
Jhelum	S1449	9	4	1	55	30	2	7	1	0	0	100
Chenab	S1450	1	2	0	31	19	16	30	1	0	0	100
Ravi	S1451	1	14	0	42	20	3	18	1	0	0	100
Sutlej	S1467	6	10	0	8	36	15	26	1	1	0	100
Beas	S2284	1	13	1	41	26	4	8	5	0	1	100

Q = quartz; F = feldspars (KF = K-feldspar; P = plagioclase; L = lithic grains (Lvm = volcanic and metavolcanic; Lc = carbonate and metacarbonate; Lh = chert; Lsm = shale, siltstone, slate, and metasiltstone; Lmf = felsic metamorphic; Lmb = metabasite; Lu = ultramafic); HM = heavy minerals; MI* = Metamorphic Index; tHMC = transparent heavy-mineral concentration. ZTR = zircon + tourmaline + rutile; Ttn = titanite; Ep = epidote-group minerals; Grt = garnet; SKS = staurolite + kyanite + sillimanite; Amp = amphibole; Px = pyroxene (Cpx = clinopyroxene; Opx = orthopyroxene, mostly hypersthene); & tHM = other transparent heavy minerals (apatite, chloritoid, Cr-spinel, olivine, prehnite, pumpellyite, brookite, andalusite, barite).

Table 6.2. An average age structure of the zircon U-Pb ages from Sindh and Cholistan, together with the lower Indus and an average of all the Punjabi tributaries.

	Era	**Mioc**	**Oli/Eocen**	**Paleoc**	**Up-C**	**Lw-C**	**J**	**Tr**	**P**	**Neop**	**Mesop**	**Paleop**	**Arc**
	Ages	<25	25-50	50-70	70-99	99-145	145-201	200-252	252-541	541-1000	1000-1600	1600-2500	2500->3200
Cholistan	259	2%	9%	5%	5%	10%	1%	1%	9%	25%	5%	26%	2%
		0%	***0%***	***2%***	***3%***	***1%***	***1%***	***1%***	***4%***	***3%***	***4%***	***8%***	***2%***
Sindh	582	3%	4%	6%	3%	8%	2%	1%	14%	28%	7%	24%	2%
		0%	***1%***	***2%***	***2%***	***3%***	***0%***	***1%***	***2%***	***5%***	***2%***	***4%***	***2%***
Indus River	588	2%	5%	7%	8%	11%	2%	1%	8%	23%	7%	25%	3%
		1%	***3%***	***2%***	***9%***	***7%***	***1%***	***1%***	***2%***	***0%***	***4%***	***18%***	***0%***
Punj Trib	521	0%	1%	1%	1%	1%	0%	0%	20%	32%	8%	33%	4%
		0%	***2%***	***2%***	***1%***	***1%***	***0%***	***1%***	***18%***	***11%***	***4%***	***17%***	***2%***

Table 6.3. The contribution of the heavy minerals into the Indus (Lower and Upper) River and Thar (Cholistan and Sindh) Desert from different NW Himalaya sources.

Sources	**Samples**	**Upper Indus**	**Lower Indus**	**Sindh**	**Cholistan**
Karakorum	S1749	17%	36%	31%	5%

Ladakh	S4430	6%	11%	8%	5%
Kohistan	S1440	27%	25%	26%	25%
Himalaya	S4419	37%	19%	19%	48%
Nanga Parbat	S1432	13%	9%	16%	17%

Table 6.4. Detrital Zircon contribution in percentages in the Thar (Sindh and Cholistan) Desert and Indus River with NW Himalayas and Punjabi tributaries.

Sources	Sindh	TH-10 (7 ka)	KB-40 (14 ka)	Lower Indus	Cholistan	MAROT-6 (7 ka)	MAROT-12 (<49 ka)
Karakorum and Hindu Kush	25%	65%	30%	7%	15%	22%	14%
Nanga Parbat	8%	7%	3%	15%	3%	7%	9%
Kohistan	10%	6%	10%	6%	3%	3%	3%
Ladakh	10%	6%	28%	6%	11%	7%	7%
Sutlej	21%	5%	8%	23%	5%	16%	11%
Beas	8%	6%	8%	6%	15%	19%	29%
Punjab Tributaries	17%	5%	12%	39%	49%	26%	27%
Total Punjab	**47%**	**16%**	**28%**	**67%**	**69%**	**61%**	**67%**

Chapter 7

Major-Trace elements and Rutile geochemistry with Sr-Nd isotopes to manifest the provenance analysis and chemical weathering on Western Thar Desert

Publication (Under Review): Journal of Geophysics Research: Earth Surface

Muhammad Usman, Peter D. Clift, Giovanni Vezzoli, Guido Pastore, Muhammad Jawad Ahmed, Mubashir Ali, Eduardo Garzanti

7.1. Introduction

Landscape evolution is linked to the competing effects of physical erosion and chemical weathering that in turn are controlled by tectonics and climate change (Burbank *et al.*, 2003; Reiners *et al.*, 2003; Riebe *et al.*, 2004; Gabet and Mudd, 2009; Clift *et al.*, 2020). Changing intensities of these processes result in changing sediment compositions that may be preserved in the final depocenter, albeit modulated by buffering between source and sink (Allen, 2008; Clift and Giosan, 2014; Kuehl *et al.*, 2016). Sediments may be stored and then released from flood plains and dryland regions, including deserts that affect the rate and composition of sediment reaching the final depocenter. Changing climate can influence patterns of erosion and in turn the origin of the sediment, which is eventually delivered to the lower reaches of any given catchment (Fryirs, 2013). Depending on the rate of sediment transport, significant amounts of chemical weathering may occur in floodplains on the way between mountain sources and the river mouth and lower reaches (Lupker *et al.*, 2012). Reworking of these weathered flood plain sediments can be important in controlling river sediment composition, as does recycling from desert regions, proximal to the river. Patterns and rates of erosion are also influenced by tectonic processes, rejuvenating, or diminishing source terrains, as well as by climate-modulated surface processes that vary over orbital and shorter timescales ($<10^5$ y) (Clift *et al.*, 2010; Colin *et al.*, 2010; Fildani *et al.*, 2016; Mason *et al.*, 2019). Over Earth's history, changing climate and sediment supply have been responsible for the formation of deserts within drainage basins where they may influence sediment source-to-sink processes (Blum and Törnqvist, 2000). Deserts are preferentially found in mid-latitudes where descending dry air masses (Cronin, 1999; Bostock *et al.*, 2006), result in greater aridity than found in the tropics.

Changes in global climate may enhance the width and location of these mid latitude arid regions. However, it should also be remembered that deserts will preferentially form in the rain shadow areas of tectonically generated mountain ranges. Deserts may accumulate significant volumes of material that can buffer the flux of sediment between mountain sources and their final depocenter.

In this study, we attempt to understand the origin of sediment supply to the Thar Desert of Southwest Asia, and to understand its links with the drainage of the Indus River, and its tributaries that lie immediately to the west of the desert (Fig. 7.1). The semi-arid Thar Desert in the northwestern Indian sub-continent is significantly influenced by the southwest Monsoon system. The sediments of the Thar Desert are largely derived from the western Himalaya, with supply from tributaries flowing from the east, as well as from the Indus mainstream River that brings material from the Karakorum and associated ranges, such as Kohistan and Nanga Parbat (Fig. 7). The Thar Desert comprises sediment dunes that are affected by monsoon winds over a variety of timescales. These same winds bring rain especially focused on the southern flank of the western Himalaya (Bookhagen and Burbank, 2006) from where much of the sediment is supplied. This study addresses the origin of sediments in the modern desert through a series of proxies that attempt to quantify the primary sources to different parts of the desert, as well as to understand the impact of chemical weathering on the composition of sediment now stored in the desert. We use a combination of grain size analysis, bulk sediment major and trace element geochemistry to constrain the origin of the desert sands, and to better understand the processes that have allowed the desert to form. Sr and Nd radiogenic isotopes and single grain rutile trace element analyses were used to further constrain the source of Thar dune sediments.

7.2. Results

7.2.1. Major Elements

There is a wide range of major element compositions in the Thar dune sands. The major oxides analyzed from the Thar Desert sediments are SiO_2 (Sindh 62–72 %; Cholistan 64-71 %), Al_2O_3 (Sindh 5–10 %, Cholistan 9-10 %), Fe_2O_3 (Sindh 5–10 %, Cholistan 9-10 %), MgO (Sindh 5–10 %, Cholistan 9-10 %), CaO (Sindh 9-10 %Cholistan 5–10 %,), Na_2O (Sindh 1–2 %, Cholistan 2-3 %), K_2O (Sindh 1.5-1.8 %, Cholistan 1.6-2.0 %), TiO_2 (Sindh 0.2–0.7 %, Cholistan 0.3-0.6 %), P_2O_5 (Sindh 0.1–0.3 %, Cholistan 0-0.2 %), and MnO (Sindh and Cholistan <0.1 %) (Fig. 7.2). In

general, the sediments from Cholistan contain more SiO_2 and less CaO than those from Sindh. The major element geochemistry of the dune sediments might be expected to correlate with grain size (Tables 7.1 and 7.2). Figure 7.3A shows that in the Sindh Desert the grain size is generally greater than seen in Cholistan, and the SiO_2 contents are mostly lower on average. CaO contents in the Sindh dunes are higher compared to those from Cholistan with a significant range of 9-10 % and 5–10 % respectively. There is a clear positive relationship between mean grain size and CaO content in the desert sands (Fig. 7.3B). Significant differences exist in the distribution of major element oxides between the Cholistan and Sindh deserts.

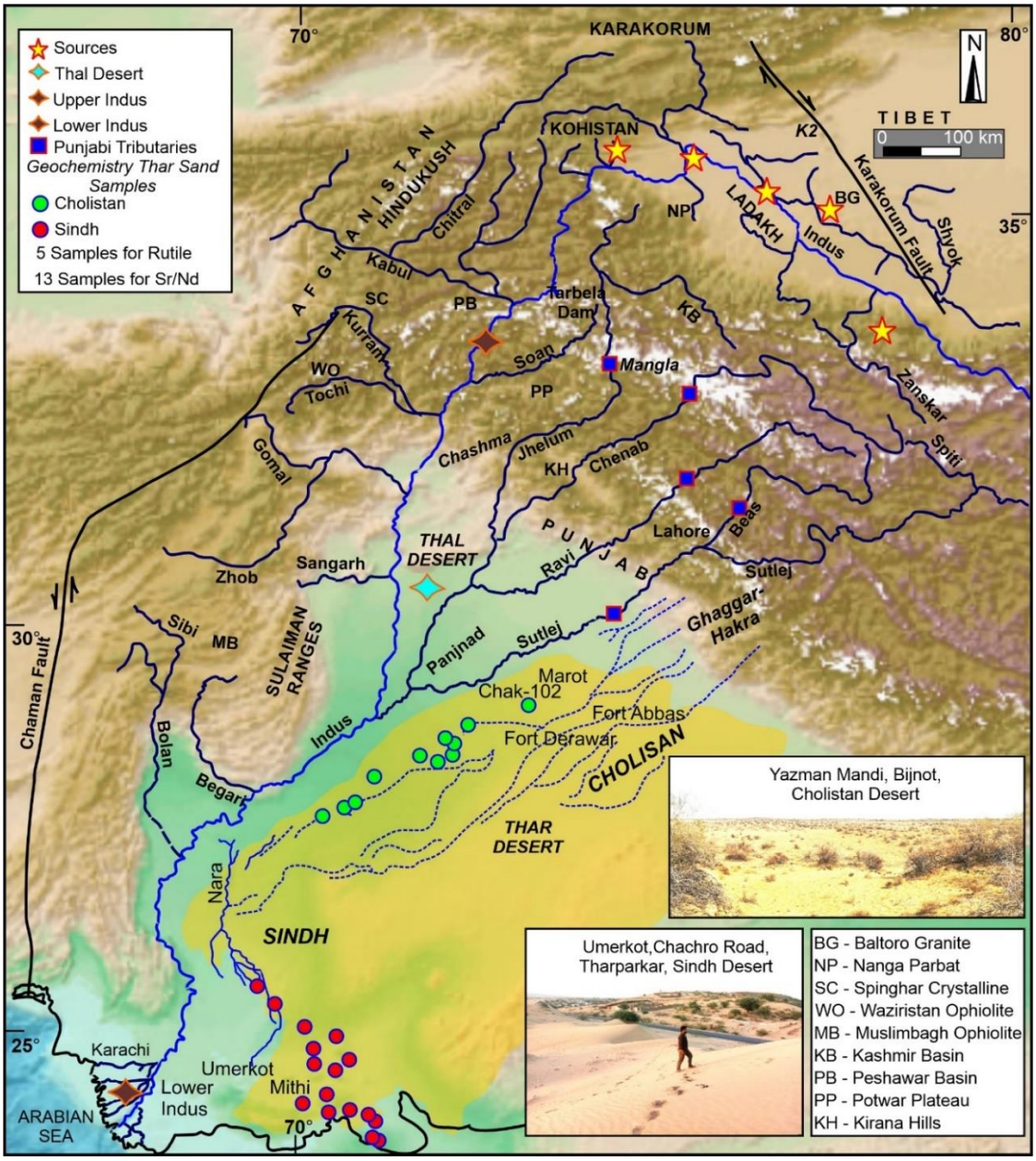

Figure 7.1. Digital Elevation Model (DEM) of Pakistan and adjacent regions (from https://download.gebco.net/). Map shows sampling locations for desert sand and modern rivers.

Note the distribution of the sediments collected during this study in Cholistan and further south in eastern Sindh. Inserted photographs in the map to present the attractive scenecs of the Thar Desert.

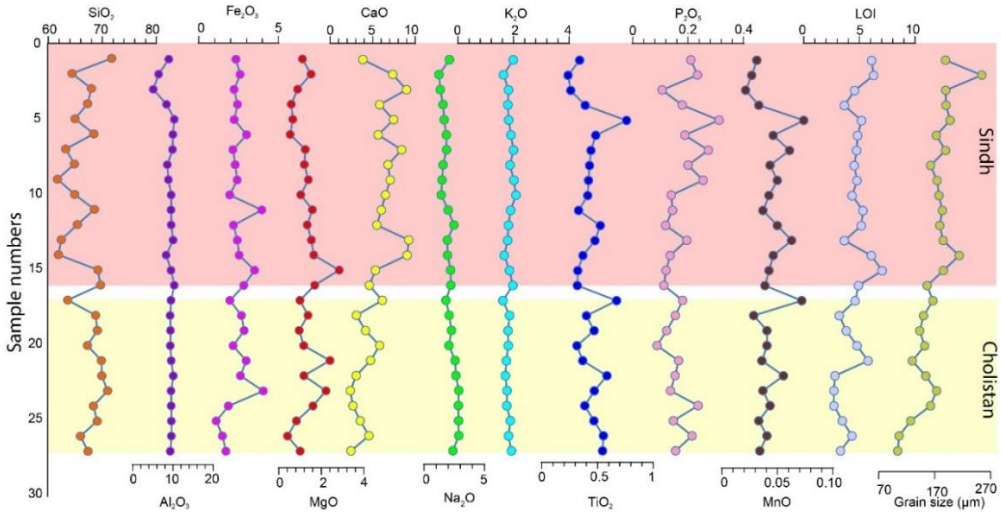

Figure 7.2. Range of major element concentration in the Thar dune sands with Grain Size and LOI.

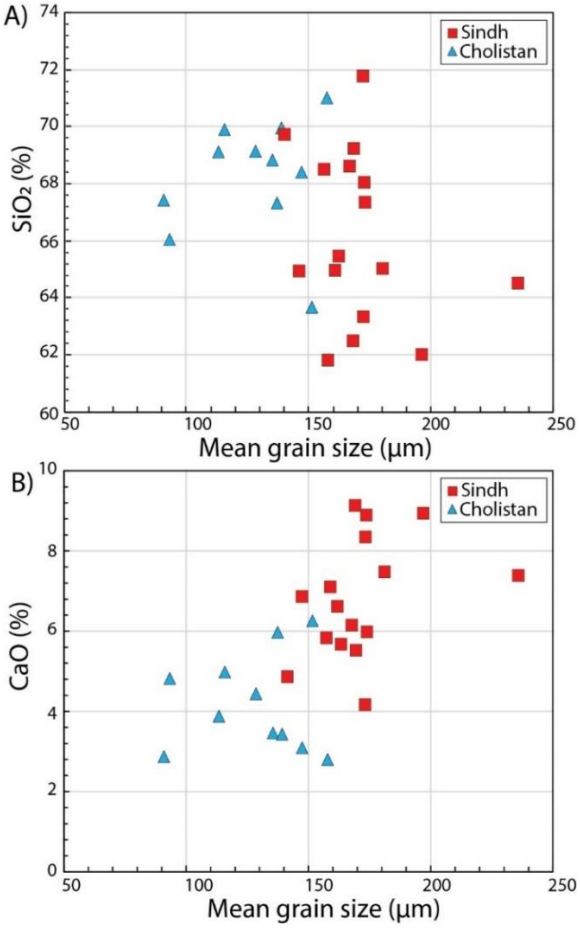

Figure 7.3. Cross plot showing A) SiO_2 versus mean grain size shwoing that the Sindh Desert has coarser sediment but lower SiO_2 content on average, and B) CaO versus mean grain size showing positive correlation and higher CaO contents in Sindh.

Figure 7.4 (A-I) shows the inter-element relationships and correlation trends. SiO_2 and Al_2O_3 exhibit essentially opposing trends and are poorly correlated (Sindh $R^2 = 0.002$; Cholistan $R^2 = 0.49$). Fe_2O_3 (Sindh $R^2 = 0.5375$; Cholistan $R^2 = 0.1516$), CaO (Sindh $R^2 = 0.01249$; Cholistan $R^2 = 0.0289$), MgO (Sindh $R^2 = 0.3425$; Cholistan $R^2 = 0.2122$), Na_2O (Sindh $R^2 = 0.3554$; Cholistan $R^2 = 0.2211$), K_2O (Sindh $R^2 = 0.2118$; Cholistan $R^2 = 0.2016$), Ti_2O (Sindh $R^2 = 0.3504$; Cholistan $R^2 = 0.1885$), P_2O_5 (Sindh $R^2 = 0.0367$; Cholistan $R^2 = 0.0803$) and MnO (Sindh $R^2 = 0.5004$; Cholistan $R^2 = 0.196$) are roughly positively correlated with Al_2O_3, except for CaO, especially in Sindh where there is greater range in Al_2O_3 contents.

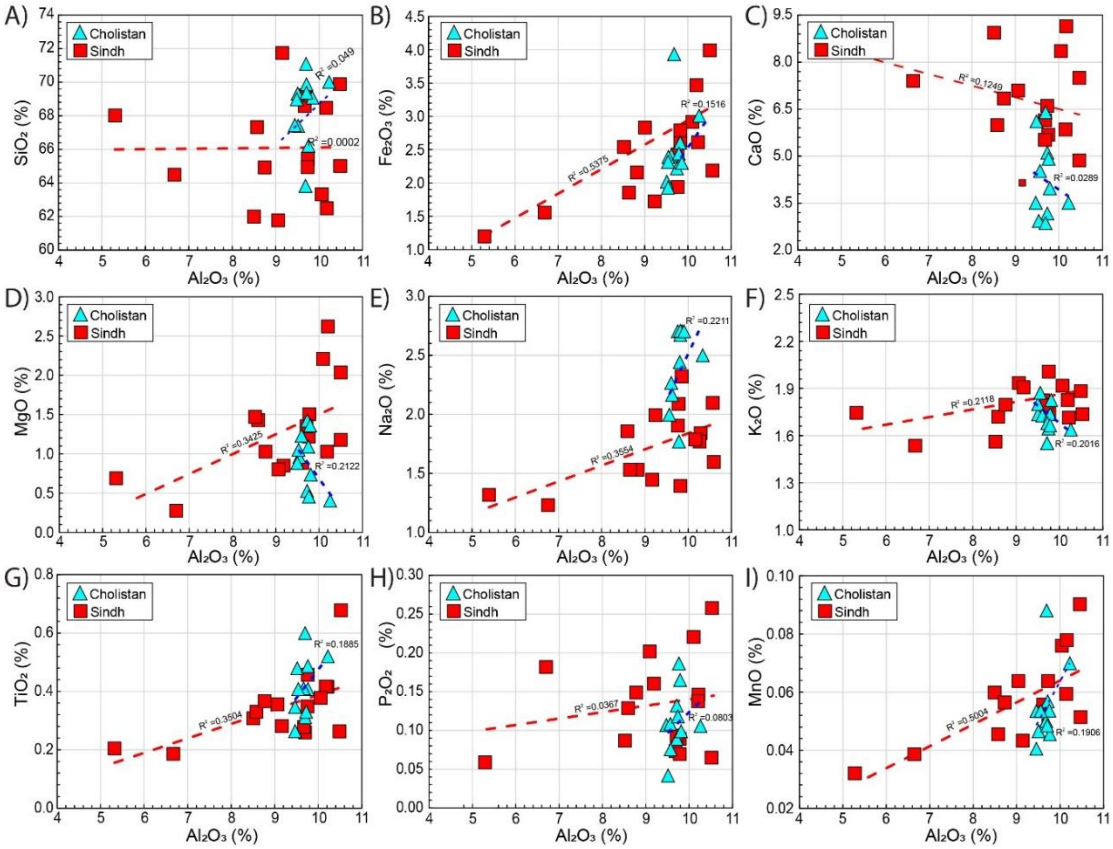

Figure 7.4 (A-I). Crossplots for the major elements of the Sindh and Cholistan desert sands compared to Al_2O_3 content showing the inter-relationship between different elements in each area. Note the greater variability in Sindh.

7.2.2. Trace Elements

The trace element composition of the sediments in both desert regions is quite variable but can be visualized by normalizing these compositions again that of the Upper Continental Crust (UCC). Figure 7.5A shows the range of compositions for Cholistan and Sindh as well as average compositions from the Upper and Lower Indus

River derived from the earlier study by Garzanti *et al.* (2020) (Fig. 7.5B). In general, the sediments from Sindh show relative enrichment in Cr, Nb and Sb. They also show relative depletion in Mo, As, Cu and S. In contrast, sediments from Cholistan show stronger depletion in As, Cu, Mo, as well as La. Both desert regions show some similarity with sediments from the Indus River, although there are significant departures from the general trend in terms of Cd, Sb and Pb (Fig. 7.5A and Table 7.3).

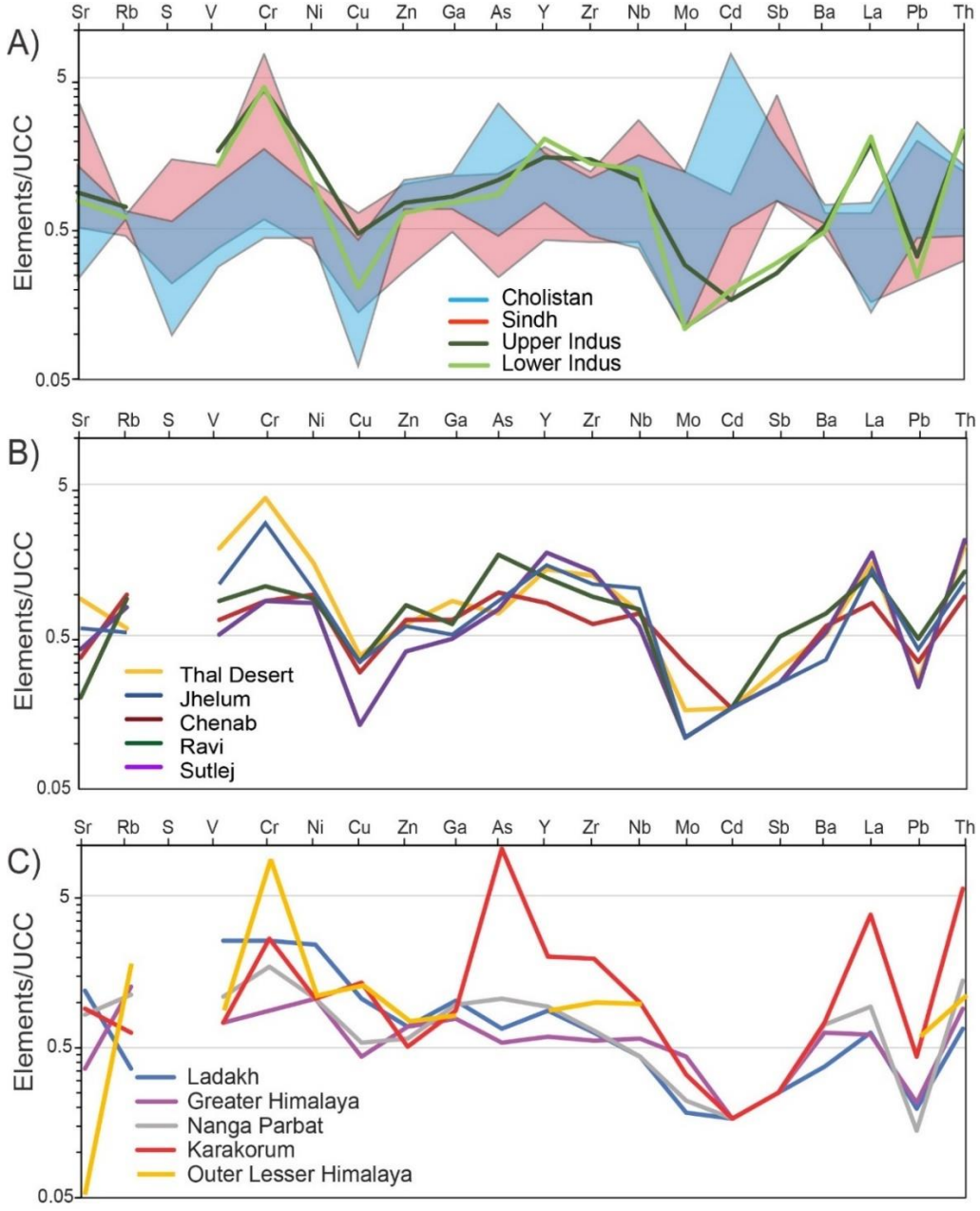

Figure 7.5. The Upper Continental Crust normalized trace element compositions of A) the range of Sindh and Cholistan sands analyzed in this study together with average compositions from the Upper and Lower Indus River. B) Thal Desert sands and the major Punjabi tributaries, and C) major potential source compositions from Garzanti *et al.* (2020).

7.2.3. Sr and Nd Isotopes

In terms of the radiogenic isotope composition, the sediments from the two desert regions considered are shown in Figure 7.6 and Table 7.4. In general sediments from Sindh show higher ε_{Nd} values (-9 to -12) compared to those from Cholistan (-11.76 to 13.98). Sediments from the latter region have slightly higher $^{87}Sr/^{86}Sr$ values. Both desert sediments show higher ε_{Nd} values than sediments previously analyzed from the Holocene Indus Delta (Clift *et al.*, 2010). When compared with potential source regions, we see that the desert sands are similar to those in the recent Indus River and delta in plotting between potential basement end members in the Karakorum, and various Himalayan ranges, suggestive of a mixed source.

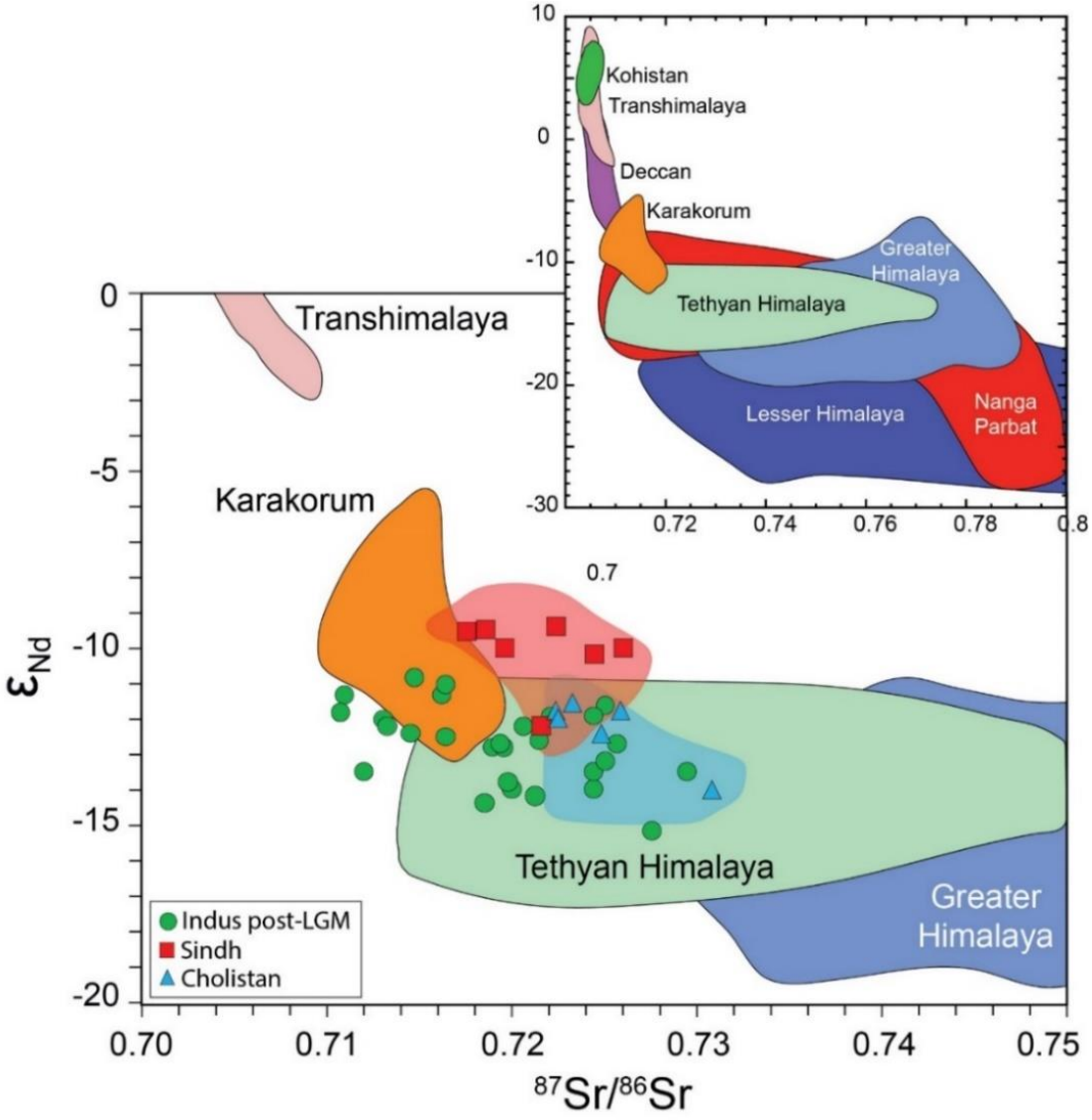

Figure 7.6. Cross plot of Sr and Nd isotope values for the Sindh and Cholistan dunes compared to other sources and the Indus Delta since 15 ka (Clift *et al.*, 2010). Transhimalaya data are from Rolland *et al.* (2002b), Singh *et al.* (2002), and Khan *et al.* (1997). Greater Himalayan

data are from Ahmad *et al.* (2000), Deniel *et al.* (1987), Inger *et al.* (1993) and Parrish and Hodges (1996). Karakorum data are from Crawford and Searle (1992) and Schärer *et al.* (1990).

7.2.4. Rutile Trace Elements

Single grain rutile trace element compositions are relatively similar in both Sindh and Cholistan desert regions (Appendix). The general compositions can be quickly compared by normalizing an average composition for the two desert regions against UCC (Fig. 7.7). The average compositions of rutile grains in both Sindh and Cholistan desert sediments are quite similar and show high relative enrichment in Ti, Cr and Nb, as might be anticipated for this mineral. Grains from Sindh tend to be higher in Mn and Zr and slightly depleted in Sb relative to Cholistan.

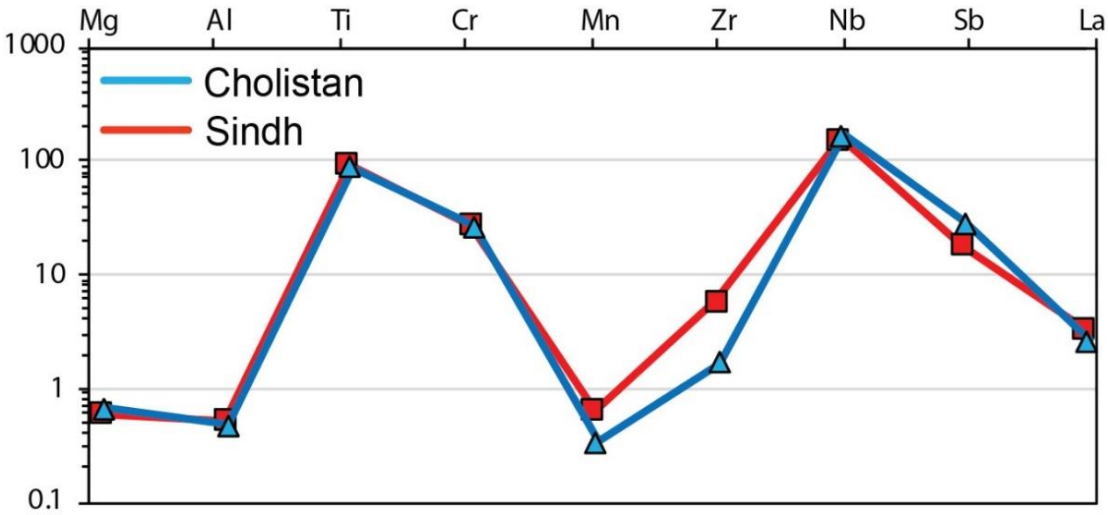

Figure 7.7. The Upper Continental Crust (UCC; Taylor and McLennan, 1995) normalized single grain rutile trace element conversations are relatively similar between both Sindh and Cholistan desert regions.

7.3. Major Element Characteristics

The overall geochemical characteristics of the desert sands can be assessed in relation to their major element compositions and compared with potential source regions. Figure 7.8A shows the range of major element compositions for sediment from both Cholistan and Sindh and compares these with the Indus River after normalizing to the UCC (Taylor and McLennan, 1995). In general, the trend of all the sands is quite similar and relatively close to the UCC, which is not too surprising, given the large extent of the drainage basin and the generally continental character of the lithologies.

The similarity between the sands and the Indus River is noteworthy. In contrast, if we compare the desert sands with the eastern tributaries and the Thal Desert (Fig. 7.8B),

we see some important differences. Many of the eastern tributaries show a low value in CaO, an elevated value in Na_2O and high values in TiO_2 which we do not see in the desert to the same extent. In terms of the major element chemistry, the desert sands look much more like the mainstream of the Indus River, rather than its tributaries. However, we have to exercise caution because major element compositions are dependent, not only on the source composition, but also on hydraulic sorting during sediment transport and we do not consider major element compositions by themselves to be the most reliable provenance proxy. We now consider the degree of alteration of the sediments in the rivers and the deserts in order to compare their extent of chemical weathering. Although this is not dependent on the source, this can also provide some constraints about where the sediment is being derived from (Garzanti and Resentini 2016; Dinis *et al.* 2017). Sediment which has been stored and recycled in floodplains, for instance, has the opportunity to experience much greater degrees of chemical weathering and simple geochemical proxies can be used to identify this recycling process within the overall source-to-sink system.

7.4. Geochemical Indices of Weathering

Different geochemical indices are used to estimate the quantitative degree of rock/sediment alteration and chemical weathering (i.e., Duzgoren-Aydin *et al.*, 2002; Maslov *et al.*, 2003; Price and Velbel, 2003; Yudovich and Ketris, 2011). These indices are calculated as molecular or weight percentages, of various oxides. Because of chemical weathering, more unstable minerals (e.g., K-feldspar and plagioclase) are depleted in Ca^{2+}, K^+ and Na^+ and transformed into minerals that are more stable under surface conditions, i.e., clays. Mafic minerals are even more unstable and breakdown rapidly as they lose Mg. As the intensity of weathering increases, sediments become relatively enriched in Al, Ti, Fe, and Mn (Minyuk *et al.*, 2014).

7.4.1. Chemical Index of Alteration (CIA):

The CIA was defined as follows by Nesbitt and Young (1982) using molecular proportions:

$$CIA = [Al_2O_3 / (Al_2O_3 + CaO + NaO + K_2O)] \times 100$$

with CaO being the amount of CaO incorporated in the silicate fraction of the rock, i.e., not including biogenic carbonate or eroded limestones. The CIA measures the

proportion of Al_2O_3 versus more labile oxides and reflects the relative amount of feldspars and clay minerals in a sample. A CIA value of 50 corresponds to unaltered albite, anorthite, and potassic feldspar. Typical values of the CIA are 30 to 40 for basalt, 45 to 55 for granites and granodiorites, 75 to 85 for illite, 75 for muscovite, and close to 100 for kaolinite and chlorite (Nesbitt and Young, 1982). CIA* is corrected only for phosphate bound CaO according to the formula:

$$CIA^* = [Al_2O_3 / (Al_2O_3 + CaO - 10/3\ P_2O_5 + Na_2O + K_2O)] \times 100$$

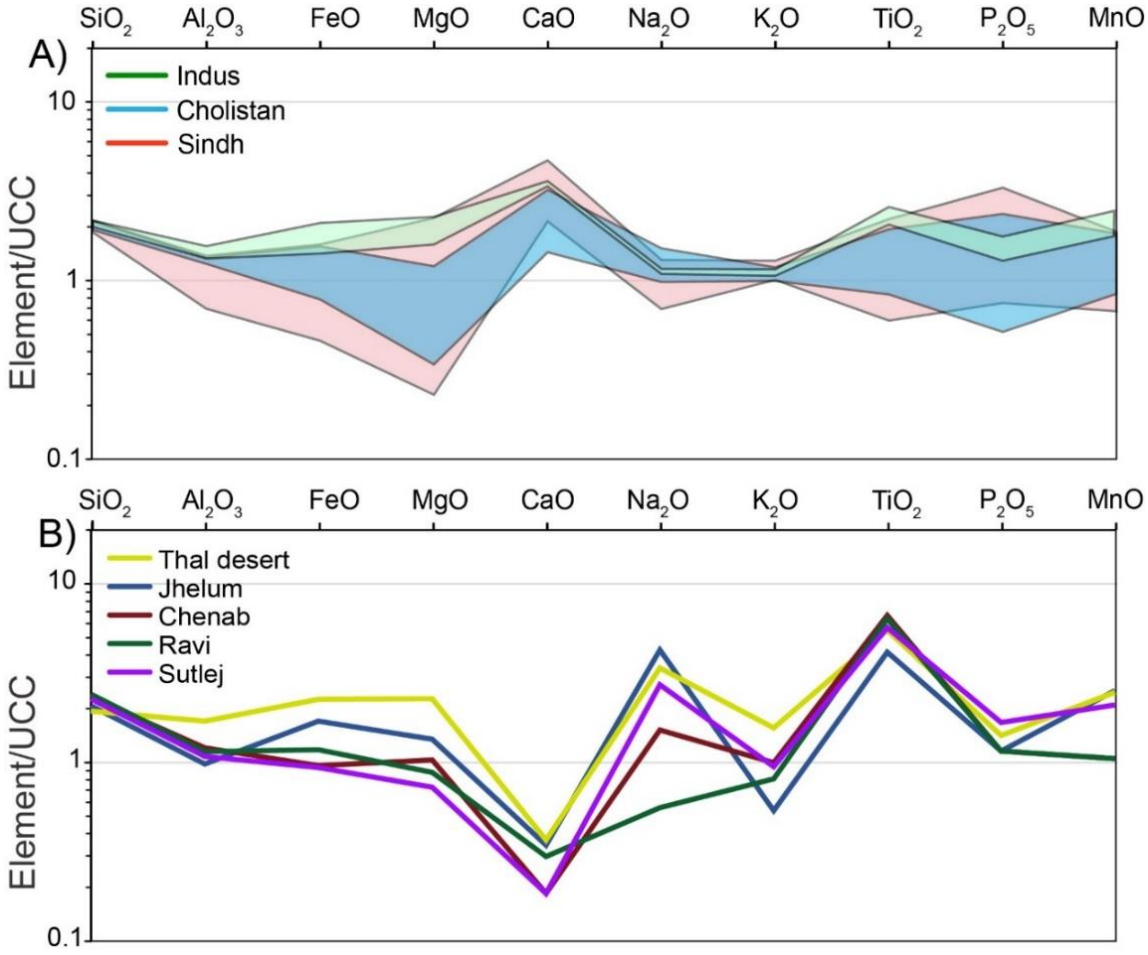

Figure 7.8. The Upper Continental Crust (UCC) normalized major element compositions of A) the range of Sindh and Cholistan sands analyzed in this study together with average compositions from the Upper and Lower Indus River. B) Thal Desert sands and the major Punjabi tributaries from Garzanti *et al.* (2020).

7.4.2. Plagioclase Index of Alteration (PIA)

The PIA proxy estimates the weathering intensity of plagioclase feldspar in the sample (Fedo *et al.*, 1995). PIA is employed when weathering affects sediment eroded from sources with a high level of plagioclase. It is calculated as follows:

$$PIA = [(Al_2O_3 - K_2O) / (Al_2O_3 + CaO + Na_2O + K_2O)] \times 100$$

7.5. Thar Sand Major Elements

7.5.1. Sand Classification and Transportation

The overall geochemical character of the sediments can be assessed using major element discrimination diagrams. The major elemental ratios of log (Na_2O/K_2O) versus log (SiO_2/Al_2O_3) from Pettijohn (1972) are used to assign the sediments to general compositional categories (Fig. 7.9). The sediments from Sindh and Cholistan are largely composed of subarkosic to litharenitic sand, whereas sediments from the Thal Desert and Indus River are mainly litharenitic. The Punjabi tributaries are subarkosic. Sedimentary rocks from the Siwalik Group, which are older foreland basin deposits, are mainly arkose to sub-arkose with minor sublitharenite, and with a much wider range of values than seen in the modern rivers and desert (Vögeli *et al.*, 2017; Exnicios *et al.* 2022).

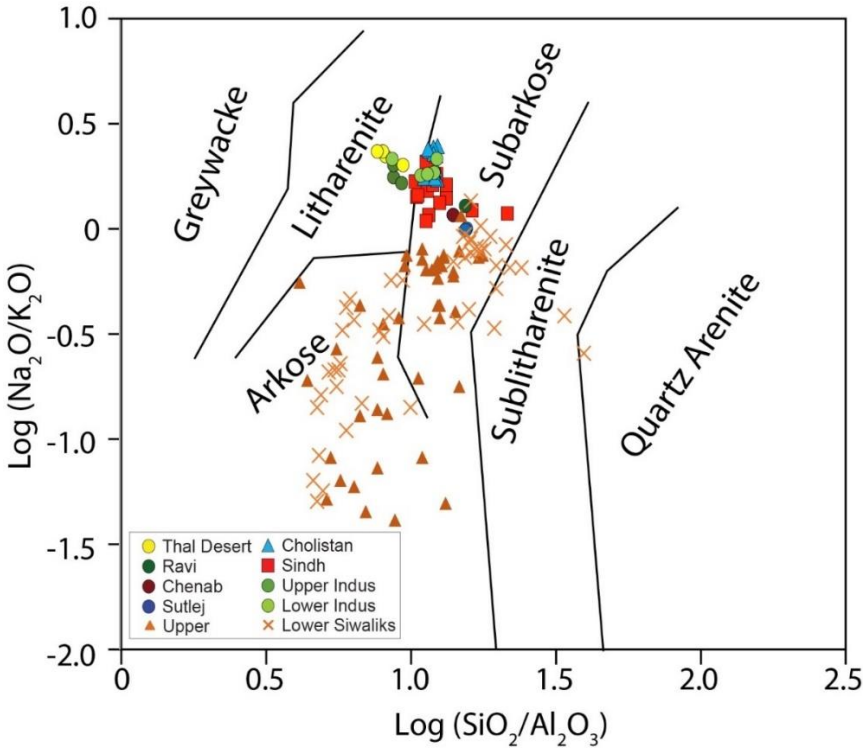

Figure 7.9. Bulk sediment geochemical discrimination diagram from Pettijohn *et al.* (1972). Sindh and Cholistan sands plot largely within the subarkose field. They are compared with data

from the Thal Desert, the Upper Indus, Punjabi tributaries from Garzanti *et al.* (2020), the lower Indus from Clift *et al.* (2010) and the Siwalik Group from Vögeli *et al.* (2017) and Exnicios *et al.* (2022).

The ternary CN-A-K (Ca + Na)-Al-K diagram (Fedo *et al.*, 1995) (Fig. 7.10A) can be used to understand the degree of chemical weathering of the Indus River sediments. There is a wide range of compositions found in the Sindh and Cholistan sediments comparable with other sediments from the Thal Desert, Indus River, and Punjabi tributaries. The desert sediments form an array trending toward the smectite to kaolinite end members in the top left-hand part of the diagram (Fig. 7.10A), indicating progressively more chemical weathering towards these clay minerals. The sediments are generally displaced to the left side of the plot indicating more plagioclase rather than K-feldspar in the sources. The Sindh sediments generally show a higher degree of alteration (Chemical Index of Alteration, CIA*) averaging 54, as compared to sediments in Cholistan (average 50). However, both of sediments are essentially only weakly altered. Sediments from the Punjabi tributaries and the Thal Desert have similar compositions as the Cholistan Desert.

Sediments from the Lower Indus River plot closer to the cluster of data from the Sindh Desert. Data from the Siwalik Group forms a continuation of the general trend in these sediments, but with greater alteration and a modest deviation towards an end member between kaolinite and illite. In contrast, sediments from the Holocene Indus Canyon (Li *et al.*, 2018) and post-glacial Indus Delta (Clift *et al.*, 2010) show more chemical weathering compared to Cholistan and usually more than Sindh, with a trend towards the illite end member. These marine sediments are generally more enriched in K_2O and tend to be finer grained than Thar Desert sediments. However, the sediments from the Indus Delta are often sandy, but also show more alteration than seen in the Thar Desert. To understand the impact of transportation on the sediment compositions, the major elemental ratio Al_2O_3/SiO_2 is plotted vs. Fe_2O_3/SiO_2 and exhibits a wide variation of all the Indus River sediments compared to the average of UCC, which may represent the source bedrock composition (Fig. 7.10B). This is because it might be expected that the sediments from the Sindh, Cholistan, and Thal deserts, as well as from the Punjabi tributaries, Indus River, Indus Canyon, Indus Delta and Siwalik Group were derived from erosion of wide areas of the continental crust. It is interesting to note that the Holocene and Recent sediments are all displaced towards a quartz-rich end member, indicating preferential loss of clay and micas as well as an enrichment in quartz during

transport. Sediments from the Indus delta and some Sindh samples indicate more quartz enrichment. This is not diagnostic of provenance but simply reflects hydrodynamic sorting during transport. The apparent depletion of quartz in many of the Siwalik sedimentary rocks may reflect further alteration during diagenesis as well as changing source compositions.

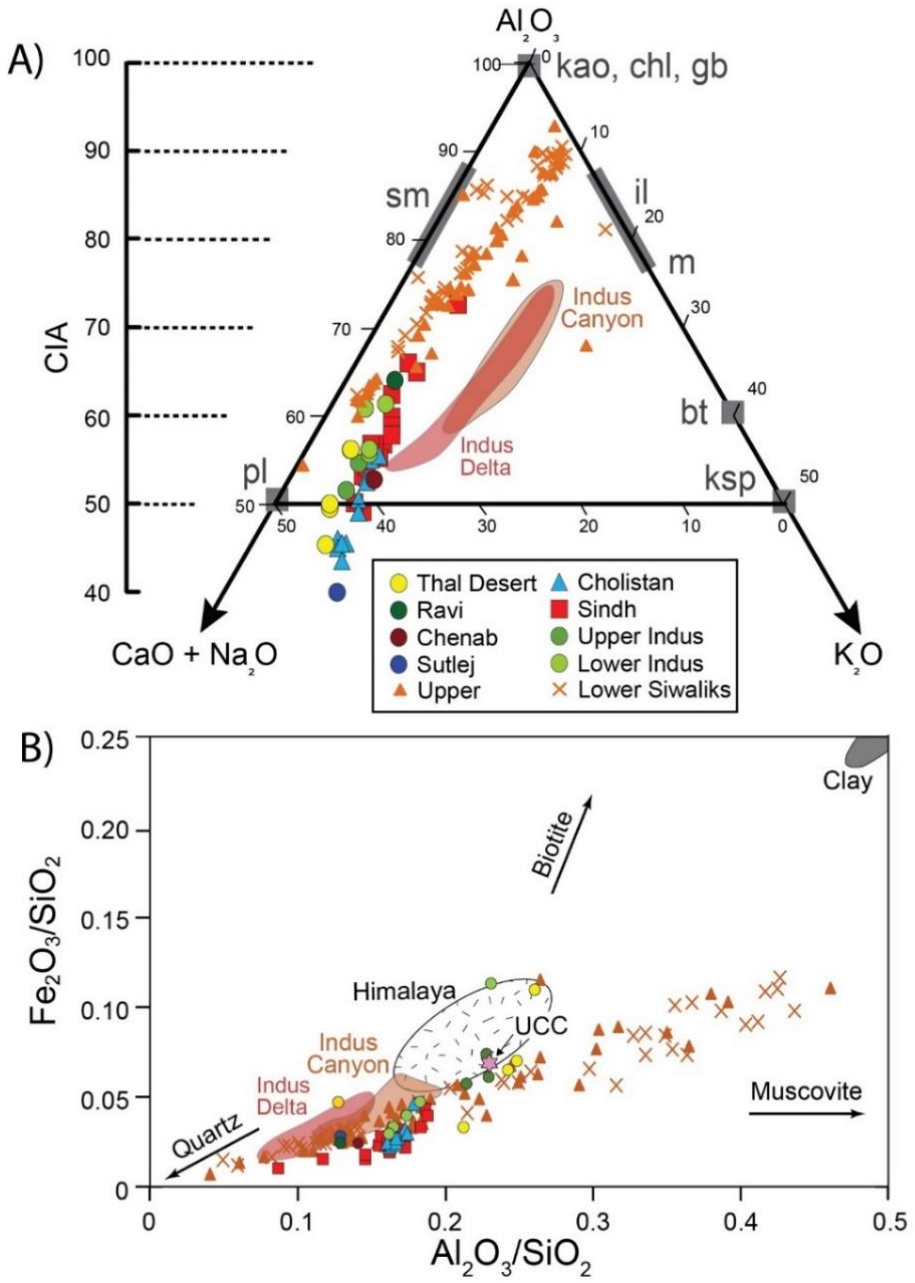

Figure 7.10. A) Geochemical signature of the analyzed samples illustrated by a CN-A-K ternary diagram (Fedo *et al.*, 1995). CN denotes the mole weight of Na_2O and CaO* (CaO* represents the CaO associated with silicate, excluding all the carbonate). A and K indicate the content of Al_2O_3 and K_2O respectively. Samples closer to Al_2O_3 are rich in kaolinite, chlorite and/or gibbsite (represented by Kao, Chl and Gib). CIA values are also calculated and shown

on the left side. Abbreviations: sm (smectite), pl (plagioclase), ksp (K-feldspar), il (illite), m (muscovite). IODP data are compared with Holocene sediments from the Indus Canyon (Li *et al.*, 2018) and onshore delta (Clift *et al.*, 2010). B) Cross plot of Fe_2O_3/SiO_2 versus Al_2O_3/SiO_2 from Singh *et al.* (2005) showing effects of hydrodynamic sorting on an array of sediments from the Indus catchment. Canyon data are from Li *et al.* (2018). Delta data are from Clift *et al.* (2010). Siwalik Group from Vögeli *et al.* (2017) and Exnicios *et al.* (2022). Himalayan field is from Galy and France-Lanord (2001).

7.5.2. Weathering and Major Elements

Various geochemical indices are used as proxies to track weathering intensity (Nesbitt and Young 1982; Price and Velbel 2003) and can be useful for provenance work under certain conditions. However, such proxies are also controlled by grain size (von Eynatten *et al.* 2012, 2016), provenance, hydraulic sorting, or quartz addition by recycling (Figs. 7.11 and 7.12). The Chemical Index of Alteration (CIA*), Mg/Al, K/Al and the Plagioclase Index of Alteration (PIA) proxies are significantly affected by the mineralogy of the sediment sources. The different chemical weathering proxies have different sensitivities to weathering intensity because of the different minerals which affect the values of different elements. We attempt to compare the different weathering processes by cross-plotting data from this study against one another. For example, in Figure 7.11A we show how CIA* compares to Mg/Al, in an attempt to see if these two proxies are closely related to one another. This plot shows a rough negative correlation with sediments that are quite altered in terms of CIA* being relatively unaltered in relation to Mg/Al. This is suggestive of a strong source control over the latter proxy, probably reflecting the Mg-rich mafic sources in Kohistan and the Karakorum. When we consider some of the other proxies, such as PIA, K/Al, and the loss on ignition (LOI), there are several incoherencies. There is a weak correlation between the CIA* and K/Al (Fig. 7.11B), with the Sindh and tributary sediments displaced to higher K/Al values compared with Indus and Cholistan sediments with similar CIA*. This may reflect the influence of K-rich granite sources in the Greater Himalaya. CIA* and PIA show little relationship (Fig. 7.11C). However, the LOI shows a relatively good correlation with CIA*, suggesting that these proxies are controlled by the same processes. Both proxies suggest that the sediments in Cholistan are the least altered, whereas those from the Upper and Lower Indus River are the most altered. Desert sediments from the Sindh dunes lie at intermediate values (Fig. 7.11D). We now explore the relationship between different weathering proxies, such as CIA*, K/Al, K/Rb and

LOI with the mean grain size. It might be expected that finer grained sediments would be more weathered because of the greater surface area to volume in smaller grains. However, Figure 7.12A shows that if anything the coarser sediments have higher values of CIA*, which is the reverse of what might be anticipated, suggesting a significant role for source composition and recycling of sediment in controlling CIA* values. There is no coherent relationship between K/Al and the grain size (Fig. 7.12B).

In contrast, finer grained sediments have lower values of K/Rb (Fig. 7.12C), indicating that this proxy may be sensitive to grain size. Finally, there is no clear relationship between the LOI and grain size (Fig. 7.12D), again implying that grain size is not the dominant control over the intensity of chemical alteration in this system. Considering CIA* and LOI, then we can infer that Sindh sediments are more strongly weathered, despite their coarser grain size, suggestive of recycling from older coarse-grained sediment. This pattern is probably linked to anthropogenic activities (e.g., farming) and more recycling of sediments in the Sindh Desert compared to Cholistan. Only K/Rb indicates that Sindh is less weathered, and we interpret that to mean that K/Rb is more sensitive than the other properties employed in the study.

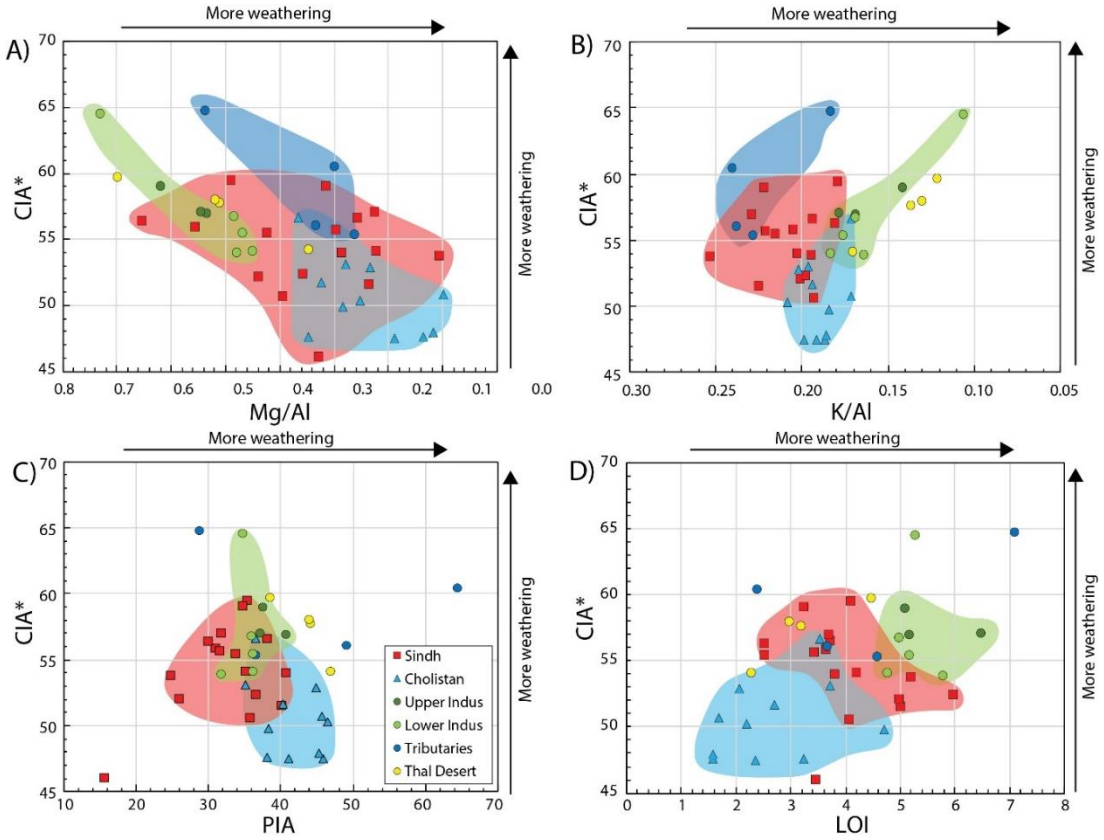

Figure 7.11. Cross plots of geochemical proxies sensitive to chemical weathering. A) Chemical Index of Alteration (CIA*) versus Mg/Al, B) CIA* versus K/Al, C) Plagioclase Index of

Alteration (PIA) versus CIA*, and D) CIA* versus Loss-on-Ignition (LOIs). Sindh and Cholistan data are from this study. Thal Desert, Upper Indus and Punjabi tributary data are from Garzanti *et al.* (2020). Lower Indus data are from Clift *et al.* (2010).

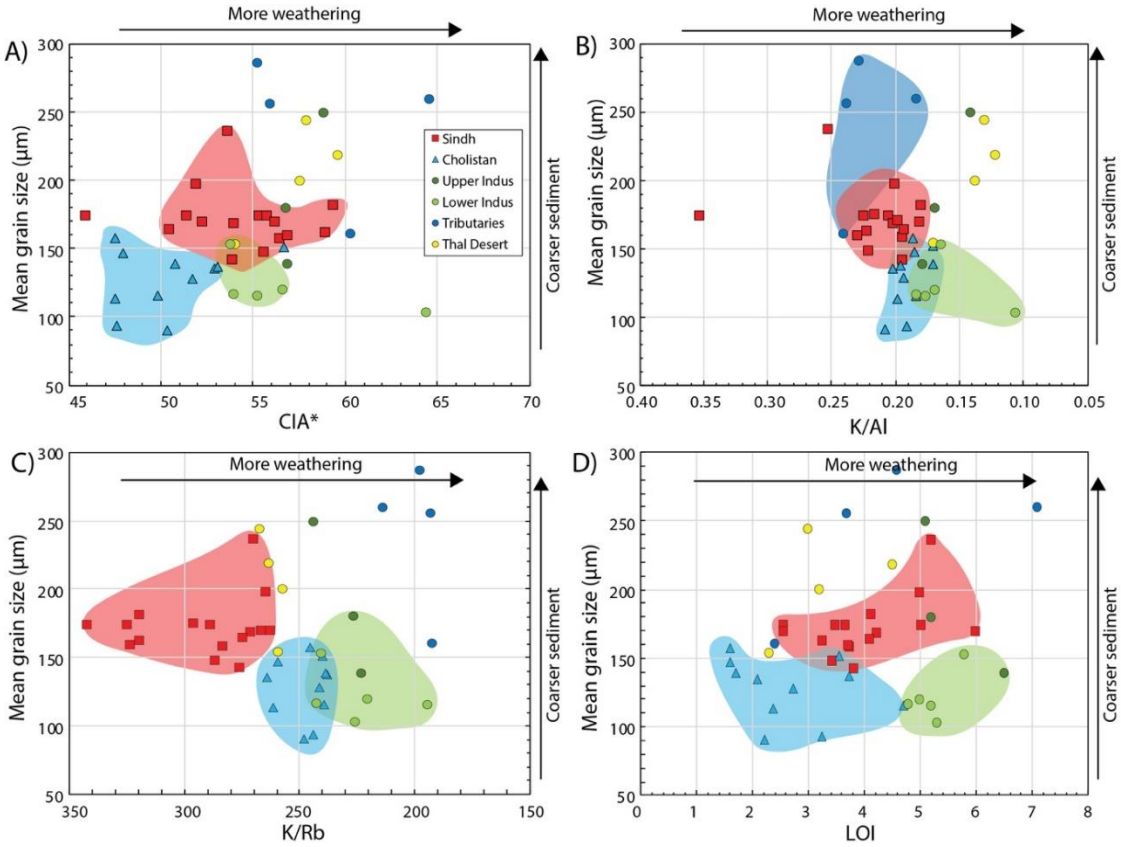

Figure 7.12. Cross plots, showing the relationship between mean grain size and a variety of chemical weathering indices for sediment from both Sindh and Cholistan deserts, as well as Upper and Lower Indus and the major Punjabi tributaries. A) Mean grain size versus CIA*, B) versus K/Al, C) versus K/Rb and D) versus LOI.

We use the Si/Al versus K/Si alteration diagram from Lupker *et al.* (2012) to assess how the sediments in the desert compare with those further downstream in the Indus canyon and delta and that were deposited during the Holocene. This is designed to show the degree of chemical weathering while accounting for grain size variability, which is proxied by Al/Si (Fig. 7.13). All the sediments form a relatively continuous array with the sediments in the desert continuous with those in the canyon and delta. The marine sediments are simply finer grained and further transported. In contrast, the sediments in the Indus River and Thal Desert have lower K/Si values at the same Al/Si values, implying that these are more altered.

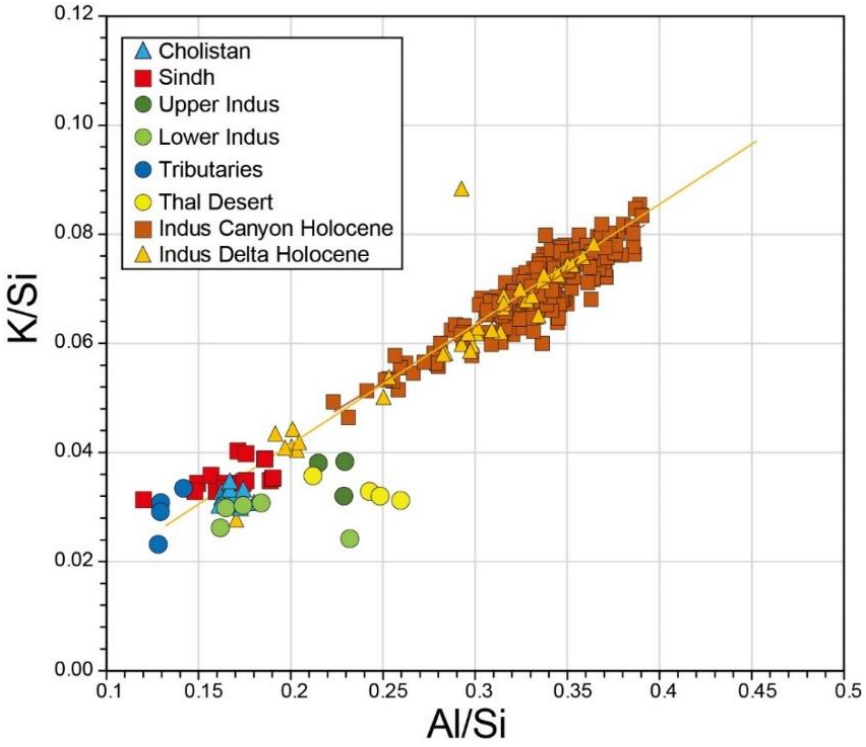

Figure 7.13. Cross plot of K/Si versus Al/Si, for data from the offshore in the submarine canyon and the Holocene Indus delta compared to the desert sands. This plot reveals differences in overall weathering intensity based on the gradient of the array (Lupker *et al.*, 2012). The gradient defined by the offshore fine-grained sediments is consistent with the desert sediments as well as Upper and Lower Indus and the major Punjabi tributaries, indicating that they are part of a coherent sediment grouping. Canyon data are from Li *et al.* (2018). Delta data are from Clift *et al.* (2010).

7.5.3. Mixing Models for Sediment Supply with Major and Trace Elements

The relative contributions from each potential source to the aeolian sand of the Thar Desert can be estimated by forward mixing modelling, following the method of Garzanti *et al.* (2012) and Resentini *et al.* (2017). This is based on the geochemical composition of the end-member sources. The analysis involves calculations that are non-unique and inherently uncertain, being impacted by various uncertainties in the source compositions and dependent on unverified assumptions. The major element composition of desert sediment is also strongly influenced by the fluvial and aeolian processes that transport this material from source to sink.

The end members for the Thar (Sindh and Cholistan) Desert are defined by the bulk geochemistry of the sediments sampled in each region and can be compared with the potential source rock units and the supplying rivers using multidimensional scalar

(MDS) statistics, based on principle component analysis of the combined major and trace element compilation for each source (Fig. 7.14).

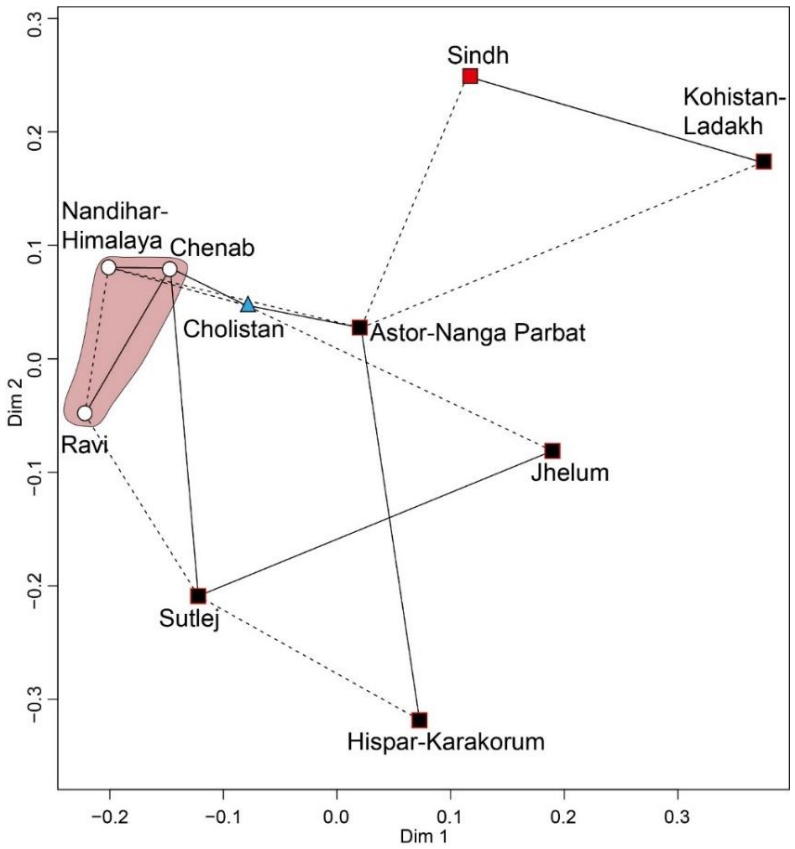

Figure 7.14. Multidimensional scale (MDS) diagram based on principal component analysis for chemical dataset and used to define the best end members for unmixing both Sindh and Cholistan Deserts in order to estimate the relative importance of sediment supply, i.e., the Karakorum, the Jhelum River, the Sutlej River, rivers in Ladakh, and the other Punjabi tributaries and Nandihar from Himalaya units (pink field).

This analysis implies that the Sindh sediments are most closely related to Kohistan and the Ladakh batholith and to a lesser extent the Nanga Parbat Massif. In contrast, the Cholistan sediments plot is closest to Nanga Parbat and to the Himalayan sourced rivers, Nandihar and Chenab. The desert sediments plot far from the Hispar River in the Karakorum. Linear mixing modelling can be used to estimate the relative proportions of sediment derived from different resolvable end members into the mixed sediment. The result of the modelling based on the bulk geochemistry of the desert sands suggests that ~50% of the sediment in the Sindh dunes is from Kohistan-Ladakh, compared to ~38% of the sediment being eroded from the Karakorum, as represented by sediment from the Hispar River. ~12% is supplied by Punjabi tributaries from the Himalaya and ~5% from the Nanga Parbat Massif, as represented by sediment in the

Aster River (Fig. 7.15A). In contrast, sediments for the Cholistan Desert are ~71% derived from Punjabi tributaries (Chenab and Ravi) and eroded from the Himalaya. ~6% of Cholistan sediments are from the Jhelum and Sutlej rivers each, and ~17% are from the Karakorum (Fig. 7.15B).

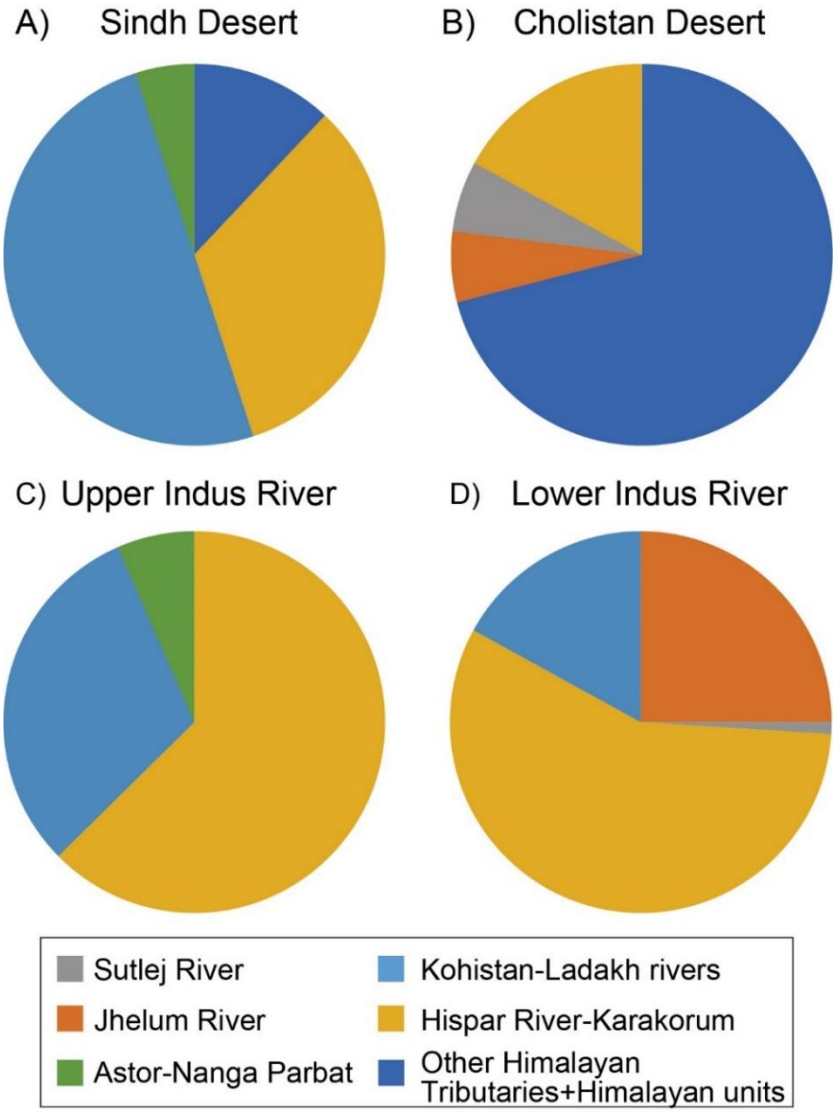

Figure 7.15. Sediments supply from different rock units by various rivers as end members of the NW Himalayas for the Sindh and Cholistan deserts as well as for the Upper and Lower Indus River. Kohistan-Ladakh rivers only drain the batholith (Kandia, Swat and Domkar rivers from Garzanti *et al.* (2020)).

The Upper Indus River is modelled to comprise ~67% of sediment eroded from the Karakorum, with only ~33% of the sediment eroded from the Kohistan-Ladakh arc, and ~7% from the Nanga Parbat Massif (Fig. 7.15C). In contrast, the detrital material in the Lower Indus River contains ~57% of sediment from the Karakorum, ~17% from Kohistan-Ladakh, and ~25% from Jhelum. Just ~1% is modelled to be supplied from

the Sutlej tributary draining the Himalaya (Fig. 7.15D). These estimated percentages need to be treated with caution because the abundance of particular minerals is strongly affected by hydraulic sorting, as well as source fertility. This consideration, together with the fact that many of the minerals are not unique to any particular source region means that this approach is necessarily not yielding unique results in terms of defining provenance.

7.6. Provenance Based on Major and Trace Elements

We now use a series of geochemical discrimination diagrams that have been employed in past studies to resolve competing source contributions in order to constrain where the sediment in the two desert regions has been derived from, as well as comparing them with sediment in the Himalayan tributaries and the mainstream of the Indus River to understand how the river and desert may have interacted with one another in the past. Mafic/ultramafic sediment sources, such as ophiolites and arc terranes, may be differentiated using high MgO and Ni/Al_2O_3 values (Fig. 7.16A) (Amorosi *et al.*, 2007; Greggio *et al.*, 2018; Amorosi *et al.*, 2022). In the cross plot most sediments exhibit a general positive correlation between MgO and Ni/Al_2O_3 values (Fig. 7.16A), reflecting increasing contributions from mafic-ultramafic ophiolite source rocks. In general, the desert sediments have lower values of these elements, compared to the mainstream Indus River, as well as the Thal Desert. If the sediments in the desert are more strongly weathered then chemically unstable, mafic minerals would have broken down and be relatively depleted compared to the rivers. We note that the Sindh sediments tend to be higher in MgO compared to those in Cholistan for the same Ni/Al_2O_3 composition, implying more influence from ultramafic sources in the Sindh Desert. The discrimination diagram plotting Cr/V against Y/Ni (Hiscott, 1988) is also used to constrain the sources of the sediments (Fig. 7.16B). Sindh sediments clearly have higher Cr/V values compared to the other sediments that cluster at the bottom of the plot. The implication of this diagram is that sediments in Sindh may have greater amounts of sediment eroded from ultramafic, ophiolitic sources compared with many of the other sediments in this system. In general, the other sediments show greater influence from granitic sources compared to Sindh. The high Cr/V values above any seen in the source rivers themselves suggests that sediment transport and potentially chemical weathering may be increasing the concentration of chromite in the sediment in Sindh.

The original tectonic setting of the potential source regions can be gauged by trace element discrimination (Bhatia and Crook, 1986) (Fig. 7.16C). This shows that the modern sediments of the Sindh and Cholistan desert mostly belong to the continental to oceanic island arc fields, rather than passive or active margins, implying sources in Kohistan-Ladakh and the Karakorum, which were originally formed in subduction settings. We note that the sediments from the Upper Indus and major tributaries lie outside all the defined fields and represent sediments derived from a complex mixture of sources, rather than a single simple tectonic setting. Nonetheless, we note that in alternative trace element diagrams sands from the Thal and Sindh Deserts, as well as the Upper Indus, also show strong influence from primitive, mafic arc-ophiolite sources (Fig. 7.16D).

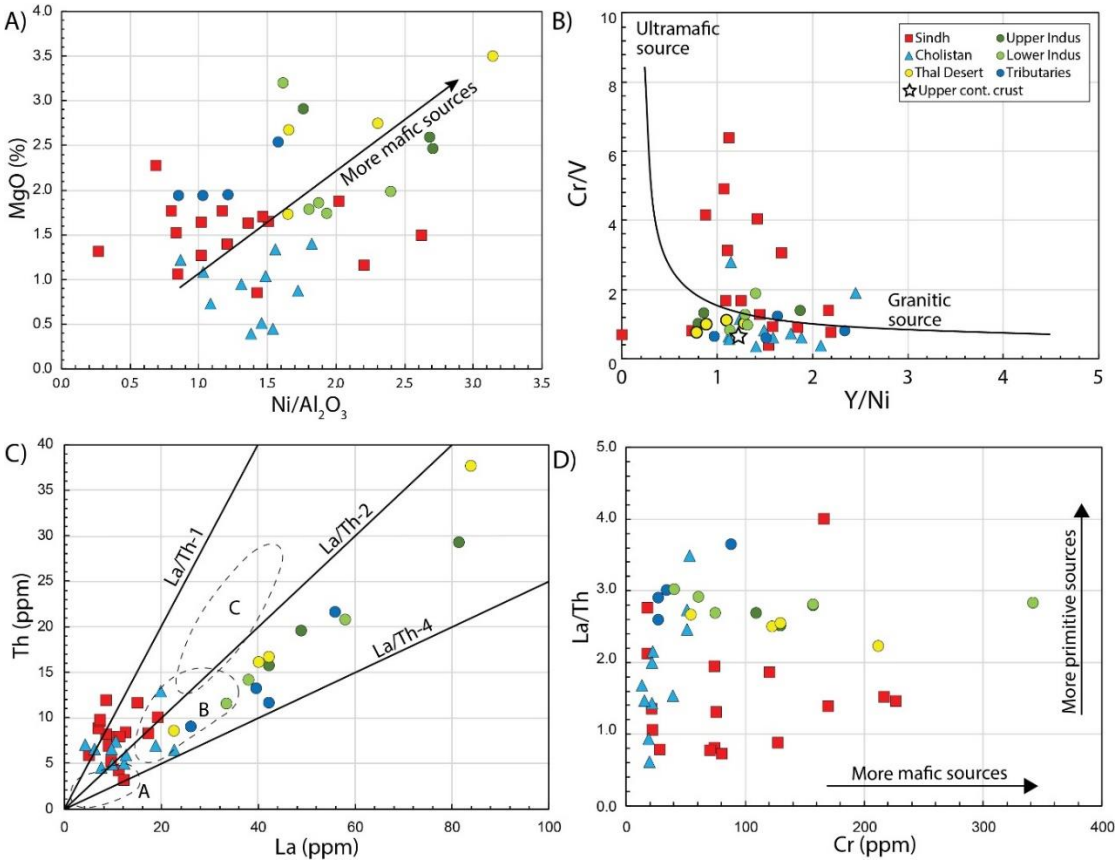

Figure 7.16. A) Cross plot of MgO versus Ni/Al_2O_3 from Amorosi *et al.* (2022) designed to highlight erosion from mafic, ophiolitic sources with high MgO and Ni/Al_2O_3 values. B) Cross plot of Cr/V against Y/Ni from Hiscott (1984) designed to distinguish between Sindh and Cholistan, largely based on the proportion of mafic, primarily ophiolitic sources and those eroded from felsic sources. Sindh desert sand shows a preference for mafic sources. C) Th versus La, with tectonic fields from Bhatia and Crook (1986). A = oceanic island arc, B = continental island arc, C = active or passive margin. D) cross plot of La/Th versus Cr.

7.7. Weathering Patterns in the Western Thar Desert

Trends in geochemical ratios can be used to understand the effects of weathering, recycling, and grain size on geochemistry, especially when compared to the UCC average (Fig. 7.17A). In these discrimination diagrams (Garzanti *et al.*, 2019) the vertical axis shows the total concentration of water-mobile elements (Na, K, Ca and Mg) that are susceptible to chemical weathering, while the horizontal axis plots SiO_2 that is a proxy for the quartz content or Al_2O_3, which is a proxy for clay mineral abundance.

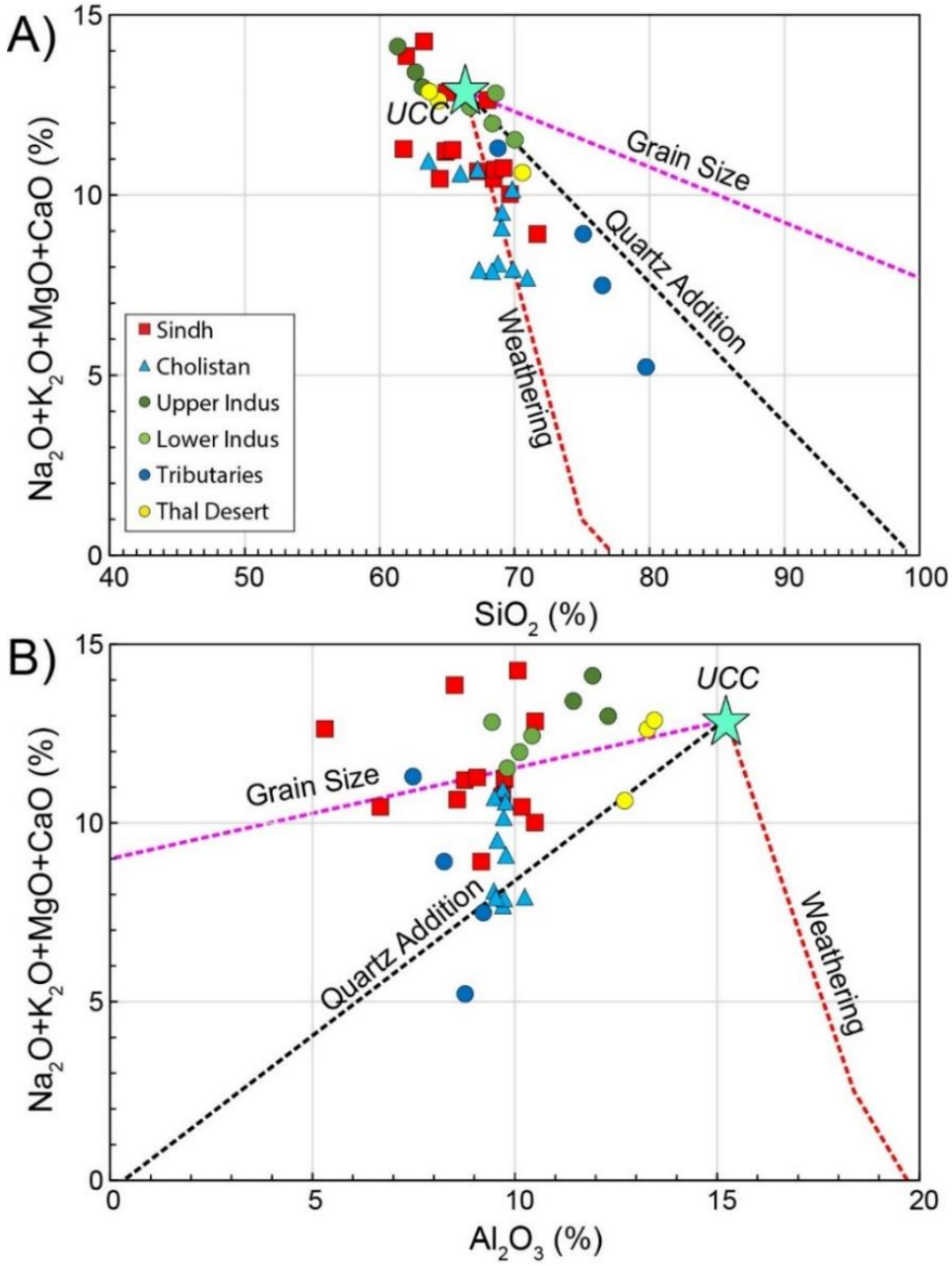

Figure 7.17. Discriminating the effects of weathering, recycling, and grain size on geochemical data. Theoretical trends are calculated starting from the UCC (upper continental crust) standard:

the quartz-addition trend represents progressive addition of SiO_2. The weathering trend shows progressive subtraction of mobile metals relative to Si and Al. The grain-size trend is based on data from Alpine and Himalayan sediments (Garzanti *et al.* 2010a, 2011, 2012). In both panels, samples following the quartz-addition trend, reflect recycling of Sindh and Cholistan sands with Indus River and Thal Desert, as well as with Punjabi Tributaries to various degrees. Coherent trends reflect quartz addition from the Indus River (Upper and Lower) with Punjabi Tributaries to the Sindh and Cholistan deserts.

On Figure 7.17A the quartz-addition trend reflects progressive addition of SiO_2, while the weathering trend is caused by progressive loss of mobile elements relative to Si or Al (Fig. 7.17B). Sand follows the quartz-addition trend, with the Punjabi tributaries probably affected more by the sediment transport than other river or desert sediments, or because the Himalayan sources tend to be more quartz-rich. Figure 7.17A implies a stronger weathering effect in the desert sediments compared to the river sediments, with Cholistan more affected than Sindh. Sediment samples broadly follow the weathering trend. Figure 7.17B also shows a strong quart enrichment in the tributaries but also in Cholistan. This figure shows the dominant effect of grain size on major elements chemistry, rather than weathering, especially with regard to the Sindh Desert and its presumed sources in the Indus River.

7.8. Rutile Geochemistry for Sources

Single grain rutile trace element data can be used for provenance studies by comparison with source rocks (Smith and Perseil, 1997; Rice *et al.*, 1998; Zack *et al.*, 2004a, b; Meinhold *et al.*, 2008, 2010). Al, Cr and Nb elemental contents were analyzed to distinguish various mantle derived source rocks, such as eclogite, metasomatic rutile-dominated nodules compared with crustal sources, including meta-sedimentary rocks (Dawson and Smith, 1977).

7.8.1. Nb–Cr Systematic Content

The Nb and Cr cross relationship for the rutile geochemistry is used to discriminate grains eroded from metabasic/metamafic sources (i.e., eclogites and mafic granulites) and those from metapelites (i.e., mica-schists) paragneisses, and felsic granulites (Zack *et al.*, 2004a, b; Meinhold *et al.*, 2008; Meinhold, 2010). We use the cross plot of Meinhold, (2010) for Nb and Cr applied to detrital rutiles. This plot was derived from the study of amphibolites to resolve those of sedimentary or mafic igneous origins (Fig. 7.18A). The grains from the Sindh and Cholistan deserts show that the analyzed rutile

grains have low Cr and high Nb concentrations in most of the rutile grains, implying that they are derived by erosion of metapelitic source rocks. Those with <800 ppm Nb indicate erosion from metabasites or metamafic sources, which are in the minority.

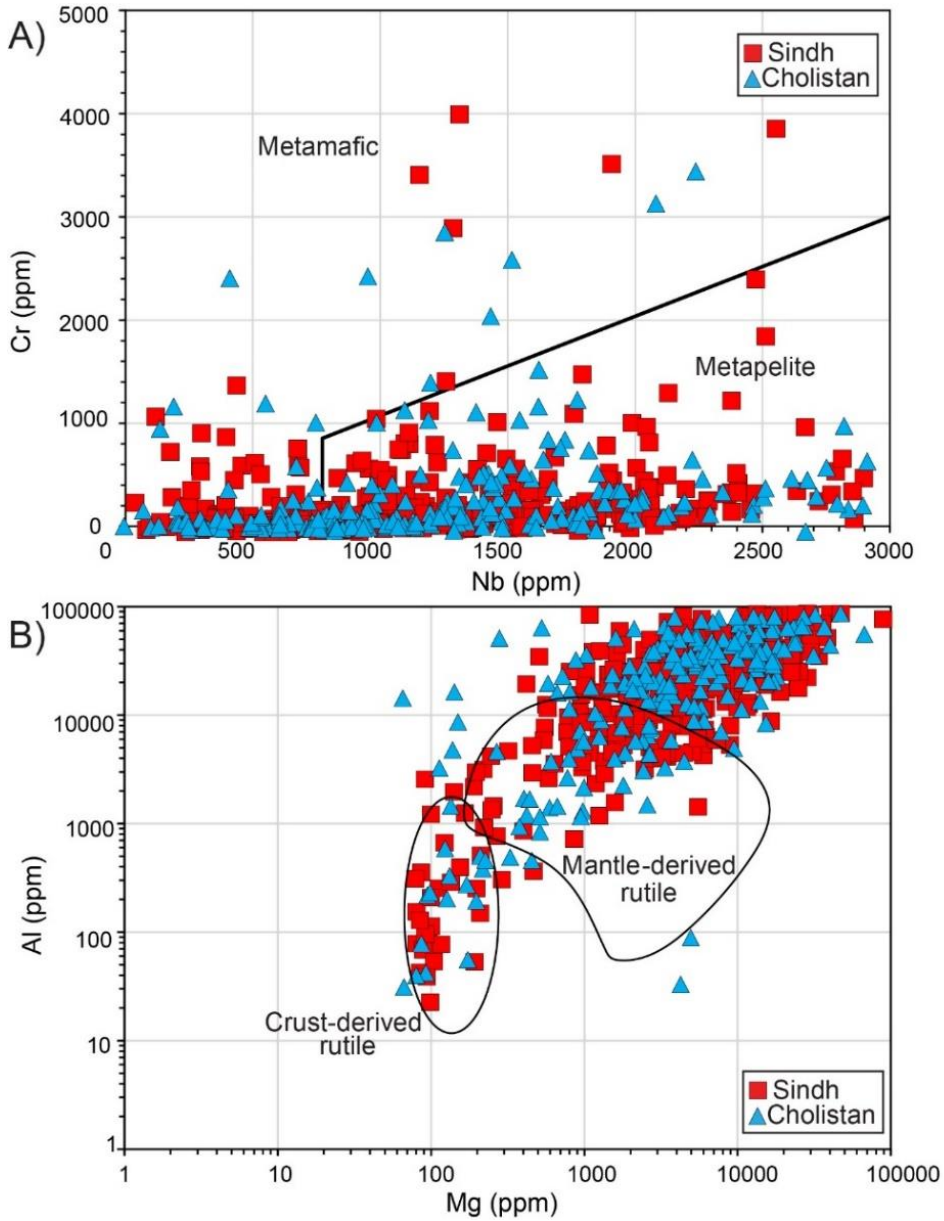

Figure 7.18. Rutile discrimination diagrams based on single grain analyses. A) Cr versus Nb from Meinhold *et al.* (2008), and B) Al versus Mg from Smythe *et al.* (2008).

7.8.2. Mg-Al Systematic Content

Interpretation of the trace Mg and Al contents of single rutile grains are studied to interpret how many of the grains are derived from rocks of crustal or mantle sources (Smythe *et al.*, 2008). Mg is known as the least compatible element in rutile because of its ionic charge to radius ratio (Meinhold, 2010). As a result, Mg-rich rutile is most

likely to be formed in high pressure (HP) and ultra-high pressure (UHP) conditions, commonly in mantle rocks. Rutile grains with high Mg and Al content are often derived from mantle rocks (e.g., diamondiferous eclogite) (Sobolev and Yefimova, 2000). The rutile grains from the Sindh and Cholistan deserts also mostly indicate derivation from mantle rocks because of the high content of Mg and Al (Fig. 7.18B). There are also crust-derived rutile grains in the desert, as indicated by relatively low contents of Mg and Al, although these are in the minority.

7.8.3. Zr Geothermometer in Rutile

Zr contents in rutile were first used by Zack *et al.* (2004a) as a thermometer to estimate the minimum temperature of the source rocks. Zr-in-rutile as a thermometric method was revised by Watson *et al.* (2006) and was constrained for natural rutile based on the following equation:

$$T(℃) = \frac{4470}{7.36 - log10\ (Zr\ ppm)} - 273$$

According to this calculation the Sindh rutile Zr-thermometer shows that most of the grains were eroded from basement heated to a range spanning the greenschist facies (400–550°C; Fig. 7.19B) to the amphibolite facies (550–750°C). Most grains are eroded from source rocks heated between 400 and 700°C, although with a maximum around 500–600°C (Fig. 7.19A). In contrast Cholistan rutiles show a weak bimodal distribution, although with generally a greater percentage of grains from amphibolite grade sources, compared to those seen in Sindh. Also spanning the range between 400 650°C. These can be assigned to two zones, one from 470°C to 550°C (greenschist facies) and a second from 550°C to 600°C (amphibolite facies). The same discrimination diagram suggests that the vast majority of rutile grains in our sediments are derived from pelitic source rocks, rather than mafic ones (Fig. 7.19B). It should be remembered that these grains may not be necessarily eroded directly from metamorphic source rocks, but could be recycled from earlier eroded, sedimentary rocks. There are amphibolite facies potential source rocks, both in the Greater Himalayas, as well as in the Karakorum Likewise, greenschist grade metamorphic rocks are found in many parts of the Himalaya (Lesser and Tethyan), and further north in Kohistan and parts of the Karakorum (Wallis *et al.*, 2014). Consequently, these data do not strongly constrain precisely where within the mountains the desert sediments have been derived.

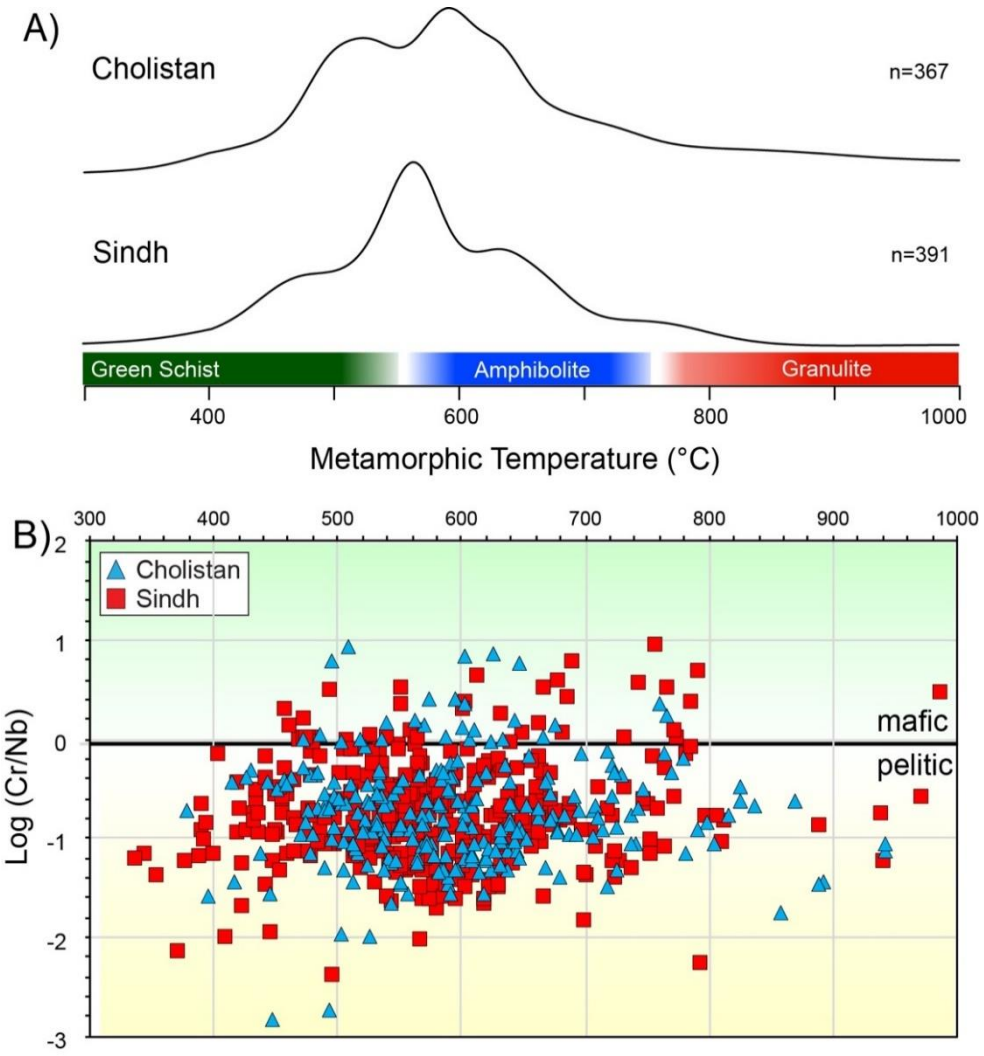

Figure 7.19. (A) KDE diagram showing the distribution of estimated rutile crystallization temperatures for sands from the Sindh and Cholistan deserts, with the range known for greenschist, amphibolite and granulite, (B) Cross plot of Log (Cr/Nb) against temperature from designed to distinguish erosion of rutile largely from pelitic and from mafic rocks (Zack *et al.*, 2004a).

7.9. Sr and Nd Radiogenic Isotope for Provenance

Sindh sand has higher ε_{Nd} values (-9 to -12) compared with samples from Cholistan (-11.76 to 13.98). In general, the sediments from the Sindh desert have higher ε_{Nd} values than those found in Cholistan. Sindh desert sediments have higher ε_{Nd} values than almost any sediments found within the Indus River basin (Fig. 7.20A) and are most similar to the modern mainstream Indus River as sampled where it reaches the flood plains at the Tarbela Dam. In contrast, sediments from Cholistan show significant overlap with analyses from the Indus Delta, that postdate, the Last Glacial Maximum

(LGM), including those in the early and mid-Holocene. The ε_{Nd} values in Cholistan are slightly lower than those found at the glacial (LGM) Indus River mouth (Clift *et al.* 2008). Both the desert sands show very little similarity with the range of ε_{Nd} values measured in sediments found in the Sutlej and Jhelum tributaries (Tripathi *et al.* 2004) and which are sourced from the Himalaya, resulting in relatively negative ε_{Nd} values. Likewise, sediments from the Punjabi floodplains also show significantly more negative ε_{Nd} values than those found in the desert. This comparison suggests that the Himalayan influence over sediment supply to both Cholistan and Sindh deserts is relatively moderate, and that most of the sediment is coming from Indus mainstream River sources. Cholistan sediments may be interpreted as having more influence from the Himalayas than similar sediments in the Sindh desert.

We can compare the isotope ε_{Nd} values in the desert with the various bedrock sources in the hinterland. Both the deserts of Cholistan and Sindh are closest in ε_{Nd} values to those found in the Karakorum. They are generally more positive in ε_{Nd} values compared to Himalayan sources, although with more potential link between the Cholistan desert, and the Himalaya than those seen in Sindh. All of the desert sediments have much lower ε_{Nd} values than those measured from the bedrock in Kohistan and Ladakh, suggesting that these areas are not significant suppliers of sediment to the desert (Fig. 7.20B). Because this is a mixed signal, we cannot definitively say that the Karakorum is the dominant source, only that these data are consistent with this idea. In reality a mixture between Himalayan sources with those in Kohistan/Ladakh could also produce intermediate ε_{Nd} values, although the simplest explanation is a dominant sediment supply from the Karakorum to both deserts.

7.10. Synthesis

We now consider and compare the different lines of evidence presented above in order to narrow down where the sediment in the Thar Desert is coming from. We have already established that the sediments considered in this study tend to be coarser grained when sampled from Sindh compared to those in Cholistan (Fig. 7.4). This may just reflect the chance location of the sampling but might also indicate that Sindh is positioned closer to the source of the sediment, which would imply a derivation from the Indus delta, consistent with earlier work from the detrital U-Pb zircon dating (East *et al.*, 2015).

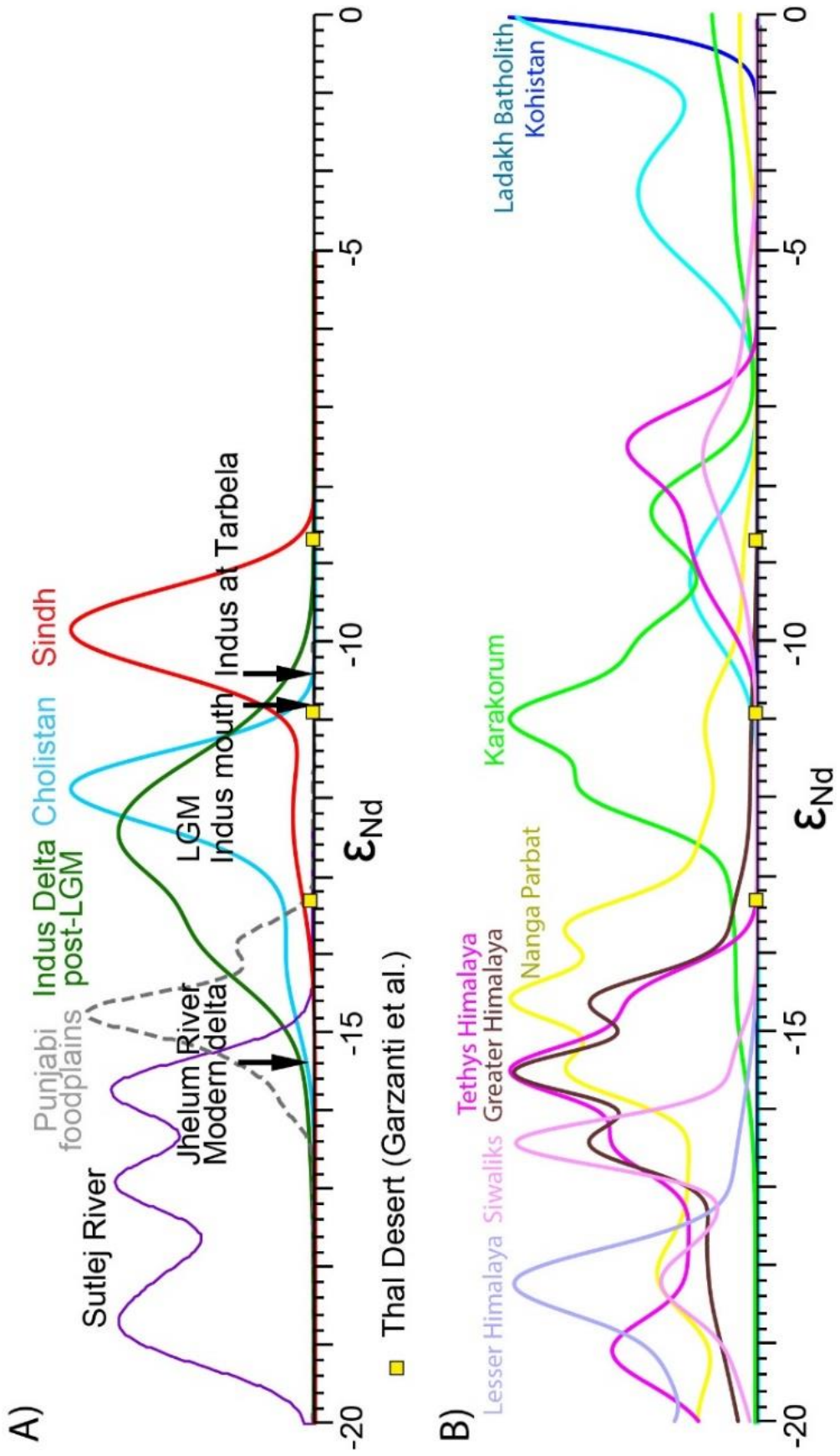

Figure 7.20. A) KDE plot of Nd isotope values for the sand sediments from Sindh and Cholistan, compared with the Sutlej and Jhelum rivers (Clift *et al.*, 2002), the Holocene

sediments of the Punjabi flood plains (Alizai *et al.*, 2011; East *et al.*, 2015), the post-LGM Indus delta (Clift *et al.*, 2008), the Indus mainstream at Tarbela (Garzanti *et al.*, 2020) and the river mouth/delta at the LGM and present day (Clift *et al.*, 2002; Clift *et al.*, 2008). B) Nd isotope values from the various bedrock sources in the headwaters of the Indus catchment. Kohistan data are from Petterson *et al.* (1993), Khan *et al.* (1997), Jagoutz *et al.* (2019). Ladakh batholith data are from Rolland *et al.* (2002a). Karakorum data are from Schärer *et al.* (1990), Crawford and Searle (1992), Mahéo *et al.* (2009) and Jagoutz *et al.* (2019). Nanga Parbat data are from George *et al.* (1993), Gazis *et al.* (1998), Whittington *et al.* (1999), Foster (2000), and Argles *et al.* (2003). Tethys Himalayan data are from Whittington *et al.* (1999), Ahmad *et al.* (2000), Robinson *et al.* (2001). Greater Himalaya data are from Deniel *et al.* (1987), Stern *et al.* (1989), Bouquillon *et al.* (1990), France-Lanord *et al.* (1993), Parrish and Hodges (1996), Ahmad *et al.* (2000), Miller *et al.* (2001), Robinson *et al.* (2001), Martin *et al.* (2005). Lesser Himalaya data are from Bouquillon *et al.* (1990), Parrish and Hodges (1996), Ahmad *et al.* (2000), Robinson *et al.* (2001). Siwalik data are from Huyghe *et al.* (2001) and Chirouze *et al.* (2015).

In general Sindh sediments tend to be richer in Ca which may imply a greater percentage of plagioclase in the source rocks, consistent with erosion from intermediate and lower silica content igneous sources, such as those found in the Karakoram. Sediments from Cholistan are richer in Na, which may indicate a greater percentage of mica and albite-rich plagioclase in their source regions, such as in felsic igneous rocks (Fig. 7.4).

Overall, the two desert sediment sample groups show significant similarity in terms of their bulk trace element composition compared to the Indus River and to each other (Fig. 7.5). A general positive anomaly in La concentrations and a negative anomaly in Pb is similar to characteristics of Karakorum bedrock (Fig. 7.5C). However, in general, the rivers of the Indus basin show significant similarity in terms of their trace element composition, suggesting that this may not be a very good provenance proxy for resolving different sources. When we consider the Nd and Sr isotopes there are strong similarities with the Karakorum (Fig. 7.6), although the desert sediments plot between bedrock values in the Karakorum and the Himalaya, pointing to erosion from both sources in meaningful quantities. Dominant supply of sediment from the Karakorum seems more likely, although there is more influence from the Himalaya in Cholistan (Fig. 7.20).

When we consider the major element composition of the desert sediments, there is great similarity to the Indus. However, the desert sands are depleted in Fe and Mg, but

not in the water-mobile elements, Na and K. Again, it seems unlikely that major element compositions can act as a very effective provenance proxy. The composition of the desert sands shows a slight difference with those in the Indus River, which are classified as being litharenite, whereas the desert sediments show is more subarkose composition (Fig. 7.9), more compositionally mature. Both desert and Indus sediments are different from the old foreland basin sediments preserved in the Siwalik Group, suggestive of a different weathering regime in the geological past and ruling out the Siwaliks as being an important source of sediment to the recent desert. The major element characteristics (Fig. 7.10) show that the sediments in the desert are rather poorly weathered, but they are more weathered and more altered than those found in the Indus River. They are relatively quartz-enriched in both Cholistan and Sindh and depleted in their mica contents. Cholistan is less weathered than the sediments from Sindh when we consider the CIA and loss on ignition (LOI) values (Fig. 7.11). The Sindh desert sediments are similar to, or slightly less weathered than those found in the Indus River. The difference in weathering between the two deserts is indicative of them being supplied by sediment from different sources. Figure 7.12 however indicates that some of this difference may be related to grain size characteristics rather than source compositions. For example, the weathering proxy K/Rb is shown to be grain size sensitive although this helps to resolve between the two deserts, but mainly as a function of the finer grain size found in Cholistan.

When we compare the desert sediments, with those further downstream in the delta and offshore in the Arabian Sea, using K/Si versus Al/Si (Fig. 7.13) this indicates a relatively continuous weathering spectrum, so that sediments from the desert may be considered part of a continuous sediment supply network, only being more sandy than those found in the marine offshore. Attempts to undertake linear mixing modelling yielded results often inconsistent with some of the other proxies. for example, showing strong influence from Kohistan on the Sindh desert which other proxies indicate to be unlikely. The mixing modelling does, however, highlight the stronger degree of Himalayan influence in Cholistan, compared to Sindh (Fig. 7.15). It is noteworthy that this mixing modelling is much more accurate and consistent with other proxies when applied to the Indus River sediment itself, but less so in the desert. Figure 7.16 shows that trace element composition of Sindh sediments favors more erosion for mafic sources compared to those in Cholistan, although both deserts show less mafic influence than noted in the Indus River itself. Potentially sediment in the desert has been

chemically weathered to a greater extent than seen in the Indus, so that the more unstable minerals supplied by the Indus are broken down by the time the sediment reaches the desert.

Cholistan sediments show greater quartz enrichment based on water-mobile element contents (Fig. 7.17). Cholistan sediments are more weathered using this proxy, although this may be reflection of the grain size. When we consider the potential use of rutile trace elements as a providence proxy, this is of limited use. This favors dominant erosion of sediment from metapelitic sources, with only a moderate influence of erosion from mantle rock sources, especially in Cholistan. The rutile data favors most erosion from metamorphic rocks in the greenschist and amphibolite facies, although with more erosion from amphibolite rocks in Cholistan and more greenschist in Sindh (Figs. 7.18 and 7.19). This is consistent with some of the other more distinctive proxies employed in the study in that favor, more erosion from the Himalaya in Cholistan, and a greater emphasis on erosion from the Karakorum in Sindh. Our work suggests that the desert is not perfectly mixed, and that the Himalayan tributaries like the Sutlej are having greater impact on the composition of sediment in the northern part of the Thar desert, whereas the southern part is dominated by sediment supply from the Indus delta, which itself is heavily influenced by sediment supply from the Karakorum (Fig. 7.20).

Conclusions

This study employs major and trace element compositions of sediments in the Thar Desert and compares those with the modern Indus River and its tributaries, in order to understand the origin of the sediment in the desert, and turn, what processes control the growth of the desert through geological time. Major elements are often not very effective provenance proxies because they are often present in similar concentrations in quite different source regions. Major elements are strongly influenced by sediment grain size than by the nature of the bedrock sources from which they were derived. Our work indicates that even when using trace elements consideration of grainsize is important when using such data to constrain the origin of the sediment. There is a general affiliation between sediments in the southern Sindh desert with sediments from the lower Indus and delta, whereas those in the northern part of the desert in Cholistan show similarities with both the Indus River and with its Himalayan tributaries. This comparison is consistent with the much more reliable provenance proxies provided by Sr and Nd isotopes, which are more sensitive to erosion from the Himalaya versus the

Karakorum. Provenance proxies linked to erosion from mafic versus felsic sources are the most useful in resolving between the different sediment sources, with generally more influence from mafic sources in the southern Sindh Desert, reflecting the greater influence from igneous rocks in Kohistan and the Karakorum on the mainstream Indus, compared to its Himalayan tributaries. These are dominated by more felsic continental rocks eroded from the Greater Himalayas. These sources show more influence in Cholistan.

Our work emphasizes the fact that the desert is not homogenous, but it is dominated by supply from the lower Indus River with some influence from the Himalayan tributaries in the north. This is suggestive of most eolian sediment transport being linked to summer monsoon winds that blow sediment from the delta region towards the NE. Although this is unlikely to be constant through geologic time because of the variable strength of the monsoon. Because the desert sediments and the Indus River are relatively similar in major element composition, although with slightly greater degrees of chemical weathering in the desert, it may be difficult to separate the relative influence of sediment in the river from those recycled out of the desert into the Arabian Sea. Major elements do not provide a good test as to whether the desert is acting as a significant sediment buffer to the composition of sediment in the Indus delta. Detrital rutile trace element data is likewise of limited use, although it does demonstrate the importance of metamorphic rocks and particularly those eroded from metapelitic rocks in supplying sediment to the Indus River and turn to the desert. Some sources imply the importance of higher grade, metamorphic rocks and the Karakorum and Greater Himalaya, although some of this may also be recycled. The dissimilarity between the modern river, desert, and ancient foreland sediments in the Siwalik Group, however, implies that any recycling must be relatively short-lived.

Table 7.1. Summary of grain size analysis for the Thar Desert samples presented in this study.

Desert	Site	Sample	Lat	Long	Mean GSZ	Median GSZ	Mean/ Median	Mode	Skewness
Sindh	NE Chotiari	S5986	26.108	69.245	173.13	173.13	1.00	187.50	-0.05
Sindh	NE Khipro	S5990	25.890	69.454	235.79	229.40	1.03	187.50	0.09
Sindh	N Naya Chor	S5996	25.609	69.836	173.64	173.64	1.00	187.50	-0.06
Sindh	Sajan Jo Par	S5998	25.527	70.258	173.95	173.95	1.00	187.50	-0.11
Sindh	Ratnaur Road	S6002	25.397	69.949	181.08	181.08	1.00	187.50	0.03
Sindh	Chhapar	S6006	25.269	70.423	157.34	164.06	0.96	187.50	-0.23
Sindh	Kantio	S6008	25.177	69.971	173.32	173.32	1.00	187.50	-0.08

Sindh	Chachro	S6010	25.117	70.245	147.34	156.42	0.94	187.50	-0.25
Sindh	E Mithi	S6012	24.742	69.813	158.95	163.43	0.97	187.50	-0.23
Sindh	W Arniyaro	S6017	24.836	70.142	161.82	165.77	0.98	187.50	-0.21
Sindh	Khakhanhar Bajeer	S6019	24.645	70.166	167.67	167.67	1.00	187.50	-0.17
Sindh	Ade Ka Tar	S6023	24.666	70.437	163.35	165.41	0.99	187.50	-0.20
Sindh	SE Bhaiwah	S6026	24.603	70.669	169.12	169.12	1.00	187.50	-0.17
Sindh	NW Virawah	S6029	24.528	70.761	196.91	188.82	1.04	187.50	0.15
Sindh	N Sardharo	S6031	24.350	70.736	169.44	171.32	0.99	187.50	-0.04
Sindh	S Ghartiari	S6034	24.306	70.794	141.40	150.41	0.94	187.50	-0.23
Cholistan	Kandera	S6112	28.094	70.073	151.68	159.85	0.95	187.50	-0.26
Cholistan	Monza Lunda	S6117	28.192	70.369	135.49	142.52	0.95	187.50	-0.17
Cholistan	Basti Baloch	S6120	28.269	70.523	128.60	130.55	0.99	187.50	-0.05
Cholistan	Abdullah Wali	S6124	28.568	70.753	137.41	144.56	0.95	187.50	-0.17
Cholistan	Ahmedpur	S6126	28.803	71.337	115.85	110.14	1.05	94.00	0.17
Cholistan	Ahmedpur	S6130	28.751	71.558	139.21	148.43	0.94	187.50	-0.23
Cholistan	Yazman Bijnot	S6133	28.720	71.777	157.84	163.53	0.97	187.50	-0.23
Cholistan	Yazman	S6135	28.834	71.741	147.44	156.70	0.94	187.50	-0.26
Cholistan	Yazman Mandi	S6138	29.000	71.666	113.39	107.12	1.06	94.00	0.20
Cholistan	Kandera	S6140	29.172	71.979	93.33	93.33	1.00	94.00	0.17
Cholistan	Hasilpur	S6142	29.406	72.743	90.95	90.95	1.00	94.00	0.15

Table 7.2. Grain size (µm) Content of major elements (wt%) in the western Thar (Sindh and Cholistan) Desert measured by the X-Ray Florescence (XRF) with different weathering proxies.

Desert	**Samp**	**GSZ**	**SiO_2**	**Al_2O_3**	**Fe_2O_3**	**MgO**	**TiO_2**	**CaO**	**Na_2O**	**K_2O**	**P_2O_5**	**MnO**	**LOI**
Sindh	5986	173	71.7	9.2	1.7	0.8	0.3	4.2	2.0	1.9	0.2	0.0	5
Sindh	5990	236	64.5	6.7	1.5	0.3	0.2	7.4	1.2	1.6	0.2	0.0	5
Sindh	5996	174	68.0	5.3	1.2	0.7	0.2	8.9	1.3	1.7	0.1	0.0	3
Sindh	5998	174	67.3	8.6	1.9	1.4	0.3	6.0	1.5	1.7	0.1	0.0	3
Sindh	6002	181	65.0	10.5	4.0	2.0	0.7	7.5	1.6	1.7	0.3	0.1	4
Sindh	6006	157	68.5	10.2	2.6	1.0	0.4	5.8	1.8	1.8	0.1	0.1	4
Sindh	6008	173	63.3	10.1	3.0	2.2	0.4	8.4	1.8	1.9	0.2	0.1	4
Sindh	6010	147	64.9	8.8	2.2	1.0	0.4	6.9	1.5	1.8	0.1	0.1	3
Sindh	6012	159	61.8	9.1	2.8	0.8	0.4	7.1	1.5	1.9	0.2	0.1	4
Sindh	6017	162	64.9	9.8	2.7	1.2	0.3	6.6	1.4	2.0	0.1	0.1	3
Sindh	6019	168	68.6	9.7	2.0	0.8	0.3	6.2	1.9	1.8	0.1	0.0	4
Sindh	6023	163	65.4	9.8	2.8	1.5	0.5	5.7	2.3	1.7	0.1	0.1	4

Sindh	6026	169	62.5	10.2	3.5	2.6	0.4	9.1	1.9	1.7	0.1	0.1	3
Sindh	6029	197	62.0	8.5	2.5	1.5	0.3	8.9	1.9	1.6	0.1	0.1	5
Sindh	6031	169	69.2	9.7	2.4	1.4	0.3	5.5	2.1	1.8	0.1	0.1	6
Sindh	6034	141	69.7	10.5	2.2	1.2	0.3	4.9	2.1	1.9	0.1	0.1	4
Cholistan	6112	152	63.6	9.7	3.9	1.4	0.6	6.3	1.8	1.5	0.1	0.1	4
Cholistan	6117	135	68.8	9.5	2.0	0.9	0.3	3.5	2.0	1.8	0.1	0.0	2
Cholistan	6120	129	69.1	9.6	2.4	1.2	0.4	4.4	2.2	1.7	0.1	0.1	3
Cholistan	6124	137	67.3	9.5	2.3	1.0	0.3	6.0	2.0	1.7	0.0	0.1	4
Cholistan	6126	116	69.8	9.7	2.2	1.1	0.3	5.0	2.4	1.7	0.1	0.0	5
Cholistan	6130	139	69.9	10.3	3.0	0.4	0.5	3.4	2.5	1.6	0.1	0.1	2
Cholistan	6133	158	71.0	9.7	2.2	0.5	0.4	2.8	2.7	1.7	0.1	0.0	2
Cholistan	6135	147	68.4	9.7	2.4	0.5	0.3	3.1	2.7	1.7	0.2	0.1	2
Cholistan	6138	113	69.1	9.8	2.2	0.7	0.4	3.9	2.7	1.8	0.1	0.0	2
Cholistan	6140	93	66.0	9.8	2.6	1.3	0.5	4.8	2.7	1.7	0.2	0.1	3
Cholistan	6142	91	67.4	9.5	2.4	1.0	0.5	2.9	2.3	1.8	0.1	0.0	2

Table 7.3. Content of trace elements (ppm) in the western Thar (Sindh and Cholistan) Desert measured by the X-Ray Florescence (XRF).

Desert	Samp	Sr	Rb	S	V	Cr	Ni	Zn	Ga	As	Y	Zr	Nb	Sb	Ba	La	Pb	Th
Sindh	5986		59		48	18	10	40	13	3	15	108	8	0	346	11	16	4
Sindh	5990		52		32	22	9	41	12	2		160	34	1	274	9	30	8
Sindh	5996	397	45	397	27	22	12	34	7	3	9	85	8	2	334	9	16	7
Sindh	5998		52		24	19	7	16	8	1	16	132	12	1	359	17	34	8
Sindh	6002	549	49	549	85	76	20	46	13	2	36	244	7	1	324	15	15	12
Sindh	6006	774	58	774	45	75	17	42	14	3	21	126	7	1	334	7	9	9
Sindh	6008	1034	53	1034	58	81	12	36	9	1	25	111	9	1	372	9	11	12
Sindh	6010	1034	56	1034	31	29	11	41	9	3	18	111	8	1	347	8	32	10
Sindh	6012	876	53	876	43	71	16	58	11	4	17	134	12	1	349	8		10
Sindh	6017	451	56	451	59	74	14	42	8	2	20	131	8	1	388	19	10	10

Sindh	6019	188	60	188	39	121	15	37	13	2	16	94	8	1	333	10	15	5
Sindh	6023	157	57	157	42	170	16	33	12	1	23	182	11	1	376	11	24	8
Sindh	6026	262	57	262	71	218	15	44	17	2	25	129	9	1	363	13	4	8
Sindh	6029	169	54	169	26	128	15	36	15	2	16	100	9	1	374	5	26	6
Sindh	6031	246	61	246	36	227	16	38	11	2	18	99	5	1	347	12	16	8
Sindh	6034	204	61	204	40	166	19	30	14	1	16	87	6	1	372	12	25	3
Cholistan	6112	122	58	122	65	40	18	59	13	3	33	223	8	1	418	20	17	13
Cholistan	6117		60		19	52	16	43	13	2	19	92	5	0	389	12	27	5
Cholistan	6120	145	64	145	28	53	8	43	15	2	20	132	7	1	396	23	20	7
Cholistan	6124	168	65	168	44	52	14	40	14	3	17	117	8	1	433	19	14	7
Cholistan	6126	405	62	405	57	22	10	49	14	9	21	156	10	1	426	11	8	7
Cholistan	6130	71	61	71	27	23	14	62	15	12	21	162	13	1	417	13	13	6
Cholistan	6133	79	62	79	34	22	14	41	16	4	16	132	12	0	354	10	30	5
Cholistan	6135	236	58	236	33	19	15	56	18	12	17	123	14	0	399	6	15	7
Cholistan	6138		62		25	15	11	56	11	13	17	135	13	0	408	10	19	7
Cholistan	6140		64		36	14	15	52	18	8	21	213	20	1	394	8	33	5
Cholistan	6142		67		27	20	13	45	13	4	22	162	13	0	336	4	45	7

Table 7.4. $^{87}Sr/^{86}Sr$ and $^{143}Nd/^{144}Nd$ were determined by Thermo "Neptune" multi-collector inductively coupled plasma mass spectrometer (MC-ICP-MS).

Desert	Site	Sample	Latitude	Longitude	$^{87}Sr/^{86}Sr$	$^{143}Nd/^{144}Nd$	eNd
Sindh	NE Chotiari	S5986	26.10780	69.24479	0.71769	0.51215	-9.60
Sindh	N Naya Chor	S5996	25.60942	69.83648	0.72038	0.51212	-10.03
Sindh	Chhapar	S6006	25.26939	70.42267	0.72245	0.51215	-9.52
Sindh	Chachro	S6010	25.11747	70.24490	0.72168	0.51201	-12.21
Sindh	Khakhanhar	S6019	24.64451	70.16614	0.71958	0.51215	-9.60
Sindh	SE Bhaiwah	S6026	24.60269	70.66868	0.72410	0.51212	-10.18
Sindh	S Ghartiari	S6034	24.30586	70.79413	0.72528	0.51212	-10.05
Cholistan	Kandera	S6112	28.09389	70.07278	0.72235	0.51204	-11.76
Cholistan	Basti Baloch	S6120	28.26944	70.52306	0.72593	0.51204	-11.72
Cholistan	Ahmedpur	S6126	28.80250	71.33694	0.72253	0.51202	-11.98
Cholistan	Yazman Bijnot	S6133	28.72028	71.77694	0.72479	0.51200	-12.39
Cholistan	Yazman	S6135	28.83444	71.74056	0.72326	0.51205	-11.55
Cholistan	Hasilpur	S6142	29.40556	72.74278	0.73087	0.51192	-13.99

Chapter 8

Conclusion

Finally, by carefully examining geological and geomorphological elements, this PhD thesis offers a thorough grasp of the sediment dynamics in the Minjiang River and the Thar Desert. Minjiang River is in the centre to southern Longmenshan fault system and inside the tectonically active Songpan Ganzi, the segmented Minjiang River provides an excellent laboratory for research on sediment formation and erosion. K-feldspar and plagioclase content in quartzo-feldspathic sands found in Triassic granites is subequal, it also includes quite very-high-rank metamorphic rock (gneiss, amphibolite) and granitoid rocks. In a weak tHM suite, blue/green hornblende predominates, and zircon grains show a clear Late Triassic peak (32% of ages; mode at 213 Ma). The catchment's northern, middle, and southern regions demonstrate that the Triassic strata are composed of a variety of quartzo-lithic sand compositions. As towards the Paleozoic units have high metamorphic ranks with a variety of lithological and mineral suites. The minerals tourmaline, apatite, amphibole, and zircon have extremely low tHM suites in recycled sands. Silurian unit sand samples from several valleys show litho-quartzose to quartzo-lithic metamorphic sands. Apatite, amphibole, epidote, and tourmaline are among the several tHM suites. The distribution of zircon grains is polymodal, with the majority of the grains being Tonian (30%), followed by subordinate Silurian-Triassic (25%), Orosirian (12%), and Siderian-Neoarchean (9%). There are plenty of metasedimentary rock fragments and uncommon feldspar in the sands draining the Devonian to Lower Triassic successions. A tHM suite with a variety of mineral assemblages is dominated by tourmaline and apatite in the Triassic Strata. Only Shaotanghe River sands with a quartzo-feldspathic composition is originate from the Neoproterozoic granitoid basement setting. This river of the Minjiang is supplying rare apatite, titanite, and zircon are present in this rich tHM suite, which is dominated by amphibole, epidote, and minor clinopyroxene. Tonian ages make up the majority of the zircon-age spectrum (98%, 88% between 800 and 860 Ma), suggesting a predominance of Neoproterozoic beginnings.

The provenance budget study shows the complex contribution of different rock units to sediment supply using geological domains and unique petrographic and heavy-mineral fingerprints. The main source of sand-sized bed sediments, accounting for almost 65% of the Minjiang River catchment, is the basement rocks of the Pengguan

massif (PM) and Baoxing massif (BM). This is evident in the Minjiang River's watershed, especially in the Dixie to Yinxiu catchment, the Triassic, Paleozoic, and basement rock units' varying contributions and rates of erosion are explained by the sediment generation index (SGI). 10% of the region is covered by a basement as granitoid rocks are the primary source of metamorphic grains at the confluence point as metagranitoid rocks, which has an SGI of 6.66, indicating significant sediment generation. SGI values differ, indicating the different responsibilities played by the Paleozoic and Triassic strata, which provide 0.88 and 0.35, respectively. Although the Triassic granite contributes very little to the linear mixing model (0%), it is nevertheless important because it makes up 14% of the catchment area and when the geological background is taken into account, the real contribution is estimated to be between 1 and 2%, with an accompanying SGI of 0.07. The 1,906 km² (8% of the area) of basement rocks greatly increase the amount of sediment yield as 1,679 $tkm^{-2}a^{-1}$ of sediment with an erosion rate of 0.604 mm/a from the southern and central Longmenshan regions. The 9% contribution from Triassic granites results in 38 $tkm^{-2}a^{-1}$ at an erosion rate of 0.014 mm/a. With a 0.075 mm/a erosion rate, the 67% contribution comes from the Triassic strata, which produce 204 $tkm^{-2}a^{-1}$. With a contribution rate of 14%, the Paleozoic strata yield 460 $tkm^{-2}a^{-1}$ at an erosion rate of 0.165 mm/a. Despite being hard rock, basement rocks continue to be the major end component with a high-focused erosion rate, driven by steep slopes and high altitudes. Secondary end members that are impacted by the soft lithological variation of Songpan Ganzi flysch deposits are the Triassic and Paleozoic strata. Because of the strong resistance of nearby rocks and their low altitude, Triassic granites have a less important role. The research delves into the intricate relationships between geological elements that affect sediment output and erosion rates in several sub-catchments, including Shaotanghe, Heishuihe and Zagunaohe rivers. The study also examines how tectonic events, like the Wenchuan earthquake, affect sediment outflow and finds a marked rise in post-seismic activity. The study emphasizes the relationship between changes in sediment and catastrophic occurrences, especially debris flows brought on by regular rainfall. The results highlight the significant impact of major strike-slip faults, tectonic activity, and landslides on the sediment dynamics of the mountainous Minjiang River and its catchment.

Turning our studies towards the Thar Desert, the thesis uses an integrated provenance technique to determine sediment origins. The study illustrates the unique features of the sediments in Sindh and Cholistan desert using bulk petrography, heavy

minerals, and detrital U-Pb zircon dating. Different conclusions are drawn from the provenance methodologies, which highlight the value of all-encompassing strategies. Both the Sindh and the Cholistan sediments are litho-feldspatho-quartoze sands with comparable bulk petrographic features. Metamorphic lithic fragments are the most common type in Cholistan, and they resemble the heavy minerals found in the Punjabi tributaries that drain the Himalaya to the east of the Indus mainstream. On the other hand, the upper Indus River and the heavy minerals found in Sindh dune sands are most similar. When U-Pb detrital zircon grain ages are taken into account, it becomes evident that the zircon grains found in Sindh and Cholistan are primarily derived from the erosion of the Karakorum, the Himalaya, and Nanga Parbat. This suggests aeolian reworking, most likely from the south, as there is no means to directly supply material from the Karakorum and Nanga Parbat to Cholistan. The composition of the desert is influenced by aeolian reworking of material, particularly that originates from the Himalayan orogeny. The Cholistan Desert receives a greater amount of sediment from Punjabi streams, which were formerly eroded from Himalayan bedrock. There is a preference for the Karakorum in Sindh, as well as sediment from Kohistan and Nanga Parbat, as the initial source of the sediment.

Sindh dunes are closest to Indus Delta sediments dated between ~7 and 14 ka, whereas Cholistan dunes are closest to samples from the Marot borehole in Cholistan dated as ~7 and > 49 ka. Which were likely connected to the paleo Ghaggar-Hakra than they do to contemporary tributaries that are located close to the northwest limit of the desert, such as the Sutlej River. These two datasets suggest that before 7 ka, sediment supplied the desert in significant amounts. Here it would have been a period of intense summer monsoon if this construction had taken place during the early Holocene or late pre-Holocene deglaciation. The most likely method of transportation appears to be through aeolian processes during a severe summer monsoon. It's possible that hardly much new sediment has reached the desert since 7 ka, despite the fact that it has moved recently.

Furthermore, an analysis is conducted on the major and trace element compositions in order to comprehend the origin of the desert's sediments and their function in the evolution of geology over time. The study highlights how crucial it is to take grain size into account when analyzing major and trace element data. Sr and Nd isotopes give information on the sediment origins; mafic sources are predominant in the southern Sindh Desert, while felsic sources are found in Cholistan. Grain size in the sediment

has a greater influence on major elements than the makeup of the bedrock sources from which they were extracted. Sediments in the northern section of the Cholistan Desert have similarities with both the Indus River and its Himalayan tributaries, whereas sediments in the southern Sindh Desert are generally affiliated with sediments from the delta and lower Indus. As Sr and Nd isotopes are more vulnerable to erosion from the Himalaya than the Karakorum, they provide far more trustworthy provenance proxies, and our comparison supports that finding.

When attempting to distinguish between the various sediment sources, provenance proxies associated with erosion from mafic versus felsic sources are the most helpful. In general, mafic sources have a greater influence in the southern Sindh Desert than in the Himalayan tributaries of the Indus, indicating the greater influence of igneous rocks in Kohistan and the Karakorum on the mainstream of the Indus. More felsic continental rocks that have been eroded from the Greater Himalayas make up the majority of them. These sources indicate that Cholistan has a greater impact. Our research highlights the fact that the desert is not a homogeneous area but rather is mostly supplied by the lower Indus River, with some effect also coming from the northern Himalayan tributaries. This suggests that summer monsoon winds, which carry sediment from the delta region towards the northeast, are primarily responsible for the majority of eolian sediment movement. Although it does show the significance of metamorphic rocks, especially those eroded from metapelitic rocks, in giving sediment to the Indus River and turning it into the desert, detrital rutile trace element data is likewise not very useful. Although part of this may also be recycled, some sources suggest the significance of the Greater Himalaya, the Karakorum, and higher-grade metamorphic rocks. However, the Siwalik Group's ancient foreland sediments and current river sediments differ enough to suggest that any recycling would have to be quite brief.

The understanding of sediment dynamics in the Minjiang River and the Thar Desert has been greatly advanced by this PhD thesis, to sum up. The results have consequences for investigating natural hazards in tectonically active areas, environmental management, and geomorphological research. In order to further our understanding of the evolution of landscapes and the mechanisms involved in sediment movement, the comprehensive studies and integrated provenance methodologies open up new avenues for future study in comparable geological environments.

References

- Ahmad, F. (2008). Runoff farming in reducing rural poverty in Cholistan Desert. *Sociedade & Natureza, 20*, 177-188.
- Ahmad, F. (2011). Soil classification and micromorphology: A case study of Cholistan Desert. *Journal of Soil Science and Environmental Management, 2*(11), 321-329.
- Ahmad, T., Harris, N., Bickle, M., Chapman, H., Bunbury, J., & Prince, C. (2000). Isotopic constraints on the structural relationships between the Lesser Himalayan Series and the High Himalayan Crystalline Series, Garhwal Himalaya. *Geological Society of America Bulletin, 112*(3), 467-477.
- Akbar, G., Khan, T. N., & Arshad, M. (1996). Cholistan Desert, Pakistan. *Rangelands, 18*, 124-128.
- Akhter, R., & Arshad, M. (2006). Arid rangelands in the Cholistan desert (Pakistan). *Science et changements planétaires/Sécheresse, 17*(1), 210-217.
- Alizai, A., Carter, A., Clift, P. D., VanLaningham, S., Williams, J. C., & Kumar, R. (2011a). Sediment provenance, reworking and transport processes in the Indus River by U–Pb dating of detrital zircon grains. *Global and Planetary Change, 76*(1-2), 33-55.
- Alizai, A., Clift, P. D., Giosan, L., VanLaningham, S., Hinton, R., Tabrez, A. R., ... & Facility, T. E. I. M. (2011b). Pb isotopic variability in the modern-Pleistocene Indus River system measured by ion microprobe in detrital K-feldspar grains. *Geochimica et Cosmochimica Acta, 75*(17), 4771-4795.
- Alizai, A., Clift, P. D., & Still, J. (2016). Indus Basin sediment provenance constrained using garnet geochemistry. *Journal of Asian Earth Sciences, 126*, 29-57.
- Allen, P. A. (2008). Time scales of tectonic landscapes and their sediment routing systems. *Geological Society, London, Special Publications, 296*(1), 7-28.
- Alok, A., Pant, N. C., Das, K., Tsutsumi, Y., Petrie, C. A., Kumar, P., ... & Khan, A. A. (2023). New insights into the geological evolution of palaeorivers and their relationship to the Indus Civilization and Early Historic settlements on the plains of Haryana, NW India. *Geological Society, London, Special Publications, 515*(1), 233-249.
- Amorosi, A., Sammartino, I., Dinelli, E., Campo, B., Guercia, T., Trincardi, F., & Pellegrini, C. (2022). Provenance and sediment dispersal in the Po-Adriatic source-to-sink system unraveled by bulk-sediment geochemistry and its linkage to catchment geology. *Earth-Science Reviews, 234*, 104202. doi:10.1016/j.earscirev.2022.104202.
- Amundson, R., Pendall, E., & Meadow, R. H. (1986). Pedology and Late Quaternary environments surrounding Harappa: a review and synthesis. *Harappa excavations, 1990*, 13-27.

- Argles, T., Foster, G., Whittington, A., Harris, N., & George, M. (2003). Isotope studies reveal a complete Himalayan section in the Nanga Parbat syntaxis. *Geology, 31*(12), 1109-1112.
- Bagnold, R. A. (1946). Motion of waves in shallow water. Interaction between waves and sand bottoms. *Proceedings of the Royal Society of London. Series A. Mathematical and Physical Sciences, 187*(1008), 1-18.
- Basu, A., & Valloni, R. (2003). A perspective on quantitative provenance analysis. In R. Valloni & A. Basu (Eds.), *Quantitative Provenance Studies in Italy* (pp. 11–22). Memorie Descrittive della Carta Geologica dell'Italia, 61.
- Belnap, J., Munson, S. M., & Field, J. P. (2011). Aeolian and fluvial processes in dryland regions: the need for integrated studies. *Ecohydrology, 4*(5), 615-622.
- Bhatia, M. R., & Crook, K. A. W. (1986). Trace element characteristics of graywackes and tectonic setting discrimination of sedimentary basins. *Contributions to Mineralogy and Petrology, 92*(2), 181-193. doi:10.1007/BF00375292.
- Billi, P., D'Agostino, V., Lenzi, M. A., & Marchi, L. (1998). Bedload, slope and channel processes in a high-altitude alpine torrent. In *Gravel-Bed Rivers in the Environment-GBR IV* (Vol. 4, pp. 15-38). Water Resources Pubblications.
- Blinkhorn, J. (2014). Late Middle Palaeolithic surface sites occurring on dated sediment formations in the Thar Desert. *Quaternary International, 350*, 94-104.
- Blinkhorn, J., Achyuthan, H., Jaiswal, M., & Singh, A. K. (2020). The first dated evidence for Middle-Late Pleistocene fluvial activity in the central Thar Desert. *Quaternary Science Reviews, 250*, 106656.
- Blöthe, J. H., & Korup, O. (2013). Millennial lag times in the Himalayan sediment routing system. *Earth and Planetary Science Letters, 382*, 38-46.
- Blum, M. D., & Törnqvist, T. E. (2000). Fluvial responses to climate and sea-level change: a review and look forward. *Sedimentology, 47*, 2-48.
- Bookhagen, B. (2010). Appearance of extreme monsoonal rainfall events and their impact on erosion in the Himalaya. *Geomatics, Natural Hazards and Risk, 1*(1), 37-50.
- Bookhagen, B., & Burbank, D. W. (2006). Topography, relief, and TRMM-derived rainfall variations along the Himalaya. *Geophysical Research Letters, 33*(8).
- Boos, W. R., & Kuang, Z. (2010). Dominant control of the South Asian monsoon by orographic insulation versus plateau heating. *Nature, 463*(7278), 218-222.
- Borromeo, L., Andò, S., Bersani, D., Garzanti, E., Gentile, P., Mantovani, L., & Tribaudino, M. (2022). Detrital orthopyroxene as a tracer of geodynamic setting: A Raman and SEM-EDS provenance study. Chemical Geology, 596, 120809.
- Bostock, H.C., Opdyke, B.N., Gagan, M.K., Kiss, A.E., & Fifield, L.K. (2006). Glacial/interglacial changes in the East Australian current. Climate Dynamics, 26, 645-659.
- Bouquillon, A., France-Lanord, C., Michard, A., Tiercelin, J. (1990). Sedimentology and isotopic chemistry of the Bengal Fan sediments: the denudation of the Himalaya. In: Cochran, J.R., Stow, D.A.V., Auroux, C. (Eds.), Proceedings

of the Ocean Drilling Program, Scientific Results, 116, Ocean Drilling Program, College Station, TX, 43-58.

- Bouvier, A., Vervoort, J.D., & Patchett, P.J. (2008). The Lu–Hf and Sm–Nd isotopic composition of CHUR: constraints from unequilibrated chondrites and implications for the bulk composition of terrestrial planets. Earth and Planetary Science Letters, 273(1-2), 48-57.
- Bracken, L.J., Turnbull, L., Wainwright, J., & Bogaart, P. (2015). Sediment connectivity: a framework for understanding sediment transfer at multiple scales. Earth Surface Processes and Landforms, 40(2), 177-188.
- Bullard, J.E., & Livingstone, I. (2002). Interactions between aeolian and fluvial systems in dryland environments. Area, 34(1), 8-16.
- Bullard, J.E., & McTainsh, G.H. (2003). Aeolian-fluvial interactions in dryland environments: examples, concepts, and Australia case study. Progress in Physical Geography, 27(4), 471-501.
- Burbank, D.W., Beck, R.A., Mulder, T., Yin, A., & Harrison, T.M. (1996). The Himalayan foreland basin. In World and regional geology, 149-190.
- Burbank, D.W., Blythe, A.E., Putkonen, J., Pratt-Sitaula, B.G.A.B.E.T., Gabet, E., Oskin, M., Barros, A., & Ojha, T.P. (2003). Decoupling of erosion and precipitation in the Himalayas. Nature, 426(6967), 652-655.
- Burchfiel, B.C., Chen, Z.L., Liu, Y.P., & Royden L.H. (1995). Tectonics of the Longmen Shan and adjacent regions. International Geology Review, 37(8), 661–735.
- Caley, T., Malaizé, B., Zaragosi, S., Rossignol, L., Bourget, J., Eynaud, F., Martinez, P., Giraudeau, J., Charlier, K., & Ellouz-Zimmermann, N. (2011). New Arabian Sea records help decipher orbital timing of Indo-Asian monsoon. Earth and Planetary Science Letters, 308(3-4), 433-444.
- Chang, E.Z. (2000). Geology and tectonics of the Songpan-Ganzi fold belt, southwestern China. International Geology Review, 42(9), 813-831.
- Chatterjee, A., & Ray, J.S. (2017). Sources and depositional pathways of mid-Holocene sediments in the Great Rann of Kachchh, India: Implications for fluvial scenario during the Harappan Culture. Quaternary International, 443, 177-187.
- Chauhan, S.S. (2003). Desertification control and management of land degradation in the Thar desert of India. Environmentalist, 23, 219-227.
- Chen, S.F., & Wilson, C.J. (1996). Emplacement of the Longmen Shan Thrust—Nappe Belt along the eastern margin of the Tibetan Plateau. Journal of Structural Geology, 18(4), 413-430.
- Chirouze, F., Huyghe, P., Chauvel, C., van der Beek, P., Bernet, M., & Mugnier, J.-L. (2015). Stable Drainage Pattern and Variable Exhumation in the Western Himalaya since the Middle Miocene. *Journal of Geology,
- Clark, P. U., Archer, D., Pollard, D., Blum, J. D., Rial, J. A., Brovkin, V., ... Roy, M. (2006). The middle Pleistocene transition: Characteristics, mechanisms, and implications for long-term changes in atmospheric pCO2. Quaternary Science Reviews, 25(23-24), 3150-3184.

- Clemens, S., Prell, W., Murray, D., Shimmield, G., & Weedon, G. (1991). Forcing mechanisms of the Indian Ocean monsoon. Nature, 353(6346), 720-725.
- Clemens, S. C., & Prell, W. L. (2003). A 350,000 year summer-monsoon multi-proxy stack from the Owen Ridge, Northern Arabian Sea. Marine Geology, 201(1-3), 35-51.
- Clift, P. D., & Jonell, T. N. (2021). Monsoon controls on sediment generation and transport: Mass budget and provenance constraints from the Indus River catchment, delta and submarine fan over tectonic and multimillennial timescales. Earth-Science Reviews, 220, 103682.
- Clift, P. D., Campbell, I. H., Pringle, M. S., Carter, A., Zhang, X., Hodges, K. V., ... Allen, C. M. (2004). Thermochronology of the modern Indus River bedload: New insight into the controls on the marine stratigraphic record. Tectonics, 23(5).
- Clift, P. D., Campbell, I. H., Pringle, M. S., Carter, A., Zhang, X., Hodges, K. V., ... Allen, C. M. (2004). Thermochronology of the modern Indus River bedload: New insight into the control on the marine stratigraphic record. Tectonics, 23(TC5013). doi:10.1029/2003TC001559.
- Clift, P. D., Carter, A., Giosan, L., Durcan, J., Duller, G. A., Macklin, M. G., ... Fuller, D. Q. (2012). U-Pb zircon dating evidence for a Pleistocene Sarasvati River and capture of the Yamuna River. Geology, 40(3), 211-214.
- Clift, P. D., Giosan, L., Blusztajn, J., Campbell, I. H., Allen, C., Pringle, M., ... Carter, A. (2008). Holocene erosion of the Lesser Himalaya triggered by intensified summer monsoon. Geology, 36(1), 79-82.
- Clift, P. D., Giosan, L., Carter, A., Garzanti, E., Galy, V., Tabrez, A. R., ... Allen, C. (2010). Monsoon control over erosion patterns in the western Himalaya: Possible feed-back into the tectonic evolution. Geological Society, London, Special Publications, 342(1), 185-218.
- Clift, P. D., Kulhanek, D. K., Zhou, P., Bowen, M. G., Vincent, S. M., Lyle, M., & Hahn, A. (2020). Chemical weathering and erosion responses to changing monsoon climate in the Late Miocene of Southwest Asia. Geological Magazine, 157(6), 939-955.
- Clift, P. D., Lee, J. I., Hildebrand, P., Shimizu, N., Layne, G. D., Blusztajn, J., ... Khan, A. A. (2002). Nd and Pb isotope variability in the Indus River System: Implications for sediment provenance and crustal heterogeneity in the Western Himalaya. Earth and Planetary Science Letters, 200(1-2), 91-106.
- Clift, P. D., Mark, C., Alizai, A., Khan, H., & Jan, M. Q. (2022). Detrital U–Pb rutile and zircon data show Indus River sediment dominantly eroded from East Karakoram, not Nanga Parbat. Earth and Planetary Science Letters, 600, 117873.
- Clift, P. D., Shimizu, N., Layne, G. D., Blusztajn, J. S., Gaedicke, C., Schluter, H. U., ... Amjad, S. (2001). Development of the Indus Fan and its significance for the erosional history of the Western Himalaya and Karakoram. Geological Society of America Bulletin, 113(8), 1039-1051.

- Colin, C., Siani, G., Sicre, M. A., & Liu, Z. (2010). Impact of the East Asian monsoon rainfall changes on the erosion of the Mekong River basin over the past 25,000 yr. Marine Geology, 271(1-2), 84-92.
- Comas Cufí, M., & Thió i Fernández de Henestrosa, S. (2011, May). CoDaPack 2.0: A stand-alone, multi-platform compositional software. In © International Workshop on Compositional Data Analysis (4th: 2011: Sant Feliu de Guíxols, Girona). CODAWORK 2011: International Workshop on Compositional Data Analysis, held on May 9-13rd, 2011, Sant Feliu de Guíxols, Girona. Universitat Politècnica de Catalunya. Centre Internacional de Mètodes Numèrics en Enginyeria (CIMNE).
- Crawford, M. B., & Searle, M. P. (1992). Field relationships and geochemistry of pre-collisional (India-Asia) granitoid magmatism in the central Karakoram, northern Pakistan. Tectonophysics, 206(1-2), 171-192.
- Critelli, S., & Ingersoll, R. V. (1994). Sandstone petrology and provenance of the Siwalik Group (northwestern Pakistan and western-southeastern Nepal). Journal of Sedimentary Research, 64(4a), 815-823.
- Cronin, T. M. (1999). Principles of paleoclimatology. Columbia University Press.
- Dawson, J. B., & Smith, J. V. (1977). The MARID (mica–amphibole–rutile–ilmenite–diopside) suite of xenoliths in kimberlite. Geochemica et Cosmochimica Acta, 41, 309–323.
- Debon, F., Le Fort, P., Dautel, D., Sonet, J., & Zimmermann, J. L. (1987). Granites of western Karakorum and northern Kohistan (Pakistan): A composite Mid-Cretaceous to upper Cenozoic magmatism. Lithos, 20(1), 19-40.
- Deng, Q., Chen, S., & Zhao, X. (1995). Tectonics, Seismicity, and Dynamics of Longmenshan Mountains and Its Adjacent Regions. In Chinese Science Abstracts Series B (Vol. 3, No. 14, p. 59).
- Deniel, C., Vidal, P., Fernandez, A., Lefort, P., & Peucat, J. J. (1987). Isotopic Study of the Manaslu Granite (Himalaya, Nepal) - Inferences on the Age and Source of Himalayan Leukogranites. Contributions to Mineralogy and Petrology, 96(1), 78-92.
- DePaolo, D. J., & Wasserburg, G. J. (1976). Nd isotopic variations and petrogenetic models. Geophysical Research Letters, 3(5), 249-252.
- Dhir, R. P., & Singhvi, A. K. (2012). The Thar Desert and its antiquity. Current Science, 1001-1008.
- Dhir, R. P., Singhvi, A. K., Andrews, J. E., Kar, A., Sareen, B. K., Tandon, S. K., ... Thomas, J. V. (2010). Multiple episodes of aggradation and calcrete formation in Late Quaternary aeolian sands, Central Thar Desert, Rajasthan, India. Journal of Asian Earth Sciences, 37(1), 10-16.
- Dhir, R. P., Singhvi, A. K., Andrews, J. E., Kar, A., Sareen, B. K., Tandon, S. K., ... Thomas, J. V. (2010). Multiple episodes of aggradation and calcrete formation in Late Quaternary aeolian sands, Central Thar Desert, Rajasthan, India. Journal of Asian Earth Sciences, 37(1), 10-16.
- Dickinson, W. (1997). Panel throws down gauntlet. GSA Today, 7(9), 25.

- Ding Hairong, Li Yong, Yan Liang, Yan Zhaokun, Zhao Guohua, Ma Chao. (2013). Influences of disaster chain driven by Wenchuan earthquake on sediment discharge in upper Minjiang River, Sichuan, China. Journal of Chengdu University of Technology (Science & Technology Edition), 40, 712-720. In Chinese.
- Ding, H., Yuan, Z., Yin, J., Shi, X., & Shi, M. (2023). Evaluating ecosystem stability based on the dynamic time warping algorithm: A case study in the Minjiang river Basin, China. Ecological Indicators, 154, 110501.
- Dong, Y., Zhang, G., Neubauer, F., Liu, X., Genser, J., & Hauzenberger, C. (2011). Tectonic evolution of the Qinling orogen, China: Review and synthesis. J. Asian Earth Sci., 203(1), 692–706. https://doi.org/10.1093/gji/ggv321.
- Draper, N. R., & Smith, H. (1998). Applied regression analysis (Vol. 326). John Wiley & Sons.
- Du, S., Wu, Y., & Tan, L. (2018). Geochemical evidence for the provenance of aeolian deposits in the Qaidam Basin, Tibetan Plateau. Aeolian research, 32, 60-70.
- Durcan, J. A. (2012). Luminescence dating of sediments in Punjab, Pakistan: implications for the collapse of the Harappan Civilisation (Doctoral dissertation, Aberystwyth University).
- Durcan, J. A., Roberts, H. M., Duller, G. A. T., & Alizai, A. H. (2010). Testing the use of range-finder OSL dating to inform field sampling and laboratory processing strategies. Quaternary Geochronology, 5(2-3), 86-90.
- Durcan, J. A., Thomas, D. S., Gupta, S., Pawar, V., Singh, R. N., & Petrie, C. A. (2019). Holocene landscape dynamics in the Ghaggar-Hakra palaeochannel region at the northern edge of the Thar Desert, northwest India. Quaternary International, 501, 317-327.
- East, A. E., Clift, P. D., Carter, A., Alizai, A., & VanLaningham, S. (2015). Fluvial–eolian interactions in sediment routing and sedimentary signal buffering: an example from the Indus Basin and Thar Desert. Journal of Sedimentary Research, 85(6), 715-728.
- Einsele, G., & Hinderer, M. (1998). Quantifying denudation and sediment-accumulation systems (open and closed lakes): basic concepts and first results. Palaeogeogr. Palaeoclimatol. Palaeoecol., 140(1–4), 7–21.
- El-Baz, F. (1983). A geological perspective of the desert. In S. G. Wells & D. R. Haragan (Eds.), Origin and Evolution of Deserts. University of New Mexico Press, Albuquerque, pp. 163–83.
- Exnicios, E. M., Carter, A., Najman, Y., & Clift, P. D. (2022). Late Miocene unroofing of the Inner Lesser Himalaya recorded in the NW Himalaya foreland basin. Basin Research, 34(6), 1894-1916. doi:10.1111/bre.12689.
- Fedo, C. M., Wayne Nesbitt, H., & Young, G. M. (1995). Unraveling the effects of potassium metasomatism in sedimentary rocks and paleosols, with implications for paleoweathering conditions and provenance. Geology, 23(10), 921-924.
- Feller, W. (1948). On the Kolmogorov-Smirnov limit theorems for empirical distributions. Ann. Math. Stat., 19, 177–189.

- Field, J. P., Breshears, D. D., & Whicker, J. J. (2009). Toward a more holistic perspective of soil erosion: why aeolian research needs to explicitly consider fluvial processes and interactions. Aeolian Research, 1(1-2), 9-17.
- Fielding, L., Najman, Y., Millar, I., Butterworth, P., Garzanti, E., Vezzoli, G., Barfod, D. N., & Kneller, B. (2018). The initiation and evolution of the River Nile. Earth Planet. Sci. Lett., 489, 166–178.
- Fildani, A., McKay, M.P., Stockli, D., Clark, J., Dykstra, M.L., Stockli, L. and Hessler, A.M., (2016). The ancestral Mississippi drainage archived in the late Wisconsin Mississippi deep-sea fan. Geology, 44(6), 479-482.
- Flint, J.J. (1974). Stream gradient as a function of order, magnitude, and discharge. Water Resources Research, 10(5), 969-973.
- Folk, R.L., & Ward, W.C. (1957). Brazos River bar [Texas]; a study in the significance of grain size parameters. Journal of sedimentary research, 27(1), 3-26.
- Foster, G.L. (2000). The pre-Neogene thermal history of the Nanga Parbat Haramosh Massif and the NW Himalaya. The Open University.
- France-Lanord, C., Derry, L., & Michard, A. (1993). Evolution of the Himalaya since Miocene time: Isotopic and sedimentologic evidence from the Bengal Fan. In P.J. Treloar & M.P. Searle (Eds.), Himalayan Tectonics (Special Publications, 74, Geological Society, London, pp. 603–621).
- Fryirs, K. (2013). (Dis) Connectivity in catchment sediment cascades: a fresh look at the sediment delivery problem. Earth Surface Processes and Landforms, 38(1), 30-46.
- Gabet, E.J., & Mudd, S.M. (2009). A theoretical model coupling chemical weathering rates with denudation rates. Geology, 37(2), 151-154.
- Gabriel, K.R. (1971). The biplot graphic display of matrices with application to principal component analysis. Biometrika, 58(3), 453-467.
- Gábris, G., & Nádor, A. (2007). Long-term fluvial archives in Hungary: response of the Danube and Tisza rivers to tectonic movements and climatic changes during the Quaternary: a review and new synthesis. Quaternary Science Reviews, 26(22-24), 2758-2782.
- Galy, A., & France-Lanord, C. (2001). Higher erosion rates in the Himalaya: Geochemical constraints on riverine fluxes. Geology, 29(1), 23-26.
- Garzanti, E., & Andò, S. (2019). Heavy minerals for junior woodchucks. Minerals, 9(3), 148.
- Garzanti, E., & Van Haver, T. (1988). The Indus clastics: forearc basin sedimentation in the Ladakh Himalaya (India). Sedimentary Geology, 59(3-4), 237-249.
- Garzanti, E., & Vezzoli, G. (2003). A classification of metamorphic grains in sands based on their composition and grade. Journal of Sedimentary Research, 73(5), 830-837.
- Garzanti, E. (2017). The maturity myth in sedimentology and provenance analysis. Journal of Sedimentary Research, 87(4), 353-365.

- Garzanti, E. (2019). Petrographic classification of sand and sandstone. Earth-Science Reviews, 192, 545-563.
- Garzanti, E., Andò, S., & Vezzoli, G. (2020a). Provenance of Cenozoic Indus Fan sediments (IODP Sites U1456 and U1457). Journal of Sedimentary Research, 90(9), 1114-1127.
- Garzanti, E., Liang, W., Andò, S., Clift, P.D., Resentini, A., Vermeesch, P., & Vezzoli, G. (2020b). Provenance of Thal Desert sand: Focused erosion in the western Himalayan syntaxis and foreland-basin deposition driven by latest Quaternary climate change. Earth-science reviews, 207, 103220.
- Garzanti, E., Andò, S., Padoan, M., Vezzoli, G., & El Kammar, A. (2015b). The modern Nile sediment system: processes and products. Quat. Sci. Rev., 130, 9–56.
- Garzanti, E., Andò, S., & Vezzoli, G. (2009). Grain-size dependence of sediment composition and environmental bias in provenance studies. Earth Planet. Sci. Lett., 277(3–4), 422–432.
- Garzanti, E., Andò, S., Vezzoli, G., Lustrino, M., Boni, M., & Vermeesch, P. (2012). Petrology of the Namib Sand Sea: Long-distance transport and compositional variability in the wind-displaced Orange Delta. Earth-Science Reviews, 112(3-4), 173-189.
- Garzanti, E., Casnedi, R., & Jadoul, F. (1986). Sedimentary evidence of a Cambro-Ordovician orogenic event in the northwestern Himalaya. Sedimentary Geology, 48(3-4), 237-265.
- Garzanti, E., Critelli, S., & Ingersoll, R.V. (1996). Paleogeographic and paleotectonic evolution of the Himalayan Range as reflected by detrital modes of Tertiary sandstones and modern sands (Indus transect, India and Pakistan). Geological society of america bulletin, 108(6), 631-642.
- Garzanti, E., Dinis, P., Vermeesch, P., Andò, S., Hahn, A., Huvi, J., Limonta, M., Padoan, M., Resentini, A., Rittner, A., & Vezzoli, G. (2018a). Sedimentary processes controlling ultralong cells of littoral transport: Placer formation and termination of the Oranges and highway in southern Angola. Sedimentology, 65, 431–460.
- Garzanti, E., Resentini, A., Andò, S., Vezzoli, G., & Vermeesch, P. (2015a). Physical controls on sand composition and relative durability of detrital minerals during ultra-long distance littoral and eolian transport (coastal Namibia). Sedimentology, 62, 971–996.
- Garzanti, E., Resentini, A., Vezzoli, G., Andò, S., Malusà, M., & Padoan, M. (2012). Forward compositional modelling of Alpine orogenic sediments. Sedimentary Geology, 280, 149-164.
- Garzanti, E., Vermeesch, P., Al-Ramadan, K., Andò, S., Limonta, M., Rittner, A., & Vezzoli, G. (2018b). Tracing Transcontinental Sand Transport: from Anatolia–Zagros to the Rub' Al Khali Sand Sea. J. Sediment. Res., 87(11), 1196–1213.
- Garzanti, E., Vermeesch, P., Ando, S., Lustrino, M., Padoan, M., & Vezzoli, G. (2014). Ultralong distance littoral transport of Orange sand and provenance of the Skeleton Coast Erg (Namibia). Mar. Geol., 357, 25–36.

- Garzanti, E., Vermeesch, P., Andò, S., Vezzoli, G., Valagussa, M., Allen, K., Kadi, K.A., & Al-Juboury, A.I. (2013). Provenance and recycling of Arabian desert sand. Earth-Science Reviews, 120, 1-19.
- Garzanti, E., Vermeesch, P., Rittner, M., & Simmons, M. (2018). The zircon story of the Nile: Time-structure maps of source rocks and discontinuous propagation of detrital signals. Basin Research, 30(6), 1098-1117.
- Garzanti, E., Vezzoli, G., Andò, S., Paparella, P., & Clift, P.D. (2005). Petrology of Indus River sands: a key to interpret the erosion history of the Western Himalayan Syntaxis. Earth and Planetary Science Letters, 229(3-4), 287-302.
- Gazis, C., Blum, J., Chamberlain, C., & Poage, M. (1998). An isotopic study of granite genesis: Nanga-Parbat Haramosh Massif, Pakistan Himalaya. American Journal of Science, 298, 673-698.
- Gehrels, G. (2014). Detrital zircon U-Pb geochronology applied to tectonics. Annual Review of Earth and Planetary Sciences, 42, 127-149.
- George, M. T., Harris, N. B. W., & Butler, R. W. H. (1993). The tectonic implications of contrasting granite magmatism between the Kohistan island arc and the Nanga Parbat-Haramosh Massif, Pakistan Himalaya. Geological Society, London, Special Publications, 74(1), 173-191. doi:10.1144/GSL.SP.1993.074.01.13.
- Giosan, L., Clift, P. D., Macklin, M. G., Fuller, D. Q., Constantinescu, S., Durcan, J. A., ... Adhikari, R. (2012). Fluvial landscapes of the Harappan civilization. Proceedings of the National Academy of Sciences, 109(26), E1688-E1694.
- Glennie, K. W., Singhvi, A. K., Lancaster, N., & Teller, J. T. (2002). Quaternary climatic changes over southern Arabia and the Thar Desert, India. Geological Society, London, Special Publications, 195(1), 301-316.
- Godard, V., Lavé, J., Carcaillet, J., Cattin, R., Bourlès, D., & Zhu, J. (2010). Spatial distribution of denudation in Eastern Tibet and regressive erosion of plateau margins. Tectonophysics, 491(1-4), 253-274.
- Goldstein, S. L., O'Nions, R. K., & Hamilton, P. J. (1984). A Sm-Nd isotopic study of atmospheric dusts and particulates from major river systems. Earth and Planetary Science Letters, 70(2), 221-236.
- Grey, I. E., & Reid, A. F. (1975). The structure of pseudorutile and its role in the natural alteration of ilmenite. American Mineralogist: Journal of Earth and Planetary Materials, 60(9-10), 898-906.
- Griffin, W. L. (2008). GLITTER: data reduction software for laser ablation ICP-MS. In Laser Ablation ICP-MS in the Earth Sciences: Current practices and outstanding issues (pp. 308-311).
- Guillot, S., Garzanti, E., Baratoux, D., Marquer, D., Mahéo, G., & de Sigoyer, J. (2003). Reconstructing the total shortening history of the NW Himalaya. Geochemistry, Geophysics, Geosystems, 4(7).
- Guo, X., Chen, X., Chen, Y., & Wang, Y. (2016). Impacts of climate variability and human activities on runoff of Minjiang river basin. Science of Soil and Water Conservation, 14(2), 88–94. (In Chinese with English Abstract)

- Gurnell, A. M., Warburton, J., & Clark, M. J. (1988). A Comparison of the Sediment Transport and Yield Characteristics of Two Adjacent Glacier Basins, Val d'Herens, Switzerland. In Sediment Budgets (IAHS Publication, 174).
- Hack, J. T. (1957). Studies of longitudinal stream profiles in Virginia and Maryland (Vol. 294). US Government Printing Office.
- Hacker, B. R., Ratschbacher, L., Webb, L., Ireland, T., Walker, D., Shuwen, D. (1998). U/Pb zircon ages constrain the architecture of the ultrahigh-pressure Qinling-Dabie Orogen, China. Earth Planet. Sci. Lett., 161(1–4), 215–230. https://doi.org/10.1016/S0012-821X(98)00152-6.
- Hairong, D., Yong, L., Chongjian, S., Svirchev, L., Qiang, X., Zhaokun, Y., Liang, Y., Shijun, N., & Zeming, S. (2017). Mechanism of post-seismic floods after the Wenchuan earthquake in the upper Minjiang River, China. Journal of Earth System Science, 126, 1-15.
- Harrowfield, M. J., & Wilson, C. J. L. (2005). Indosinian deformation of the Songpan Garze Fold Belt, northeast Tibetan Plateau. J. Struct. Geol., 27(1), 101–117.
- Haughton, P. D. W., Todd, S. P., & Morton, A. C. (1991). Sedimentary provenance studies. Geological Society, London, Special Publications, 57(1), 1-11.
- Hay, W. W. (1998). Detrital sediment fluxes from continents to oceans. Chemical Geology, 145(3–4), 287–323.
- He, M., Zheng, H., Bookhagen, B., & Clift, P. D. (2014). Controls on erosion intensity in the Yangtze River basin tracked by U–Pb detrital zircon dating. Earth-Science Reviews, 136, 121-140.
- Henderson, A. L., Najman, Y., Parrish, R., BouDagher-Fadel, M., Barford, D., Garzanti, E., & Andò, S. (2010). Geology of the Cenozoic Indus Basin sedimentary rocks: Paleoenvironmental interpretation of sedimentation from the western Himalaya during the early phases of India-Eurasia collision. Tectonics, 29(6).
- Herman, F., & Champagnac, J. D. (2016). Plio-Pleistocene increase of erosion rates in mountain belts in response to climate change. Terra Nova, 28(1), 2-10.
- Hinderer, M. (2001). Late Quaternary denudation of the Alps, valley and lake fillings and modern river loads. Geodin. Acta, 14, 231–263.
- Hinderer, M., Kastowski, M., Kamelger, A., Bartolini, C., & Schlunegger, F. (2013). River loads and modern denudation of the Alps—A review. Earth-Science Reviews, 118, 11-44.
- Hiscott, R. N. (1984). Ophiolitic source rocks for Taconic-age flysch: Trace-element evidence. GSA Bulletin, 95(11), 1261-1267. doi:10.1130/0016-7606(1984)95<1261:Osrftf>2.0.Co;2.
- Hollands, C. B., Nanson, G. C., Jones, B. G., Bristow, C. S., Price, D. M., & Pietsch, T. J. (2006). Aeolian–fluvial interaction: evidence for Late Quaternary channel change and wind-rift linear dune formation in the northwestern Simpson Desert, Australia. Quaternary Science Reviews, 25(1-2), 142-162.
- Hovius, N., & Leeder, M. R. (1998). Clastic sediment supply to basins. Basin Research, 10, 1–5.

- Hu, X., Garzanti, E., Moore, T., & Raffi, I. (2015). Direct stratigraphic dating of India-Asia collision onset at the Selandian (middle Paleocene, 59±1 Ma). Geology, 43(10), 859-862.
- Hubert, J. F. (1962). A zircon-tourmaline-rutile maturity index and the interdependence of the composition of heavy mineral assemblages with the gross composition and texture of sandstones. Journal of Sedimentary Research, 32(3), 440-450.
- Huntington, K. W., Blythe, A. E., & Hodges, K. V. (2006). Climate change and Late Pliocene acceleration of erosion in the Himalaya. Earth and Planetary Science Letters, 252(1-2), 107-118.
- Huyghe, P., Galy, A., Mugnier, J.-L., & France-Lanord, C. (2001). Propagation of the thrust system and erosion in the Lesser Himalaya: Geochemical and sedimentological evidence. Geology, 29(11), 1007–1010.
- Inger, S., & Harris, N. (1993). Geochemical constraints on leucogranite magmatism in the Langtang Valley, Nepal Himalaya. Journal of Petrology, 34(2), 345-368.
- Ingersoll, R. V. (1990). Actualistic sandstone petrofacies: discriminating modern and ancient source rocks. Geology, 18(8), 733-736.
- Ingersoll, R. V., Bullard, T. F., Ford, R. L., Grimm, J. P., Pickle, J. D., & Sares, S. W. (1984). The effect of grain size on detrital modes: A test of the Gazzi-Dickinson point-counting method. Journal of Sedimentary Petrology, 54(1), 103-116.
- Ingersoll, R. V., Graham, S. A., & Dickinson, W. R. (1995). Remnant Ocean basins. In C. J. Busby & R. V. Ingersoll (Eds.), Tectonics of sedimentary basins (pp. 363–391). Oxford, Blackwell Science.
- Jackson, S. E., Pearson, N. J., Griffin, W. L., & Belousova, E. A. (2004). The application of laser ablation-inductively coupled plasma-mass spectrometry to in situ U–Pb zircon geochronology. Chemical Geology, 211(1-2), 47-69.
- Jagoutz, O., Bouilhol, P., Schaltegger, U., & Müntener, O. (2019). The isotopic evolution of the Kohistan Ladakh arc from subduction initiation to continent arc collision. Geological Society, London, Special Publications, 483(1), 165-182. doi:10.1144/SP483.7.
- Jain, A. K., & Banerjee, D. M. (2020). The Indian subcontinent: Its tectonics. Proceedings of the Indian National Science Academy, 86, 775-875.
- Jian, X., Zhang, W., Yang, S., & Kao, S. J. (2020). Climate-dependent sediment composition and transport of mountainous rivers in tectonically stable, subtropical East Asia. Geophysical Research Letters, 47(3), e2019GL086150.
- Jiang, H., Mao, X., Xu, H., Yang, H., Ma, X., Zhong, N., & Li, Y. (2014). Provenance and earthquake signature of the last deglacial Xinmocun lacustrine sediments at Diexi, East Tibet. Geomorphology, 204, 518-531.
- Johnsson, M. J., Stallard, R. F., & Meade, R. H. (1988). First-cycle quartz arenites in the Orinoco River basin, Venezuela and Colombia. The Journal of Geology, 96(3), 263-277.

- Jonell, T. N., Carter, A., Böning, P., Pahnke, K., & Clift, P. D. (2017). Climatic and glacial impact on erosion patterns and sediment provenance in the Himalayan rain shadow, Zanskar River, NW India. Bulletin, 129(7-8), 820-836.
- Jonell, T. N., Owen, L. A., Carter, A., Schwenniger, J. L., & Clift, P. D. (2018). Quantifying episodic erosion and transient storage on the western margin of the Tibetan Plateau, upper Indus River. Quaternary Research, 89(1), 281-306.
- Kar, A. (2013). Quaternary geomorphic processes and landform development in the Thar Desert of Rajasthan. Landforms Process. Environ. Manag, 225-256.
- Kar, A., Felix, C., Rajaguru, S. N., & Singhvi, A. K. (1998). Late Holocene growth and mobility of a transverse dune in the Thar Desert. Journal of Arid Environments, 38(2), 175–185. DOI:10.1006/jare.1997.0343.
- Kazmi, A. H. (1984). Geology of the Indus delta. In Marine geology and oceanography of Arabian Sea and coastal Pakistan (pp. 71-84).
- Khan, M. A., Stern, R. J., Gribble, R. F., & Windley, B. F. (1997). Geochemical and isotopic constraints on subduction polarity, magma sources, and palaeogeography of the Kohistan intra-oceanic arc, northern Pakistan Himalaya. Journal of the Geological Society, London, 154, 935–946.
- Kocurek, G., & Lancaster, N. (1999). Aeolian system sediment state: theory and Mojave Desert Kelso dune field example. Sedimentology, 46(3), 505-515.
- Kruskal, J. B., & Wish, M. (1978). Multidimensional scaling. Sage Publications, Quantitative applications in the social sciences (Sage Univer. Paper Ser. 07-011, 92).
- Kuehl, S. A., Alexander, C. R., Blair, N. E., Harris, C. K., Marsaglia, K. M., Ogston, A. S., ... Carter, L. (2016). A source-to-sink perspective of the Waipaoa River margin. Earth-Science Reviews, 153, 301-334.
- Kumari, D., Prajapat, G., Goyal, S., & Agrawal, A. (2023). Modification of desert sand to soil using polymers for its agricultural potential. Journal of Arid Environments, 209, 104899.
- Kump, L. R., Brantley, S. L., & Arthur, M. A. (2000). Chemical weathering, atmospheric CO2, and climate. Annual Review of Earth and Planetary Sciences, 28(1), 611-667.
- Lane, E. W., & Borland, W. M. (1951). Estimating bed-load. Transactions of the American Geophysical Union, 321, 121–123.
- Langford, R. P. (1989). Fluvial-aeolian interactions: Part I, modern systems. Sedimentology, 36(6), 1023-1035.
- Lee, J. I., Clift, P. D., Layne, G., Blum, J., & Khan, A. A. (2003). Sediment flux in the modern Indus River inferred from the trace element composition of detrital amphibole grains. Sedimentary Geology, 160(1-3), 243-257.
- Lemennicier, Y., Le Fort, P., Lombardo, B., Pêcher, A., & Rolfo, F. (1996). Tectonometamorphic evolution of the central Karakorum (Baltistan, northern Pakistan). Tectonophysics, 260(1-3), 119-143.

- Li, Hong, You, L., Wang, D., & Wang, H. (2021). Comprehensive analysis and treatment countermeasures to siltation of Zipingpu Reservoir. China Water Resources, 45-48, 51. (In Chinese).
- Li, X. D., Masuda, H., & Liu, C. Q. (2008). Chemical and isotopic compositions of the Minjiang River, a headwater tributary of the Yangtze River. Journal of Environmental Quality, 37(2), 409-416.
- Li, Y., Clift, P. D., Böning, P., Blusztajn, J., Murray, R. W., Ireland, T., ... & Giosan, L. (2018). Continuous Holocene input of river sediment to the Indus Submarine Canyon. Marine Geology, 406, 159-176. doi:10.1016/j.margeo.2018.09.011.
- Liang, W., Garzanti, E., Andò, S., Gentile, P., & Resentini, A. (2019). Multimineral fingerprinting of Transhimalayan and Himalayan sources of Indus-derived Thal Desert sand (central Pakistan). Minerals, 9(8), 457.
- Liang, W., Resentini, A., Guo, R., & Garzanti, E. (2020). Multimineral fingerprinting of modern sand generated from the Tethys Himalaya (Nianchu River, Tibet). Sedimentary Geology, 399, 105604.
- Limonta, M., Andò, S., Bersani, D., & Garzanti, E. (2022). Discrimination of clinozoisite–epidote series by Raman spectroscopy: an application to Bengal Fan Turbidites (IODP Expedition 354). Geosciences, 12(12), 442.
- Lin, C. (1995). A study on the characteristics and quantity of the pebble bed load at the Minjiang River. Acta Geographica Sinica, 50(3), 224-233. (in Chinese)
- Lining, W. A. N. G., Zhuxin, C. H. E. N., Benliang, L. I., Yongliang, L., & Shuyu, Y. (2014). Structural characteristics of the northern Longmenshan fold-thrust belt and the favorable exploration areas, Sichuan Basin, Southwest China. Petroleum Exploration and Development, 41(5), 591-597.
- Liu, C. (2020). Based on the theory of optimizing the allocation of research of sustainable utilization of water resources of the upper reaches of Minjiang River. Natural Resources, 11(10), 473.
- Liu, F., Li, J., & Yang, S. (2015). Landslide erosion associated with the Wenchuan earthquake in the Minjiang River watershed: Implication for landscape evolution of the Longmen Shan, eastern Tibetan Plateau. Natural Hazards, 76, 1911-1926.
- Livingstone, I., & Warren, A. (Eds.). (2019). Aeolian geomorphology: a new introduction.
- Ludwig, K. R. (1998). On the treatment of concordant uranium-lead ages. Geochimica et Cosmochimica Acta, 62(4), 665-676.
- Ludwig, R. (1874). Geologische Bilder aus Italien: (mit 26 Figuren). Typographie der Universität.
- Lupker, M., France-Lanord, C., Galy, V., Lave, J., Gaillardet, J., Gajured, A. P., ... & Sinha, R. (2012). Predominant floodplain over mountain weathering of Himalayan sediments (Ganga basin). Geochimica et Cosmochimica Acta, 84, 410-432.
- Mahéo, G., Blichert-Toft, J., Pin, C., Guillot, S., & Pêcher, A. (2009). Partial Melting of Mantle and Crustal Sources beneath South Karakorum, Pakistan: Implications for the Miocene Geodynamic Evolution of the India–Asia

Convergence Zone. Journal of Petrology, 50(3), 427-449. doi:10.1093/petrology/egp006.

- Malusà, M. G., Resentini, A., & Garzanti, E. (2016). Hydraulic sorting and mineral fertility bias in detrital geochronology. Gondwana Research, 31, 1-19.
- Mark, C., O'Sullivan, G., Glorie, S., Simpson, A., Andò, S., Barbarano, M., ... & Gilbert, S. (2023). Detrital Garnet Geochronology by In Situ U-Pb and Lu-Hf Analysis: A Case Study from the European Alps. Journal of Geophysical Research: Earth Surface, 128(9), e2023JF007244.
- Martin, A. J., DeCelles, P. G., Gehrels, G. E., Patchett, P. J., & Isachsen, C. (2005). Isotopic and structural constraints on the location of the Main Central Thrust in the Annapurna Range, central Nepal Himalaya. Geological Society of America Bulletin, 117(7-8), 926-944.
- Martinsen, O. J., Sømme, T. O., Thurmond, J. B., Helland-Hansen, W., & Lunt, I. (2010). Source-to-sink systems on passive margins: theory and practice with an example from the Norwegian continental margin. Geological Society, London, Petroleum Geology Conference series, 7(1), 913-920.
- Mason, C. C., Romans, B. W., Stockli, D. F., Mapes, R. W., & Fildani, A. (2019). Detrital zircons reveal sea-level and hydroclimate controls on Amazon River to deep-sea fan sediment transfer. Geology, 47(6), 563-567.
- Meade, R. H. (1982). Sources, sinks, and storage of river sediment in the Atlantic drainage of the United States. Journal of Geology, 90, 235-252.
- Meade, R. H. (1972). Sources and sinks of suspended matter on continental shelves. In: Swift, D. J. P., Duane, D. B., & Pilkey, O. H. (Eds.), Shelf Sediment Transport. Dowden, Hutchinson & Ross, Stroudsburg, 249-262.
- Meinhold, G., Anders, B., Kostopoulos, D., & Reischmann, T. (2008). Rutile chemistry and thermometry as a provenance indicator: An example from Chios Island, Greece. Sedimentary Geology, 203(1), 98-111. doi:10.1016/j.sedgeo.2007.11.004.
- Meng, Q.-R., & Zhang, G.-W. (2000). Geologic framework and tectonic evolution of the Qinling orogen, central China. Tectonophysics, 323(3–4), 183–196. doi:10.1016/S0040-1951(00)00106-2.
- Meunier, S. (1877). Composition et origine du sable diamantifere de Du Toit's Pan (Afrique australe). CR Acad. Sci., Paris, 84, 250-252.
- Michel-Lévy, A. (1878). Note on some minerals contained in the sands of Mesvrin, near Autun. Bulletin de Mineralogy, 1(3), 39-41.
- Miller, C., Thöni, M., Frank, W., Grasemann, B., Klotzli, U., Guntli, P., & Draganits, E. (2001). The early Paleozoic magmatic event in the northwest Himalaya, India: source, tectonic setting and age of emplacement. Geological Magazine, 138, 237-251.
- Morton, A. C., & Hallsworth, C. R. (1999). Processes controlling the composition of heavy mineral assemblages in sandstones. Sedimentary Geology, 124(1-4), 3-29.
- Mücke, A., & Chaudhuri, J. B. (1991). The continuous alteration of ilmenite through pseudorutile to leucoxene. Ore Geology Reviews, 6(1), 25-44.

- Mughal, M. R. (1997). Ancient Cholistan - Archaeology and Architecture. Ferozsons (Pvt.) Ltd., Lahore, pp. 21.
- Mughal, M. R., Iqbal, F., Afzal, M., & Hassan, M. (1996). Archaeological sites and monuments in Punjab: Preliminary results of explorations, 1992–96. Pa. Archaeol, 29, 1-474.
- Najman, Y., Garzanti, E., Pringle, M., Bickle, M., Stix, J., & Khan, I. (2003). Early-Middle Miocene paleodrainage and tectonics in the Pakistan Himalaya. Geological Society of America Bulletin, 115(10), 1265-1277.
- Najman, Y., Jenks, D., Godin, L., Boudagher-Fadel, M., Millar, I., Garzanti, E., Horstwood, M., & Bracciali, L. (2017). The Tethyan Himalayan detrital record shows that India–Asia terminal collision occurred by 54 Ma in the Western Himalaya. Earth and Planetary Science Letters, 459, 301-310.
- Nesbitt, H., & Young, G. M. (1982). Early Proterozoic climates and plate motions inferred from major element chemistry of lutites. Nature, 299(5885), 715-717.
- Neubeck, N., Carter, A., Rittenour, T., & Clift, P. D. (2023). Climate and anthropogenic impacts on North American erosion and sediment transport since the Last Glacial Maximum: Evidence from the detrital zircon record of the Lower Mississippi Valley, USA. Geological Society of America Bulletin.
- Nesbitt, H. W., & Markovics, G. (1980). Chemical processes affecting alkalis and alkaline earths during continental weathering. Geochimica et Cosmochimica Acta, 44(11), 1659-1666.
- Nordstrom, K. F. (2014). Living with shore protection structures: a review. Estuarine, Coastal and Shelf Science, 150, 11-23.
- Norton, K., & Schlunegger, F. (2011). Migrating deformation in the central Andes from enhanced orographic rainfall. Nature Communications, 2. https://doi.org/10.1038/ncomms1590. #584
- Oldham, R.D. (1999). On probable changes in the geography of the Punjab and its rivers-An historico-geographical study. Memoirs-Geological Society of India, 81-88.
- Palomares, M., Arribas, J., Johnsson, M.J., & Basu, A. (1993). Modern stream sands from compound crystalline sources: composition and sand generation index. Special Papers-Geological Society of America, 313.
- Parrish, R.R., & Hodges, K.V. (1996). Isotopic constraints on the age and provenance of the Lesser and Greater Himalayan sequences, Nepalese Himalaya. Geological Society of America Bulletin, 108(7), 904-911.
- Pastore, G., Garzanti, E., Vermeesch, P., Bayon, G., Resentini, A., Braquet, N., & Overare, B. (2023). The Zircon Story of the Niger River: Time-Structure Maps of the West African Craton and Discontinuous Propagation of Provenance Signals Across a Disconnected Sediment-Routing System. Journal of Geophysical Research: Earth Surface, 128(11), e2023JF007342.
- Pease, P. P., & Tchakerian, V. P. (2002). Composition and sources of sand in the Wahiba Sand Sea, Sultanate of Oman. Annals of the Association of American Geographers, 92(3), 416-434.

- Petter, A.L., Steel, R.J., Mohrig, D., Kim, W., & Carvajal, C. (2013). Estimation of the paleoflux of terrestrial-derived solids across ancient basin margins using the stratigraphic record. Bulletin, 125(3-4), 578-593.
- Petterson, M.G., Crawford, M.B., & Windley, B.F. (1993). Petrogenetic implications of neodymium isotope data from the Kohistan batholith, North Pakistan. Journal of the Geological Society, 150(1), 125-129. doi:10.1144/gsjgs.150.1.0125.
- Pettijohn, F. J., Potter, P. E., & Siever, R. (1987). Introduction and source materials. Sand and Sandstone, 1-21.
- Pettijohn, F.J., Potter, P.E., & Siever, R. (1972). Production and Provenance of Sand. In Sand and Sandstone (pp. 294-326). Springer US. doi:10.1007/978-1-4615-9974-6_8.
- Prell, W.L. (1984). Variation of monsoonal upwelling: a response to changing solar radiation. Climate processes and climate sensitivity, 29, 48-57.
- Prins, M.A., Zheng, H., Beets, K., Troelstra, S., Bacon, P., Kamerling, I., Wester, W., Konert, M., Huang, X., Ke, W., & Vandenberghe, J. (2009). Dust supply from river floodplains: the case of the lower Huang He (Yellow River) recorded in a loess–palaeosol sequence from the Mangshan Plateau. Journal of Quaternary Science: Published for the Quaternary Research Association, 24(1), 75-84.
- Pye, Kenneth, & Tsoar, H. (2008). Aeolian sand and sand dunes. Springer Science & Business Media.
- Rahaman, W., Singh, S.K., Sinha, R., & Tandon, S.K. (2009). Climate control on erosion distribution over the Himalaya during the past~ 100 ka. Geology, 37(6), 559-562.
- Ramsey, M.S., Christensen, P.R., Lancaster, N., & Howard, D.A. (1999). Identification of sand sources and transport pathways at the Kelso Dunes, California, using thermal infrared remote sensing. Geological Society of America Bulletin, 111(5), 646-662.
- Rehman, S.S., Sabir, M.A., & Khan, J. (1997). Discharge characteristics and suspended load from rivers of Northern Indus Basin, Pakistan. Geol. Bull. (Univ. Peshawar), 30, 325-336.
- Reiners, P.W., Ehlers, T.A., Mitchell, S.G., & Montgomery, D.R. (2003). Coupled spatial variations in precipitation and long-term erosion rates across the Washington Cascades. Nature, 426(6967), 645-647.
- Resentini, A., Andò, S., Garzanti, E., Malusà, M. G., Pastore, G., Vermeesch, P., ... & Dall'Asta, M. (2020). Zircon as a provenance tracer: Coupling Raman spectroscopy and U-Pb geochronology in source-to-sink studies. Chemical Geology, 555, 119828.
- Resentini, A., Goren, L., Castelltort, S., & Garzanti, E. (2017). Partitioning sediment flux by provenance and tracing erosion patterns in Taiwan. Journal of Geophysical Research: Earth Surface, 122(7), 1430-1454.
- Retgers, J. W. (1895). Über die mineralogische und chemische Zusammensetzung der Dünensande Hollands und über die Wichtigkeit von Fluss-und

Meeressanduntersuchungen im allgemeinen. Neuen Jahrbuch für Mineralogie etc, 1, 16-74.

- Rice, C.M., Darke, K.E., & Still, J.W. (1998). Tungsten-bearing rutile from the Kori Kollo gold mine, Bolivia. Mineral. Mag. 62, 421– 429.
- Riebe, C.S., Kirchner, J.W., & Finkel, R.C. (2004). Erosional and climatic effects on long-term chemical weathering rates in granitic landscapes spanning diverse climate regimes. Earth and Planetary Science Letters, 224(3-4), 547-562.
- Rittner, M., Vermeesch, P., Carter, A., Bird, A., Stevens, T., Garzanti, E., ... & Lu, H. (2016). The provenance of Taklamakan desert sand. Earth and Planetary Science Letters, 437, 127-137.
- Robinson, D.M., DeCelles, P.G., Patchett, P.J., & Garzione, C.N. (2001). The kinematic evolution of the Nepalese Himalaya interpreted from Nd isotopes. Earth and Planetary Science Letters, 192(4), 507-521.
- Roger, F., Jolivet, M., & Malavieille, J. (2010). The tectonic evolution of the Songpan-Garzê (North Tibet) and adjacent areas from Proterozoic to Present: A synthesis. Journal of Asian Earth Sciences, 39(4), 254-269.
- Rolland, Y., Mahéo, G., Guillot, S., & Pêcher, A. (2001). Tectono-metamorphic evolution of the Karakorum Metamorphic complex (Dassu–Askole area, NE Pakistan): Exhumation of mid-crustal HT–MP gneisses in a convergent context. Journal of Metamorphic Geology, 19(6), 717-737.
- Rolland, Y., Pecher, A., & Picard, C. (2000). Middle Cretaceous back-arc formation and arc evolution along the Asian margin: the Shyok Suture Zone in northern Ladakh (NW Himalaya). Tectonophysics, 325(1-2), 145-173.
- Rolland, Y., Picard, C., Pecher, A., Lapierre, H., Bosch, D., & Keller, F. (2002a). The Cretaceous Ladakh arc of NW Himalaya—slab melting and melt–mantle interaction during fast northward drift of Indian Plate. Chemical Geology, 182, 139–178.
- Rolland, Y., Picard, C., Pecher, A., Lapierre, H., Bosch, D., & Keller, F. (2002b). The Cretaceous Ladakh arc of NW Himalaya—slab melting and melt–mantle interaction during fast northward drift of Indian Plate. Chemical Geology, 182(2), 139-178. doi:10.1016/S0009-2541(01)00286-8.
- Roy, P.D., & Smykatz-Kloss, W. (2007). REE geochemistry of the recent playa sediments from the Thar Desert, India: an implication to playa sediment provenance. Geochemistry, 67(1), 55-68.
- Royden, L.H., Burchfiel, B.C., King, R.W., Wang, E., Chen, Z.L., Shen, F., & Liu, Y.P. (1997). Surface deformation and lower crustal flow in Eastern Tibet. Science, 276, 788–790.
- Russell, M.J., & Allison, I. (1985). Agalmatolite and the maturity of sandstones of the Appin and Argyll groups and Eriboll Sandstone. Scottish Journal of Geology, 21(2), 113-122.
- Russell, R.D. (1937). Mineral composition of Mississippi River sands. Geol. Soc. Am. Bull. 48, 1307–1348.

- Saini, H.S., Tandon, S.K., Mujtaba, S.A.I., Pant, N.C., & Khorana, R.K. (2009). Reconstruction of buried channel-floodplain systems of the northwestern Haryana Plains and their relation to the 'Vedic' Saraswati. Current Science, 97(11), 1634-1643.
- Sam, L., Gahlot, N., & Prusty, B.G. (2015). Estimation of dune celerity and sand flux in part of West Rajasthan, Gadra area of the Thar Desert using temporal remote sensing data. Arabian Journal of Geosciences, 8, 295-306.
- Saylor, J.E., & Sundell, K.E. (2016). Quantifying comparison of large detrital geochronology data sets. Geosphere, 12(1), 203-220.
- Schärer, U., Copeland, P., Harrison, T.M., & Searle, M.P. (1990). Age, cooling history, and origin of post-collisional leucogranites in the Karakoram Batholith: A multi-system isotope study. Journal of Geology, 98(2), 233–251.
- Schwanghart, W., & Scherler, D. (2014). TopoToolbox 2 – MATLAB-based software for topographic analysis and modeling in Earth surface sciences. Earth Surf. Dyn., 2, 1–7. https://doi.org/10.5194/esurf-2-1-2014.
- Searle, M.P., Khan, M.A., Fraser, J.E., Gough, S.J., & Jan, M.Q. (1999). The tectonic evolution of the Kohistan-Karakoram collision belt along the Karakoram Highway transect, north Pakistan. Tectonics, 18(6), 929-949.
- Searle, M.P., Parrish, R.R., Thow, A.V., Noble, S.R., Phillips, R.J., & Waters, D.J. (2010). Anatomy, age and evolution of a collisional mountain belt: the Baltoro granite batholith and Karakoram Metamorphic Complex, Pakistani Karakoram. Journal of the Geological Society, 167(1), 183-202.
- Searle, M.P., Rex, A.J., Tirrul, R., Rex, D.C., Barnicoat, A., & Windley, B.F. (1989). Metamorphic, magmatic and tectonic evolution of the Central Karakoram in the Biafo-Baltoro-Hushe regions of north Pakistan. Geological Society of America Special Paper, 232, 47-73.
- Shroder Jr, J.F., Owen, L.A., Seong, Y.B., Bishop, M.P., Bush, A., Caffee, M.W., Copland, L., Finkel, R.C., & Kamp, U. (2011). The role of mass movements on landscape evolution in the Central Karakoram: Discussion and speculation. Quaternary International, 236(1-2), 34-47.
- Singh, A., & Sinha, R. (2019). Fluvial response to climate change inferred from sediment cores from the Ghaggar–Hakra paleochannel in NW Indo–Gangetic plains. Palaeogeography, Palaeoclimatology, Palaeoecology, 532, 109247.
- Singh, M., Sharma, M., Tobschall, H.J. (2005). Weathering of the Ganga alluvial plain, northern India: implications from fluvial geochemistry of the Gomati River. Applied Geochemistry, 20, 1-21.
- Singh, S.K., & France-Lanord, C. (2002). Tracing the distribution of erosion in the Brahmaputra watershed from isotopic compositions of stream sediments. Earth and Planetary Science Letters, 202(3-4), 645-662.
- Singhvi, A.K., & Kar, A. (2004). The aeolian sedimentation record of the Thar Desert. Journal of Earth System Science, 113, 371-401.
- Singhvi, A.K., & Kar, A. (1992). Thar Desert in Rajasthan. Geological Society of India, Bangalore, p. 191.

- Singhvi, A.K., Kaushal, R.K., & Parida, S. (2022). Luminescence dating and Quaternary Geology: The Indian Narrative. Journal of the Palaeontological Society of India, 67(1), 183-210.
- Singhvi, A.K., Williams, M.A.J., Rajaguru, S.N., Misra, V.N., Chawla, S., Stokes, S., Chauhan, N., Francis, T., Ganjoo, R.K., & Humphreys, G.S. (2010). A ~ 200 ka record of climatic change and dune activity in the Thar Desert, India. Quaternary Science Reviews, 29(23-24), 3095-3105.
- Sinha, R., Yadav, G.S., Gupta, S., Singh, A., & Lahiri, S.K. (2013). Geo-electric resistivity evidence for subsurface palaeochannel systems adjacent to Harappan sites in northwest India. Quaternary International, 308, 66-75.
- Sláma, J., Košler, J., Condon, D.J., Crowley, J.L., Gerdes, A., Hanchar, J.M., Horstwood, M.S., Morris, G.A., Nasdala, L., Norberg, N., & Schaltegger, U. (2008). Plešovice zircon—a new natural reference material for U–Pb and Hf isotopic microanalysis. Chemical Geology, 249(1-2), 1-35.
- Smith, D.C., & Perseil, E.A. (1997). Sb-rich rutile in the manganese concentrations at St. Marcel-Praborna, Aosta Valley, Italy: petrology and crystal-chemistry. Mineral. Mag., 61, 655–669.
- Smythe, D., Schulze, D., & Brenan, J. (2008). Rutile as a kimberlite indicator mineral: minor and trace element geochemistry, International Kimberlite Conference: Extended Abstracts.
- Snyder, N., Whipple, K., Tucker, G., & Merritts, D. (2000). Landscape response to tectonic forcing: digital elevation model analysis of stream profiles in the Mendocino triple junction region, northern California. Geol. Soc. Am. Bull., 112, 1250–1263.
- Sobolev, N.V., & Yefimova, E.S. (2000). Composition and petrogenesis of Ti-oxides associated with diamonds. International Geology Review, 42, 758–767.
- Srivastava, A., Thomas, D.S., Durcan, J.A., & Bailey, R.M. (2020). Holocene palaeoenvironmental changes in the Thar Desert: An integrated assessment incorporating new insights from aeolian systems. Quaternary Science Reviews, 233, p.106214.
- Stein, A. (1942). A survey of ancient sites along the "lost" Sarasvati River. The Geographical Journal, 99(4), 173-182.
- Stern, C.R., Kligfield, R., Schelling, D., Virdi, N.S., Futa, K., Peterman, Z.E. (1989). The Bhagirathi leucogranite of High Himalaya (Garhwal, India): age, petrogenesis, and tectonic implications. In: Malinconico, L.L. (Ed.), Tectonics of the Western Himalayas. Special paper, 232, Geological Society of America, Boulder, CO, 33–45.
- Sundell, K.E., & Saylor, J.E. (2017). Unmixing detrital geochronology age distributions. Geochemistry, Geophysics, Geosystems, 18(8), 2872-2886.
- Telfer, M.W., & Hesse, P.P. (2013). Palaeoenvironmental reconstructions from linear dunefields: recent progress, current challenges and future directions. Quaternary Science Reviews, 78, 1-21.

- Thomas, D.S., & Wiggs, G.F. (2008). Aeolian system responses to global change: challenges of scale, process and temporal integration. Earth Surface Processes and Landforms: The Journal of the British Geomorphological Research Group, 33(9), 1396-1418.
- Thomas, P.J., Juyal, N., Kale, V.S., & Singhvi, A.K. (2007). Luminescence chronology of late Holocene extreme hydrological events in the upper Penner River basin, South India. Journal of Quaternary Science: Published for the Quaternary Research Association, 22(8), 747-753.
- Thürach, H. (1884). Über das Vorkommen mikroskopischer Zirkone und Titan-Mineralien in den Gesteinen. Stahel.
- Treloar, P.J., Petterson, M.G., Jan, M.Q., & Sullivan, M.A. (1996). A re-evaluation of the stratigraphy and evolution of the Kohistan arc sequence, Pakistan Himalaya: implications for magmatic and tectonic arc-building processes. Journal of the Geological Society, 153(5), 681-693.
- Trimble, S.W. (1983). A sediment budget for Coon Creek basin in the Driftless Area, Wisconsin, 1853-1977. American Journal of Science, 283(5), 454-474.
- Turowski, J.M., Rickenmann, D., & Dadson, S.J. (2010). The partitioning of the total sediment load of a river into suspended load and bedload: a review of empirical data. Sedimentology, 57(4), 1126-1146.
- Usman, M., Clift, P.D., Pastore, G., Vezzoli, G., Andò, S., Barbarano, M., Vermeesch, P., Garzanti, E. (in review). Climatic Influence on Sediment Distribution and Transport in the Thar Desert (Sindh and Cholistan, Pakistan). Earth-Science Reviews, 249, 104674.
- Valdiya, K.S. (2002). Saraswati: the river that Disappeared. Hyderabad, India: 1st University Press, 116 p.
- van de Kamp, P.C., & Leake, B.E. (1985). Petrography and geochemistry of feldspathic and mafic sediments of the northeastern Pacific margin. Earth and Environmental Science Transactions of the Royal Society of Edinburgh, 76(4), 411-449.
- Velbel, M.A., & Saad, M.K. (1991). Palaeoweathering or diagenesis as the principal modifier of sandstone framework composition? A case study from some Triassic rift-valley redbeds of eastern North America. Geological Society, London, Special Publications, 57(1), 91-99.
- Vermeesch, P. (2013). Multi-sample comparison of detrital age distributions. Chemical Geology, 341, 140-146.
- Vermeesch, P. (2018). IsoplotR: A free and open toolbox for geochronology. Geoscience Frontiers, 9(5), 1479-1493.
- Vermeesch, P. (2021). On the treatment of discordant detrital zircon U–Pb data. Geochronology, 3(1), 247-257.
- Vermeesch, P., Rittner, M., Petrou, E., Omma, J., Mattinson, C., & Garzanti, E. (2017). High throughput petrochronology and sedimentary provenance analysis by automated phase mapping and LAICPMS. Geochemistry, Geophysics, Geosystems, 18(11), 4096-4109.

- Verstraete, M.M. (1986). Defining desertification: a review. Climatic Change, 9(1-2), 5-18.
- Vezzoli, G., & Garzanti, E. (2009). Tracking paleodrainage in Pleistocene foreland basins. The Journal of Geology, 117(4), 445-454.
- Vezzoli, G., Garzanti, E., & Monguzzi, S. (2004). Erosion in the western Alps (Dora Baltea basin): 1. Quantifying sediment provenance. Sedimentary Geology, 171(1-4), 227-246.
- Vezzoli, G., Garzanti, E., Limonta, M., & Radeff, G. (2020). Focused erosion at the core of the Greater Caucasus: Sediment generation and dispersal from Mt. Elbrus to the Caspian Sea. Earth-Science Reviews, 200, 102987.
- Vezzoli, G., Ghielmi, G., Mondaca, G., Resentini, A., Villarroel, E.K., Padoan, M., & Gentile, P. (2013). Quantifying modern erosion rates and river-sediment contamination in the Bolivian Andes. Journal of South American Earth Sciences, 45, 42-55.
- Vögeli, N., van der Beek, P., Huyghe, P., & Najman, Y. (2017). Weathering in the Himalaya, an East-West Comparison: Indications from Major Elements and Clay Mineralogy. The Journal of Geology, 125, 515–529. DOI: 10.1086/692652.
- von Eynatten, H. (2004). Statistical modelling of compositional trends in sediments. Sedimentary Geology, 171(1-4), 79-89.
- Wallis, S., Tsujimori, T., Aoya, M., Kawakami, T., Terada, K., Suzuki, K., & Hyodo, H. (2003). Cenozoic and Mesozoic metamorphism in the Longmenshan orogen: Implications for geodynamic models of eastern Tibet. Geology, 31(9), 745-748.
- Wang, B., Ding, Q., Fu, X., Kang, I.S., Jin, K., Shukla, J., & Doblas-Reyes, F. (2005). Fundamental challenge in simulation and prediction of summer monsoon rainfall. Geophysical Research Letters, 32(15).
- Wang, X.Q., Li, Y.R., Yuan, Y., Zhou, Z., & Wang, L.S. (2014). Palaeoclimate and palaeoseismic events discovered in Diexi barrier lake on the Minjiang River, China. Natural Hazards and Earth System Sciences, 14(8), 2069-2078.
- Wang, Y., Zhao, B., & Li, J. (2018). Mechanism of the catastrophic June 2017 landslide at Xinmo village, Songping river, Sichuan province, China. Landslides, 15, 333-345.
- Warren, A. (2013). Dunes: dynamics, morphology, history. John Wiley & Sons.
- Wasson, R.J., Smith, G.I., & Agrawal, D.P. (1984). Late Quaternary sediments, minerals, and inferred geochemical history of Didwana Lake, Thar Desert, India. Palaeogeography, palaeoclimatology, palaeoecology, 46(4), 345-372.
- Watson, E.B., Wark, D.A., & Thomas, J.B. (2006). Crystallization thermometers for zircon and rutile. Contributions to Mineralogy and Petrology, 151, 413–433.
- Weltje, G.J. (1997). End-member modeling of compositional data: Numerical-statistical algorithms for solving the explicit mixing problem. Mathematical Geology, 29, 503-549.
- Weltje, G.J., & von Eynatten, H. (2004). Quantitative provenance analysis of sediments: review and outlook. In: Weltje, G.J., von Eynatten, H. (Eds.), Quantitative Provenance Analysis of Sediments, Sediment. Geol. 171, 1–11.

- Werner, B. T. (1995). Eolian dunes: computer simulations and attractor interpretation. Geology, 23(12), 1107-1110.
- West, A.J., Galy, A., & Bickle, M. (2005). Tectonic and climatic controls on silicate weathering. Earth and Planetary Science Letters, 235(1-2), 211-228.
- Whipple, K.X. (2001). Fluvial landscape response time: How plausible is steady-state denudation?. American Journal of Science, 301(4-5), 313-325.
- Whipple, K.X. (2004). Bedrock rivers and the geomorphology of active orogens. Annu. Rev. Earth Planet. Sci., 32, 151–185.
- Whittington, A., Foster, G., Harris, N., Vance, D., & Ayres, M. (1999). Lithostratigraphic correlations in the western Himalaya - An isotopic approach. Geology, 27(7), 585-588.
- Wiedenbeck, M., Hanchar, J. M., Peck, W. H., Sylvester, P., Valley, J., Whitehouse, M., Kronz, A., Morishita, Y., Nasdala, L., Fiebig, J., Franchi, I., Girard, J.-P., Greenwood, R. C., Hinton, R., Kita, N., Mason, P. R. D., Norman, M., Ogasawara, M., Piccoli, P. M., … Zheng, Y.-F. (2004). Further Characterisation of the 91500 Zircon Crystal. Geostandards and Geoanalytical Research, 28(1), 9–39.
- Wobus, C.W., Whipple, K.X., Kirby, E., Snyder, N., Johnson, J., Spyropolou, K., Crosby, B., Sheehan, D. (2006). Tectonics from topography: procedures, promise, and pitfalls. Geol. Soc. Am. Spec. Pap., 398, 55–74.
- Wright, R., Schuldenrein, J., Khan, M.A., & Mughal, M.R. (2005). The emergence of satellite communities along the Beas drainage: Preliminary results from Lahoma Lal Tibba and Chak Purbane Syal. In South Asia Archaeology 2001 (pp. 327-335). Editions Recherce sur les Civilisations-ADPF.
- Wu, Z., Yin, H., Li, C., Yang, X., Wang, L., Wang, F., Dong, S., & Jia, D. (2021). Influence of regional erosion and sedimentary loading on fault activities in active fold-thrust belts: Insights from discrete element simulation and the southern and central Longmen Shan fold-thrust belt. Frontiers in Earth Science, 9, p.659682.
- Xu, H., Chen, J., Cui, Z., & Chen, R. (2020). Sedimentary facies and depositional processes of the Diexi Ancient Dammed Lake, Upper Minjiang River, China. Sedimentary Geology, 398, 105583.
- Xu, Q., Li, W., Tang, C., Fan, X., Luo, Y., Zhu, J., Xu, C., Xing, A., Zhuang, Y., & Towhata, I. (2022). Report on Landslides Triggered by the 2008 Wenchuan Earthquake. In Coseismic Landslides: Phenomena, Long-Term Effects and Mitigation (pp. 1-40). Singapore: Springer Nature Singapore.
- Yang, H.F., Yang, S.L., Xu, K.H., Milliman, J.D., Wang, H., Yang, Z., Chen, Z., & Zhang, C.Y. (2018). Human impacts on sediment in the Yangtze River: A review and new perspectives. Global and Planetary Change, 162, 8-17.
- Yin, Y., Gemmer, M., Luo, Y., & Wang, Y. (2010). Tropical cyclones and heavy rainfall in Fujian Province, China. Quaternary International, 226(1-2), 122-128.
- Zack, T., Stockli, D. F., Luvizotto, G. L., Barth, M. G., Belousova, E., Wolfe, M. R., & Hinton, R. W. (2011). In situ U–Pb rutile dating by LA-ICP-MS: 208 Pb correction and prospects for geological applications. Contributions to Mineralogy and Petrology, 162, 515-530.

- Zeitler, P.K., Chamberlain, C.P., & Smith, H.A. (1993). Synchronous anatexis, metamorphism, and rapid denudation at Nanga Parbat (Pakistan Himalaya). Geology, 21(4), 347-350.
- Zhang, F., Jin, Z., West, A.J., An, Z., Hilton, R.G., Wang, J., Li, G., Densmore, A.L., Yu, J., Qiang, X., & Sun, Y. (2019). Monsoonal control on a delayed response of sedimentation to the 2008 Wenchuan earthquake. Science advances, 5(6), p.eaav7110.
- Zhang, J. P., Ye, Y. Q., & Fan, H. (2002). Studies on grassland resource and rational utilization in the Upper Reaches of Minjiang River. Journal of Mountain Science, 20, 343-348.
- Zhang, L., Wu, J. L., Tu, J. R., Wu, D., Li, N., Xia, X. P., & Ren, Z. Y. (2020). RMJG rutile: A new natural reference material for microbeam U-Pb dating and Hf isotopic analysis. Geostandards and Geoanalytical Research, 44(1), 133-145.
- Zhang, Zehua, and Hongliang Wang. "Comprehensive Provenance Analysis and Its Applications to Eocene Clastic Rocks in the Huimin Depression, Bohai Bay Basin, China." Minerals, 9(9), 517.
- Zhao, K., Luo, Y., Yang, Y., & Yang, X. (2021). High-resolution lithospheric structures of the Qinling-Dabie orogenic belt: Implications for deep subduction and delamination of continental lithosphere. Tectonophysics, 806, 228799.
- Zhisheng, A., Clemens, S.C., Shen, J., Qiang, X., Jin, Z., Sun, Y., Prell, W.L., Luo, J., Wang, S., Xu, H., & Cai, Y. (2011). Glacial-interglacial Indian summer monsoon dynamics. Science, 333(6043), 719-723.
- Zhuang, G., Najman, Y., Tian, Y., Carter, A., Gemignani, L., Wijbrans, J., Jan, M.Q., & Khan, M.A. (2018). Insights into the evolution of the Hindu Kush–Kohistan–Karakoram from modern river sand detrital geo-and thermochronological studies. Journal of the Geological Society, 175(6), 934-948.

Research Activities During the Study Period

Publications in SCI Journals

— **Usman, M.,** Clift, P.D., Pastore, G., Vezzoli, G., Andò, S., Barbarano, M., Vermeesch, P., & Garzanti, E. (2024). Climatic influence on sediment distribution and transport in the Thar Desert (Sindh and Cholistan, Pakistan). *Earth-Science Reviews*, p.104674.

— **Usman, M.,** Clift, P.D., Pastore, G., Vezzoli, G., Ali, M., & Garzanti, E. (2024). Sand provenance in the western Thar Desert (Pakistan): Sr and Nd isotopes, detrital rutile, and bulk-sediment geochemical constraints. *Journal of Geophysical Research – Earth Surface*. Under Review.

— **Usman, M.,** Garzanti, E., G., Vezzoli, Liang, W., Andò, S. (In prep.). Segmented Minjiang Sediment Routing System and Sediment Generation in the Longmenshan Belt.

— Ali, M., Coletti, G., Mariani, L., Benedetti, A., Munawar, M.J., Rehman, S.U., Sternai, P., Basso, D., Malinverno, E., Shahzad, K., Khan, S., Awais, M., **Usman, M.,** Castelltort, S., Adatte, T., & Garzanti, E. (2024). Shallow-water carbonate facies herald the onset of the Palaeocene-Eocene Thermal Maximum (Hazara basin, Northern Pakistan). *Journal of Asian Earth Sciences: X*, 11, p.100169.

Publications in Conferences and Reports

— **Usman, M.,** Clift, P. D., Vezzoli, G., Pastore, G., Ali, M., & Garzanti, E. (2024). The Thar Desert as a control of sediment flux from the Indus River to the Arabian Sea. *In 37th International Meeting of IAS (International Association of Sedimentology)* (p. XX).

— **Usman, M.,** Vezzoli, G., Andò, S., Pastore, G., Vermeesch, P., Barbarano, M., & Garzanti, E. (2023). Sediments buffering system in the Thar sand dunes for provenance studies. *In 36th International Meeting of IAS (International Association of Sedimentology)* (p. 493).

— **Usman, M.** (2023). Detrital Zircon Dating of Thar Sand dunes for Provenance Studies. *The Newsletter of the International Association of Sedimentologists*, Issue 10 (pp. 44-49), IAS Postdoctoral Research Grant Report.

— **Usman, M.,** Garzanti, E., & Vezzoli, G. (2022). Tracing sediment provenance in the Shaotanghe River (southwest China). *In CONGRESSO SGI-SIMP 2022* (p. 838).

— Ali, M., Coletti, G., Sternai, P., Mariani, L., Castelltort, S., Adatte, T., **Usman, M.,** Garzanti, E. (2024). Paleocene-Eocene Thermal Maximum and Its Impact on shallow marine benthic communities: A Multi proxies approach. *In 37th International Meeting of IAS (International Association of Sedimentology)* (p. XX).

Presentations

— **Usman, M.,** Garzanti, E., Vezzoli, G. Tracing sediment provenance in the Shaotanghe River (southwest China). *In CONGRESSO SGI-SIMP 2022*, Italia.

— **Usman, M.,** Garzanti, E., Vezzoli, G. Sediment provenance in the Minjiang River (south China). *5th WGSG Meeting* 2020. Università di Milano-Bicocca, Italia.

Abroad Periods as Training

— **10 months abroad period** as training at Louisiana State University, USA under the supervision of Professor Peter D. Clift.

— **2 months aboard period** as training at University College London, UK under the supervision of Professor Pieter Vermeersch.

— **2 months abroad period** as training at University of the Punjab, PU under the supervision of Dr. Muhammad Jawad Munawar.

Summer and Winter Schools

— 2023: Winter School, "***Active Tectonics and Climate Change Driven Landscape Evolution INQUA – TERPRO commission***" Gemmellaro Geologic Museum, Palermo (Sicily), Italia.

— 2023: Winter School, "***Climate and environmental change***" under the "The International Training Program on Climate and Environmental Change along the Belt and Road" Institute of Earth Environment, Chinese Academy of Sciences (CAS), China.

— 2022: Short course, "***Sedimentary Provenance Analysis***" Geoscience Center, Department of Sedimentology & Environmental Geology, University of Göttingen, Germany.

— 2022: Summer School, "***3rd School of Heavy Mineral Analysis***" Dipartimento di Scienze dell"Ambiente, del Territorio e di Scienze della Terra, Università di Milano-Bicocca, Italia.
— 2021: Summer School "***DEPThS: Field-based summer school on subduction forearc dynamics***" Dipartimento di Scienze dell"Ambiente, del Territorio e di Scienze della Terra, Università di Milano-Bicocca, Italia.
— 2021: Winter School, "***Young Researcher Forum on Sustainable Biomass and Climate Change***" Dipartimento di Scienze dell"Ambiente, del Territorio e di Scienze della Terra, Università di Milano-Bicocca, Italia.

Awarded Grants

— ***PhD Scholarship*** 2021-2023
— ***Extra-EU Erasmus Fellowship*** 2023
— ***International Association of Sedimentology*** (IAS) Research Grant 2023
— ***IAS Travel Grant*** for 36th IAS Annual Meeting, Dubrovnik. 2023
— ***International Union for Quaternary Research (***INQUA) grant 2022
— ***IAS Travel Grant*** Sedimentary Provenance Analysis short course in Göttingen, Germany. 2022

Acknowledgements

I express my deepest gratitude to **Allah ﷻ Almighty**, who is the eternal source of wisdom, and to the **Holy Prophet Muhammad** ﷺ, an inspiration and complete suite of life for humanity. They provided me with the courage and determination to embark on and successfully complete this Ph.D. research journey.

I am sincerely indebted to the University of Milano-Bicocca (Unimib), Italy, for awarding me a fully funded Ph.D. scholarship, enabling me to pursue and accomplish my ambitious research goals. My heartfelt appreciation extends to my esteemed tutor, **Professor Eduardo Garzanti**, and my dedicated supervisor, **Professor Giovanni Vezzoli**, for their invaluable support and guidance throughout the course of my degree and research. I extend my gratitude to **Professor Peter D. Clift** from University College London (UCL), UK, and Louisiana State University (LSU), USA for providing me with the opportunity to be affiliated with both institutions, facilitating laboratory analysis and his critical and very valuable reviews, which significantly enhanced my research skills and contributed to the publication of my work in high-impact international journals.

I wish to express special thanks to **Dr. Guido Pastore** for his constructive scientific discussions and for my studies software training crucial to my research, I also appreciate the contributions of **Prof. Sergio Andò, Prof. Pieter Vermeesch Prof. Alberto Resentini, and Dr. Mubashir Ali** for their valuable comments during the different stages of my research. I am also thankful to **Miss Marta Barbarano** for teaching and improving my laboratory skills.

My heartfelt appreciation goes to my beloved parents, **Mr. Noor Sikandar and Mrs. Mumtaz Bibi**, my siblings, and especially the memory of Late Mr. Muhammad Umar Sikandar, for their unwavering support. Despite the geographical distance, their continuous remembrance during special occasions and celebrations has been a source of strength. This journey would have been incomplete without the companionship of my dear friends from Unimib, Italy, and LSU, USA. I am sincerely thankful for their sincere and warm camaraderie, which made it possible for me to navigate life in two foreign countries while completing my research. From the depths of my heart, I express gratitude to my friends for the laughter and joyous moments we shared together.

MUHAMMAD USMAN

Registration ID: 869000

Appendix

For this PhD thesis including both projects (Minjiang, South China and Thar Desert, Pakistan), a substantial volume of datasets has been generated, each comprising a considerable amount of data. To facilitate accessibility, all datasets are stored in a dedicated Google Drive folder, along with the corresponding Excel files for the tables:

https://drive.google.com/drive/folders/1OMLWzGXiCjyvID_p4xYOJRTnFyCCf0k_?usp=drive_link

List of files in the folder:

Chapters 2 to 5: Location of the samples from Minjiang River and Thar Desert with all details including lat/long and all other possible information regarding different sites.

Chapter 4: The detailed framework of petrography and heavy minerals is added in the chapter as Table and data for Detrital zircon are here in this excel sheet.

Chapter 6: Location of the samples, framework petrography, heavy minerals data, Detrital zircon measures including *DZ* mixing *DZ* state calculations for the Thar Projects.

Chapter 7: Geochemistry data, with Sr and Nd radiogenic isotope data for the Thar Project including various geochemical indices.

Geochronological Analysis, Secondary Standard

Secondary standard GJ1 (Jackson et al., 2004) (Fig. S1) and 91500 (Wiedenbeck et al., 2004) (Fig. S2) were routinely employed during the isotopic analysis at the Geochronological London Centre at University College London to assess the accuracy of the data. 24/24 analysis of GJ1 have been accepted. The weighted mean age resulted as 595.3±2.6 and MSWD=3.4. Zircon standard 91500 resulted with a weighted average age of 1047.8±4.9 and MSWD=1.9 and 24/24 accepted analysis.

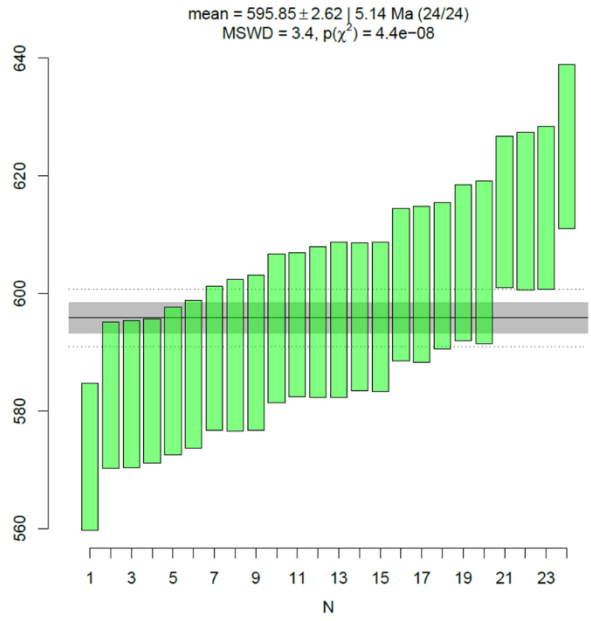

Figure S1. Showing the age variation and also the mean age for the secondary standard GJ1.

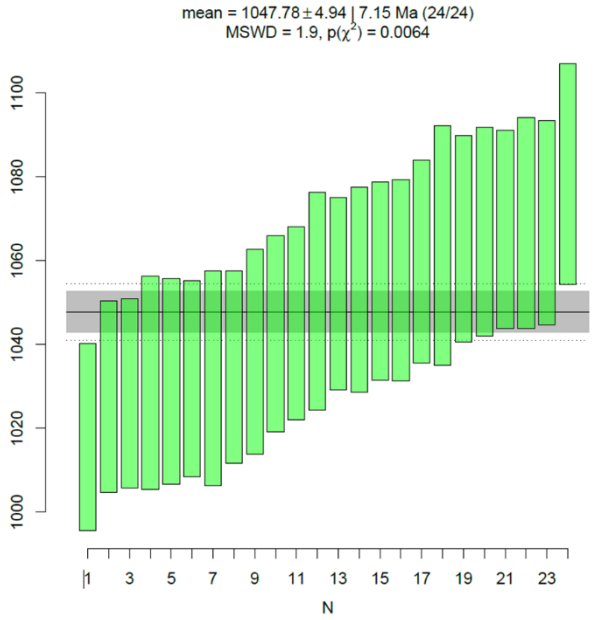

Figure S2. Showing the age variation and also the mean age for the secondary standard 91500.

Statistical Techniques

Geological data are often presented in percentages that represent relative contributions of the single variables to the whole. This means that the relevant information is contained only in the ratios between variables of the data, referred to below as compositional data, or compositions (Pawlowsky-Glahn and Buccianti, 2011). As a consequence, the sum of the variables can be set to a certain constant c, without loss of information, and compositional data are represented as row vectors on the simplex:

$$x = (x_1 \ \dots, x_D), x_i > 0, i = 1, \dots, p, \sum_{i=1}^{p} x_i = c$$

The constant c is usually chosen as 1 or 100 when the variables can be interpreted as percentages. Unfortunately, the obvious and natural properties of compositional data are in contradiction to most of the methods provided by standard multivariate statistics. In practice, standard statistical methods can lead to questionable results if they are directly applied on the original compositional data. This holds for covariance structure of compositions: by eliminating one or more variables, the covariance structure can completely change.

Another problem is connected to the relative scale of the compositional data. Variables with small values are usually represented by larger errors than the other variables, which can lead (as in the case of principal component analysis - PCA) to misleading results. Thus, variables with low contributions must be omitted before the statistical analysis of compositional data begins. Not only the above mentioned, but also many other serious problems can arise, when attempting to employ standard statistical methods to compositional data (Aitchison, 1986). The main reason is the different geometrical structure of compositions on the simplex. As a way out, a family of log-ratio transformations from the simplex to the standard Euclidean space was introduced (e.g. Egozcue et al., 2003) that makes standard statistical analysis possible, although special care must be taken when applying concrete statistical methods (Pawlowsky-Glahn and Buccianti, 2011).

This holds also for the well-known biplot for graphical display of both observations (denoted as points) and variables (rays) using results of a PCA (Gabriel, 1971). The centered log-ratio (clr) transformation, defined as:

$$clr(x) = \left(ln\frac{x_1}{\sqrt{\prod_{i=1}^{D} x_i}}, \ldots, ln\frac{x_{p1}}{\sqrt{\prod_{i=1}^{D} x_i}} \right)$$

enables construction of a reasonable biplot for compositional data (Aitchison and Greenacre, 2002; Filzmoser et al., 2009). Here, points represent as usual an approximation of the clr transformed multivariate observations on the plane (in the sense of PCA) and provide a tool to explore groups in compositional data sets. However, the interpretation of rays corresponds to another covariance structure of compositions. If the vertices of the rays coincide (or nearly so), it means that the ratio *xi/xj* between the *i-th* and *j-th* variable coincide (or nearly so). This also applies for the concept of distance between two compositions that is important in the statistical analysis of compositional data, particularly in such activities as cluster analysis and multidimensional scaling. The Aitchison's distance (Aitchison, 1986) is then given by:

$$d_a(x, y) = \left\{ \sum_{i=1}^{D} \left[log\frac{x_i}{g_m(x)} - log\frac{y_i}{g_m(y)} \right]^2 \right\}^{\frac{1}{2}}$$

where g_m is the geometric mean of the components, which can be shown to satisfy all the usual metric axioms and to depend only on perturbation distance. It is also easy to show that this metric satisfies the two key principles mentioned above.

Linear Mixing Model

Linear mixing models have been developed to summaries variation among a series of observations in terms of proportional contributions of a fixed number of (theoretical) end members. This statistical model is used to compare detrital modes from modern sand or ancient sandstone, and to objectively identify the best analogue for any sample of a modern or ancient sedimentary deposit (Garzanti et al 2012).

A decisive factor of success in this method is the use of large multiple datasets displaying sufficiently distinct values in diverse end members. Forward mixing models can be made for bulk petrography and heavy-mineral suites as well as for any physical (grain density), geochemical (element concentrations, stable-isotope ratios), or geochronological parameters (apatite fission tracks, zircon U–Pb age spectra), and separately on sediments of various sizes and transport modes (suspended load and

bedload). By comparing and integrating several independent calculations thus obtained we can then progressively obtain a more robust provenance estimate.

Fluvial sediments are complex mixtures of monocrystalline and polycrystalline grains eroded from diverse lithologic and tectonic units, supplied in various proportions by numerous streams to successive segments of a trunk river system. Sand compositions can be expressed as mixtures of a fixed number of end-members (Weltje, 1997), and the mixing can be expressed by regression analysis (Draper and Smith, 1981). The linear mixing model is formulated as follows (Weltje, 1997). Let *y* be the row vector of compositional data with *p* columns representing variables, *X* a matrix of end-member compositions with *n* rows representing observations and *p* columns representing variables, and *b* a row vector of coefficients with $q = n$ columns representing the proportional contribution of the end- members to the observation. In matrix notation, a linear regression model can be expressed as,

$$y = \beta X + e$$

The row vector *y* consists of non-negative linear combination β of q end-member compositions, and *e* is a row vector of errors with *p* columns representing variables. Following the definition of compositional data (Pawlowsky-Glahn & Buccianti, 2011), compositional variables are positive real numbers, and can be normalized to sum to a constant *c*. For the purposes of linear mixing models, this definition is extended also to the case of non-negative parts,

$$\sum_{j=1}^{p} y_{i=c,}\ y_i \geq 0$$

Solving the linear regression problem requires estimation of the row vector β describing a functional linear relation *b* between a matrix of end-member compositions *X* and an output row vector *y*. The solution of the first equation consists in the calculation of the row vector of coefficients b such that,

$$\hat{y} = bX$$

where $\hat{y}$ is a row vector of calculated compositional data with *p* columns representing variables. This equation represents a linear regression model (or perfect mixing). The model parameters are subject to the following non-negativity and constant-sum constraints,

$$\sum_{k=1}^{q} b_k = 1, \qquad b_k \geq 0$$

$$\sum_{j=1}^{p} x_{kj} = 1, \qquad x_{kj} \geq 0$$

and

$$\sum_{j=1}^{p} \hat{y}_j = c, \qquad \hat{y}_j \geq 0$$

and thus,

$$\sum_{j=1}^{p} e_j = 0$$

The goodness of fit of the forward mixing model can be assessed using a coefficient of multiple correlation *cr*,

$$cr = \sqrt{1 - \frac{RSS}{TSS}}$$

where RSS is the residual sum of squares and TSS is the total sum of squares,

$$RSS = \sum_i (y_i - \hat{y}_i)^2 \,; \;\; TSS = \sum_i (y_i - \bar{y}_i)^2$$

The coefficient *cr* departs from a decomposition of the total sum of squares into the "explained" sum of squares (the sum of squares of predicted values, in deviations from the mean) and the residual sum of squares. The coefficient of multiple correlation is a measure of the extent to which the total variation of the dependent variable is explained by the forward model. The *cr* statistic takes on a value between 0 and 1. A value of *cr* close to 1, suggesting that the model explains well the variation in the dependent variable, is obviously important if one wishes to use the model for predictive or forecasting purposes. In provenance studies, the coefficient of multiple correlation measures the correspondence between theoretical detrital modes of sediments supplied by different combinations of diverse end-member sources (e.g., tributaries, tectonic units, parent lithologies; first-order sampling scale of Ingersoll, 1990) and the observed detrital mode of one trunk-river sediment or sedimentary rock in the basin (third- order sampling scale of Ingersoll, 1990).

References cited in the Appendix

- Aitchison, J. (1986). The Statistical Analysis of Compositional Data. Chapman and Hall, London, 416 pp.

- Aitchison, J., & Greenacre, M. (2002). Biplots of compositional data. Applied Statistics, 51, 375-392.
- Alizai, A., Carter, A., Clift, P. D., VanLaningham, S., Williams, J. C., & Kumar, R. (2011). Sediment provenance, reworking and transport processes in the Indus River by U-Pb dating of detrital zircon grains. Global and Planetary Change, 76, 33-55. doi:10.1016/j.gloplacha.2010.11.008
- Clift, P. D., Mark, C., Alizai, A., Khan, H., & Jan, M. Q. (2022). Detrital U–Pb rutile and zircon data show Indus River sediment dominantly eroded from East Karakoram, not Nanga Parbat. Earth and Planetary Science Letters, 600, 117873. doi:10.1016/j.epsl.2022.117873
- Clift, P. D., Campbell, I. H., Pringle, M. S., Carter, A., Zhang, X., Hodges, K. V., Khan, A. A., & Allen, C. M. (2004). Thermochronology of the modern Indus River bedload; new insight into the control on the marine stratigraphic record. Tectonics, 23(TC5013). doi:10.1029/2003TC001559.
- Draper, N., & Smith, H. (1981). Applied Regression Analysis, 2nd ed. Wiley, New York.
- East, A. E., Clift, P. D., Carter, A., Alizai, A., & VanLaningham, S. (2015). Fluvial–Eolian Interactions In Sediment Routing and Sedimentary Signal Buffering: An Example From the Indus Basin and Thar Desert. Journal of Sedimentary Research, 85, 715-728. doi:10.2110/jsr.2015.42.
- Egozcue, J. J., Pawlowsky-Glahn, V., Mateu-Figueraz, G., & Barceló-Vidal, C. (2003). Filzmoser, P., Hron, K., & Reimann, C. (2009). Principal component analysis for compositional data with outliers. Environmetrics, 20(6), 621–632.
- Egozcue, J. J., Pawlowsky-Glahn, V., Mateu-Figueras, G., & Barcelo-Vidal, C. (2003). Isometric logratio transformations for compositional data analysis. Mathematical geology, 35(3), 279-300.
- Gabriel, K. R. (1971). The biplot graphical display of matrices with application to principal component analysis. Biometrika, 58(3), 453–467.
- Garzanti, E., Resentini, A., Vezzoli, G., Andò, S., Malusà, M., & Padoan, M. (2012). Forward compositional modelling of Alpine orogenic sediments. Sedimentary Geology, 280, 149-164.
- Garzanti, E., Liang, W., Andò, S., Clift, P. D., Resentini, A., Vermeesch, P., & Vezzoli, G. (2020). Provenance of Thal Desert sand: Focused erosion in the western

Himalayan syntaxis and foreland-basin deposition driven by latest Quaternary climate change. Earth-Sci. Rev., 207, 103220. doi:10.1016/j.earscirev.2020.103220.

- Ingersoll, R. V. (1990). Actualistic sandstone petrofacies: discriminating modern and ancient source rocks. Geology, 18(8), 733–736.
- Jackson, S. E., Pearson, N. J., Griffin, W. L., & Belousova, E. A. (2004). The application of laser ablation-inductively coupled plasma-mass spectrometry to in situ U–Pb zircon geochronology. Chemical Geology, 211(1-2), 47-69.
- Jonell, T. N., Carter, A., Böning, P., Pahnke, K., & Clift, P. D. (2017). Climatic and glacial impact on erosion patterns and sediment provenance in the Himalayan rain shadow, Zanskar River, NW India. Geological Society of America Bulletin, 129(7-8), 820-836. doi:10.1130/B31573.Filzmoser, P., Hron, K., Reimann, C. 2009. Principal component analysis for compositional data with outliers. Environmetrics 20, 621–632.
- Pawlowsky-Glahn, V., & Buccianti, A. (2011). Compositional data analysis. Chichester: Wiley.
- Sundell, K., & Saylor, J. E. (2017). Unmixing detrital geochronology age distributions. Geochemistry, Geophysics, Geosystems, 18, 2872–2886.
- Weltje, G. J. (1997). End-member modelling of compositional data: numerical statistical algorithms for solving the explicit mixing problem. Mathematical Geology, 29(4), 503–549.
- Wiedenbeck, M., Hanchar, J. M., Peck, W. H., Sylvester, P., Valley, J., Whitehouse, M., Kronz, A., Morishita, Y., Nasdala, L., Fiebig, J., Franchi, I., Girard, J.-P., Greenwood, R. C., Hinton, R., Kita, N., Mason, P. R. D., Norman, M., Ogasawara, M., Piccoli, P. M., … Zheng, Y.-F. (2004). Further Characterisation of the 91500 Zircon Crystal. Geostandards and Geoanalytical Research, 28(1), 9–39. doi:10.1111/j.1751-908X.2004.tb01041.
- Zhuang, G., Najman, Y., Tian, Y., Carter, A., Gemignani, L., Wijbrans, J., Jan, M. Q., & Khan, M. A. (2018). Insights into the evolution of the Hindu Kush-Kohistan-Karakoram from modern river sand detrital geo- and thermochronological studies. Journal of the Geological Society, London, doi:10.1144/jgs2018-007.